Order Number 9303305

# Effect of airfoil thickness on high-frequency gust interaction noise

Tsai, Chung-Tien, Ph.D.

The University of Arizona, 1992

U·M·I
300 N. Zeeb Rd.
Ann Arbor, MI 48106

# EFFECT OF AIRFOIL THICKNESS ON HIGH-FREQUENCY GUST INTERACTION NOISE

by

Chung-Tien Tsai

---

A Dissertation Submitted to the Faculty of the

DEPARTMENT OF AEROSPACE AND MECHANICAL ENGINEERING

In Partial Fulfillment of the Requirements
For the Degree of

DOCTOR OF PHILOSOPHY
WITH A MAJOR IN MECHANICAL ENGINEERING

In the Graduate College

THE UNIVERSITY OF ARIZONA

1 9 9 2

THE UNIVERSITY OF ARIZONA
GRADUATE COLLEGE

As members of the Final Examination Committee, we certify that we have read the dissertation prepared by Chung-Tien Tsai

entitled Effect of Airfoil Thickness on High-Frequency Gust Interaction Noise

and recommend that it be accepted as fulfilling the dissertation requirement for the Degree of Doctor of Philosophy

| | |
|---|---|
| Edward J. Kerschen | 7/24/92 Date |
| Thomas F. Balsa | 8/3/92 Date |
| Chuan F. Chen | 8/13/92 Date |
| George L. Lamb | 7/27/92 Date |
| | Date |

Final approval and acceptance of this dissertation is contingent upon the candidate's submission of the final copy of the dissertation to the Graduate College.

I hereby certify that I have read this dissertation prepared under my direction and recommend that it be accepted as fulfilling the dissertation requirement.

Dissertation Director Edward J. Kerschen — 8/6/92 Date

## STATEMENT BY AUTHOR

This dissertation has been submitted in partial fulfillment of requirements for an advanced degree at The University of Arizona and is deposited in the University Library to be made available to borrowers under rules of the Library.

Brief quotations from this dissertation are allowable without special permission, provided that accurate acknowledgment of source is made. Requests for permission for extended quotation from or reproduction of this manuscript in whole or in part may be granted by the head of the major department or the Dean of the Graduate College when in his judgment the proposed use of the material is in the interests of scholarship. In all other instances, however, permission must be obtained from the author.

SIGNED: ______________________

## ACKNOWLEDGMENT

I would like to thank my advisor, Professor Edward J. Kerschen, for his advice and guidance in performing this work and his willingness to share with me his tremendous physical insight. I also wish to thank Professor Thomas F. Balsa, whose interest and suggestions are very helpful in the course of this study. I am thankful to Professor George Lamb for his fruitful instructions on complex analysis and linear wave motion, and his kindness and helpfulness. The willingness of Professor Chuan F. Chen to serve on my committee is greatly appreciated.

I am grateful to Steve A. Nobe and Sekong Man for various suggestions and help. Thanks are also extended to Dr. Haldun Guvenen for helpful discussions in the course of my study. I would also like to thank my officemates, Dr. Meelan Choudhari, *Hu* Zhang and Dr. Paul Hammerton for their friendship and support. Special thanks go to Dr. Matthew R. Myers whose earlier work in airfoil-gust interactions provided much guidance for me.

Special acknowledgements go to my parents. Their encouragement motivated me undertake this work. I am thankful for their unending support financially and emotionally.

This work was funded by NASA Lewis Research Center under grant MAG3-357. I gratefully acknowledge this support.

# TABLE OF CONTENTS

TABLE OF CONTENTS--*continued*

# LIST OF ILLUSTRATIONS

LIST OF ILLUSTRATIONS--*continued*

LIST OF ILLUSTRATIONS--*continued*

## ABSTRACT

A theory is developed for the influence of airfoil thickness on sound generated by the interaction of high-frequency convected disturbances with a symmetric airfoil at zero angle of attack. Both vortical and entropic convected disturbances are considered. The analysis is based on a linearization of the inviscid equations of motion about the non-uniform mean flow past the airfoil. The mean flow is assumed to be two-dimensional and subsonic. The Mach number is assumed to be $O(1)$, although the small Mach number limit is also investigated. The analysis utilizes singular perturbation methods, and involves two asymptotic parameters: the airfoil thickness to chord ratio is assumed small ($\epsilon << 1$), and the aerodynamic reduced frequency is assumed large ($k = \omega b/U_\infty >> 1$), with $\epsilon k = O(1)$.

The singular perturbation analysis shows that the primary sound generation is concentrated in a local region surrounding the airfoil leading edge. The size of this local region scales on the disturbance wavelength. The solution in the local leading-edge region reveals several sound-generating mechanisms which involve mean flow gradients. The interaction of the convected disturbance with the trailing edge does not generate sound. However, the trailing edge is a scatterer of the sound field generated in the leading-edge region. Away from the airfoil edges, the propagation of the primary sound field from the leading edge and the secondary, scattered sound field from the trailing edge is described by geometric acoustics, with the amplitude varying on the scale of the airfoil chord and the phase varying on the much smaller scale of the disturbance wavelength. In addition, diffraction-type transition regions exist along the airfoil surfaces and downstream of the airfoil.

The influence of airfoil thickness on the total sound power is found to be controlled primarily by the Strouhal number $\mathrm{St} = \omega r_n / U_\infty$, where $r_n$ is the nose radius of the airfoil. Small values of $St$ reduce the sound power relative to the level for $St = 0$, but with further

increases of $St$ the noise level rises sharply. The increases in sound power level due to leading-edge thickness are more substantial at higher Mach numbers. Airfoil thickness produces dramatic changes in the far-field directivity. The sound power and directivity are strong functions of the gust characteristics.

# CHAPTER I

# INTRODUCTION

The sound generated by aeronautical and hydronautical vehicles has a significant impact on the utility and operational constraints for these vehicles, in both civilian and military applications. Thus there is need to develop a better understanding of, and prediction capability for, the noise mechanisms which are responsible for this noise. Much of the noise generated by these vehicles is produced by the propulsion systems. These propulsion systems generally consist of rows of airfoils, and the unsteady interaction of these airfoils with convected disturbances is an important contributor to the overall noise level produced by the vehicle. Aircraft turbofan engines or counter-rotation propfans are examples of types of propulsion systems which exhibit high levels of noise due to these unsteady interactions. In this dissertation, a theoretical study of sound generation by the interaction of airfoils with convected disturbances is presented.

Convected disturbances, often called gusts, are disturbances in a fluid which move at the local mean-flow velocity. A common example of a convected disturbance is free-stream turbulence. Convected disturbances can be separated into two types, vortical disturbances and entropic disturbances. For the high flow speeds (or high Reynolds numbers) which are characteristic of aeronautical and hydronautical propulsion systems, convection effects dominate over diffusive effects throughout most of the flow field, and in analyzing the flow it is reasonable to neglect the fluid viscosity. The general vortex laws then show that vorticity is convected at the flow speed. Similarly, neglecting thermal diffusion, entropy (or temperature) fluctuations are also convected disturbances.

In addition to atmospheric disturbances which may flow into the propulsion system, the flow field within the propulsion system contains important sources of convected disturbances. The wakes of upstream blades, vanes, struts or other bodies are a source of convected vorticity disturbances. Entropy (or temperature) fluctuations which are generated in the combustor convect downstream and interact with the turbine blade rows.

As an example, consider a single turbomachinery stage consisting of a rotor blade row and a stator vane row. This could be the fan stage of a turbofan aircraft engine. Turbomachinery geometries are generally cylindrical. However, for the purpose of analysis they can often be treated as a two-dimensional geometry involving rows with infinite numbers of blades. Figure 1.1 is a two-dimensional model for the rotor-stator interaction. The rotor blades and stator vanes appear as rows of infinite extent, with the rotor row translating vertically at a velocity $U_{rotor}$. In a reference frame translating with the rotor, the flow behind the rotor row appears steady. This flow appears to consist of a uniform velocity $U_1$ plus the spatially periodic velocity deficit $w$ corresponding to the blade wakes. In typical applications the magnitude of $w$ is very small compared to that of $U_1$, and the deficit is essentially convected at the local mean-flow velocity $U_1$. In a reference frame fixed to the stator vanes, the mean-flow velocity is $U_1 + U_{rotor}$; the wake deficits convect at this speed and are a periodic function of space and time. Thus, the unsteady interaction of the wakes with the stator vanes is an airfoil-gust interaction. The situation for a counter-rotation propfan is similar to that discussed above, except that the downstream blade row is a second rotor translating in the opposite direction.

In predicting noise generated by these airfoil-gust interactions, the airfoils involved are often modeled as zero-thickness flat plate aligned with a uniform mean flow. However, this approach ignores important physical effects, such as the distortion of the gust by the mean-flow gradients in the vicinity of the airfoils. In this dissertation, we examine the influence of airfoil thickness on the noise generated by airfoil-gust interactions.

The significance of the steady flow disturbance on the noise generation process was

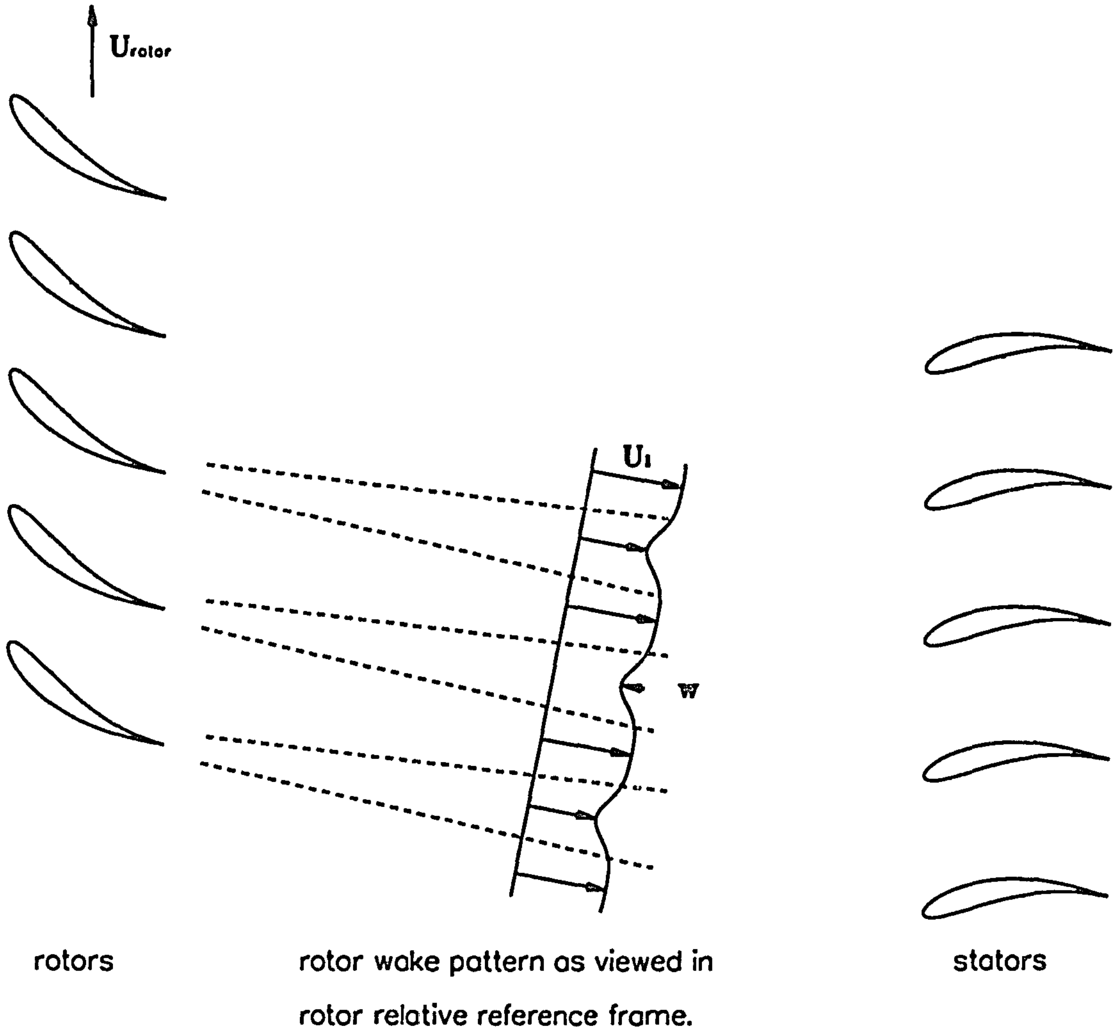


Figure 1.1 Two-dimensional model for the rotor-stator interaction.

first recognized by Ffowcs Williams and Hawkings (1969a,b). Their approach was based upon Lighthill's acoustic analogy. The acoustic analogy is a rearrangement of the equation of motion into a uniform-medium wave equation and a complicated source term. The source term is Lighthill's stress tensor, which depends on the pressure (or density) being solved for in the equation. Hence, one must have at least some prior knowledge about the source term and be able to model it in order to solve the wave equation. Ffowcs Williams and Hawkings modeled the interaction of the gust with the potential flow around the airfoil as a quadrupole source term. They used dimensional arguments to show that, at high subsonic Mach numbers, the quadrupole field should dominate the surface dipole field. Goldstein, Rosenbaum, and Albers (1974) and Mani (1974) utilized Ffowcs Williams' quadrupole formulation to produce actual prediction methods. In these methods the mean flow through the stator cascade was modeled as that due to a row of point vortices. Such an approximation is valid when the gust wavelength is long compared to the airfoil chord, but is inappropriate when the wavelength is on the order of or small compared to the airfoil chord.

In general, for acoustically compact interactions, in which the sound wavelength is large compared to the airfoil chord, the modelling of the Lighthill stress tensor is fairly insensitive to details of the source model. However, for the non-compact case, the details of the source are more crucial and heuristic modeling is less straightforward. The present analysis involves non-compact sources, since the unsteady flow has a length scale which is short compared to the airfoil chord.

For analyzing airfoil-gust interactions, rapid distortion theory (Goldstein 1978) provides an attractive alternative to the acoustic analogy. In rapid distortion theory, the inviscid-flow equations are linearized about the non-uniform, steady flow past the airfoil. Rapid distortion theory captures the influence of the mean-flow gradients on the unsteady flow in a systematic approximation to the governing equations.

The first application of rapid distortion theory to the study of airfoil-gust interactions was presented by Goldstein and Atassi (1976). Their analysis assumed an incompressible mean flow and is useful for determining the sound field in the low-frequency limit. Goldstein (1978) extended rapid distortion theory to include compressible mean flows. Goldstein's formulation requires the solution of a linear convected wave equation with a specified source term and boundary conditions. The equation has variable coefficients, which account in a natural way for the non-uniform medium of propagation. In contrast, non-uniform propagation effects in the acoustic analogy appear as distributed source terms of the constant-coefficient wave equation.

Despite its linearity, Goldstein's equation is difficult to solve since the variable coefficients and source term must in general be determined numerically. Kerschen and Balsa (1981) considered a two-dimensional mean flow and introduced the velocity potential $\phi$ and streamfunction $\psi$ as coordinates. They were able to simplify the equations considerably for the case of a fluid satisfying the tangent-gas equation of state. However, numerical methods are still required to evaluate the drift function (which will be defined later) appearing in the source term and boundary condition. With the further assumption that the mean flow is a small perturbation to a uniform flow, thin airfoil theory can be used to evaluate the drift function analytically and Goldstein's equation can be further simplified. The mean-flow perturbation velocity, which is $O(\epsilon)$ relative to the uniform flow, is assumed to be large compared to the $O(\nu)$ unsteady velocity. Kerschen and Myers (1987a) showed that the tangent-gas approximation leads to erroneous results in certain situations, including that of high-frequency gusts interacting with an airfoil. They incorporated the perfect gas thermodynamic relations in the equations of Kerschen and Balsa (1981), utilizing the small-perturbation mean-flow assumption, $\nu << \epsilon << 1$.

An additional simplification arises in the high-frequency limit. In this case the boundary conditions at the airfoil leading-edge and trailing-edge regions can be satisfied iteratively. In the iterative scheme, a leading-edge problem is first solved by assuming that the airfoil is "locally semi-infinite" in the downstream direction. To correct the resulting error in the boundary condition along the wake, a trailing-edge problem is formulated in which the airfoil is "locally semi-infinite" in the upstream direction. This correction gives the wrong boundary condition upstream of the airfoil, and another leading-edge problem arises to correct the upstream boundary condition. The iteration between leading-edge and trailing-edge regions continues in this manner.

For the simplified problem of a zero-thickness flat plate parallel to a uniform stream, Landahl (1958) showed that the resulting series converges for all disturbance wavelengths. The high-frequency approximation has been developed for the case of a uniform mean flow by Adamczyk (1974), Amiet (1975, 1976), and Martinez and Widnall (1980). Amiet (1976) showed that the first term in the high-frequency series predicts the unsteady lift on the airfoil to within ten percent accuracy, when the ratio of the acoustic wavelength $\lambda_{ac}$ to the airfoil chord $2b$ satisfies $\lambda_{ac}/2b \leq 4$. Thus, the high-frequency approximation is remarkably robust. The accuracy is even better when two terms are included in the series.

Myers and Kerschen (1984) analyzed the noise generated by a high-frequency convected gust interacting with a two-dimensional, flat-plate airfoil at a small incidence angle to a uniform stream. A singular-perturbation approach involving two parameters, $\alpha$ and $k$, was utilized in their analysis. The small parameter, $\alpha << 1$, is the angle of attack of the airfoil, and the large parameter, $k >> 1$, is the ratio of the airfoil chord to the disturbance wavelength. Their analysis involves four asymptotic regions. Local regions, which scale on the gust wavelength, are present at the airfoil leading and trailing edges. They found that the noise generation is concentrated in the local leading-edge region. The sound field generated in the leading-edge region is scattered by the trailing edge. Downstream of the airfoil trailing edge is a "wake" region related to the transition from an illuminated to a shadow region. Away from the airfoil edges and wake regions, there is an outer region in which the solution has a geometric-acoustics behavior. They found that at high frequencies, moderate levels of airfoil steady loading can dramatically increase the noise level generated by airfoil-gust interaction.

Myers and Kerschen (1986) and Kerschen and Myers (1987b) extended this work to include the influence of airfoil camber. For the problem involving camber, an additional transition region near the airfoil surface is necessary in order to account for the influence of airfoil curvature on the propagation of acoustic waves. An important conclusion of this work is that the influence of loading on the total sound power level is correlated by the combination of parameters $\alpha_{eff}\sqrt{k}/\beta_{\infty}$ where $\alpha_{eff}$, the effective leading-edge incidence angle, is a measure of the strength of the local flow around the leading edge. Trailing-edge scattering significantly influences the directivity pattern, but has little effect on the total sound power level. This work is a significant advance over the earlier point-vortex models of Goldstein, Rosenbaum, and Albers (1974) and Mani (1974).

In this dissertation, we use a similar approach to develop a closed-form asymptotic solution for noise generated by a convected gust interacting with a thin, two-dimensional, symmetric airfoil. Primary attention is focused on the case of the Joukowski airfoil, but some extensions to the case of a general airfoil shape are also presented. In Chapter 2, we present Goldstein's equations and derive the simplified form of them for a two-dimensional, small-perturbation mean flow. In Chapter 3 the disturbance equations are solved for a Joukowski airfoil at zero angle of attack to a uniform stream. A parametric study of the characteristics of the far-field sound is presented in Chapter 4. Results of the parametric study are given in the form of acoustic power calculations and pressure directivity plots. In

Chapter 5 we summarize the conclusions of our work and make some suggestions regarding directions for future research.

# CHAPTER 2

# DERIVATION OF THE DISTURBANCE EQUATIONS

In this dissertation, rapid distortion theory is utilized to calculate sound generated by the interaction of convected disturbances with an airfoil. Goldstein (1978) developed the rapid distortion theory for compressible flows, and derived a particularly attractive form of the governing equations. Simplified forms of the governing equations for two-dimensional and small-disturbance mean flows were derived by Kerschen and Balsa (1981) and Kerschen and Myers (1987a). The derivation of the equations for rapid distortion theory involves significant analysis which is not familiar to a wide audience. Therefore, in this chapter we present a review of the derivation of the governing equations for rapid distortion theory.

Rapid distortion theory is concerned with the description of small-amplitude disturbances to a steady, compressible potential flow around an obstacle. The disturbances originate far upstream from the obstacle, where the mean flow is assumed to be uniform. Kovasznay (1953) described, and Goldstein (1978) reviewed, the nature of unsteady small-amplitude disturbances that may be imposed on a uniform flow. There are three types of disturbances: vorticity waves, acoustic waves, and entropy waves. Each of the three components to the unsteady motion is a solution of the governing equations and can be imposed independently of the others.

The velocity field for the unsteady disturbances to a uniform mean flow can be divided into two parts. The first part, often called a gust, is purely convected or "frozen in the flow". It has zero divergence and there are no pressure fluctuations associated with it. All of the fluid rotation or vorticity is associated with this field; hence it is often referred to as the vortical velocity. The second part is an irrotational field which contains pressure fluctuations, and for compressible flows is an acoustic wave. The acoustic wave propagates at the speed of sound relative to the fluid.

In addition to the unsteady velocity, entropy fluctuations may be imposed on the flow. The entropy fluctuations are decoupled from the velocity and pressure but do produce density fluctuations. The entropy fluctuations are convected at the mean-flow speed, i.e, they are also "frozen in the fluid". The unsteadiness referred to in preceding paragraphs is observed in the obstacle reference frame; in a uniform mean flow, the convected fields would appear steady in a frame moving at the mean-flow speed.

Since waves generated near the obstacle decay to zero amplitude at infinity, any finite-amplitude acoustic waves which are present far upstream must be incoming waves. Because we are interested in sound generation rather than in sound scattering, we do not consider any incident acoustic waves. We impose convected vortical and entropic disturbances far upstream, which become distorted as they convect downstream due to the non-uniform mean flow around the obstacle. The calculation of the sound field generated by the interaction of the disturbances with the mean flow and the boundary is the main objective of this dissertation.

We now derive Goldstein's equation in a general form, without specifying the obstacle or making any assumptions about the convected disturbance. The body and the gust will be further specified in Chapter 3. The assumptions made here are that the fluid is an inviscid, non-heat-conducting, perfect gas. For most aeronautical applications, where the mean flow and turbulent Reynolds numbers are large, and the fluid is air, these assumptions are well justified.

The analysis begins with the inviscid equations of motion, which are

(momentum) $$\rho \frac{DU}{Dt} = -\nabla p \ , \tag{2.1a}$$

(continuity)

$$\frac{D\rho}{Dt} + \rho\,\nabla\cdot\boldsymbol{U} = 0 \ , \tag{2.1b}$$

(energy)
$$\frac{DS}{Dt} = 0 \tag{2.1c}$$

where
$$\frac{D}{Dt} = \frac{\partial}{\partial t} + \boldsymbol{U}\cdot\nabla \ . \tag{2.1d}$$

Here $\rho$ is the density, $p$ the pressure, $\boldsymbol{U}$ the velocity, and $S$ the entropy of the fluid. The following expression, which is a consequence of the perfect-gas equation of state ($p = \rho RT$) and the first law of thermodynamics, will also be utilized

$$S_1 - S_2 = c_v \ln(p_1/p_2) - c_p \ln(\rho_1/\rho_2) \ . \tag{2.1e}$$

The subscripts 1 and 2 denote two thermodynamic states. The specific heats at constant volume and constant pressure, $c_v$ and $c_p$, are assumed to be constant.

At upstream infinity the velocity and entropy fields have the form

$$\boldsymbol{U} = \boldsymbol{U}_\infty + \boldsymbol{u}'_\infty \ , \tag{2.2a}$$

$$S = s'_\infty \ , \tag{2.2b}$$

with
$$\frac{u'_\infty}{U_\infty} = O(\nu) \quad \text{and} \quad \frac{s'_\infty}{c_p} = O(\nu) \ , \ \nu << 1 \ . \tag{2.2c,d}$$

Here the scalar velocities denote the magnitude of the vector quantities. Under the condition Eqs. (2.2c,d), Eqs. (2.1) will possess a solution of the form

$$\boldsymbol{U} = \boldsymbol{U}_0(\boldsymbol{x}) + \boldsymbol{u}'(\boldsymbol{x},t) \quad , \quad p = p_0(\boldsymbol{x}) + p'(\boldsymbol{x},t) \ , \tag{2.3a,b}$$

$$\rho = \rho_0(\boldsymbol{x}) + \rho'(\boldsymbol{x},t) \quad , \quad S = s'(\boldsymbol{x},t) \tag{2.3c,d}$$

with the unsteady quantities, denoted by primes, much smaller than the steady ones. The mean flow is the steady but nonuniform flow around the obstacle one would obtain if $u'_\infty$ and $s'_\infty$ were zero. The entropy for the mean flow is everywhere equal to a constant, which we take to be zero. Since viscosity is ignored and the steady flow at upstream infinity is assumed uniform, the mean flow is irrotational. The mean-flow velocity can be expressed as the gradient of a potential function; we will utilize this property below and in Chapter 3.

Inserting Eqs. (2.3) into Eqs. (2.1), neglecting squares of unsteady terms, and subtracting out the mean-flow equations, Goldstein (1978) obtained, after several subsequent manipulations, a set of linearized disturbance equations. (The states used in Eq. (2.1e) are the actual state and the mean-flow state.) The results are:

$$\frac{D_0 s'}{Dt} = 0 \ , \tag{2.4a}$$

$$\boldsymbol{u}' = \boldsymbol{v}' + \nabla G' \ , \tag{2.4b}$$

where
$$\boldsymbol{v}' = \frac{s'}{2\,c_p}\,\boldsymbol{U}_0 + \boldsymbol{v}^* \tag{2.4c}$$

with
$$\frac{D_0 \boldsymbol{v}^*}{Dt} + \boldsymbol{v}^* \cdot \nabla \boldsymbol{U}_0 = 0 \ , \tag{2.4d}$$

and the potential $G'$ satisfies

$$\frac{D_0}{Dt}\left(\frac{1}{a_0^2}\,\frac{D_0 G'}{Dt}\right) - \frac{1}{\rho_0}\nabla\cdot(\rho_0 \nabla G') = \frac{1}{\rho_0}\nabla\cdot(\rho_0 \boldsymbol{v}') \ . \tag{2.4e}$$

The quantity $a_0$ is the speed of sound for the mean flow. The substantial derivative is with respect to the mean flow, i.e.,

$$\frac{D_0}{Dt} = \frac{\partial}{\partial t} + \boldsymbol{U}_0 \cdot \nabla \ . \tag{2.4f}$$

The pressure is obtained from the relation

$$p' = -\rho_0 \frac{D_0 G'}{Dt} \quad , \tag{2.4g}$$

and the density is related to the pressure and entropy by

$$\rho' = p'/a_0^2 - \rho_0 s'/c_p \quad . \tag{2.4h}$$

The appropriate boundary condition on the body surface is

$$\mathbf{n}\cdot\nabla G' = -\mathbf{n}\cdot\mathbf{v}' \quad , \tag{2.4i}$$

where $\mathbf{n}$ is the normal to the surface. The radiation or outgoing wave condition applies at infinity.

Goldstein's velocity decomposition, Eq. (2.4b), does not correspond to the classical decomposition of a vector field into solenoidal and irrotational parts, since in general $\mathbf{v}'$ is not divergence free. We will find that $\mathbf{v}'$ represents a velocity field convected at the local mean-flow speed, having the gust at upstream infinity as its initial condition. The acoustic field is contained in the potential $G'$. One can begin to see the nature of the sound field produced in gust-airfoil interactions by examining Eqs. (2.4). One mechanism for sound generation is the interaction of the gust $\mathbf{v}'$ with the boundary, as described by the boundary condition Eq. (2.4i). Another mechanism is the source term of the wave equation (2.4e). A volume source is produced in the fluid whenever there are significant changes in the momentum flux $\rho_0 \mathbf{v}'$ associated with the convected disturbance. (Though, as we shall see, the source term does not always produce sound.) The sound generated propagates in a non-uniform medium as evidenced by the variable coefficients in Eq. (2.4e).

Equations (2.4a) and (2.4d), being first-order partial differential equations, can be solved by the method of characteristics. We give the solution below. Equation (2.4e), however, is much more difficult to solve. Under general circumstances, even the mean-flow quantities have to be determined numerically. In order to obtain an analytical solution, additional assumptions are introduced.

Kerschen and Balsa (1981) derived a simplified form of Goldstein's equations for the case of two-dimensional mean flows. Consider a two-dimensional mean flow with $U_{0,i} = U_{0,i}(x_1,x_2)$, $i = 1,2$ and $U_{0,3} = 0$. Since the vorticity and entropy fluctuations are convected along the mean-flow streamlines, they introduced the variables $(\phi,\psi)$ in the $(x_1,x_2)$ plane as orthogonal coordinates, where $\phi$ and $\psi$ are the modified forms of the velocity potential and the streamfunction for the mean flow. The appropriate coordinate metrics are

$$h_\phi = 1/U_0 \quad , \quad h_\psi = \rho_\infty/(\beta_\infty \rho_0 U_0) \tag{2.5a,b}$$

where $\beta_\infty{}^2 = 1 - M_\infty{}^2$ and $M_\infty = U_\infty/a_\infty$ is the mean-flow Mach number at infinity. The $\beta_\infty$ in the metric corresponds to a Prandtl-Glauert transformation, i.e.,

$$\phi = \phi_o \qquad , \qquad \psi = \beta_\infty\, \psi_o \tag{2.6a,b}$$

where $\phi_o$ and $\psi_o$ are the standard velocity potential and streamfunction for the mean flow. The Prandtl-Glauert transformation will produce the final equation in canonical form. Kerschen and Balsa (1981) allowed the unsteady disturbances to be three-dimensional and introduced the variable $\chi = U_\infty x_3$ as the third coordinate, where $x_3$ is the standard Cartesian coordinate. The factor of $U_\infty$ is for dimensional consistency with the other coordinates. The metric for $\chi$ is $1/U_\infty$. In $(\phi,\psi,\chi)$ space the substantial derivative becomes $D_0/Dt = \partial/\partial t + U_0{}^2\partial/\partial\phi$.

Since the governing equations are linear, and the mean flow is uniform far upstream, an arbitrary upstream disturbance can be represented as a superposition of harmonic waves. Hence consider vortical and entropic disturbances having the following form far upstream

$$\begin{bmatrix} \mathbf{v}' \\ s' \end{bmatrix}\Bigg|_{\phi \to -\infty} = \begin{bmatrix} U_\infty (A_t, A_n, A_3) \\ 2c_p B \end{bmatrix} e^{i(k_t \phi + k_n \psi + k_3 \chi - k_t U_\infty^2 t)} \quad . \tag{2.7a}$$

The quantities $(A_t, A_n, A_3)$ and $(k_t, k_n, k_3)$ are the velocity-amplitude and wavevector components in $(\phi,\psi,\chi)$ space. Far upstream where the flow is uniform the $(\phi,\psi,\chi)$ direction vectors coincide with the standard Cartesian unit vectors. Under uniform-mean-flow conditions $\mathbf{v}'$ is solenoidal, so the wavevector and velocity components must satisfy the relation

$$A_t\, k_t + A_n\, k_n\, \beta_\infty + A_3\, k_3 = 0 \quad . \tag{2.7b}$$

That is, the gust is a transverse wave. The factor $\beta_\infty$ comes from the metric $h_\psi$ ( see Eq. (2.5) ), utilized in taking the divergence.

Equation (2.7a) is the initial condition for the equations (2.4a,d) governing the convected quantities. Kerschen and Balsa (1981) derived the solution to these equations in the $(\phi,\psi,\chi)$ coordinate system. Separating Eq. (2.4d) into its three components, integrating the resulting first-order partial differential equations, and enforcing Eq. (2.7a), they showed that

$$\mathbf{v}'(\phi,\psi,\chi,t) = (v_t', v_n', v_3') \ , \tag{2.8a}$$

$$\frac{v_t'}{U_\infty} = \left[ \frac{A_t^*\, U_\infty}{U_0} + \frac{B\, U_0}{U_\infty} \right] e^{i\sigma} \ , \tag{2.8b}$$

$$\frac{v_n'}{U_\infty} = \frac{\rho_0\, U_0}{\rho_\infty\, U_\infty} \left[ A_n + \beta_\infty A_t^*\, \frac{\partial g}{\partial \psi} \right] e^{i\sigma} \ , \tag{2.8c}$$

$$\frac{v_3'}{U_\infty} = A_3\, e^{i\sigma} \ , \tag{2.8d}$$

$$s' = 2\, c_p\, B\, e^{i\sigma} \tag{2.8e}$$

where
$$\sigma = k_t\, \phi + k_t\, g(\phi,\psi) + k_n\, \psi + k_3\, \chi - k_t\, U_\infty{}^2\, t \ , \tag{2.8f}$$

$$A_t^* = A_t - B \tag{2.8g}$$

and
$$g(\phi,\psi) = \int_{-\infty}^{\phi} \left[ \frac{U_\infty{}^2}{U_0{}^2(\varsigma,\psi)} - 1 \right] d\varsigma \quad . \tag{2.8h}$$

The function $g(\phi,\psi)$ is Lighthill's Drift function (Lighthill 1956), which represents the cumulative distortion of fluid material lines relative to uniform convection at speed $U_\infty$.

Next consider the wave equation (2.4e) for $G'$, which at this point is the only remaining unknown. Because the mean flow and body shape are independent of the spanwise coordinate and time, the $\chi$ and $t$ dependence can be factored out of Eqs. (2.4). Setting

$$s' = s\, e^{i(k_3\chi - k_t\, U_\infty{}^2 t)} \ , \tag{2.9a}$$

$$v' = (v_t\,, v_n\,, v_3)\, e^{i(k_3\chi - k_t\, U_\infty{}^2 t)} \ , \tag{2.9b}$$

$$G' = G\, e^{i(k_3\chi - k_t\, U_\infty{}^2 t)} \ , \tag{2.9c}$$

Kerschen and Balsa (1981) found that Eq. (2.4e) transforms to

$$\begin{aligned} &\frac{\partial}{\partial\phi}\left[\beta_0{}^2\,\frac{\partial G}{\partial\phi}\right] + \frac{\partial}{\partial\psi}\left[\frac{\beta_\infty{}^2\,\rho_0^2}{\rho_\infty{}^2}\,\frac{\partial G}{\partial\psi}\right] + \frac{2\,i\,k_t\,U_\infty{}^2}{a_0^2}\,\frac{\partial G}{\partial\phi} \\ &+ \frac{U_\infty{}^2}{a_0^2}\left[\frac{k_t{}^2\,U_\infty{}^2}{U_0^2} - \frac{k_3^2}{M_0^2} - 2\,i\,k_t\,\frac{\partial}{\partial\phi}(\ln(a_0))\right] G \\ &= -\frac{\partial}{\partial\phi}\left[\frac{U_\infty}{U_0}\,v_t\right] - \frac{\partial}{\partial\psi}\left[\frac{\rho_0\,U_\infty\,\beta_\infty}{\rho_\infty\,U_0}\,v_n\right] - \frac{i\,k_3\,U_\infty{}^2}{U_0^2}\,v_3 \end{aligned} \tag{2.9d}$$

where $M_0$ is the local Mach number of the mean flow and $\beta_0{}^2 = 1 - M_0{}^2$. For a general compressible flow, the mean-flow quantities which appear in Eq. (2.9d) must be determined numerically, which precludes the possibility of an analytical solution for $G$.

Kerschen and Balsa (1981) showed that introducing the tangent gas approximation (Woods 1961) leads to significant further simplifications of Eq. (2.9d). Unfortunately, the tangent-gas approximation leads to unrealistic estimates for the variation in the speed of sound. This can lead to erroneous predictions for the influence of mean-flow variations on the propagation of acoustic waves. The errors are particularly significant for situations which involve high frequencies, such as the airfoil-gust interactions investigated in this dissertation.

In order to rectify the difficulties associated with the tangent-gas approximation, Kerschen and Myers (1987a) utilized the perfect-gas equation of state. They developed a simplified form of the rapid distortion theory equations for the case of a mean flow which is a small perturbation to a uniform flow. The mean flow perturbation is assumed to be small compared to the uniform flow component, say $\epsilon \ll 1$, but large compared to the unsteady flow component, say $\epsilon \gg \nu$.

The perfect-gas relations for a small-perturbation to a uniform mean flow are

$$\frac{U_0}{U_\infty} = 1 + q \ , \tag{2.10a}$$

$$\frac{a_0}{a_\infty} = 1 - \frac{\gamma-1}{2} M_\infty^2 \, q \quad , \quad \frac{M_0}{M_\infty} = 1 + \left(1 + \frac{\gamma-1}{2} M_\infty^2\right) q \ , \tag{2.10b,c}$$

$$\frac{\beta_0}{\beta_\infty} = 1 - \left(1 + \frac{\gamma-1}{2} M_\infty^2\right) \frac{M_\infty^2}{\beta_\infty^2} q \quad , \quad \frac{\rho_0}{\rho_\infty} = 1 - M_\infty^2 \, q \ . \tag{2.10d,e}$$

The function $q$ appearing in each relation is the $O(\epsilon)$ perturbation to the normalized mean-flow speed.

Introducing Eqs. (2.10) in Eq. (2.9d), making the following generalized Miles transformation,

$$h = G\, e^{i k_t M_\infty^2 \phi/\beta_\infty^2}\, e^{-M_\infty^2 q} \tag{2.11}$$

$$= G\, e^{i k_t M_\infty^2 \phi/\beta_\infty^2} \left[1 - M_\infty^2\, q + O(\epsilon^2)\right]$$

and neglecting terms of $O(\epsilon^2)$, Kerschen and Myers (1987a) showed that the modified potential $h(\phi,\psi)$ for the unsteady disturbance satisfies

$$\frac{\partial^2 h}{\partial \phi^2} + \frac{\partial^2 h}{\partial \psi^2} + w^2 (1 - 2\,\beta_\infty^2\, q)\, h \; +$$

$$(\gamma+1)\frac{M_\infty^4}{\beta_\infty^2}\left[ q\left[\frac{\partial^2 h}{\partial \psi^2} + 2\,i\,\delta\,\frac{\partial h}{\partial \phi} + (w^2+\delta^2)\,h\right] - \frac{\partial q}{\partial \phi}\left[\frac{\partial h}{\partial \phi} - i\,\delta\, h\right]\right] = S(\phi,\psi)\, e^{i\Omega} \tag{2.12a}$$

where

$$\delta = k_t/\beta_\infty^2 \quad , \quad w^2 = (M_\infty\, \delta)^2 - (k_3/\beta_\infty)^2 \quad , \quad \Omega = \delta\,\phi + k_n\,\psi + k_t\, g(\phi,\psi) \tag{2.12b,c,d}$$

and

$$S(\phi,\psi) = 2\left[ i\left(\frac{k_t\, A_t^*}{\beta_\infty^2} - k_n\, A_n\, \beta_\infty\right) q + i\left(k_n\, A_t^* + \frac{k_t\, A_n}{\beta_\infty}\right)\mu \right.$$
$$\left. + A_t^*\,\frac{M_\infty^2}{\beta_\infty^2}\,\frac{\partial q}{\partial \phi} + \frac{A_n\, M_\infty^2}{\beta_\infty}\,\frac{\partial q}{\partial \psi}\right] . \tag{2.12e}$$

The function $\mu(\phi,\psi)$ in Eq. (2.12e) is $1/\beta_\infty$ times the mean-flow angle relative to the uniform flow at upstream infinity. For a small-perturbation mean flow, Eq. (2.8h) for the Drift function reduces to

$$g = -2\int_{-\infty}^{\phi} q(\gamma,\psi)\, d\gamma \quad , \tag{2.12f}$$

as one can see by expanding $U_\infty^2/U_0^2 = 1/(1+q)^2$. The transformed boundary condition is

$$\left[\frac{\partial h}{\partial \psi} + M_\infty^2\,\frac{\partial q}{\partial \psi}\, h\right]_{\psi=\psi_0} = -\left[\frac{A_n}{\beta_\infty}(1 - M_\infty^2\, q) - 2\, A_t^*\, \mu\right] e^{i\Omega} \tag{2.12g}$$

where $\psi = \psi_0$ on the body surface and the range of $\phi$ corresponds to the body length in the

$(\phi,\psi)$ plane.

Expressions for the unsteady pressure field will be required later. The pressure is given by Eq. (2.4g). In terms of the modified potential $h$, this expression takes the form

$$p' = -\rho_\infty U_\infty^2 \left[ \frac{\partial h}{\partial \phi} - i \frac{k_t}{\beta_\infty^2} h \right] e^{i(k_3 x - k_t U_\infty^2 t - k_t M_\infty^2 \phi/\beta_\infty^2)} + O(\epsilon h) \ . \qquad (2.13a)$$

It is convenient to work in terms of the modified pressure $p$,

$$p = \frac{p' e^{-i(k_3 x - k_t U_\infty^2 t)}}{\rho_\infty U_\infty^2} = -\left[ \frac{\partial h}{\partial \phi} - \frac{i k_t}{\beta_\infty^2} h \right] e^{-i k_t M_\infty^2 \phi/\beta_\infty^2} \ . \qquad (2.13b)$$

In the next chapter, we develop the solution to Eqs. (2.12) governing the modified unsteady-disturbance potential $h(\phi,\psi)$ for the case of a symmetric Joukowski airfoil at zero angle of attack to the mean flow. All the analysis is carried out in the Prandtl-Glauert transformed, potential-streamfunction coordinates $(\phi,\psi)$. The final results are then transformed back into physical Cartesian coordinates for interpretation.

Before proceeding with the analysis of the unsteady motion, results for the mean-flow perturbation are required. The Prandtl-Glauert transformed velocity potential $\phi$ and streamfunction $\psi$ have the expansion

$$\phi + i\psi = U_\infty \left[ x_1 + i\beta_\infty x_2 + \epsilon(\phi_1 + i\psi_1) + O(\epsilon^2) \right] \ . \qquad (2.14)$$

For a thin, symmetric airfoil whose surface is described by

$$x_2 = \pm \epsilon N(x_1) \ , \qquad 0 \le x_1 \le 2b \ , \qquad (2.15)$$

the $O(\epsilon)$ perturbation to the mean-flow velocity potential satisfies (Ashley and Landahl 1965)

$$\beta_\infty^2 \frac{\partial^2 \phi_1}{\partial x_1{}^2} + \frac{\partial^2 \phi_1}{\partial x_2{}^2} = 0 \ , \tag{2.16a}$$

$$\left.\frac{\partial \phi_1}{\partial x_2}\right|_{x_2 = 0} = \pm \frac{\partial N(x_1)}{\partial x_1} \ , \qquad 0 \le x_1 \le 2b \tag{2.16b}$$

and

$$|\nabla\phi_1| \to 0 \text{ at infinity} \ . \tag{2.16c}$$

The perturbation streamfunction $\psi_1$ is related to the perturbation velocity potential $\phi_1$ by

$$\frac{\partial \psi_1}{\partial x_2} = \beta_\infty \frac{\partial \phi_1}{\partial x_1} \ , \qquad \frac{\partial \psi_1}{\partial x_1} = -\frac{1}{\beta_\infty} \frac{\partial \phi_1}{\partial x_2} \tag{2.17a,b}$$

where the factors of $\beta_\infty$ arise from the metric Eqs. (2.5).

Equations (2.16) can be reduced to an equivalent incompressible flow problem by introducing the Prandtl-Glauert transformation

$$\overline{x_1} = x_1 \ , \ \overline{x_2} = \beta_\infty x_2 \text{ and } \overline{\phi_1} = \beta_\infty \phi_1 \ . \tag{2.18a,b,c}$$

The function $\overline{\phi_1}(\overline{x_1},\overline{x_2})$ satisfies Eqs. (2.16) with $\beta_\infty$ set to unity in Eq. (2.16a). The well-developed potential theory can be utilized to find $\overline{\phi_1}$ in terms of a complex potential $F^i(z)$, where $z = x_1 + i\beta_\infty x_2$. The perturbation velocity potential $\phi_1$ and streamfunction $\psi_1$ for the compressible flow problem are then given by

$$\phi_1 + i\,\psi_1 = F(z) = \frac{1}{\beta_\infty} F^i(z) \ , \tag{2.19}$$

Expressions for the functions $q$, $\mu$ and $g$ in the $(\phi,\psi)$ plane are required for Eqs. (2.12). From Eq. (2.14), the transformation between the $(\phi,\psi)$ and $(x_1,x_2)$ coordinates is

$$z = \frac{\zeta}{U_\infty} + O(\epsilon) \tag{2.20}$$

where $\zeta = \phi + i\psi$. Furthermore, neglecting terms of $O(\epsilon^2)$, the functions $q$ and $\mu$ are given by

$$q(\phi,\psi) \; - \; i\,\mu(\phi,\psi) \; = \; \epsilon \, dF(\varsigma)/d\varsigma \; . \tag{2.21a}$$

Finally, the drift function, Eq. (2.12f), is given by

$$g(\phi,\psi) \; = \; -\,2\,\epsilon\,\mathrm{Re}\left\{ F(\varsigma) - F(-\infty) \right\} \tag{2.21b}$$

where the arbitrary constant in the complex potential $F$ is chosen such that $F(0) = 0$ and $F(-\infty)$ represents the value of the complex potential $F$ at upstream infinity. For further details, refer to Kerschen and Myers (1987a) or Myers (1987).

For a symmetric Joukowski airfoil of chord $2b$ and midchord thickness $\epsilon b$ (see figure 3.1), the function describing the airfoil surface is

$$N(x_1) \; = \; (b - x_1/2)\sqrt{(2 - x_1/b)\,x_1/b} \; . \tag{2.22a}$$

Integrating the result for $dF^i(z)/dz$ given by Jones and Cohen (1960), converting the result to the compressible flow case, and choosing the arbitrary constant in $F$ such that $F(0) = 0$, we find

$$F(\varsigma) \; = \; b/(2\beta_\infty)\left[ (\, \varsigma/b - 2\,)\sqrt{(\varsigma/b)^2 - 2\varsigma/b} - (\varsigma/b)^2 + 3\varsigma/b \right] \tag{2.22b}$$

and

$$F(-\infty) \; = \; 3/4\beta_\infty \; . \tag{2.22c}$$

# CHAPTER 3

## ANALYSIS FOR A SYMMETRIC AIRFOIL

In this chapter, the rapid distortion theory formulated in the previous chapter is applied to the airfoil-gust-interaction problem. We consider a thin, symmetric airfoil of chord $2b$ at zero angle of attack, interacting with a convected disturbance whose wavelength $\lambda$ is short compared with the airfoil chord. Throughout most of this chapter we consider the case of a Joukowski airfoil. However, in Section 3.7 we show that only slight modifications are necessary to extend our results to the case of a general thickness distribution. A schematic of the problem is shown in figure 3.1. The airfoil thickness at mid-chord is $\epsilon b$. The maximum thickness of $3\sqrt{3}\epsilon b/4$ occurs at the quarter-chord point, $x_1 = b/2$, and the airfoil nose radius is $\epsilon^2 b$.

Singular perturbation methods are utilized to solve Eqs. (2.12) for the modified acoustic potential $h$. The airfoil is assumed to be thin ($\epsilon << 1$) and the gust frequency is assumed to be high ($k >> 1$). To compare the magnitudes of the various quantities, the following nondimensionalizations are made:

$$\phi = b\,U_\infty\,\phi^\dagger \qquad \psi = b\,U_\infty\,\psi^\dagger \qquad \chi = b\,U_\infty\,\chi^\dagger \tag{3.1a,b,c}$$

$$h = b\,U_\infty\,h^\dagger \tag{3.1d}$$

$$(k_t, k_n, k_3) = k_t\,(1, k_n/k_t, k_3/k_t) = k_t\,(1, k_n{}^\dagger, k_3{}^\dagger) \tag{3.1e}$$

$$F = b\,F^\dagger \tag{3.1f}$$

where nondimensional variables are ones with a superscribed dagger. A high-frequency parameter $k$ is defined as

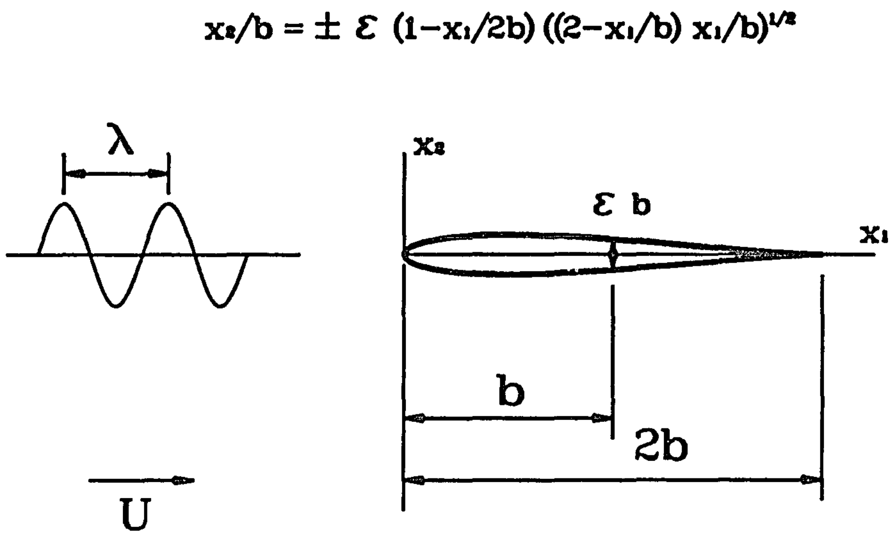


Figure 3.1 A Joukowski airfoil encountering a high-frequency convected disturbance.

$$k = b\, U_\infty\, k_t >> 1 \ . \tag{3.1g}$$

The parameter $k$ is essentially the ratio of the airfoil chord to the wavelength of the convected disturbance.

Upon inserting Eqs. (3.1) into Eqs. (2.12), rearranging the equations and dropping the superscribed daggers for ease in writing, the nondimensionalized equations are

$$\frac{\partial^2 h}{\partial\phi^2} + \frac{\partial^2 h}{\partial\psi^2} + k^2 w^2 (1 - 2\beta_\infty{}^2 q) h + \frac{(\gamma+1) M_\infty{}^4 q}{\beta_\infty{}^2} \left[ \frac{\partial^2 h}{\partial\psi^2} + 2 i k \delta \frac{\partial h}{\partial\phi} + k^2 (w^2 + \delta^2) h \right]$$
$$- \frac{(\gamma+1) M_\infty{}^4}{\beta_\infty{}^2} \frac{\partial q}{\partial\phi} \left[ \frac{\partial h}{\partial\phi} - i k \delta h \right] = k\, e^{ik\Omega}\, S(\phi,\psi) \tag{3.2a}$$

where

$$S(\phi,\psi) = \frac{2}{\beta_\infty{}^2} \Bigg[ i q (A_t^* - A_n k_n \beta_\infty{}^3) + i \beta_\infty \mu (\beta_\infty k_n A_t^* + A_n)$$
$$+ \frac{A_t^* M_\infty{}^2}{k} \frac{\partial q}{\partial\phi} + \frac{A_n M_\infty{}^2 \beta_\infty}{k} \frac{\partial q}{\partial\psi} \Bigg] , \tag{3.2b}$$

$$\Omega = \delta\phi + k_n \psi + g(\phi,\psi) , \tag{3.2c}$$

$$\delta = \frac{1}{\beta_\infty{}^2} , \tag{3.2d}$$

$$w^2 = (\delta M_\infty)^2 - (k_3/\beta_\infty)^2 , \tag{3.2e}$$

and

$$g(\phi,\psi) = -2\epsilon\, \mathrm{Re}\{ F(\zeta) - F(-\infty) \} . \tag{3.2f}$$

The boundary condition is

$$\frac{\partial h}{\partial \psi} + M_\infty{}^2 \frac{\partial q}{\partial \psi} h = \left[ \frac{-A_n}{\beta_\infty} + 2\mu A_t^* + \frac{A_n M_\infty{}^2 q}{\beta_\infty} \right] e^{ik\Omega} \qquad (3.2g)$$

on the surface $\psi = \psi_0$. Essentially, $w$ is the wavenumber of the acoustic wave and $\delta$ the wavenumber of the convected wave.

From (2.22b), the nondimensional complex potential for a Joukowski airfoil is

$$F(\varsigma) = \frac{1}{2\beta_\infty} [(\varsigma - 2)\sqrt{\varsigma^2 - 2\varsigma} - \varsigma^2 + 3\varsigma] \qquad (3.3a)$$

and $F(-\infty) = 3/4\beta_\infty$ where $\varsigma = \phi + i\psi$. The perturbations in the speed and angle of the mean flow are then given by

$$q - i\mu = \epsilon \frac{dF(\varsigma)}{d\varsigma} = \frac{\epsilon}{2\beta_\infty} \left[ \frac{2\varsigma^2 - 5\varsigma + 2}{\sqrt{\varsigma^2 - 2\varsigma}} - 2\varsigma + 3 \right]. \qquad (3.3b)$$

In nondimensional form, the relation between the Cartesian and potential-streamfunction coordinates is

$$\varsigma = z + \epsilon F(z) + O(\epsilon^2) \qquad (3.4a)$$

where $\varsigma = \phi + i\psi$ and $z = x_1 + i\beta_\infty x_2$. Hence, the surface of the airfoil in $(\phi, \psi)$ coordinates is

$$0 < \phi < 2 + \epsilon/\beta_\infty \quad \text{and} \quad \psi = \pm 0\,, \qquad (3.4b)$$

accurate to $O(\epsilon)$. Because a symmetric airfoil at zero angle of attack generates no circulation, the value of $\phi$ at the trailing edge is the same on the upper and lower surfaces of the airfoil.

Equations (3.2) through (3.4) form the basis for the analytic study of the problem. All of the variable coefficients in the differential equation and boundary condition have been approximated and obtained in closed form. The advantage of using $(\phi, \psi)$ coordinates appears in the boundary condition which is applied at a constant value of the coordinate, $\psi$, i.e., $\psi = \pm 0$.

We now proceed to develop an asymptotic solution for the case of a thin airfoil and a high-frequency gust, i.e., $\epsilon \ll 1$ and $k \gg 1$. The product $\epsilon k$ and the Mach number $M_\infty$ are assumed to be $O(1)$. The asymptotic solution has a singular-perturbation nature and involves several regions as illustrated in figure 3.2. The appropriate length scale in the local leading-edge and trailing-edge regions is the disturbance wavelength. In the outer region away from the airfoil leading and trailing edges, the mean flow varies slowly compared to the disturbance wavelength and the solution has a geometric-acoustic form, with a slowly-varying amplitude and a rapidly-varying phase. In "transition" regions of small angular extent near the airfoil surfaces and downstream of the airfoil, the geometric-acoustic form becomes invalid. The solutions in these regions retain the geometric-acoustic feature of a phase function depending on $k\phi$ and an amplitude function depending on $\phi$, but the dependence on the transverse coordinate enters as $\sqrt{k}\,\psi$.

For a symmetric Joukowski airfoil, the nose has a parabolic shape. The ratio of the nose radius to the disturbance wavelength is $O(\epsilon^2 k) \ll 1$. On the small length scale of the nose radius, the mean flow cannot be considered as a small disturbance to a uniform flow. However, the failure of the small-disturbance mean-flow approximation occurs only on a scale which is small compared to the disturbance wavelength. Thus, we believe that the sound generation process can be analyzed without resolving this local singularity, at least to the order of the solutions developed in this dissertation. As support for this viewpoint, note that this mean-flow singularity does not affect the first-order result for the lift force in thin-airfoil theory.

In the following sections, the details of the analysis in the respective regions is presented. Unless stated otherwise, upper-case letters are used for the variables in the local

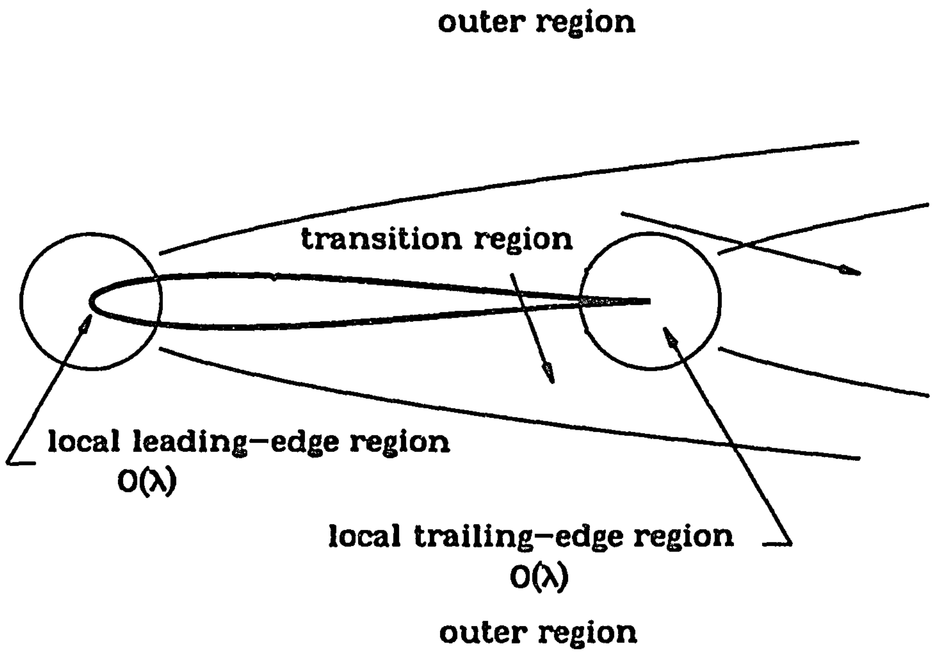


Figure 3.2 A Joukowski airfoil with asymptotic regions illustrated.

leading-edge and trailing-edge regions. Variables in the outer and transition regions are represented by lower-case letters.

### 3.1 Local Leading-Edge Region

In the local leading-edge region, the appropriate length scale is the disturbance wavelength. Thus we introduce local coordinates $(\Phi,\Psi)$ where

$$\Phi = k\phi \quad \text{and} \quad \Psi = k\psi ,$$

and the origin is at the leading edge. The cylindrical form of the local coordinates is $(R,\theta)$ where $R = \sqrt{\Phi^2+\Psi^2}$, $\theta = \tan^{-1}\Psi/\Phi$ and $0 < \theta < 2\pi$. From Eqs. (3.3), the expansions of the mean-flow quantities in local coordinates are given by

$$q - i\mu \sim \frac{\epsilon\sqrt{k}}{\sqrt{2}\beta_\infty\sqrt{R}}(-\sin\theta/2 - i\cos\theta/2) + O(\epsilon/\sqrt{k}) \tag{3.5a}$$

$$g \sim \frac{3\epsilon}{2\beta_\infty} - \frac{2\sqrt{2}\epsilon\sqrt{R}\sin\theta/2}{\beta_\infty\sqrt{k}} + O(\epsilon/k) \ . \tag{3.5b}$$

Writing Eqs. (3.2) in terms of local variables,

$$\frac{\partial^2 h}{\partial\Phi^2} + \frac{\partial^2 h}{\partial\Psi^2} + w^2 h - \left\{2w^2\beta_\infty{}^2 qh - \frac{(\gamma+1)M_\infty{}^4 q}{\beta_\infty{}^2}\left[\frac{\partial^2 h}{\partial\Psi^2} + 2i\delta\frac{\partial h}{\partial\Phi} + (w^2+\delta^2)h\right]\right.$$
$$\left. + \frac{(\gamma+1)M_\infty{}^4}{\beta_\infty{}^2}\frac{\partial q}{\partial\Phi}\left[\frac{\partial h}{\partial\Phi} - i\delta h\right]\right\} = \frac{S(\Phi,\Psi)}{k}e^{i\delta\Phi + ik_n\Psi + ikg(\Phi,\Psi)} \tag{3.6a}$$

where

$$S(\Phi,\Psi) = \frac{2}{\beta_\infty{}^2}\left[iq(A_t^* - A_n k_n\beta_\infty{}^3) + i\beta_\infty\mu(\beta_\infty k_n A_t^* + A_n)\right.$$

$$+ A_t^* M_\infty^2 \frac{\partial q}{\partial \Phi} + A_n M_\infty^2 \beta_\infty \frac{\partial q}{\partial \Psi} \Bigg] \ . \qquad (3.6b)$$

The boundary condition is

$$\frac{\partial h}{\partial \Psi} + M_\infty^2 \frac{\partial q}{\partial \Psi} h = \frac{1}{k} \left[ \frac{-A_n}{\beta_\infty} + 2\mu A_t^* + \frac{A_n M_\infty^2 q}{\beta_\infty} \right] e^{i\delta\Phi + ik_n \Psi + ikg(\Phi,\Psi)} \qquad (3.6c)$$

on the surface $\Psi = \pm 0$.

Several features of the solution in the local leading-edge region can be deduced from these equations. From the boundary condition (3.6c), the leading-order term of $h$ is expected to be $O(1/k)$. From Eqs. (3.5), $q$ and $\mu$ are $O(\epsilon\sqrt{k})$, and $k\,g(\Phi,\Psi)$ contains an $O(1)$ constant followed by a function of $O(\epsilon\sqrt{k})$. Accounting for these features, the asymptotic expansion of $h$ in the local leading-edge region has the form

$$H_l(\Phi,\Psi) = \frac{1}{k} e^{i3k\epsilon/2\beta_\infty} \left[ H_0 + \epsilon\sqrt{k}\,(H_1 + H_2 + H_3) + O(\epsilon,\epsilon^2 k) \right] . \qquad (3.7)$$

The exponential term in (3.7) is an $O(1)$ phase shift in the solution, caused by the fact that the thickness of the airfoil slows down the approach of the convected gust to the leading edge. The function $H_0$ arises from the leading-order term in the boundary condition. For convenience, the $O(\epsilon\sqrt{k})$ term has been separated into three different parts. The function $H_1$ arises from the $O(\epsilon\sqrt{k})$ terms in the boundary condition. $H_2$ arises from the volume source terms in the local leading-edge region, and $H_3$ arises from the $O(\epsilon\sqrt{k})$ contributions to the differential operator in (3.6a).

The differential equations and boundary conditions governing the functions $H_0$, $H_1$, $H_2$ and $H_3$ are presented in the following subsections. The solutions to these equations are developed using Fourier transform techniques. The radiation condition is enforced by assuming that $w$ has a small positive imaginary part. To assure convergence as $\phi \to \infty$ in evaluating Fourier transforms of the boundary conditions, $\delta$ is assumed to have a small positive imaginary part. In the local leading-edge region, the airfoil body appears to extend to downstream infinity. A number of mixed-boundary-value problems arise in the analysis. These are solved by using the Wiener-Hopf technique. The asymptotic behavior of the solutions for $R >> 1$ is determined by the method of steepest descent. When the method of steepest descent fails, uniform asymptotic expansions are derived by using Van Der Waerden's (1950) method.

### 3.1.1 Solution for $H_0$:

The differential equation and boundary condition governing $H_0$ are

$$D(H_0) = 0 \tag{3.8a}$$

and

$$\left.\frac{\partial H_0}{\partial \Psi}\right|_{\substack{\Phi > 0 \\ \Psi = 0}} = \frac{-A_n}{\beta_\infty} e^{i\delta\Phi} \tag{3.8b}$$

where

$$D = \frac{\partial^2}{\partial \Phi^2} + \frac{\partial^2}{\partial \Psi^2} + w^2 \ . \tag{3.8c}$$

The leading-order term $H_0$ satisfies the equations for the case of a zero-thickness airfoil. The differential operator $D$ has constant coefficients, corresponding to the case of a uniform mean flow. The phase of the inhomogeneous term in the boundary condition corresponds to the undistorted vortical-velocity field. It can be seen that the solution $H_0$ is generated only by the airfoil surface blocking the normal component of the undistorted vortical velocity.

From the form of the differential equation and boundary condition, it can be deduced that $H_0$ is an antisymmetric function of $\Psi$. Thus, $H_0(\Phi,0) = 0$ for $\Phi < 0$. The problem (3.8) is a mixed-boundary-value problem, since $\partial H_0(\Phi,0)/\partial\Psi$ is known for $\Phi > 0$, while $H_0(\Phi,0)$

is known for $\Phi < 0$. Such problems can be solved by the Wiener-Hopf technique (Noble 1958). In Appendix A, the Wiener-Hopf technique is applied to find an integral-form solution for the generalized problem in which the right-hand side of (3.8b) is replaced by an arbitrary function, $g(\Phi)$. In fact, Eqs. (3.8) correspond closely to the classical Sommerfeld problem of diffraction by a semi-infinite plate, for which a closed-form solution to the Wiener-Hopf problem can be found. The solution is

$$H_0 = \frac{-A_n \operatorname{sgn}(\Psi)}{\beta_\infty 2\pi\sqrt{\delta+w}} \int_{-\infty}^{\infty} \frac{e^{a(\lambda,\Phi,\Psi)}}{(\lambda+\delta)\sqrt{\lambda+w}}\, d\lambda \tag{3.9a}$$

where

$$a(\lambda,\Phi,\Psi) = -i\lambda\Phi - |\Psi|\sqrt{\lambda^2 - w^2} \ . \tag{3.9b}$$

The function $H_0$ also arose in the analysis of Myers (1987), and a detailed discussion of the derivation of (3.9) can be found there as well.

The singularities contained in $H_0$ are illustrated in figure 3.3. Branch points are present at $\lambda = \pm w$, with the branch cuts extending vertically to $\pm\infty$. The branch points correspond to acoustic wave motion. The pole at $\lambda = -\delta$ corresponds to a local hydrodynamic motion near the surface of the airfoil which is not related to the sound field.

Asymptotic matching of the local leading-edge solution with the outer solution requires the expansion of Eq. (3.9a) in outer coordinates. It is most convenient to use the polar form,

$$r = \sqrt{\phi^2 + \psi^2} = R/k \ , \qquad \theta = \tan^{-1}(\psi/\phi) = \tan^{-1}(\Psi/\Phi) \ .$$

Substituting the outer coordinates into (3.9), the exponent is seen to contain the large parameter $k$. The expansion of (3.9) in outer coordinates can then be calculated by the

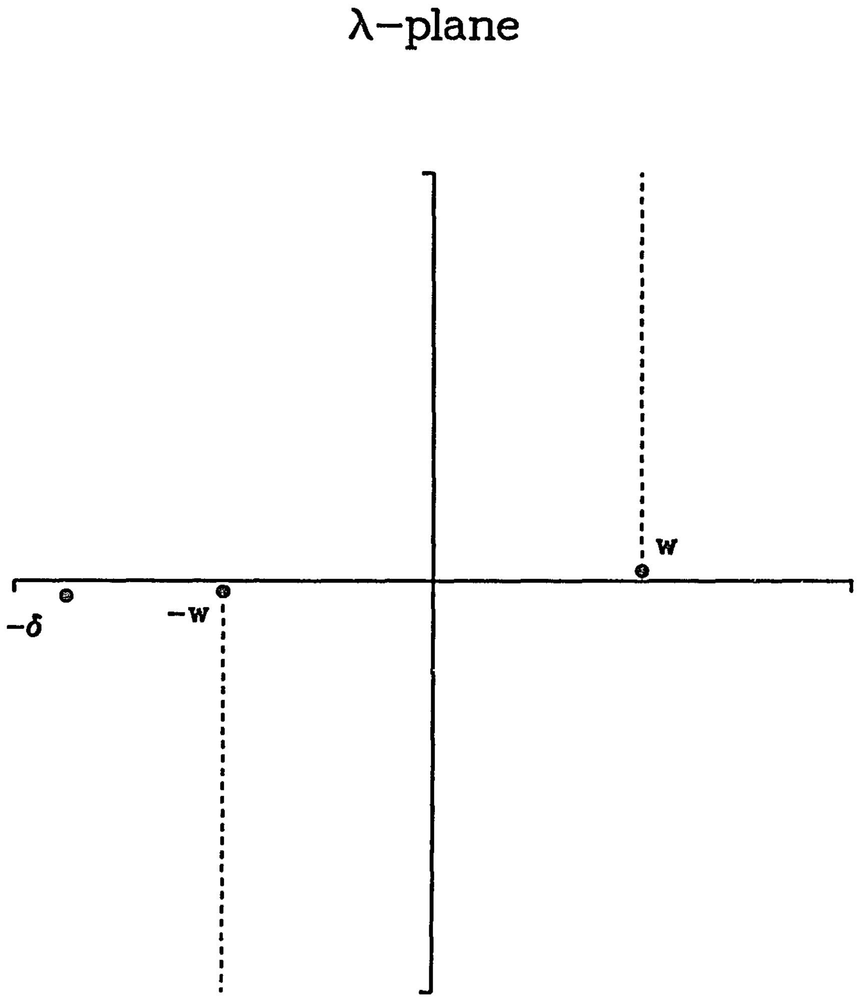


Figure 3.3 Location of singularities in the transform plane for $H_0$.

method of steepest descent (Bender and Orszag 1978), which shows that the integral is dominated by a small region in the vicinity of the saddle point of the exponent at $\lambda_0 = -w\cos\theta$. The method of steepest descent is outlined in Appendix B, which also discusses the extensions required in certain cases. Utilizing the results of Appendix B, the expansion of $H_0$ in outer coordinates is given by

$$H_0 \sim L_0(\theta)\,\frac{e^{ikwr}}{\sqrt{kr}} + O(k^{-3/2}) \tag{3.10a}$$

where

$$L_0(\theta) = \frac{-A_n\, e^{-i\pi/4}\cos\theta/2}{\sqrt{\pi}\,\sqrt{\delta + w}\,(\delta - w\cos\theta)\,\beta_\infty}\ . \tag{3.10b}$$

The formal matching with the outer region will be carried out in Section 3.2.2.

### 3.1.2 Solution for $H_1$:

The differential equation and boundary condition governing the first $O(\epsilon\sqrt{k})$ term, $H_1$, are

$$D(H_1) = 0 \tag{3.11a}$$

and

$$\left.\frac{\partial H_1}{\partial \Psi}\right|_{\substack{\Phi > 0 \\ \Psi = \pm 0}} = 2\,A_t^*\,\frac{\mathrm{sgn}(\Psi)}{\sqrt{2}\,\beta_\infty\sqrt{\Phi}}\,e^{i\delta\Phi}\ . \tag{3.11b}$$

The function $H_1$ arises from the influence of airfoil thickness on the surface boundary condition. Equation (3.5b) shows that there is no local distortion of the gust in the vicinity of the airfoil surface, since the drift function is a constant on $\theta = 0$ and $2\pi$. Hence, in the local leading-edge region, airfoil thickness influences the surface boundary condition only by changing the direction of the unit normal, which generates the result (3.11b). It is interesting to note that this boundary condition represents an unsteady source distribution, as compared to the vortex distribution for $H_0$.

It can be seen from Eqs. (3.11) that $H_1$ is a symmetric function of $\Psi$. Therefore, $\partial H_1/\partial\Psi$ must vanish on $\Psi = 0$ for $\Phi < 0$. Therefore, $\partial H_1/\partial\Psi$ is known on $\Psi = 0$ for all values of $\Phi$, and the solution for $H_1$ can be calculated by a straightforward application of a Fourier transform. We find

$$H_1 = \frac{-e^{i\pi/4} A_t^*}{\sqrt{2\pi}\,\beta_\infty} \int_{-\infty}^{\infty} \frac{e^{a(\lambda,\Phi,\Psi)}}{\sqrt{\lambda^2 - w^2}\,\sqrt{\lambda+\delta}}\, d\lambda \ . \tag{3.12}$$

The integrand of $H_1$ has a branch point at $\lambda = -\delta$, with the branch cut taken in the lower half plane. Expressing (3.12) in terms of outer coordinates, and applying the method of steepest descent, the outer expansion of $H_1$ takes the form

$$H_1 \sim L_1(\theta)\, \frac{e^{ikwr}}{\sqrt{k\,r}} + O(k^{-3/2}) \tag{3.13a}$$

where

$$L_1(\theta) = \frac{-i\, A_t^*}{\beta_\infty \sqrt{w}\,\sqrt{-w\cos\theta + \delta}}\ . \tag{3.13b}$$

The modifications to the boundary condition on the airfoil surface are seen to produce a symmetric pressure field, as compared to the antisymmetric field for $H_0$.

### 3.1.3 Solution for $H_2$:

The term $H_2$ arises from the volume source terms in the local leading-edge region. The differential equation and boundary condition satisfied by $H_2$ are

$$D(H_2) = \left[ \frac{C_1 \cos\theta/2 + C_2 \sin\theta/2}{\sqrt{R}} + \frac{C_3 \cos 3\theta/2 + C_4 \sin 3\theta/2}{R^{3/2}} \right] e^{i\delta\Phi + ik_n\Psi} \quad (3.14a)$$

$$\left. \frac{\partial H_2}{\partial \Psi} \right|_{\substack{\Phi > 0 \\ \Psi = 0}} = 0 \quad (3.14b)$$

where

$$C_1 = \frac{i\sqrt{2}\,(\beta_\infty k_n A_t^* + A_n)}{\beta_\infty^{\,2}} , \quad (3.14c)$$

$$C_2 = \frac{-i\sqrt{2}\,(A_t^* - k_n A_n \beta_\infty^{\,3})}{\beta_\infty^{\,3}} , \quad (3.14d)$$

$$C_3 = \frac{-A_n M_\infty^{\,2}}{\sqrt{2}\,\beta_\infty^{\,2}} , \quad (3.14e)$$

$$C_4 = \frac{A_t^* M_\infty^{\,2}}{\sqrt{2}\,\beta_\infty^{\,3}} . \quad (3.14f)$$

The source terms arise from the interaction of the convected disturbance with the non-uniform mean flow. Variations in both the amplitude and phase of the vortical velocity contribute to the source terms. The source terms for $H_2$ are similar to the quadrupole source of the acoustic-analogy model of Ffowcs Williams and Hawkings (1969b). Since we require $H_2$ to satisfy the no-flow boundary condition on the airfoil surface, it also contains the scattered quadrupole field discussed by Ffowcs Williams and Hall (1970).

The problem (3.14) also arose in the work of Myers (1987), but with different values of the constants $C_i$. He separated $H_2$ into a particular and a complementary solution,

$$H_2(\Phi,\Psi) = H_{2p}(\Phi,\Psi) + H_{2c}(\Phi,\Psi) . \quad (3.15)$$

Applying a double Fourier transform, he found the particular solution

$$H_{2p}(\Phi,\Psi) = \frac{-e^{i\pi/4}}{8\sqrt{\pi}(\delta^2 + k_n^{\,2})} \int_{-\infty}^{\infty} \left[ \frac{(\lambda+\delta) f_1(\lambda) + i k_n f_2(\lambda)}{\sqrt{\lambda^2 - w^2}} - \mathrm{sgn}(\Psi) f_2(\lambda) \right] \frac{e^{a(\lambda,\Phi,\Psi)}\, d\lambda}{\sqrt{\lambda+\delta}\,(\lambda-\lambda_1)(\lambda-\lambda_2)}$$

$$+ \frac{e^{i k_n \Psi + i\pi/4}}{8\sqrt{\pi}(\delta^2+k_n^2)} \int_{-\infty}^{\infty} \left[ \frac{f_1(\lambda)}{\sqrt{\lambda+\delta'}} - \frac{\mathrm{sgn}(\Psi) f_2(\lambda)}{\sqrt{\lambda+\delta}} \right] \frac{e^{hy(\lambda,\Phi,\Psi)}}{(\lambda-\lambda_1)(\lambda-\lambda_2)} d\lambda \tag{3.16a}$$

where

$$hy(\lambda,\Phi,\Psi) = -i\lambda\Phi - |\Psi| \sqrt{(\lambda+\delta)(\lambda+\delta')} , \tag{3.16b}$$

$$f_1(\lambda) = \left[ iC_2 - 2C_4(\lambda+\delta) \right] (-\delta^2 + k_n^2 - w^2 - 2\delta\lambda) + \left[ C_1 + 2iC_3(\lambda+\delta) \right] 2ik_n(\lambda+\delta) , \tag{3.16c}$$

$$f_2(\lambda) = \left[ iC_2 - 2C_4(\lambda+\delta) \right] 2ik_n(\lambda+\delta) + \left[ C_1 + 2iC_3(\lambda+\delta) \right] (-\delta^2 + k_n^2 - w^2 - 2\delta\lambda) , \tag{3.16d}$$

$$\lambda_{1,2} = \frac{-\delta}{2} \left[ \frac{\delta^2 + k_n^2 + w^2}{\delta^2 + k_n^2} \right] \pm \frac{ik_n}{2} \left[ \frac{\delta^2 + k_n^2 - w^2}{\delta^2 + k_n^2} \right] . \tag{3.16e}$$

Here $\delta$ is assumed to have a small positive imaginary part and $\delta'$ a small negative imaginary part. The poles and branch cuts which are present in the above equations are shown in figure 3.4. The phase $hy(\lambda,\Phi,\Psi)$ in $H_{2p}$ is a "hydrodynamic phase" as opposed to the "acoustic phase" $a(\lambda,\Phi,\Psi)$. For integrals containing the hydrodynamic phase, the solution many wavelengths away from the local region represents a hydrodynamic or convected motion, in contrast to the acoustic motion found for integrals containing the acoustic phase.

The complementary solution, obtained through an application of the Wiener-Hopf technique, is

$$H_{2c}(\Phi,\Psi) = \frac{-\mathrm{sgn}(\Psi) e^{i\pi/4}}{8\sqrt{\pi}(\delta^2+k_n^2)} \int_{-\infty}^{\infty} \left\{ 4i(\delta C_3 + k_n C_4) + \left[ \frac{\sqrt{\lambda+w}\, f_2(\lambda)}{\sqrt{\lambda+\delta}(\lambda-\lambda_2)} - \frac{\sqrt{\lambda_1+w}\, f_2(\lambda_1)}{\sqrt{\lambda_1+\delta}(\lambda_1-\lambda_2)} \right] \frac{1}{\lambda-\lambda_1} - \frac{(\lambda_2+\delta') f_2(\lambda_2) + ik_n f_1(\lambda_2)}{\sqrt{\lambda_2-w}\sqrt{\lambda_2+\delta'}(\lambda_2-\lambda_1)(\lambda-\lambda_2)} \right\} \frac{e^{a(\lambda,\Phi,\Psi)}}{\sqrt{\lambda+w}} d\lambda . \tag{3.17}$$

Finally, we expand $H_2$ in outer coordinates. Introducing the coordinates $(r,\theta)$ in Eqs. (3.16) and (3.17), the large parameter $k$ appears in the exponents. The integrals

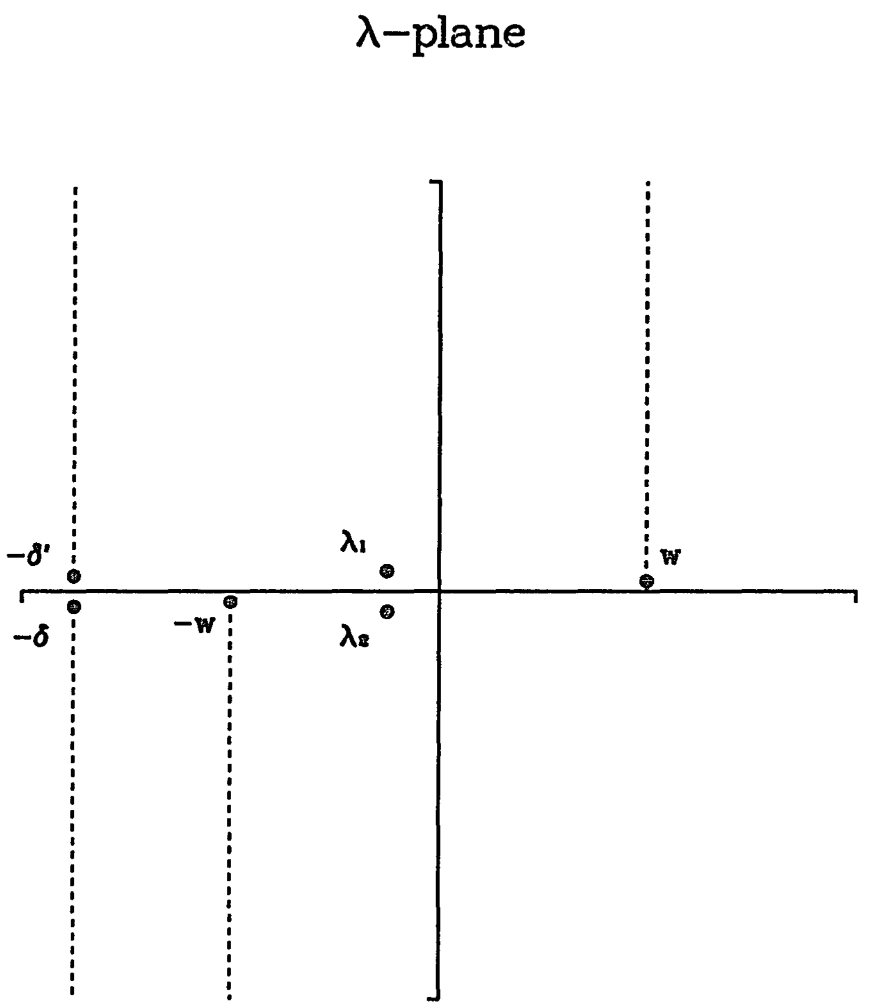


Figure 3.4 Location of singularities in the transform plane for $H_2$.

containing the acoustic phase $a(\lambda,\Phi,\Psi)$ can be expanded by the method of steepest descent, with the dominant contribution again arising from the saddle point at $\lambda_0 = -w\cos\theta$. The hydrodynamic phase $hy(\lambda,\Phi,\Psi)$ does not contain a saddle point, and the expansion is obtained by deforming the contour of integration onto two rays, along which the integral is endpoint dominated for $kr >> 1$. See Myers (1987) for details. The final result is

$$H_2 \sim \frac{e^{ik(\delta\phi+k_n\psi)}}{\sqrt{k\,r}}\left[\frac{C_1\cos\theta/2 + C_2\sin\theta/2}{\delta^2 + k_n{}^2 - w^2}\right] + \frac{L_2(\theta)\,e^{ikwr}}{\sqrt{k\,r}} + O(k^{-3/2}) \qquad (3.18a)$$

where

$$L_2(\theta) = \frac{-i\left[(\delta - w\cos\theta)f_1(-w\cos\theta) + ik_n f_2(-w\cos\theta)\right]}{4\sqrt{2w}\,(\delta^2+k_n{}^2)\sqrt{\delta - w\cos\theta}\,(\lambda_1+w\cos\theta)(\lambda_2+w\cos\theta)} - \frac{\cos\theta/2}{4(\lambda_1-\lambda_2)(\delta^2+k_n{}^2)}$$

$$\left[4(\lambda_1-\lambda_2)(i\delta C_3+ik_n C_4) + \frac{\sqrt{\lambda_1+w}\,f_2(\lambda_1)}{\sqrt{\lambda_1+\delta}\,(\lambda_1+w\cos\theta)} - \frac{(\lambda_2+\delta)f_2(\lambda_2)+ik_n f_1(\lambda_2)}{(\lambda_2+w\cos\theta)\sqrt{\lambda_2-w}\,\sqrt{\lambda_2+\delta}}\right] . \qquad (3.18b)$$

The first term in (3.18a) arises from the integrals containing $hy(\lambda,\Phi,\Psi)$, and is a hydrodynamic rather than acoustic motion. In Section 3.2.2. it will be seen to match with a particular solution in the outer region which is also a hydrodynamic motion. The second term in (3.18a) represents sound generated by the volume sources and the scattering of this sound by the airfoil leading edge. A number of typographical errors appearing in Myers (1987) have been corrected in Eqs. (3.17) and (3.18b).

### 3.1.4 Solution for $H_3$:

The term $H_3$ arises from the coefficients in the differential operator of Eq. (3.2a) which contain $q(\phi,\psi)$. Since $q$ is $O(\epsilon\sqrt{k})$ in the local leading-edge region, upon substituting the expansion (3.7) into Eq. (3.2a), these terms can be taken over to the right-hand side of the equations as effective source terms in the local leading-edge region. In order to denote the origin of these terms, we call them the "propagation source". The differential equation and boundary condition governing $H_3$ are

$$D(H_3) = \frac{-\sqrt{2}\, w^2 \beta_\infty^2 \sin\theta/2}{\sqrt{R}} H_0 + \frac{(\gamma+1) M_\infty^4 \sin\theta/2}{\sqrt{2}\, \beta_\infty^3 \sqrt{R}} \left[ \frac{\partial^2 H_0}{\partial \Psi^2} + 2 i \delta \frac{\partial H_0}{\partial \Phi} + (w^2+\delta^2) H_0 \right]$$
$$+ \frac{(\gamma+1) M_\infty^4 \sin 3\theta/2}{2\sqrt{2} \beta_\infty^3 R^{3/2}} \left[ \frac{\partial H_0}{\partial \Phi} - i \delta H_0 \right] \tag{3.19a}$$

$$\left. \frac{\partial H_3}{\partial \Psi} \right|_{\substack{\Phi > 0 \\ \Psi = \pm 0}} = \frac{M_\infty^2 \operatorname{sgn}(\Psi)}{2\sqrt{2}\, \beta_\infty\, R^{3/2}} H_0 \tag{3.19b}$$

The source term in Eq. (3.19a) is not only algebraically complex, but also contains the leading-order term $H_0$, which is known only in the form of the inverse Fourier integral (3.9). Thus, the calculation of $H_3$ requires a significant effort.

Substituting the expression (3.9) for $H_0$ into Eqs. (3.19) and differentiating under the integral sign, the equations governing $H_3$ take the form

$$D(H_3) = \frac{A_n w^2 \operatorname{sgn}(\Psi)}{\sqrt{2}\pi \sqrt{\delta + w}} \left\{ \frac{\sin\theta/2}{\sqrt{R}} \int_{-\infty}^{\infty} \left[ \frac{1}{(\lambda+\delta)\sqrt{\lambda+w}} - \frac{(\gamma+1) M_\infty^4}{2\beta_\infty^4 w^2} \frac{\lambda+\delta}{\sqrt{\lambda+w}} \right] e^{a(\lambda,\Phi,\Psi)}\, d\lambda \right.$$
$$\left. - \frac{(\gamma+1) M_\infty^4}{2\, \beta_\infty^4 w^2} \frac{i \sin 3\theta/2}{2 R^{3/2}} \int_{-\infty}^{\infty} \frac{e^{a(\lambda,\Phi,\Psi)}}{\sqrt{\lambda+w}} d\lambda \right\} \tag{3.20a}$$

$$\left. \frac{\partial H_3}{\partial \Psi} \right|_{\substack{\Phi > 0 \\ \Psi = 0}} = \frac{-A_n M_\infty^2}{4\sqrt{2}\pi \beta_\infty^2 \sqrt{\delta+w}} \frac{1}{\Phi^{3/2}} \int_{-\infty}^{\infty} \frac{e^{-i\lambda\Phi}}{(\lambda+\delta)\sqrt{\lambda+w}} d\lambda \ . \tag{3.20b}$$

A particular solution to Eq. (3.20a) can be obtained by taking advantage of the fact that each of the source terms consists of a product of a harmonic function and a solution to the Helmholtz equation. Exploiting this property, the method of undetermined coefficients can be used to find a particular solution. For example, consider a function of the form

$$F(\Phi,\Psi) = f(\Phi,\Psi) \int_{-\infty}^{\infty} C(\lambda)\, e^{a(\lambda,\Phi,\Psi)}\, d\lambda \ . \tag{3.21a}$$

Then

$$D(F) = \left[\left(\frac{\partial^2 f}{\partial\Phi^2} + \frac{\partial^2 f}{\partial\Psi^2}\right) + 2\frac{\partial f}{\partial\Phi}\frac{\partial}{\partial\Phi} + 2\frac{\partial f}{\partial\Psi}\frac{\partial}{\partial\Psi} + f\left(\frac{\partial^2}{\partial\Phi^2} + \frac{\partial^2}{\partial\Psi^2} + w^2\right)\right] \int_{-\infty}^{\infty} C(\lambda)\, e^{a(\lambda,\Phi,\Psi)}\, d\lambda \ . \tag{3.21b}$$

The terms inside the first parentheses vanish if $f$ is harmonic function, and the terms inside the last parentheses vanish since the integral is a solution of the Helmholtz equation. Then Eq. (3.21b) becomes

$$D(F) = -2i\frac{\partial f}{\partial\Phi} \int_{-\infty}^{\infty} \lambda C(\lambda) e^{a(\lambda,\Phi,\Psi)}\, d\lambda - 2\,\mathrm{sgn}(\Psi)\frac{\partial f}{\partial\Psi} \int_{-\infty}^{\infty} \sqrt{\lambda^2-w^2}\, C(\lambda) e^{a(\lambda,\Phi,\Psi)}\, d\lambda. \tag{3.21c}$$

Guided by the relation between Eqs. (3.21a) and (3.21c), we choose a particular solution of the form

$$H_{3p} = \frac{A_n w^2 \mathrm{sgn}(\Psi)}{\sqrt{2}\pi\sqrt{\delta+w}} \left[ \sqrt{R}\cos\theta/2 \int_{-\infty}^{\infty} C_1(\lambda) e^{a(\lambda,\Phi,\Psi)}\, d\lambda + \sqrt{R}\sin\theta/2 \int_{-\infty}^{\infty} C_2(\lambda) e^{a(\lambda,\Phi,\Psi)}\, d\lambda \right.$$
$$\left. + \frac{\cos\theta/2}{\sqrt{R}} \int_{-\infty}^{\infty} C_3(\lambda) e^{a(\lambda,\Phi,\Psi)}\, d\lambda + \frac{\sin\theta/2}{\sqrt{R}} \int_{-\infty}^{\infty} C_4(\lambda) e^{a(\lambda,\Phi,\Psi)}\, d\lambda \right] . \tag{3.22a}$$

The application of Eqs. (3.21) to Eq. (3.22a) leads to

$$D(H_{3p}) = \frac{A_n w^2 \mathrm{sgn}(\Psi)}{\sqrt{2}\pi\sqrt{\delta+w}} \left\{ \frac{\cos\theta/2}{\sqrt{R}} \int_{-\infty}^{\infty} \left[ -i\lambda C_1(\lambda) - \mathrm{sgn}(\Psi)\sqrt{\lambda^2-w^2}\, C_2(\lambda) \right] e^{a(\lambda,\Phi,\Psi)}\, d\lambda \right.$$
$$+ \frac{\sin\theta/2}{\sqrt{R}} \int_{-\infty}^{\infty} \left[ -\mathrm{sgn}(\Psi)\sqrt{\lambda^2-w^2}\, C_1(\lambda) + i\lambda C_2(\lambda) \right] e^{a(\lambda,\Phi,\Psi)}\, d\lambda$$

$$+ \frac{\cos 3\theta/2}{R^{3/2}} \int_{-\infty}^{\infty} \left[ i\lambda C_3(\lambda) - \mathrm{sgn}(\Psi)\sqrt{\lambda^2 - w^2}\, C_4(\lambda) \right] e^{a(\lambda,\Phi,\Psi)}\, d\lambda$$

$$+ \frac{\sin 3\theta/2}{R^{3/2}} \int_{-\infty}^{\infty} \left[ \mathrm{sgn}(\Psi)\sqrt{\lambda^2 - w^2}\, C_3(\lambda) + i\lambda C_4(\lambda) \right] e^{a(\lambda,\Phi,\Psi)}\, d\lambda \Bigg\} . \qquad (3.22b)$$

Equating the coefficients of $\cos\theta/2$, $\sin\theta/2$, $\cos 3\theta/2$ and $\sin 3\theta/2$ in Eqs. (3.20a) and (3.22b), a set of linear algebraic equations for $C_1(\lambda)$, $C_2(\lambda)$, $C_3(\lambda)$ and $C_4(\lambda)$ is obtained. Solving for the $C_i(\lambda)$ and substituting the results back into Eq. (3.22a), a particular solution of Eq. (3.20a) is given by

$$H_{3p} = \frac{A_n}{\sqrt{2}\pi\sqrt{\delta + w}} \Bigg\{ \sqrt{R}\, \cos\theta/2 \int_{-\infty}^{\infty} \sqrt{\lambda - w}\, (\lambda + \delta) \left[ \frac{1}{(\lambda+\delta)^2} - \frac{(\gamma+1) M_\infty^{\ 4}}{2\, \beta_\infty^{\ 4}\, w^2} \right] e^{a(\lambda,\Phi,\Psi)}\, d\lambda$$

$$- i\,\mathrm{sgn}(\Psi)\sqrt{R}\sin\theta/2 \int_{-\infty}^{\infty} \frac{\lambda(\lambda+\delta)}{\sqrt{\lambda + w}} \left[ \frac{1}{(\lambda+\delta)^2} - \frac{(\gamma+1) M_\infty^{\ 4}}{2\, \beta_\infty^{\ 4}\, w^2} \right] e^{a(\lambda,\Phi,\Psi)}\, d\lambda$$

$$- \frac{(\gamma+1) M_\infty^{\ 4}}{4\, \beta_\infty^{\ 4}\, w^2} \frac{i \cos\theta/2}{\sqrt{R}} \int_{-\infty}^{\infty} \sqrt{\lambda - w}\, e^{a(\lambda,\Phi,\Psi)}\, d\lambda$$

$$+ \mathrm{sgn}(\Psi) \frac{(\gamma+1) M_\infty^{\ 4}}{4\, \beta_\infty^{\ 4}\, w^2} \frac{\sin\theta/2}{\sqrt{R}} \int_{-\infty}^{\infty} \frac{\lambda}{\sqrt{\lambda + w}} e^{a(\lambda,\Phi,\Psi)}\, d\lambda \Bigg\} . \qquad (3.22c)$$

Before proceeding to the calculation of the complementary solution $H_{3c}$, we first examine the behavior of $H_{3p}$ for $R \ll 1$. This asymptotic behavior is determined by deforming the contours of integration in the various terms of (3.22c) around the branch cuts in the upper or lower half of the $\lambda$ plane, and then using the method of composite expansions to determine uniformly valid approximations to the integrands for $R \ll 1$. The details of this procedure are presented in Appendix C. The particular solution is found to have the following asymptotic behavior:

$$H_{3p} \sim \frac{A_n\, e^{i\pi/4}}{\sqrt{2\pi}\,\sqrt{\delta+w}} \frac{(\gamma+1)M_\infty{}^4}{2\,\beta_\infty{}^4\, w^2} \left[ \frac{\sin 2\theta}{R^2} + \frac{i\,\delta \sin\theta}{R} + O(\sqrt{R}) \right] . \tag{3.23}$$

Thus, the function $H_{3p}$ exhibits strongly singular behavior at the origin, with both a quadrupole and a dipole term. For comparison, the leading-order term $H_0$ is $O(\sqrt{R})$ for $R << 1$.

In order to determine the appropriate level of singularity for $H_3$ at the origin, a local integration of the differential equation (3.19a) was carried out. Near the origin, the differential operator in (3.19a) reduces to the Laplacian, and as mentioned above $H_0 = O(\sqrt{R})$. The local integration of the differential equation is carried out in Appendix D. This local analysis shows that the appropriate behavior for $H_{3p}$ near the origin is

$$H_{3p} \sim -\frac{A_n\, e^{i\pi/4}}{\sqrt{2\pi}\,\sqrt{\delta+w}} \frac{(\gamma+1)M_\infty{}^4}{2\,\beta_\infty{}^4\, w^2} \frac{w^2}{4} \sin 2\theta + O(\sqrt{R}) . \tag{3.24}$$

Thus, the strong singularities in $H_{3p}$ are non-physical behavior that is an artifact of the procedure by which the particular solution was calculated. This non-physical behavior can be eliminated by adding to the particular solution appropriate solutions of the homogeneous equation $D(H_3) = 0$. The solutions of the homogeneous equation which match the leading terms of (3.23) for $R << 1$ and satisfy the radiation condition for $R >> 1$ are $H_2^{(1)}(wR)\sin 2\theta$ and $H_1^{(1)}(wR)\sin\theta$, where $H_1^{(1)}$ and $H_2^{(1)}$ are Hankel functions of first kind of order one and two, respectively. Choosing the coefficients of these functions to cancel the non-physical singularities in $H_{3p}$, we obtain a modified particular solution

$$H_{3p}^* = H_{3p} + \frac{A_n\, e^{i\pi/4}}{\sqrt{2\pi}\,\sqrt{\delta+w}} \frac{(\gamma+1)M_\infty{}^4}{2\,\beta_\infty{}^4\, w^2} \left[ \frac{-i\pi w^2}{4} H_2^{(1)}(wR)\sin 2\theta + \frac{\pi w \delta}{2} H_1^{(1)}(wR)\sin\theta \right] . \tag{3.25}$$

The leading term of $H_{3p}^*$ as $R \to 0$ is consistent with the result (3.24) obtained by local analysis.

In order to satisfy the boundary condition (3.20b), a complementary solution is required. Setting

$$H_3 = H_{3p}^* + H_{3c} \; , \tag{3.26}$$

the complementary solution satisfies

$$D(H_{3c}) = 0 \tag{3.27a}$$

$$\left.\frac{\partial H_{3c}}{\partial \Psi}\right|_{\substack{\Phi > 0 \\ \Psi = 0}} = d(\Phi) \tag{3.27b}$$

where

$$d(\Phi) = \frac{A_n\, M_\infty^2\, e^{i\delta\Phi}\, \mathrm{erf}(e^{i\pi/4}\sqrt{(\delta - w)\Phi})}{2\sqrt{2}\,\beta_\infty^2\,\sqrt{\delta + w}\,\sqrt{\delta - w}\,\Phi^{3/2}} - \left.\frac{\partial H_{3p}^*}{\partial \Psi}\right|_{\substack{\Phi > 0 \\ \Psi = 0}} \tag{3.27c}$$

$$\left.\frac{\partial H_{3p}^*}{\partial \Psi}\right|_{\substack{\Phi > 0 \\ \Psi = 0}} = \frac{A_n}{\sqrt{2\pi}\sqrt{\delta + w}} \left\{ \frac{\sqrt{\pi}\, e^{i\delta\Phi}}{\sqrt{\delta - w}} \left[ 2(\delta^2 - w^2)\sqrt{\Phi} - \frac{i\delta}{\sqrt{\Phi}} \right] \mathrm{erf}(e^{i\pi/4}\sqrt{(\delta - w)\Phi}) \right.$$

$$- 2i(\delta + w)e^{iw\Phi + i\pi/4} + \frac{(\gamma+1)M_\infty^4}{2\,\beta_\infty^4\, w^2}\, e^{iw\Phi + i\pi/4} \left[ \frac{2}{\Phi^3} + \frac{i(\delta - 2w)}{\Phi^2} + \frac{w(\delta - w)}{\Phi} \right]$$

$$\left. - \frac{(\gamma+1)M_\infty^4}{2\,\beta_\infty^4\, w^2}\, \frac{e^{i\pi/4}\pi w}{2} \left[ \frac{iw}{\Phi} H_2^{(1)}(w\Phi) - \frac{\delta}{\Phi} H_1^{(1)}(w\Phi) \right] \right\} \tag{3.27d}$$

and erf is the error function.

It is simple to deduce from Eqs (3.27) that $H_{3c}(\Phi,0) = 0$ for $\Phi < 0$. Thus, Eqs. (3.27) define a mixed-boundary-value problem which can be solved by the Wiener-Hopf technique. However, due to the complexity of the boundary condition, a solution in closed form does not seem possible. Therefore, we shall develop the solution in an integral form which is suitable for numerical computation. In Appendix A, the Wiener-Hopf technique is utilized to determine a solution in integral form for the case of an arbitrary function $d(\Phi)$.

An integral form of the asymptotic expansion for $R >> 1$, required for matching with the outer solution, is also derived. The final results require evaluation of integrals containing $d(\Phi)$ which extend over the infinite range $0 \leq \Phi \leq \infty$. However, to avoid difficulties in the numerical evaluation of these integrals, it is necessary to extract certain terms from $d(\Phi)$ and treat these analytically. Therefore we set

$$d(\Phi) = d_1(\Phi) + d_2(\Phi) + d_3(\Phi) \tag{3.28a}$$

where

$$d_1(\Phi) = \frac{-A_n}{\sqrt{2}\,\sqrt{\delta^2 - w^2}}\, e^{i\delta\Phi} \left[ 2(\delta^2 - w^2)\sqrt{\Phi} - \frac{i\delta}{\sqrt{\Phi}} \right], \tag{3.28b}$$

$$d_2(\Phi) = \frac{A_n\, w e^{i\pi/4}}{\sqrt{2\pi}\,\sqrt{\delta + w}\,(\delta - w)} \left[ 1 - \frac{(\gamma+1) M_\infty^{\,4}}{2\,\beta_\infty^{\,4}\, w^2} (\delta - w)^2 \right] \frac{e^{iw\Phi}}{\Phi}, \tag{3.28c}$$

$$\begin{aligned}
d_3(\Phi) = \frac{A_n\, e^{i\pi/4}}{\sqrt{2\pi}\sqrt{\delta + w}} \Bigg\{ & 2i(\delta + w) - \frac{w}{(\delta - w)\Phi} - \frac{(\gamma+1) M_\infty^{\,4}}{2\,\beta_\infty^{\,4}\, w^2} \left[ \frac{2}{\Phi^3} + \frac{i(\delta - 2w)}{\Phi^2} \right] \\
& + \frac{\sqrt{\pi}\, e^{i(\delta - w)\Phi - i\pi/4}}{\sqrt{\delta - w}} \left[ 2(\delta^2 - w^2)\sqrt{\Phi} - \frac{i\delta}{\sqrt{\Phi}} \right] \operatorname{erfc}\!\left(e^{i\pi/4}\sqrt{(\delta - w)\Phi}\right) \\
& + \frac{(\gamma+1) M_\infty^{\,4}}{2\,\beta_\infty^{\,4}\, w^2}\, \frac{\pi w e^{-iw\Phi}}{2} \left[ \frac{iw}{\Phi} H_2^{(1)}(w\Phi) - \frac{\delta}{\Phi} H_1^{(1)}(w\Phi) \right] \Bigg\}\, e^{iw\Phi} \\
& + \frac{A_n M_\infty^{\,2}\, e^{i\delta\Phi}}{2\sqrt{2}\,\beta_\infty^{\,2}\,\sqrt{\delta^2 - w^2}\,\Phi^{3/2}} \operatorname{erf}\!\left(e^{i\pi/4}\sqrt{(\delta - w)\Phi}\right).
\end{aligned} \tag{3.28d}$$

As mentioned previously, $\delta$ is assumed to have a small positive imaginary part in order to assure convergence of Fourier transforms which arise in the analysis. At the conclusion of the analysis, the small imaginary part is allowed to approach zero. For example, the imaginary part of $\delta$ produces convergence of integrals containing $d_1(\Phi)$.

However, in the numerical integrations required to calculate $H_{3c}$, it is convenient to set the imaginary part of $\delta$ to zero at the outset. Since the term in $d_1$ containing $\sqrt{\Phi}$ would then cause the related integral to diverge at infinity, this function has been separated out for analytical evaluation. The second term in $d_1$ has been separated out as well in order to speed the rate of convergence of the numerical integral as $\Phi \rightarrow \infty$. Separating out the term $d_2$ has a further beneficial effect on the numerical integration, but there is a second reason for analytical treatment of this term. It will be seen below that $d_2$ generates a contribution to $H_{3c}$ which must be treated separately because its asymptotic expansion for $R$ >>1 requires a modification of the method of steepest descent. The function $d_3$ decays as $\Phi^{-3/2}$ for large $\Phi$ and $\Phi^{1/2}$ for small $\Phi$, simplifying the numerical evaluation of the resulting integrals.

Setting

$$H_{3c} = \sum_{j=1}^{3} H_{3c_j} \tag{3.29}$$

and utilizing Eq. (A.16) from Appendix A, the complementary solutions are given by

$$H_{3c_j} = -\frac{\operatorname{sgn}(\Psi)}{2\pi} \int_{-\infty}^{\infty} F_{+_j}(\lambda)\, \frac{e^{a(\lambda,\Phi,\Psi)}}{\sqrt{\lambda + w}}\, d\lambda \tag{3.30a}$$

From Eq. (A.17), the $F_{+_j}(\lambda)$ are found to be

$$F_{+_1} = \frac{\sqrt{\pi}\, A_n\, e^{-i\pi/4}}{\sqrt{2}\sqrt{\delta^2 - w^2}} \left\{ \frac{\delta^2 - w^2}{\sqrt{\lambda - w}\,(\lambda+\delta)^{3/2}} \left[ 1 - \frac{2}{\pi} \left[ \sin^{-1}\left( \frac{\sqrt{\lambda+\delta}}{\sqrt{w+\delta}} \right) - \frac{i\sqrt{(\lambda+\delta)(\lambda - w)}}{\delta + w} \right] \right] \right.$$
$$\left. - \frac{\delta}{\sqrt{\lambda - w}\sqrt{\lambda+\delta}} \left[ 1 - \frac{2}{\pi} \sin^{-1}\left( \frac{\sqrt{\lambda+\delta}}{\sqrt{w+\delta}} \right) \right] \right\}, \tag{3.30b}$$

$$F_{+_2} = \frac{A_n w e^{i\pi/4}}{\sqrt{2\pi}\sqrt{\delta+w}(\delta-w)\sqrt{\lambda-w}} \left[1 - \frac{(\gamma+1)M_\infty{}^4}{2\beta_\infty{}^4 w^2}(\delta-w)^2\right] \ln\left[\frac{\sqrt{2w}+i\sqrt{\lambda-w}}{\sqrt{2w}-i\sqrt{\lambda-w}}\right], \quad (3.30c)$$

$$F_{+_3} = \int_0^\infty \operatorname{erf}(e^{i\pi/4}\sqrt{(\lambda-w)x}) \frac{d_3(x)\, e^{i\lambda x}}{\sqrt{\lambda-w}} dx . \quad (3.30d)$$

In calculating $F_{+_1}$ from Eq. (A.17) it is most convenient to evaluate the integral with respect to $x$ first, while for $F_{+_2}$ the opposite order is simplest.

For matching with the outer region, the expansion of $H_3$ in outer coordinates is required. Applying the method of steepest descent, the outer expansion of $H_{3p}$ is

$$H_{3p}^* \sim \frac{-A_n e^{i\pi/4} w\sin\theta\, e^{iwkr}}{\sqrt{2\pi}\sqrt{\delta+w}(\delta-w\cos\theta)} \left[1 - \frac{(\gamma+1)M_\infty{}^4}{2\,\beta_\infty{}^4 w^2}(\delta-w\cos\theta)^2\right] + L_{3p}(\theta)\frac{e^{iwkr}}{\sqrt{kr}} + O(1/k) \quad (3.31a)$$

where

$$L_{3p}(\theta) = \frac{iA_n\sqrt{w}}{2\sqrt{\delta+w}} \frac{(\gamma+1)M_\infty{}^4}{2\,\beta_\infty{}^4 w^2}\left[\frac{w}{2}\sin 2\theta - \delta\sin\theta\right], \quad (3.31b)$$

and the outer expansion of $H_{3c_1}$ is

$$H_{3c_1} \sim L_{3c_1}(\theta)\frac{e^{ikwr}}{\sqrt{kr}} + O(k^{-3/2}) \quad (3.31c)$$

where

$$L_{3c_1}(\theta) = \frac{\operatorname{sgn}(\Psi) A_n \delta}{2\sqrt{w}\sqrt{\delta^2-w^2}\sqrt{\delta-w\cos\theta}}\left[1 - \frac{2}{\pi}\sin^{-1}\left(\frac{\sqrt{\delta-w\cos\theta}}{\sqrt{w+\delta}}\right)\right]$$
$$- \frac{\operatorname{sgn}(\Psi) A_n\sqrt{\delta^2-w^2}}{2\sqrt{w}(\delta-w\cos\theta)^{3/2}}\left[1 - \frac{2}{\pi}\left[\sin^{-1}\left(\frac{\sqrt{\delta-w\cos\theta}}{\sqrt{w+\delta}}\right) - \frac{\sqrt{\delta-w\cos\theta}\sqrt{w(1+\cos\theta)}}{\delta+w}\right]\right]. \quad (3.31d)$$

Utilizing Eq. (A.19), the expansion of $H_{3c_3}$ is given by

$$H_{3c_3} \sim L_{3c_3}(\theta)\,\frac{e^{ikwr}}{\sqrt{kr}} + O(k^{-3/2}) \tag{3.31e}$$

where

$$L_{3c_3}(\theta) = \frac{-\operatorname{sgn}(\Psi)e^{i\pi/4}}{\sqrt{2\pi w}} \int_0^\infty e^{-iw\cos\theta x}\,\operatorname{erf}(e^{-i\pi/4}\sqrt{w(1+\cos\theta)x})\,d_3(x)\,dx\ . \tag{3.31f}$$

The integral in Eq. (3.31f) is evaluated by direct numerical integration.

Finally, consider the expansion of $H_{3c_2}$ in outer coordinates. Application of the method of steepest descent leads to the result

$$H_{3c_2} \sim L_{3c_2}(\theta)\,\frac{e^{ikwr}}{\sqrt{kr}} + O(k^{-3/2}) \tag{3.32a}$$

where

$$L_{3c_2}(\theta) = \frac{-\operatorname{sgn}(\Psi)A_n\,i\sqrt{w}}{2\pi\sqrt{\delta+w}\,(\delta-w)}\left[1 - \frac{(\gamma+1)M_\infty{}^4}{2\,\beta_\infty{}^4\,w^2}(\delta-w)^2\right]\ln\left[\frac{\sqrt{2}+\sqrt{1+\cos\theta}}{\sqrt{2}-\sqrt{1+\cos\theta}}\right]\ . \tag{3.32b}$$

It can be seen that $L_{3c_2}(\theta)$ is singular as $\theta \to 0$ (or $2\pi$). The method of steepest descent fails for small angles owing to the proximity of the saddle point at $\lambda = -w\cos\theta$ to the logarithmic branch point at $\lambda = -w$. In order to develop an expansion which is uniformly valid in $\theta$, the logarithmic branch point must be isolated and integrated separately. In Appendix B, this is carried out using Van Der Waerden's (1950) method. The final result corresponds to replacing the directivity function $L_{3c_2}(\theta)$ in (3.32a) by the function

$$L^u_{3c_2}(r,\theta) = \frac{-\operatorname{sgn}(\Psi)A_n\,i\sqrt{w}}{2\pi\sqrt{\delta+w}\,(\delta-w)}\left[1 - \frac{(\gamma+1)M_\infty{}^4}{2\,\beta_\infty{}^4\,w^2}(\delta-w)^2\right]$$

$$\left\{\frac{2\sqrt{2}}{\sqrt{\pi}\,\sqrt{1+\cos\theta}}\left[\frac{\sqrt{\pi}}{2}\ln(kr) - \int_{-\infty}^{\infty}\ln(s + e^{i\pi/4}\sqrt{w(1-\cos\theta)kr})e^{-s^2}\,ds\right]\right.$$

$$+ \ln\left[\frac{\sqrt{2} + \sqrt{1+\cos\theta}}{\sqrt{2} - \sqrt{1+\cos\theta}}\right] + \frac{\sqrt{2}\,\ln(1-\cos\theta)}{\sqrt{1+\cos\theta}} + \frac{i\pi + 2\ln(w)}{\sqrt{2}\,\sqrt{1+\cos\theta}}\Bigg\} \, . \tag{3.32c}$$

The expansions (3.31) and (3.32) will be formally matched with the outer solution in Section 3.3.2.

## 3.2 Outer Region

In the outer region, the mean flow varies on the length scale of the airfoil chord, which is large compared to the disturbance wavelength. Thus, a multiple-scales type solution is appropriate in this region. The governing equation and boundary condition are Eqs. (3.2). No rescaling is necessary in the outer region.

The solution in the outer region is separated into four parts,

$$h \;=\; h_p \;+\; h_c \;+\; h_l \;+\; h_t \;, \tag{3.33}$$

where $h_p$ is a particular solution generated by the volume source term in Eq. (3.2a), $h_c$ is a complementary solution which combines with the particular solution to satisfy the boundary condition on the airfoil surface, and $h_l$ and $h_t$ are acoustic ray fields which emanate from the airfoil leading and trailing edges.

The particular solution is solved for first. In the source term of Eq. (3.2a), the phase $k\Omega$ varies rapidly compared to the amplitude $S(\phi,\psi)$. Therefore, a particular solution which also has this rapidly varying phase is sought. The particular solution is found to be

$$h_p \;=\; \frac{1}{k}\,\frac{S(\phi,\psi)\;e^{ik\,\Omega(\phi,\psi)}}{w^2 - \delta^2 - k_n{}^2} \;+\; O(\epsilon^2/k,\;\epsilon/k^2) \;. \tag{3.34}$$

The complementary solution $h_c$ is chosen to cancel the velocity component normal to the airfoil surface produced by the gust and by the particular solution. Thus, the complementary solution satisfies the boundary condition

$$\frac{\partial h_c}{\partial \psi} + M_\infty^2 \frac{\partial q}{\partial \psi} h_c = \left[ \frac{-A_n}{\beta_\infty} + 2\mu(\phi,0) A_t^* + \frac{q(\phi,0) A_n M_\infty^2}{\beta_\infty} - \frac{i k_n S(\phi,\psi)}{w^2 - \delta^2 - k_n^2} \right] e^{ik\Omega(\phi,0)}$$

$$+ \; O(\epsilon/k,\, k^{-2}) \qquad (3.35a)$$

on $\psi = 0$. It can be seen from the boundary condition that the complementary solution must also contain the rapidly varying phase $e^{ik\Omega(\phi,0)}$. Furthermore, since this phase corresponds to convection by the subsonic mean flow, we anticipate that the complementary solution will decay exponentially with distance from the surface, and be exponentially small outside of a boundary-layer region where $\psi = O(1/k)$. Restricting attention to the boundary-layer region, we set

$$h_c = f(y,\phi)\, e^{ik\Omega(\phi,0)} \qquad (3.35b)$$

where

$$y = k\,|\psi| \qquad (3.35c)$$

is a variable which scales on the thickness of the boundary-layer region. Substituting (3.35) into (3.2a) and (3.2g), $f(y,\phi)$ is found to satisfy

$$-k^2 \left( \delta + \frac{\partial g(\phi,0)}{\partial \phi} \right)^2 f + 2ik\delta \frac{\partial f}{\partial \phi} + k^2 \frac{\partial^2 f}{\partial \phi^2} + k^2 w^2 (1 - 2\beta_\infty^2 q) f$$

$$+ \frac{(\gamma+1) M_\infty^4 q}{\beta_\infty^2} \left[ k^2 \frac{\partial^2 f}{\partial y^2} - 2k^2 \delta^2 f + k^2 (w^2 + \delta^2) f \right] + \text{H.O.T.} = 0 \; . \qquad (3.36a)$$

and

$$k \frac{\partial f}{\partial y} = \frac{-A_n}{\beta_\infty} + 2\mu A_t^* + \frac{A_n M_\infty^2 q}{\beta_\infty} - \frac{i k_n S(\phi,0)}{w^2 - \delta^2 - k_n^2} + \text{H.O.T.} \qquad (3.36b)$$

on the surface $y = \pm 0$. The complementary solution can then be found as

$$h_c(\phi,\psi) = \frac{\operatorname{sgn}(\psi)}{k\sqrt{\delta^2 - w^2}} \left[ \frac{A_n}{\beta_\infty} - \omega_1 \frac{A_n}{\beta_\infty} - 2\mu(\phi,0) A_t^* - \frac{q(\phi,0) A_n M_\infty^2}{\beta_\infty} + \frac{i k_n S(\phi,\psi)}{w^2 - \delta^2 - k_n^2} \right]$$
$$e^{-y(1+\omega_1)\sqrt{\delta^2 - w^2}} \, e^{ik\Omega(\phi,0)} \tag{3.37a}$$

where

$$\omega_1 = \frac{w^2 \beta_\infty^2 q(\phi,0) - 2\delta q(\phi,0)}{\delta^2 - w^2} . \tag{3.37b}$$

The solution applies for $0 < \phi < 2$. However, in the analysis of the local trailing-edge region, $h_c$ is found to be continued into the wake region where $\phi > 2$. As anticipated, $h_c$ is exponentially small except when $\psi = O(1/k)$, i.e., very near the body or wake.

Both $h_p$ and $h_c$ contain the phase $k\Omega$ which is the phase of the vortical velocity $v'$. Thus the disturbances corresponding to $h_p$ and $h_c$ convect with the mean flow and are not sound waves, although these disturbances are irrotational. Therefore, we conclude that, to the order of our analysis, all the noise is generated in the local leading-edge and trailing-edge regions. The sound generation processes in the local leading-edge region have already been investigated. It will be shown later that the trailing edge simply scatters sound which was generated in the local leading-edge region. The propagation into the outer region of the sound generated in the local leading-edge region and that scattered by the local trailing-edge region is described by the two remaining parts of the outer solution, $h_l$ and $h_t$. The solutions $h_l$ and $h_t$ have a geometric-acoustic form. We first solve the leading-edge ray field.

### 3.2.1 Leading-Edge Ray Field:

The expansions of the local leading-edge solutions in outer coordinates contained cylindrical acoustic waves emanating from the airfoil leading edge. We now develop the outer solution corresponding to these acoustic waves. Anticipating that the solution has a geometric-acoustic form, we set

$$h_l = \frac{A_l(r,\theta)}{k^{3/2}} e^{ik\sigma_l(r,\theta)} \tag{3.38}$$

where $(r,\theta)$ are the polar form of the outer coordinates with the origin at the leading edge, i.e., $r = \sqrt{\phi^2+\psi^2}$ and $\theta = \tan^{-1}(\psi/\phi)$. The factor $k^{-3/2}$ in Eq. (3.38) has been introduced in anticipation of the matching with the local leading-edge solution Eq. (3.7). Substituting this expression into Eq. (3.2a) and collecting the terms with the same order of $k$, a variable-coefficient eikonal equation for $\sigma_l$ is obtained,

$$\left(\frac{\partial\sigma_l}{\partial r}\right)^2 + \frac{1}{r^2}\left(\frac{\partial\sigma_l}{\partial\theta}\right)^2 - w^2 + q\left[2w^2\beta_\infty{}^2 + \frac{(\gamma+1)M_\infty{}^4}{\beta_\infty{}^2}\left[\left(\frac{\partial\sigma_l}{\partial\psi}\right)^2 + 2\delta\frac{\partial\sigma_l}{\partial\phi} - \delta^2 - w^2\right]\right] = 0. \tag{3.39}$$

A perturbation solution is sought,

$$\sigma_l = \sigma_{l\,0} + \sigma_{l\,1} + O(\epsilon^2, \epsilon/k) \tag{3.40}$$

where $\sigma_{l\,0}$ is $O(1)$ and $\sigma_{l\,1}$ is $O(\epsilon)$. The leading-order term is

$$\sigma_{l\,0} = w\,r \tag{3.41}$$

which is the cylindrical-wave phase appropriate for a uniform mean flow. Substituting Eq. (3.41) into Eq. (3.39), the terms of next order in $k$ are

$$2w\frac{\partial\sigma_{l\,1}}{\partial r} + q\left[2w^2\beta_\infty{}^2 - \frac{(\gamma+1)M_\infty{}^4}{\beta_\infty{}^2}(\delta - w\cos\theta)^2\right] = 0\ . \tag{3.42a}$$

Thus the solution for the first-order correction to the phase is

$$\sigma_{l\,1} = V(\theta)\int_0^r q(r',\theta)\,dr' + g_1(\theta)\ , \tag{3.42b}$$

where

$$V(\theta) = -\beta_\infty^2 w \left[1 - \frac{(\gamma+1)M_\infty^4}{2\beta_\infty^4 w^2}(\delta - w\cos\theta)^2\right] . \tag{3.42c}$$

and the function $g_1(\theta)$ will be found in the matching with the local leading-edge solution. Using the fact that the perturbation speed $q$ is the real part of an analytic function, the integral of $q$ can be expressed in a more convenient form.

$$\int_0^r q(r',\theta)\, dr' = \mathrm{Re}\left\{\int_0^r \left[q(r',\theta) - i\mu(r',\theta)\right] dr'\right\} = \mathrm{Re}\left\{e^{-i\theta}\int_0^z (q - i\mu)\, dz\right\}$$

$$= \epsilon\, \mathrm{Re}\left\{e^{-i\theta}\left[F(z) - F(0)\right]\right\} \tag{3.43}$$

where $F$ is the perturbation complex potential for the mean flow. The next correction to the phase is $O(k\epsilon^2)$, which is neglected to the desired accuracy.

When the geometric-acoustic form (3.38) was substituted into Eq. (3.2a) the leading-order terms produced the eikonal equation. At the next order in $k$, we obtain the transport equation

$$2\frac{\partial\sigma_l}{\partial r}\frac{\partial A_l}{\partial r} + \frac{\partial\sigma_l}{\partial r}\frac{A_l}{r} + O(\epsilon, 1/k) = 0 . \tag{3.44a}$$

Substituting the result for $\sigma_l$ and neglecting terms of $O(\epsilon A_l)$, Eq. (3.44a) becomes

$$\frac{\partial}{\partial r}(\sqrt{r}\, A_l) = 0 \tag{3.44b}$$

which has the solution

$$A_l = \frac{K_l(\theta)}{\sqrt{r}} + O(k^{-5/2}) . \tag{3.45}$$

The standard geometric-acoustic form is an amplitude expansion in powers of $1/k$. Our perturbation approach has introduced an additional small parameter $\epsilon$. The matching with the local leading-edge solution will show that a term of $O(\epsilon\sqrt{k})$ must be included in the outer solution. The $O(\epsilon\sqrt{k})$ term also satisfies Eq. (3.44a) independently. Hence set

$$K_l = K_0(\theta) + \epsilon\sqrt{k}\,K_1(\theta)\,. \tag{3.46}$$

### 3.2.2 Matching of Local Leading-Edge and Outer Solutions:

The asymptotic matching process is carried out using Van Dyke's (1975) rule. In matching the local leading-edge and outer solutions, Van Dyke's rule can be expressed as follows. The two-term outer solution, when rewritten in local variables and expanded to two terms, must agree with the two-term local solution, when rewritten in outer variables and expanded to two terms. The comparison of the two expressions may be carried out in either local or outer variables. Since our main interest is in the acoustic field, only the matching for the acoustic components of the solutions is presented. The matching of the hydrodynamic solutions provides a consistency check, but does not influence the sound field.

The two-term outer acoustic solution, rewritten in local variables, is

$$h_l \sim (K_0(\theta) + \epsilon\sqrt{k}\,K_1(\theta))\,\frac{e^{iwR + ik\sigma_{l1}(R/k,\theta)}}{k\sqrt{R}} \tag{3.47a}$$

where $r$ has been replaced by $R/k$ in $\sigma_{l1}$. Utilizing Eq. (3.42b), the two-term expansion of Eq. (3.47a) for large $k$ is

$$\left[K_0(\theta) + \epsilon\sqrt{k}\left[K_1(\theta) - \frac{V(\theta)\,i\sqrt{2}}{\beta_\infty}\sqrt{R}\,\sin\theta/2\;K_0(\theta)\right]\right]\frac{e^{iwR + ikg_1(\theta)}}{k\sqrt{R}}\,. \tag{3.47b}$$

The local leading-edge solution has been found in Section 3.1. The expansion of the various components of the local leading solution in outer coordinates is given by Eqs. (3.10), (3.13), (3.18), (3.31) and (3.32). Collecting these results together, the two-term, outer-variable expansion of the two-term local leading-edge solution is given by

$$H_l = \frac{e^{iwkr+i3k\epsilon/2\beta_\infty}}{k^{3/2}\sqrt{r}}\Bigg\{L_0(\theta) + \epsilon\sqrt{k}\Bigg[L_1(\theta) + L_2(\theta) + L_{3p}(\theta) + L_{3c_1}(\theta) + L_{3c_2}(\theta) + L_{3c_3}(\theta)$$

$$- \frac{A_n e^{i\pi/4} w\sqrt{k}\sqrt{r}\sin\theta}{\sqrt{2\pi}\sqrt{\delta+w}(\delta - w\cos\theta)}\left[1 - \frac{(\gamma+1)M_\infty^4}{2\beta_\infty^4 w^2}(\delta - w\cos\theta)^2\right]\Bigg] + O(\epsilon,\ 1/k)\Bigg\} . \qquad (3.47c)$$

Since the matching is being carried out for $O(1)$ values of $\theta$, Eq. (3.32b) has been used in forming the above result. The matching principle requires that Eqs. (3.47b) and (3.47c) be identical, when expressed in the same variables. Reverting to local variables in (3.47c) and comparing with (3.47b), we find

$$K_0(\theta) = L_0(\theta) , \qquad (3.48a)$$

$$K_1(\theta) = L_1(\theta) + L_2(\theta) + L_{3p}(\theta) + L_{3c_1}(\theta) + L_{3c_2}(\theta) + L_{3c_3}(\theta) , \qquad (3.48b)$$

$$g_1(\theta) = \frac{3\epsilon}{2\beta_\infty} . \qquad (3.48c)$$

Note that the secular term of Eq. (3.47c) has matched with the expansion of $\sigma_{l1}$ from the outer solution. Thus this secular term is only the local expansion of the phase distortion of the outer region.

The geometric-acoustic field emanating from the local leading-edge region is then given by

$$h_l = \frac{e^{ik\sigma_l(r,\theta)}}{k^{3/2}\sqrt{r}}\left\{L_0(\theta) + \epsilon\sqrt{k}\left[L_1(\theta) + L_2(\theta) + L_{3p}(\theta) + L_{3c_1}(\theta) + L_{3c_2}(\theta) + L_{3c_3}(\theta)\right]\right\} \qquad (3.49a)$$

where

$$\sigma_l(r,\theta) = wr + V(\theta)\int_0^r q(r',\theta)\,dr' + \frac{3\epsilon}{2\beta_\infty} . \qquad (3.49b)$$

The expansion of $\sigma_l$ for $r >> 1$ will be required in the far-field solution. For $r >> 1$,

$$\sigma_l(r,\theta) = wr + \frac{3\epsilon}{4\beta_\infty} V(\theta)\cos\theta + \frac{3\epsilon}{2\beta_\infty} + O(r^{-1}) \ . \tag{3.49c}$$

### 3.2.3 Trailing-Edge Ray Field

The trailing-edge ray field can be derived in the same manner as the leading-edge ray field; only the coordinate system changes. We introduce a trailing-edge coordinate system $(\phi_t, \psi_t)$, with the origin shifted to the trailing edge, given by

$$\phi = 2 + \epsilon/\beta_\infty + \phi_t \quad \text{and} \quad \psi = \psi_t \ . \tag{3.50}$$

The corresponding cylindrical coordinate system is denoted by $(r_t, \theta_t)$, where $r_t = \sqrt{\phi_t^{\,2} + \psi_t^{\,2}}$, $\theta_t = \tan^{-1}(\psi_t/\phi_t)$ and $-\pi < \theta_t < \pi$. Since the derivation of $h_t$ is quite similar to that of $h_l$, we simply quote the final results.

$$h_t = A_t(r_t, \theta_t)\, e^{ik\sigma_t(r_t,\theta_t)} \tag{3.51a}$$

$$A_t(r_t, \theta_t) = \frac{K_t(\theta_t)}{k^2\sqrt{r_t}} \tag{3.51b}$$

$$\sigma_t = wr_t + \sigma_{t_1} + O(\epsilon^2, \epsilon/k) \tag{3.51c}$$

$$\sigma_{t_1} = V(\theta_t)\int_0^{r_t} q(r_t', \theta_t)\, dr_t' + g_2(\theta_t) \tag{3.51d}$$

$$\int_0^{r_t} q(r_t', \theta_t)\, dr_t' = \epsilon \,\mathrm{Re}\left\{e^{-i\theta_t} F_t(z_t)\right\} . \tag{3.51e}$$

In Section 3.4.1, the matching of the outer and local trailing-edge solutions will show that the function $g_2(\theta_t)$ is zero. $F_t$ is the complex potential for the mean-flow perturbation, written in local trailing-edge coordinates and with the arbitrary constant in $F_t$ chosen so that

$F_t$ vanishes at the trailing edge, i.e.,

$$F_t(z_t) = \frac{1}{2\beta_\infty}\left[z_t^{3/2}\sqrt{z_t+2} - z_t^2 - z_t\right] . \tag{3.51f}$$

The expansion of $\sigma_t$ for $r >> 1$ will be required in the far-field solution. For $r >> 1$,

$$\sigma_t(r_t,\theta_t) = wr_t - \frac{\epsilon}{4\beta_\infty}V(\theta_t)\cos\theta_t + O(r_t^{-1}) . \tag{3.51g}$$

### 3.3 Leading-Edge Transition Solution

In calculating the geometric-acoustic fields $h_l$ and $h_t$ in the outer region, the boundary condition on the airfoil surface was not enforced. In fact, since the phase and amplitude functions $\sigma(r,\theta)$ and $A(r,\theta)$ satisfy ordinary differential equations along the acoustic rays, it is not possible to directly impose the surface boundary condition on the geometric-acoustic solutions. Hence, in order for the acoustic field to satisfy the boundary condition on the airfoil surface, an additional complementary solution is required. In this section, we develop the complementary solution corresponding to the geometric-acoustic field $h_l$ which emanates from the airfoil leading edge.

The calculation of the complementary solution is treated as a diffraction problem. Essentially, the geometric-acoustic field $h_l$ is treated as an incident wave field whose interaction with the airfoil surface generates a reflected wave field. The rays of the geometric-acoustic field are nearly tangent to the airfoil surface, implying that the reflected wave field is concentrated at shallow angles. This feature will be seen to play an important role in the analysis of the reflected wave field. The present situation has some similarities with the problem of the electromagnetic field generated by a source on the surface of a convex body. Fock and Leontovich (1946) used asymptotic methods to analyze the latter problem (see Fock 1965). In particular, they examined a region surrounding the source in which the transition from the illuminated region to the shadow region develops. For convenience, we refer to the region near the airfoil surface where the complementary solution is concentrated as a "transition region". The solution in this region is represented in the form

$$h_{ltr} = h_l + h_{ls} \tag{3.52}$$

where $h_{ls}$ is the complementary solution. The analysis is first presented for the upper surface of the airfoil $\psi > 0$, and then the results are extended to the lower surface.

The geometric-acoustic field $h_l$ was determined in Section 3.2.2 by matching the local leading-edge and outer solutions. This matching considered $O(1)$ values of $\theta$, and showed that the $O(\epsilon\sqrt{k})$ term $K_1(\theta)$ of the amplitude function contains the directivity function $L_{3c_2}(\theta)$ corresponding to $H_{3c_2}$. However, in this section it is necessary to consider small values of $\theta$. The function $L_{3c_2}(\theta)$ has a logarithmic singularity as $\theta \to 0$, due to a failure of the method of steepest descent. The somewhat more complicated function $L^u_{3c_2}(r,\theta)$ defined by Eq. (3.32c) is a replacement for $L_{3c_2}(\theta)$ that provides uniform validity for all values of $\theta$. Thus, prior to formulating the diffraction problem, we replace $L_{3c_2}(\theta)$ by $L^u_{3c_2}(r,\theta)$ in Eq. (3.49a). This replacement extends the validity of the matching between the local leading-edge and outer regions to shallow angles. It can be verified by direct substitution that the modified form of $h_l$ satisfies the homogeneous form of the differential equation (3.2a) to the same order of accuracy.

The complementary solution $h_{ls}$ satisfies the homogeneous form of the differential equation (3.2a) and the boundary condition

$$\left[\frac{\partial h_{Is}}{\partial \psi} + M_\infty{}^2 \frac{\partial q}{\partial \psi} h_{Is}\right]\Bigg|_{\psi=0} = -\left[\frac{\partial h_I}{\partial \psi} + M_\infty{}^2 \frac{\partial q}{\partial \psi} h_I\right]\Bigg|_{\psi=0} . \tag{3.53}$$

It can be seen from Eq. (3.49a) that the right-hand side of Eq. (3.53) contains the factor $e^{ik\sigma_I(r,0)}$, corresponding to the phase of the grazing ray. It is natural to anticipate that the complementary solution $h_{Is}$ will contain this phase factor as well. Finally, a number of features suggest that a rescaling of the vertical coordinate is appropriate. Firstly, the grazing nature of the incident field suggests that the reflected field $h_{Is}$ will be concentrated at shallow angles. Secondly, for $k >> 1$ and $r = O(1)$ the function $L^u_{3c_2}(r,\theta)$ exhibits a boundary-layer structure with a distinguished limit corresponding to $\theta = O(k^{-1/2})$. Finally, the inability of the geometric-acoustic solution $h_I$ to satisfy the boundary condition on the airfoil surface stems from the fact that the transport equation governing the amplitude function contains only a first-order derivative with respect to $\psi$. A rescaling of the normal coordinate as

$$\eta = \sqrt{k}\,\psi \tag{3.54a}$$

is consistent with the boundary layer structure of $L^u_{3c_2}(r,\theta)$, and will be seen to bring a second-order derivative with respect to $\psi$ into the equation governing the amplitude function.

Setting

$$h_{Is}(\phi,\psi) = \frac{\epsilon}{k} G(\phi,\eta) \exp\left[ikw\phi + ikV(0)\int_0^r q(r',0)\,dr' + \frac{3ik\epsilon}{2\beta_\infty}\right] , \tag{3.54b}$$

and substituting into the homogeneous form of the differential equation (3.2a), the function $G(\phi,\eta)$ is found to satisfy

$$2iw\frac{\partial G}{\partial\phi} + \frac{\partial^2 G}{\partial\eta^2} = 0 \tag{3.54c}$$

where terms of relative order $O(k^{-1/2})$ have been neglected. The exponential function in (3.54b) corresponds to the phase of the grazing ray. Since the rescaling of the normal coordinate has brought a second derivative into the differential equation (3.54c) governing $G(\phi,\eta)$, this function can satisfy the boundary condition on the airfoil surface as well as the radiation condition for large $\eta$. The factor $\epsilon/k$ in (3.54b) has been introduced in anticipation of the form of the boundary condition on $\eta = 0$. Since our analysis has neglected terms smaller than $O(\epsilon/k)$, only the leading-order solution for $G(\phi,\eta)$ is required.

The no-flow boundary condition (3.53) on the airfoil surface is applicable only over the airfoil chord length, $0 < \phi < 2$. However, it proves convenient to enforce (3.53) for the full range $\phi > 0$, and to correct the boundary condition for $\phi > 2$ at a later stage of the analysis. Evaluating the right-hand side of Eq. (3.53), the boundary condition satisfied by $G(\phi,\eta)$ is

$$\left.\frac{\partial G}{\partial\eta}\right|_{\eta=0} = b(\phi) \tag{3.54d}$$

where

$$b(\phi) = \frac{-A_n\, w e^{i\pi/4}}{2\sqrt{\pi}\sqrt{\delta+w}\,(\delta-w)}\left[1 - \frac{(\gamma+1)M_\infty{}^4}{2\beta_\infty{}^4\, w^2}(\delta-w)^2\right]\frac{\sqrt{2} - \sqrt{2-\phi}\,(\phi+1)}{\phi} \tag{3.54e}$$

for $0 < \phi < 2$ and

$$b(\phi) = \frac{-A_n\, w e^{i\pi/4}}{2\sqrt{\pi}\sqrt{\delta+w}\,(\delta-w)}\left[1 - \frac{(\gamma+1)M_\infty{}^4}{2\beta_\infty{}^4\, w^2}(\delta-w)^2\right]\frac{\sqrt{2}}{\phi} \tag{3.54f}$$

for $\phi > 2$. It is interesting to note that contributions to the function $b(\phi)$ arise only from derivatives of the function $\sigma_l$ and $L^u_{3c_2}$. Finally, a boundary condition on $G(0,\eta)$ is required to complete the specification of the problem for $G(\phi,\eta)$. The analysis of Section 3.2.2

demonstrated the match of the local leading-edge solution and the geometric-acoustics field $h_l$, to $O(\epsilon/k)$ when the functions are expressed in terms of the local leading-edge variables. Thus, we must set

$$G(0,\eta) = 0 \ . \qquad (3.54g)$$

Additional discussion concerning the formulation of the equations governing $G(\phi,\eta)$ can be found in Myers and Kerschen (1991), who recently carried out an extensive analysis of the near-surface field governed by a system of the type (3.54).

The solution to Eqs. (3.54) is developed utilizing a Laplace transform with respect to $\phi$, defined as

$$\overline{G}(s,\eta) = \int_0^\infty G(\phi,\eta)\, e^{-s\phi}\, d\phi \ . \qquad (3.55a)$$

with the inverse transform given by

$$G(\phi,\eta) = \frac{1}{2\pi} \int_{c-i\infty}^{c+i\infty} \overline{G}(s,\eta)\, e^{s\phi}\, ds \qquad (3.55b)$$

where $c$ is a positive real number. Applying the transform to (3.54c) and utilizing (3.54g), we obtain

$$\frac{\partial^2 \overline{G}}{\partial \eta^2} + 2\, i\, w\, s\, \overline{G} = 0 \ . \qquad (3.56a)$$

The solutions of this ordinary differential equation are

$$\exp(e^{-i\pi/4} \sqrt{2ws}\, \eta) \qquad \text{and} \qquad \exp(-e^{-i\pi/4} \sqrt{2ws}\, \eta) \ .$$

The branch cut in the $s$ plane is shown in figure 3.5. For values of $s$ in the right half-plane, the first solution grows exponentially as $\eta \to \infty$. Rejecting this solution, we have

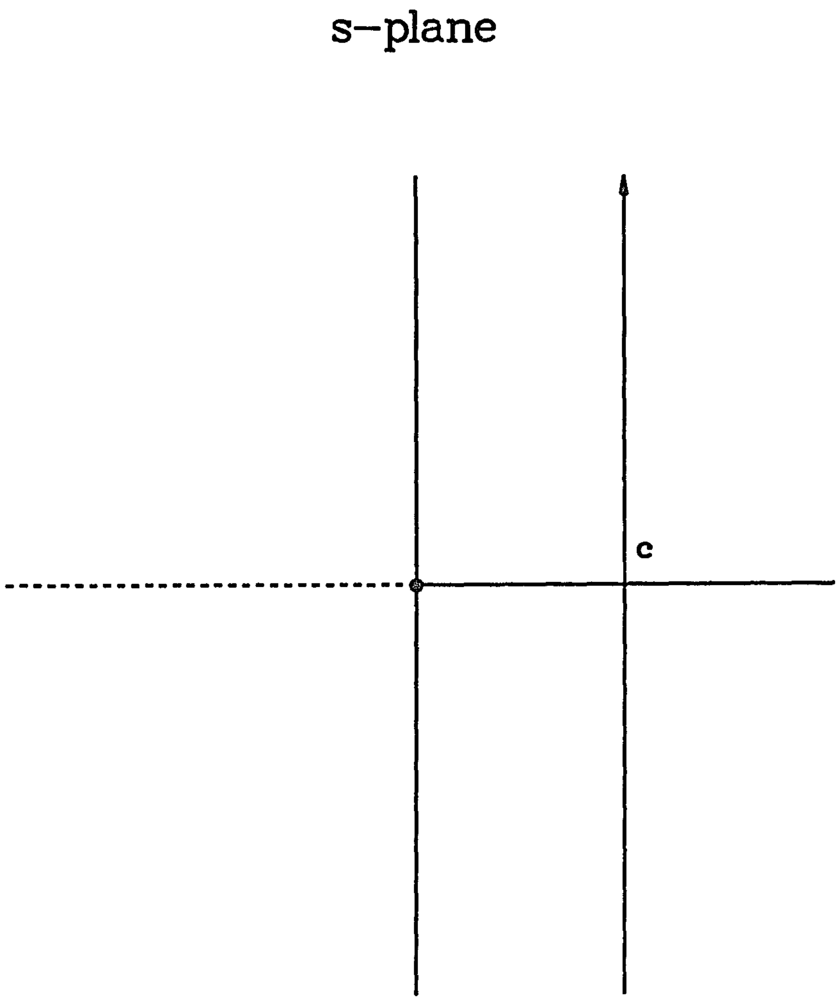


Figure 3.5 Location of singularities and a contour of integration in the transform plane for $G$.

$$\overline{G}(s,\eta) = D(s)\exp(-e^{-i\pi/4}\sqrt{2ws}\,\eta) \ . \tag{3.56b}$$

Applying the boundary condition (3.54d), the function $D(s)$ is found as

$$D(s) = -\frac{e^{i\pi/4}}{\sqrt{2ws}}\,\overline{b}(s) \ . \tag{3.56c}$$

Therefore, the Laplace transform of $G$ is

$$\overline{G} = -\frac{e^{i\pi/4}}{\sqrt{2w}}\,\frac{\exp(-e^{-i\pi/4}\sqrt{2ws}\,\eta)}{\sqrt{s}}\,\overline{b}(s) \ . \tag{3.56d}$$

The inverse transform is calculated using the Laplace convolution formula, which states that the Laplace transform of the convolution

$$f * g = \int_0^x f(x-\xi)\,g(\xi)\,d\xi \tag{3.57}$$

is equal to the product of the Laplace transforms of $f(x)$ and $g(x)$. Evaluating the inverse transform of the factor multiplying $\overline{b}(s)$ in Eq. (3.56d) and applying the convolution, $G(\phi,\eta)$ is given by

$$G(\phi,\eta) = -\frac{e^{i\pi/4}}{\sqrt{2w\pi}}\int_0^\phi e^{iw\eta^2/2(\phi-\xi)}\,\frac{b(\phi)}{\sqrt{\phi-\xi}}\,d\xi \tag{3.58a}$$

Substitution of Eqs. (3.54e) and (3.54f) into (3.58a) yields

$$G(\phi,\eta) = \frac{iA_n\sqrt{w}}{2\sqrt{2}\pi\sqrt{\delta+w}\,(\delta-w)}\left[1 - \frac{(\gamma+1)M_\infty^{\;4}}{2\,\beta_\infty^{\;4}\,w^2}(\delta-w)^2\right]$$
$$\int_0^\phi \frac{e^{iw\eta^2/2(\phi-\xi)}}{\sqrt{\phi-\xi}}\,\frac{\sqrt{2}-\sqrt{2-\xi}\,(\xi+1)}{\xi}\,d\xi \tag{3.58b}$$

for $0 < \phi < 2$ and

$$G(\phi,\eta) = \frac{iA_n\sqrt{w}}{2\sqrt{2}\pi\sqrt{\delta+w}(\delta-w)}\left[1-\frac{(\gamma+1)M_\infty{}^4}{2\,\beta_\infty{}^4\,w^2}(\delta-w)^2\right]$$
$$\left\{\int_0^2 \frac{e^{iw\eta^2/2(\phi-\xi)}}{\sqrt{\phi-\xi}}\,\frac{\sqrt{2}-\sqrt{2-\xi}(\xi+1)}{\xi}\,d\xi + \int_2^\phi \frac{e^{iw\eta^2/2(\phi-\xi)}}{\sqrt{\phi-\xi}}\,\frac{\sqrt{2}}{\xi}\,d\xi\right\} \tag{3.58c}$$

for $\phi > 2$.

From the standpoint of numerical evaluation, an unattractive feature of the above integrals is that the wavelength of the oscillatory terms is a function of the value of the integration variable $\xi$, with infinitely rapid variation near some of the limits of integration. Since the expression for $\phi > 2$ will be used in several places in the ensuing analysis, we introduce $\tau = \xi(\phi-2)/(\phi-\xi)$. After some algebraic manipulations, this leads to

$$G(\phi,\eta) = \frac{iA_n\sqrt{w}}{2\pi\sqrt{\delta+w}\,(\delta-w)}\left[1-\frac{(\gamma+1)M_\infty{}^4}{2\,\beta_\infty{}^4\,w^2}(\delta-w)^2\right]e^{iw\eta^2/2\phi}\,\frac{\sqrt{\phi-2}}{\sqrt{\phi}}$$
$$\left\{\int_0^2 \frac{\exp\left(\dfrac{iw\eta^2\tau}{2\phi(\phi-2)}\right)}{\tau\sqrt{\tau+\phi-2}}\left[1-\sqrt{1-\frac{\phi\tau}{2(\tau+\phi-2)}}\left(\frac{\phi\tau}{\tau+\phi-2}+1\right)\right]d\tau\right.$$
$$\left.+\int_2^\infty \frac{\exp\left(\dfrac{iw\eta^2\tau}{2\phi(\phi-2)}\right)}{\tau\sqrt{\tau+\phi-2}}\,d\tau\right\} \tag{3.58d}$$

for $\phi > 2$. The exponential terms are now seen to have a wavelength which is independent of the variable of integration.

In order to correct the boundary condition on $\psi = 0$ for $\phi > 2$, the value of the transition solution $h_{t_r}(\phi,\psi)$ for $\psi = 0\pm$ and $\phi > 2$ will be required. The value for $\psi = 0+$ is obtained by evaluating (3.58d) on $\eta = 0$, substituting the result into (3.54b) and combining with the result for $h_i(r,\theta)$ evaluated at $\theta = 0$. To extend the result to $\psi = 0-$, note that the incident field for the lower field corresponds to $h_i(r,\theta)$ evaluated at $\theta = 2\pi$, and $\eta = -\sqrt{k}\psi$. The results for $\phi > 2$ and $\psi = 0+$ and $0-$ can then be expressed in the form,

$$h_{l_{tr}}(\phi,0\pm) = \frac{e^{ik\sigma_l(\phi,0)}}{k^{3/2}\sqrt{\phi}}\Bigg\{L_0(0\pm) + \epsilon\sqrt{k}\Bigg\{L_1(0\pm) + L_2(0\pm) + L_{3p}(0\pm) + L_{3c_1}(0\pm) + L_{3c_3}(0\pm)$$

$$\mp \frac{A_n i\sqrt{w}}{2\pi\sqrt{\delta+w}\,(\delta-w)}\left[1 - \frac{(\gamma+1)M_\infty{}^4}{2\,\beta_\infty{}^4\,w^2}(\delta-w)^2\right]\left[\ln(32wk\phi) - \frac{i\pi}{2} + \Gamma\right.$$

$$\left.\left. \left. - \frac{\sqrt{\phi}}{\sqrt{2}}\int_0^2 \frac{\sqrt{2} - \sqrt{2-\xi}(\xi+1)}{\sqrt{\phi-\xi}\;\xi}d\xi - \ln(2) + 2\ln(\sqrt{\phi} - \sqrt{\phi-2})\right]\right\}\right\} \qquad (3.59)$$

where $\Gamma = 0.57721566490\cdots\cdots$ is Euler's constant. The argument of the directivity functions is $\theta = 0$ on the upper surface $\psi = 0+$, while on the lower surface $\psi = 0-$ the argument of the directivity functions is $\theta = 2\pi$. The phase function $\sigma_l$ has the same value on the upper and lower surfaces.

Finally, expressions for the transition solution in the far field $\phi >> 1$ will be required. The original scaling (3.54a) for the transition region assumed that $\eta$ and $\phi$ were both $O(1)$. However, from the phase functions in Eq. (3.58d), it can be seen that the appropriate extension of the transition region to the far field is given by $\eta = O(\phi)$. Neglecting terms which are higher order in $1/\phi$, Eq. (3.58d) then simplifies to

$$G(\phi,\eta) = \frac{iA_n\sqrt{w}}{2\pi\sqrt{\delta+w}\,(\delta-w)}\left[1 - \frac{(\gamma+1)M_\infty{}^4}{2\,\beta_\infty{}^4\,w^2}(\delta-w)^2\right]\frac{e^{iw\eta^2/2\phi}}{\sqrt{\phi}}$$

$$\left\{\int_0^2 \frac{e^{iw\eta^2\tau/2\phi^2}}{\sqrt{2}\,\tau}\left[\sqrt{2} - \sqrt{2-\tau}(\tau+1)\right]d\tau + \int_2^\infty \frac{e^{iw\eta^2\tau/2\phi^2}}{\tau}d\tau\right\}. \qquad (3.60)$$

where for the moment we are again restricting attention to $\psi > 0$. To determine the far-field sound, the complementary solution $h_{l_s}$ must be added to the geometric-acoustic field $h_l$. (The corresponding contributions for the sound field emanating from the local trailing-edge region are considered in following sections.) The analysis in this section has considered only the transition region, corresponding to $O(k^{-1/2})$ values of $\theta$ in the far field. However, an asymptotic expansion of Eq. (3.60) for $\eta/\phi >> 1$ shows that $G$ is $O(k^{-1})$ for $\theta = O(1)$.

Hence, for $\theta = O(1)$ the function $h_{ls}$ is smaller than the order of the terms we have chosen to retain in the outer region, and to the desired order of accuracy the solution for all values of $\theta$ can be considered as the sum of $h_l$ and $h_{ls}$.

In combining $h_l$ and $h_{ls}$ for $r >> 1$ and $O(1)$ values for $\theta$, it is useful to examine the transition-region expansion of the phase of the geometric-acoustic solution $h_l$. Substituting the transition-region variables into Eq. (3.49b), we obtain the expansion

$$k\,\sigma_l(r,\theta) \;=\; k w \phi + \frac{w\eta^2}{2\phi} + k\,V(0)\int_0^r q(r',0)\,dr' + \frac{3k\epsilon}{2\beta_\infty} + O(k^{-1/2}) \;. \tag{3.61}$$

It can then be seen that the phase of $h_{ls}$ (corresponding to the sum of the phase term in (3.60) and that extracted in (3.54b)) is then simply $\sigma_l(r,\theta)$. In addition, expanding the quantity $k(1-\cos\theta)$, which appears in $L^u_{3c_2}$, in terms of the transition-region variables, we find

$$k\,(1 - \cos\theta) \;=\; \eta^2/2\phi^2 \;+\; O(k^{-1}) \;.$$

Thus in determining an expression for the acoustic far field which is uniformly valid in $\theta$, we express $h_{ls}$ in the form

$$h_{ls}(\phi,\psi) = \frac{\epsilon\, e^{ik\sigma_l(r,\theta)}}{k\sqrt{r}}\;\frac{A_n\, i\sqrt{w}}{2\pi\sqrt{\delta+w}\,(\delta-w)}\left[1 - \frac{(\gamma+1)M_\infty{}^4}{2\,\beta_\infty{}^4\, w^2}(\delta-w)^2\right]$$
$$\left[\int_0^2 e^{ikw(1-\cos\theta)\tau}\;\frac{\sqrt{2}-\sqrt{2-\tau}\,(\tau+1)}{\sqrt{2}\,\tau}\,d\xi_1 + \int_2^\infty \frac{e^{ikw(1-\cos\theta)\tau}}{\tau}\,d\tau\right] \;. \tag{3.62}$$

The solution $h_{ls}$ for $\psi < 0$ can be found in a similar fashion. The final result is simply the negative of the above solution. This can be understood by noting that $h_{ls}(\phi,\psi)$ is the continuation of $H_{3c_2}$ into the transition region, and $L^u_{3c_2}$ is an anti-symmetric function of $\psi$.

In the far field, the distance $r$ is very large and therefore $r(1-\cos\theta) = O(1)$ for essentially all angles. Then the method of steepest descent can be applied to the integral in $L^u_{3c_2}$ given by Eq. (3.32c), and the far-field expansion for $L^u_{3c_2}$ reverts to $L_{3c_2}$. Combining $h_l$ and $h_{ls}$, the far-field solution for the leading edge, incorporating transition region effects, is then

$$h^u_l(r,\theta) \sim \frac{e^{ik\sigma_l(r,\theta)}}{k^{3/2}\sqrt{r}} \Bigg\{ L_0(\theta) + \epsilon\sqrt{k} \Bigg\{ L_1(\theta) + L_2(\theta) + L_{3p}(\theta) + L_{3c_1}(\theta) + L_{3c_2}(\theta) + L_{3c_3}(\theta)$$
$$+ \frac{\text{sgn}(\psi) A_n\, i\sqrt{w}}{2\pi\sqrt{\delta+w}\,(\delta-w)} \left[ 1 - \frac{(\gamma+1) M_\infty{}^4}{2\,\beta_\infty{}^4\, w^2} (\delta-w)^2 \right]$$
$$\left[ \int_0^2 e^{ikw(1-\cos\theta)\tau}\, \frac{\sqrt{2} - \sqrt{2-\tau}\,(\tau+1)}{\sqrt{2}\,\tau}\, d\tau + \int_2^\infty \frac{e^{ikw(1-\cos\theta)\tau}}{\tau}\, d\tau \right] \Bigg\} \Bigg\}. \tag{3.63}$$

Closed-form expansions for the leading-edge directivity functions $L_i(\theta)$ were given in Section 3.1. The contribution from the transition region is represented by the two integrals in the above expression. The transition-region contribution cancels the logarithmic singularity in $L_{3c_2}$ as $\theta \to 0$ or $2\pi$.

### 3.4 Local Trailing-Edge Region

In the singular-perturbation structure, a local region is present at the trailing edge. In this section, we analyze the local problem in this trailing-edge region. There is a crucial difference in the boundary condition for the local leading-edge region and the local trailing-edge region. In the leading-edge region, in its initial development the boundary layer remains attached to the body surface, and hence the flow streamline goes around the leading edge following the body surface. In contrast, boundary-layer separation occurs at the sharp trailing edge, and the flow on the two surfaces of the airfoil continues downstream rather than going around the trailing edge. The influence of this viscous phenomenon on the inviscid flow is represented by the unsteady Kutta condition (Crighton 1985), which states that the total unsteady flow must leave the trailing edge tangentially. Since the flow speed on the upper and lower surfaces is not necessarily the same, a vortex sheet exists downstream of the trailing edge. The pressure must be continuous across this vortex sheet.

The local solution in the trailing-edge region contains two components, one due to the interaction of the convected gust with the trailing edge, and the other due to the interaction of the leading-edge sound field with the trailing edge. These two components are considered separately below.

We first consider the interaction of the convected disturbance with the trailing edge. To analyze the trailing-edge region, we introduce local coordinates scaled on the disturbance wavelength,

$$\Phi_t = k\,\phi_t \ , \tag{3.64b}$$

$$\Psi_t = k\,\psi_t \ . \tag{3.64c}$$

where $(\phi_t, \psi_t)$ are given by (3.50). The local trailing-edge expansion of the mean-flow perturbation is

$$q - i\,\mu = \frac{\epsilon}{2\,\beta_\infty}\left[3 - \frac{\sqrt{R_t}\,(\cos\theta_t/2 + i\,\sin\theta_t/2)}{\sqrt{2}\,\sqrt{k}} + O(\epsilon)\right] . \tag{3.65}$$

Where $(R_t, \theta_t)$ are the polar form of $(\Phi_t, \Psi_t)$ and $-\pi < \theta_t < \pi$. The interaction of this mean-flow perturbation with the convected gust produces a source term similar to that in Eq. (3.14a) for the leading edge, but the source term for the trailing edge is $O(1/k)$ weaker than that for the leading edge. Hence, the source term $S$ in Eq. (3.2a) can be neglected to the order of approximation. Though the volume source term is negligible, sound might still be generated by the change in boundary condition, representing the interaction of the convected disturbance with the trailing edge. The boundary condition Eq. (3.2g) and the homogeneous part of Eq. (3.2a), rewritten in local trailing-edge coordinates, apply. However, the mean-flow perturbation quantities are $O(\epsilon)$ or smaller and can be ignored.

The governing equations corresponding to the interaction of the convected gust with the trailing edge are then

$$\frac{\partial^2 H_t}{\partial \Phi_t^{\,2}} + \frac{\partial^2 H_t}{\partial \Psi_t^{\,2}} + w^2 H_t = 0 \ , \tag{3.66a}$$

$$\left.\frac{\partial H_t}{\partial \Psi_t}\right|_{\substack{\Phi_t < 0 \\ \Psi_t = 0}} = \frac{-A_n}{k\,\beta_\infty} e^{ik\epsilon 3/2\beta_\infty} e^{ik\delta(2+\epsilon/\beta_\infty)} e^{i\delta\Phi_t} + O(\epsilon k^{-3/2})) \ . \tag{3.66b}$$

The phase factor $k\epsilon 3/2\beta_\infty$ is an $O(1)$ shift in the phase of the convected gust which occurs upstream of the airfoil, caused by the airfoil thickness slowing down the approach of the gust. The phase factor involving $\delta$ represents the change in the phase of the gust in convecting the length of the airfoil, with the term containing $\epsilon$ again being the influence of airfoil thickness. Downstream of the trailing edge, the boundary conditions on $\Psi = 0\pm$ are that the unsteady components of pressure and transverse velocity must be continuous across the vortex sheet, i.e.,

$$\left[\frac{\partial H_t}{\partial \Psi_t} - i\,\delta\, H_t\right]_{\substack{\Phi_t > 0 \\ \Psi_t = 0^+}} = \left[\frac{\partial H_t}{\partial \Psi_t} - i\,\delta\, H_t\right]_{\substack{\Phi_t > 0 \\ \Psi_t = 0^-}} \ , \tag{3.66c}$$

and

$$\left.\frac{\partial H_t}{\partial \Psi_t}\right|_{\substack{\Phi_t > 0 \\ \Psi_t = 0^+}} = \left.\frac{\partial H_t}{\partial \Psi_t}\right|_{\substack{\Phi_t > 0 \\ \Psi_t = 0^-}} \ . \tag{3.66d}$$

Equations (3.66) are mixed-boundary-value problem which can be solved by the Wiener-Hopf technique. The uniqueness of the solution requires that the edge condition be specified for the behavior as the $\Phi_t \to 0$. From the unsteady Kutta condition, we require that the pressure and transverse velocity be bounded as $\Phi_t \to 0\pm$, respectively. The solution satisfying Eqs. (3.66) is

$$H_t = \frac{\mathrm{sgn}(\Psi_t) A_n}{k\, \beta_\infty \sqrt{\delta^2 - w^2}}\, e^{i k \epsilon 3/2 \beta_\infty}\, e^{i k \delta (2 + \epsilon/\beta_\infty)}\, e^{i \delta \Phi_t - |\Psi_t| \sqrt{\delta^2 - w^2}} \quad . \tag{3.67}$$

Eq. (3.67) is an extension into the local trailing-edge region of the hydrodynamic solution Eq. (3.37a). It exhibits the same form for $\Phi_t > 0$ and $\Phi_t < 0$. This result is a consequence of the unsteady Kutta condition, which causes a wake of shed vorticity to be generated by the time-dependent motion. The shed vorticity in this wake is essentially a smooth continuation of bound vorticity in the airfoil which cancels the gust velocity $v'$. In the local trailing-edge region, both the bound and shed vorticity convect at the free-stream speed, hence no pressure fluctuations are generated. Thus, the interaction of the convected disturbance with the trailing edge produces no sound.†

In addition to the convected disturbance, there are pressure fluctuations associated with the leading-edge acoustic field. In general, the leading-edge acoustic field is different above and below the airfoil. Thus a pressure difference across the trailing edge is produced. In order to cancel this difference, a scattered field arises at the trailing edge. The scattered field in the local trailing-edge region becomes the source of the trailing-edge acoustic field

---

† Note that the above result does not contradict trailing-edge noise theories (Howe 1978). Since our theory has ignored the presence of the boundary layer, the vorticity is convected at free-stream speed. In contrast, trailing-edge noise theories consider boundary-layer turbulence, which convects at speed less than free-stream speed. In this situation, pressure fluctuations are generated and the trailing-edge region is a local sound source.

which extends into the outer region.

The modified pressure for the leading-edge acoustic field, $p_l$, can be found by Eq. (2.13b). In calculating $\partial h/\partial\phi$, the derivative on the rapidly varying phase dominates. Hence, after non-dimensionalization,

$$p_l \;=\; i\,k\,(\delta - w\cos\theta)\,e^{-ik\delta M_\infty{}^2\phi}\,h_{l\,tr}(r,\theta) \;+\; O(k^{-3/2},\,\epsilon/\sqrt{k}) \;. \tag{3.68}$$

to the order which is retained in this dissertation. Thus, from Eq. (3.59), the jump in modified pressure across the wake is

$$p_l\Big|_{\psi=0^+} - p_l\Big|_{\psi=0^-} \;=\; \frac{pj(\phi_t)}{\sqrt{k}}\,e^{ikw\phi_t - i\delta M_\infty{}^2 k\phi}\,\exp\left[ikV(0)\left[\int_0^{\phi} q(r',0)\,dr' - \frac{\epsilon}{\beta_\infty}\right]\right] \tag{3.69a}$$

where

$$\begin{aligned} pj(\phi_t) = e^{ik\sigma_l(2+\epsilon/\beta_\infty,0)}\,\frac{i(\delta-w)}{\sqrt{2+\phi_t}}\Bigg\{ & L_0(0) - L_0(2\pi) + \epsilon\sqrt{k}\Bigg\{L_1(0) - L_1(2\pi) + L_2(0) - L_2(2\pi) + L_{3p}(0) \\ & - L_{3p}(2\pi) + L_{3c_1}(0) - L_{3c_1}(2\pi) + L_{3c_3}(0) - L_{3c_3}(2\pi) - \frac{A_n\,i\sqrt{w}}{\pi\sqrt{\delta + w(\delta - w)}}\left[1 - \frac{(\gamma+1)M_\infty{}^4}{2\,\beta_\infty{}^4\,w^2}(\delta - w)^2\right] \\ & \left[\ln(16kw(\phi_t+2)) - \frac{i\pi}{2} + \Gamma - \frac{\sqrt{\phi_t+2}}{\sqrt{2}}\int_0^2 \frac{\sqrt{2} - \sqrt{2-\xi}\,(\xi+1)}{\sqrt{\phi_t+2-\xi}\;\xi}\,d\xi + 2\ln(\sqrt{\phi_t+2} - \sqrt{\phi_t})\right]\Bigg\}\Bigg\} \end{aligned} \tag{3.69b}$$

and

$$\sigma_l(2+\epsilon/\beta_\infty,0) \;=\; w\,(2 + \epsilon/\beta_\infty) + \epsilon\,V(0)/\beta_\infty + 3\epsilon/2\beta_\infty \;. \tag{3.69c}$$

The local trailing-edge field which cancels this pressure jump satisfies the Helmholtz equation in local trailing-edge variables:

$$\frac{\partial^2 H_t}{\partial \Phi_t{}^2} + \frac{\partial^2 H_t}{\partial \Psi_t{}^2} + w^2 H_t \;=\; 0 \;. \tag{3.70a}$$

In contrast to the local leading-edge region, the non-uniform propagation effects are $O(\epsilon)$ and can be neglected. Introducing the local trailing-edge variables $(\Phi_t, \Psi_t)$ in Eqs. (3.69), the local trailing-edge solution $H_t$ satisfies the following boundary condition across the wake vortex sheet.

$$\left[ \frac{\partial H_t}{\partial \Psi_t} - i\,\delta\, H_t \right]_{\substack{\Phi_t > 0 \\ \Psi_t = 0^+}} - \left[ \frac{\partial H_t}{\partial \Psi_t} - i\,\delta\, H_t \right]_{\substack{\Phi_t > 0 \\ \Psi_t = 0^-}} = \frac{p\,j(0)}{k^{3/2}}\, e^{i w \Phi_t} \ . \tag{3.70b}$$

It can be seen that the variation of the amplitude at the pressure jump with $\phi_t$ does not enter in this local region. In addition to continuity of pressure, the vertical velocity must also be continuous across the vortex sheet, i.e.,

$$\left. \frac{\partial H_t}{\partial \Psi_t} \right|_{\substack{\Phi_t > 0 \\ \Psi_t = 0^+}} = \left. \frac{\partial H_t}{\partial \Psi_t} \right|_{\substack{\Phi_t > 0 \\ \Psi_t = 0^-}} \ . \tag{3.70c}$$

Finally, the no-flow condition must be enforced on the airfoil surface, i.e.,

$$\left. \frac{\partial H_t}{\partial \Psi_t} \right|_{\substack{\Phi_t < 0 \\ \Psi_t = 0}} = 0 \ . \tag{3.70d}$$

In order to satisfy the unsteady Kutta condition, it is further assumed that $\partial H_t / \partial \Psi_t$ is finite as $R_t$ approaches zero.

Equations (3.70) can be solved by the Wiener-Hopf technique. The result is

$$H_t(\Phi_t, \Psi_t) = \frac{\mathrm{sgn}(\Psi_t)\, i\, \sqrt{w}\, p\,j(0)}{2\sqrt{2}\, \pi\, k^{3/2}} \int_{-\infty}^{\infty} \frac{e^{-i\lambda\Phi_t - |\Psi_t| \sqrt{\lambda^2 - w^2}}}{(\lambda + \delta)\,(\lambda + w)\,\sqrt{\lambda - w}}\, d\lambda \ . \tag{3.71a}$$

For matching with the outer and transition regions, asymptotic expansions of (3.71a) for $R_t >> 1$ are required. An asymptotic expansion for $R_t \rightarrow \infty$ and $\theta_t = O(1)$ can be obtained by the method of steepest descent as

$$H_t \sim \frac{T(\theta_t)\, e^{ikwr_t}}{k^2\sqrt{r_t}} + O(k^{-5/2}) \tag{3.71b}$$

where

$$T(\theta_t) = \frac{-\operatorname{sgn}(\psi_t)\, e^{-i\pi/4}\, pj(0)}{2\sqrt{\pi}\sqrt{w}\sqrt{1-\cos\theta_t}\,(\delta - w\cos\theta_t)}\,. \tag{3.71c}$$

Equation (3.71c) is singular for small $\theta_t$. The method of steepest descent fails for small angles due to the proximity of the saddle point at $\lambda = -w\cos\theta_t$ to the pole at $\lambda = -w$.

In developing an asymptotic expansion of (3.71a) for $R_t >> 1$ which is uniformly valid in $\theta_t$, it is convenient to separate the integral into two parts, i.e.,

$$\int_{-\infty}^{\infty} \frac{e^{-i\lambda\Phi_t - |\Psi_t|\sqrt{\lambda^2-w^2}}}{(\lambda+\delta)(\lambda+w)\sqrt{\lambda-w}}\,d\lambda = \int_{-\infty}^{\infty} \frac{e^{-i\lambda\Phi_t - |\Psi_t|\sqrt{\lambda^2-w^2}}}{(\delta-w)(\lambda+w)\sqrt{\lambda-w}}\,d\lambda - \int_{-\infty}^{\infty} \frac{e^{-i\lambda\Phi_t - |\Psi_t|\sqrt{\lambda^2-w^2}}}{(\delta-w)(\lambda+\delta)\sqrt{\lambda-w}}\,d\lambda\,.$$

The method of steepest descent is applicable to the second integral in the right side of the equation. A uniform asymptotic expansion is developed for the first integral in Appendix B. The final result corresponds to replacing the function $T(\theta_t)$ in Eq. (3.71b) by the function

$$T^u(r_t,\theta_t) = \frac{\operatorname{sgn}(\psi_t)\, i\, pj(0)}{2(\delta-w)}\left[\operatorname{erfc}\!\left(e^{-i\pi/4}\sqrt{w(1-\cos\theta_t)kr_t}\right) e^{ikwr_t(\cos\theta_t - 1)}\sqrt{kr_t} - \frac{\sqrt{2}\sqrt{w}\,e^{i\pi/4}\,|\sin\theta_t/2|}{\sqrt{\pi}(\delta - w\cos\theta_t)}\right]. \tag{3.71d}$$

Note that the amplitude of the function $T^u(r_t,\theta_t)$ is constant along the vortex sheet $\theta_t = 0$. This is to be expected, since the decay of the amplitude of the leading-edge pressure field did not enter in forming the boundary condition (3.70b). Thus, the asymptotic expansion (3.71d) is valid only for $1/k << r_t << 1$, and the trailing-edge outer solution at shallow angles cannot be obtained by simply extending the directivity function $T^u(r_t,\theta_t)$ into the outer region. A separate trailing-edge transition region is necessary to describe the behavior of the solution at shallow angles for $r_t = O(1)$.

### 3.4.1 Matching of Local Trailing-Edge and Outer Solutions:

In this section, the local trailing-edge solution (3.71) and the corresponding outer solution (3.51) are matched for $O(1)$ values of $\theta_t$. The matching procedure is nearly identical to the matching carried out for the leading edge in Section 3.2.2. The final result is

$$h_t = \frac{T(\theta_t)\, e^{ik(wr_t + \sigma_{t_1})}}{k^2 \sqrt{r_t}} \tag{3.72}$$

where $\sigma_{t_1}$ is given in Eq. (3.51d) and $g_2(\theta_t) = 0$.

The outer solution (3.72) contains $T(\theta_t)$, which is singular as $\theta_t$ approaches zero. This singularity signifies that the geometric-acoustic assumption is violated for small values of $\theta_t$. Thus a transition region is needed to describe the sound field at shallow angles. This solution is developed in the following section.

## 3.5 Trailing-Edge Transition Solution

In formulating the analysis in the trailing-edge transition region, it is useful to note that the solution $H_t(\Phi_t, \Psi_t)$ in the local trailing-edge region is simply a complementary solution to the governing equations which cancels the jump in the leading-edge pressure field across the vortex sheet ($\Phi_t > 0$, $\Psi_t = 0$). This feature also holds for the trailing-edge transition region, to the order of the analysis carried out here. Thus, in continuing the local trailing-edge solution into the transition region, we seek a complementary solution $h_{ts}$ which cancels the pressure jump across the vortex sheet due to the leading-edge transition field, i.e. we set

$$h_{ttr} = h_{ltr} + h_{ts} \tag{3.73}$$

where $h_{ltr}(\phi,\eta)$ is the leading-edge transition solution.

Guided by analysis of the leading-edge transition region in Section 3.3, we introduce a transverse coordinate

$$\eta_t = \sqrt{k}\, \psi_t \ . \tag{3.74a}$$

The function $h_{ts}$ exhibits a multiple-scales dependence on $\phi_t$. The dependence on the short scale of the disturbance wavelength is suppressed by factoring out a phase function. Thus we set

$$h_{ts} = \frac{1}{k^{3/2}} G_t(\phi_t, \eta_t)\, e^{ik\sigma_t(\phi_t, 0)} \tag{3.74b}$$

where the factor $k^{-3/2}$ has been introduced in anticipation of the matching with the local trailing-edge region.

Substituting Eq. (3.73) into the differential equation (3.2a) and introducing the trailing-edge transition region variables, the function $G_t(\phi_t, \eta_t)$ is found to satisfy

$$2\,i\,w \frac{\partial G_t}{\partial \phi_t} + \frac{\partial^2 G_t}{\partial {\eta_t}^2} = 0 \ . \tag{3.75a}$$

One boundary condition is provided by continuity of pressure across the vortex sheet. In order to cancel the pressure associated with the leading-edge field, we have

$$G_t \Big|_{\substack{\phi_t > 0 \\ \eta_t = 0^+}} - G_t \Big|_{\substack{\phi_t > 0 \\ \eta_t = 0^-}} = \frac{i\, pj(\phi_t)}{\delta - w} \ . \tag{3.75b}$$

Note that the function $pj(\phi_t)$ contains terms of $O(1)$, $O(\epsilon\sqrt{k}\ln k)$ and $O(\epsilon\sqrt{k})$. The second boundary condition that the vertical velocity is continuous across the vortex sheet leads to

$$\left.\frac{\partial G_t}{\partial \eta_t}\right|_{\substack{\phi_t > 0 \\ \eta_t = 0^+}} = \left.\frac{\partial G_t}{\partial \eta_t}\right|_{\substack{\phi_t > 0 \\ \eta_t = 0^-}} \quad . \tag{3.75c}$$

The function $h_{ts}$ must represent an outgoing wave as $|\eta_t| \to \infty$; this condition is enforced by introducing an appropriate small imaginary quantity in the analysis and requiring that

$$G_t \to 0 \qquad \text{as} \qquad |\eta_t| \to \infty \ . \tag{3.75d}$$

Finally, a boundary condition on $G_t$ is required at $\phi_t = 0$. This condition arises from the matching of the local trailing-edge solution and the trailing-edge transition solution. Consider the expansion of these two solutions in a common region $\Phi_t = O(k^{1/2})$, $\Psi_t = O(k^{1/2})$, corresponding to $\phi_t = O(k^{-1/2})$, $\eta_t = O(1)$. It can be seen from Eq. (3.71b) that the leading term of $H_t$ is $O(k^{-7/4})$ in this region. In order to match with this result, the leading term of $G_t$ must be $O(k^{-1/4})$ in this region. Taking the limit $k \to \infty$, the leading order term of $G_t$ must vanish as $\phi_t \to 0$. A similar argument holds for the higher-order terms in the expansion for $G_t$, as shown for a related problem by Myers and Kerschen (1992). Thus, we set

$$G_t(0,\eta_t) = 0 \ . \tag{3.75e}$$

The solution to Eqs. (3.75) can be developed utilizing the Laplace transform. The details of the analysis are similar to those in Section 3.3. The final result in convolution form is

$$G_t = \frac{\sqrt{w}\, e^{i\pi/4}}{2\sqrt{2}\sqrt{\pi}\,(\delta - w)} \int_0^{\phi_t} \frac{\eta_t\, pj(\phi_t)\, e^{iw\eta_t^2/2(\phi_t - \xi)}}{(\phi_t - \xi)^{3/2}}\, d\xi \ . \tag{3.76a}$$

It can be seen that $G_t$ is an antisymmetric function of $\eta_t$. Substituting (3.69b) into (3.76a), introducing the change of variable $\xi_1 = |\eta_t|/\sqrt{\phi_t - \xi}$, and integrating term by term, we obtain

$$
\begin{aligned}
G_t \;=\; & -\frac{\operatorname{sgn}(\psi_t)\, pj(0)\, e^{i w \eta_t^2/2(\phi_t+2)}}{2\sqrt{\phi_t+2}} \operatorname{erfc}\!\left(e^{-i\pi/4}\sqrt{w}\,|\eta_t|/\sqrt{\phi_t(\phi_t+2)}\right) \\
& -\frac{\epsilon\sqrt{k}\operatorname{sgn}(\psi_t) A_n\, i\sqrt{w}\, e^{ik\sigma_t(2+\epsilon/\beta_\infty,0)}}{2\pi\sqrt{\delta+w}\,(\delta-w)} \left[1-\frac{(\gamma+1)M_\infty^{\,4}}{2\beta_\infty^{\,4} w^2}(\delta-w)^2\right] \\
& \left\{ \frac{2e^{-i\pi/4}\sqrt{w}}{\sqrt{\pi}} \frac{|\eta_t|}{\sqrt{\phi_t}\,(\phi_t+2)} e^{i w \eta_t^2/2(\phi_t+2)} \right. \\
& \quad \int_2^\infty e^{i w \eta_t^2 \xi^2/4\phi_t(\phi_t+2)} \left[\ln(2) + \ln\!\left[1 - \frac{1}{\phi_t+2} - \frac{2\phi_t}{(\phi_t+2)\xi^2} + \sqrt{\frac{\phi_t}{\phi_t+2}}\sqrt{1-\frac{4}{\xi^2}}\right]\right] d\xi \\
& + \int_0^2 \frac{\sqrt{2}-\sqrt{2-\tau}(\tau+1)}{\sqrt{2}\,\tau} \frac{e^{i w \eta_t^2/2(\phi_t+2-\tau)}}{\sqrt{\phi_t+2-\tau}} \operatorname{erfc}\!\left(\frac{\sqrt{2-\tau}\, e^{-i\pi/4}\sqrt{w}\,|\eta_t|}{\sqrt{2}\sqrt{\phi_t}\sqrt{\phi_t+2-\tau}}\right) d\tau \\
& \left. + \left[2 - 2\ln(2)\right] \frac{e^{i w \eta_t^2/2(\phi_t+2)}}{\sqrt{\phi_t+2}} \operatorname{erfc}\!\left(e^{-i\pi/4}\sqrt{w}\,|\eta_t|/\sqrt{\phi_t(\phi_t+2)}\right) \right\}. \qquad (3.76b)
\end{aligned}
$$

In the following sections, (3.76b) is matched with the solutions in local trailing-edge region and the outer region.

### 3.5.1 Matching of Local Trailing-Edge and Trailing-Edge Transition Solutions:

The acoustic fields in both the local trailing-edge region and the trailing-edge transition region consist of the sum of the leading-edge transition solution $h_{ltr}$ and a scattered field. Thus, in examining the matching between these regions, we shall consider only the scattered fields, $H_t(\Phi_t, \Psi_t)$ and $h_{ts}(\phi_t, \eta_t)$. In deriving Eq. (3.75e), we considered the asymptotic matching of these fields in a square region, $\Phi_t$ and $\Psi_t = O(k^{1/2})$. That limit corresponds to $\phi_t \to 0$ with $\eta_t = O(1)$. In this section we consider a different limit which captures the thin-layer structure of the solutions. Specifically, the variable $\rho_t = |\eta_t|/\sqrt{\phi_t} = |\Psi_t|/\sqrt{\Phi_t}$ is held constant in the matching process. We utilize Van Dyke's rule, expressing the local trailing-edge expansion (3.71d) in terms of $\phi_t$ and $\rho_t$, and expanding the trailing-edge transition solution (3.76b) in terms of $\Phi_t$ and $\rho_t$. The transition-variables expansion of the local trailing-edge solution takes the form

$$- \frac{\operatorname{sgn}(\psi_t)\ pj(0)\ e^{ikw\phi_t}}{2\sqrt{2}\ k^{3/2}} \operatorname{erfc}(e^{-i\pi/4}\sqrt{w}\,\rho_t/\sqrt{2})$$

which is identical to the local expansion of the transition solution when $\Phi_t$ is replaced by $k\phi_t$, showing that the matching condition is satisfied. This result verifies that the trailing-edge transition solution is the proper continuation of the thin layer at shallow angles identified in Eq. (3.71d).

### 3.5.2 Matching of Trailing-Edge Transition and Outer Solutions:

Next we consider the matching of the trailing-edge transition region with the outer solution. The outer solution (3.72) (with 3.71c) of $O(k^{-2})$ is expressed in terms of transition region variables and expanded to $O(k^{-3/2},\ \epsilon/k)$, while the transition region solution (3.76b) of $O(k^{-3/2},\ \epsilon/k)$ is expressed in terms of outer variables and expanded to $O(k^{-2})$. Comparing these expressions in transition region variables, we find the common term

$$h_t^c \ = \ - \frac{\operatorname{sgn}(\psi_t)\ e^{i\pi/4}\ pj(0)\ \sqrt{\phi_t}}{2\sqrt{\pi}\ \sqrt{w}\ |\eta_t|\ k^{3/2}}\ e^{ikw\phi_t + iw\eta_t^2/2\phi_t + ik\sigma_{t_1}(r_t,0)} \quad . \tag{3.77}$$

A uniformly valid composite solution can be formed from Eqs. (3.72), (3.76b) and (3.77) as

$$h_t^u \ = \ h_t \ + \ h_{ts} \ - \ h_t^c \ . \tag{3.78}$$

We now utilize the composite solution (3.78) to evaluate the the far-field sound. Before taking the limit $r_t >> 1$, we express the composite solution in terms of outer variables. First note that the phase of the geometric-acoustic solution $h_t$, when expanded in transition region variables, takes the form

$$k\,\sigma_t(r_t,\theta_t) \;=\; k\,w\,\phi_t \;+\; \frac{w\,\eta_t^{\,2}}{2\,\phi_t} \;+\; k\,\sigma_{t_1}(\phi_t,0) \;+\; O(k^{-1})\;. \tag{3.79a}$$

Thus, the phase factors in $h_{ts}$ and $h_t^c$ can be expressed compactly in terms of the phase function $k\sigma_t$. Secondly, guided by the combination of variables which appears in Eq. (3.71d), we find the expansion in transition region variables

$$2\,k\,(1-\cos\theta_t) \;=\; \eta_t^{\,2}/\phi_t^{\,2} \;+\; O(k^{-1})\;. \tag{3.79b}$$

Utilizing this result to replace $\eta_t$ in $h_{ts}$ and $h_t^c$, and neglecting terms of $O(1/\phi_t)$, the far-field form of the composite solution for the trailing-edge acoustic field is

$$\begin{aligned}
h_t^u(r_t,\theta_t) \sim\; & \frac{\operatorname{sgn}(\psi_t)\,e^{ik\sigma_t(r_t,\theta_t)}}{2\,k^2\sqrt{r_t}}\Bigg\{\frac{pj(0)\sqrt{w}\,e^{i\pi/4}\,|\sin\theta_t/2|}{\sqrt{\pi}\,(\delta-w\cos\theta_t)} \\
& - pj(0)\,e^{-2ikw(1-\cos\theta_t)}\sqrt{k}\,\operatorname{erfc}\!\left(e^{-i\pi/4}\sqrt{2kw(1-\cos\theta_t)}\right) \\
& - \frac{\epsilon k A_n\, i\sqrt{w}\,e^{ik\sigma_t(2+\epsilon/\beta_\infty,0)-2iwk(1-\cos\theta_t)}}{\pi\sqrt{\delta+w}\,(\delta-w)}\left[1-\frac{(\gamma+1)M_\infty^{\,4}}{2\,\beta_\infty^{\,4}\,w^2}(\delta-w)^2\right] \\
& \Bigg\{\frac{\sqrt{2}\sqrt{wk(1-\cos\theta_t)}\,e^{-i\pi/4}}{\sqrt{\pi}}\int_2^{\infty} e^{ikw(1-\cos\theta_t)\xi^2/2}\left[\ln(2)+\ln\!\left(1-2/\xi^2+\sqrt{1-4/\xi^2}\right)\right]d\xi \\
& + \int_0^2 \frac{\sqrt{2}-\sqrt{2-\tau}\,(\tau+1)}{\sqrt{2\tau}}\,e^{ikw(1-\cos\theta_t)\tau}\operatorname{erfc}\!\left(e^{-i\pi/4}\sqrt{(2-\tau)kw(1-\cos\theta_t)}\right)d\tau \\
& + \left[2-2\ln(2)\right]\operatorname{erfc}\!\left(e^{-i\pi/4}\sqrt{2kw(1-\cos\theta_t)}\right)\Bigg\}\Bigg\}\;.
\end{aligned} \tag{3.80}$$

### 3.6 Total Far-Field Acoustic Solution

In this section, the far-field composite solutions for the leading edge and trailing edge are combined together to form the total acoustic far field. The total far-field acoustic solution is

$$h = h_l^u + h_t^u \tag{3.81}$$

where $h_l^u$ and $h_t^u$ are given by Eqs. (3.63) and (3.80), respectively. The expression (3.63) for the leading-edge field $h_l^u$ contains the directivity functions $L_0(\theta)$, $L_1(\theta)$, $L_2(\theta)$, $L_{3p}(\theta)$, $L_{3c_1}(\theta)$, $L_{3c_2}(\theta)$ and $L_{3c_3}(\theta)$, which are given by Eqs. (3.10b), (3.13b), (3.18b), (3.31b), (3.31d), (3.32b) and (3.31f), respectively. The phase function $\sigma_l(r,\theta)$ which appears in $h_l^u$ is given by Eqs. (3.49b) and (3.42c). The expression (3.80) for $h_t^u$ contains the functions $pj(0)$, $\sigma_t(r_t,\theta_t)$ and $\sigma_l(2+\epsilon/\beta_\infty,0)$. The leading-edge field pressure jump at the trailing edge, $pj(0)$, can be calculated from Eq. (3.69b), the phase of the leading-edge field evaluated at the trailing edge, $\sigma_l(2+\epsilon/\beta_\infty,0)$, is given by Eq. (3.69c), and the phase of the trailing-edge field, $\sigma_t(r_t,\theta_t)$, is given by Eq. (3.51g). In Eq. (3.80), $r_t$ and $\theta_t$ can be replaced by $r$ and $\theta$ without introducing extra errors, excluding the phase term $\sigma_t(r_t,\theta_t)$ which is considered separately below.

An important feature of the far-field directivity pattern is the constructive and destructive interference which occurs between the leading-edge and trailing-edge acoustic fields. It is the difference in the phase of the disturbances emanating from the leading and trailing edge regions which creates this effect. Therefore it is convenient to extract the leading-edge phase function from the trailing-edge field. The total phase for the trailing-edge field $h_t^u$ is $k\sigma_t(r_t,\theta_t)+k\sigma_l(2+\epsilon/\beta_\infty,0)$. (Note that $pj(0)$ includes the phase factor $e^{ik\sigma_l(2+\epsilon/\beta_\infty,0)}$.) The difference in the far-field phase

$$k\sigma_d(\theta) = k\sigma_t(r_t,\theta_t) + k\sigma_l(2+\epsilon/\beta_\infty,0) - k\sigma_l(r,\theta) \ , \tag{3.82a}$$

is given by

$$k\sigma_d(\theta) = kw(2+\epsilon/\beta_\infty)\,(1-\cos\theta) + \frac{k\epsilon}{\beta_\infty}\Big[V(0)-V(\theta)\cos\theta\Big] \tag{3.82b}$$

$$= kw\Big[2+\epsilon F(2)\Big]\,(1-\cos\theta) + k\Big[V(0)-V(\theta)\cos\theta\Big]\,\epsilon\, F(2) \tag{3.82c}$$

where terms of $O(k^{-1})$ have been neglected. Equation (3.82b) is the result for a Joukowski airfoil, while Eq. (3.82c) is the generalized form for the case of a symmetric airfoil of arbitrary thickness distribution, included here in anticipation of the discussion in Section 3.7.

The total far-field acoustic solution for a symmetric Joukowski airfoil, Eq. (3.81), can then be written as

$$h = \frac{e^{ik\sigma_l(r,\theta)}}{k^{3/2}\sqrt{r}}\Bigg\{L_0(\theta)+\epsilon\sqrt{k}\,f_l(k,\theta) + e^{ik\sigma_d(\theta_t)}\Big[pj(0)\,e^{-ik\sigma_l(2+\epsilon/\beta_\infty,0)}f_{t_0}(k,\theta_t)+\epsilon\sqrt{k}\,f_{t_1}(k,\theta_t)\Big]\Bigg\}\,. \tag{3.83}$$

Airfoil thickness enters in two ways in this equation, through the combination $\epsilon\sqrt{k}$ and implicitly through the phase functions $\sigma_l$ and $\sigma_d$. The combination $\epsilon\sqrt{k}$ arose in the analysis of the local leading-edge region, where the airfoil shape essentially reduces to a parabola whose nose radius matches that of the airfoil. For a Joukowski airfoil shown in figure (3.1), the nose radius is $r_n = \epsilon^2 b$. The combination $\epsilon\sqrt{k}$ can then be expressed in terms of a Strouhal number based on the gust frequency and the airfoil nose radius, i.e.,

$$St = \omega r_n/U_\infty = \epsilon^2 k\ . \tag{3.84}$$

Thus, the effect of airfoil thickness on the amplitudes of the leading-edge field and the trailing edge field is proportional to the square root of a Strouhal number based on the airfoil nose radius.

The airfoil thickness also modifies the phase of the far-field sound through the function $\sigma_l(r,\theta)$. The phase of the sound field is usually of much less interest than the amplitude. A more important influence on the sound field which arises as a result of phase effects is due to the phase difference between the leading-edge and trailing-edge fields, $\sigma_d(\theta)$. This function controls the pattern of constructive and destructive interference between the leading- and trailing-edge fields. The phase function $\sigma_d$ is determined by the global airfoil thickness distribution, but its only influence on the far-field sound is a shift in the angular locations of the lobes of the directivity pattern. A change in the gust frequency $k$ also shifts the angular locations of these lobes, even for the case of a zero-thickness airfoil.

Equation (3.83) also illustrates that the local leading-edge region is the primary sound source. The trailing edge field arises only due to the scattering of the pressure field $pj(0)$ which was generated in the local leading-edge region. The amplitude of the leading-edge acoustic field depends solely on the nose radius of the airfoil. In the parametric study of Chapter 4, we present results in terms of the airfoil thickness ratio, defined as the maximum thickness of the airfoil divided by the airfoil chord. For a Joukowski airfoil the thickness ratio is $3\sqrt{3}\epsilon/8$. However, it should be emphasized that the primary physical parameter is the Strouhal number based on the airfoil nose radius, rather than the airfoil thickness ratio.

### 3.7 Thin Airfoil with Parabolic Nose

In this section, the case of a thin airfoil with a parabolic nose but with a shape other than a Joukowski airfoil is considered. The nose radius of this airfoil is assumed to be $\epsilon^2$. In the vicinity of the airfoil nose, the profile of the airfoil satisfies the equation, $x_2 = \pm\epsilon\sqrt{x_1}/\sqrt{2}$, which agrees with the Joukowski airfoil.

For a thin airfoil with a profile

$$x_2 = \pm \epsilon T(x_1)/2 , \qquad 0 < x_1 < 2, \tag{3.85}$$

the first-order perturbation velocity is

$$\phi_{1_{x_1}} - i\phi_{1_{x_2}} = \frac{1}{2\pi\beta_\infty}\int_0^2 \frac{dT(\xi)}{d\xi}\,\frac{d\xi}{z-\xi} \tag{3.86}$$

where $z=x_1+ix_2$. For points on the airfoil surface, the integral must be evaluated as a Cauchy principal value. Since the solution for a Joukowski airfoil is already known, we separate the thickness distribution into two parts,

$$T(x_1) = T_1(x_1) + T_2(x_1) \tag{3.87a}$$

where

$$T_1(x_1) = (2-x_1)\sqrt{2x_1 - x_1^2} \tag{3.87b}$$

is the thickness distribution for the Joukowski airfoil and $T_2(x_1)$ represents the deviation of the airfoil thickness distribution from that for the Joukowski airfoil. We assume that $T_2(x_1)$ vanishes at the airfoil edges $x_1 = 0$ and 2, that this function is linear or weaker in the vicinity of the edges, and that $dT_2(x_1)/dx_1$ is $O(1)$ or smaller at all points along the airfoil chord. This is equivalent to assuming that the airfoil has a smooth thickness distribution. The first-order perturbation velocity then takes the form

$$\phi_{1_{x_1}} - i\phi_{1_{x_2}} = \frac{1}{\beta_\infty}\left[\frac{2-z}{\sqrt{z^2-2z}}+2\sqrt{z^2-2z}-2z+3\right] + \frac{1}{2\pi\beta_\infty}\int_0^2 \frac{dT_2(\xi)}{d\xi}\,\frac{d\xi}{z-\xi} . \tag{3.88}$$

Similarly, the perturbation complex potential for the mean flow can then be expressed as

$$F(z) = \frac{1}{\beta_\infty}\int_0^z \left[\phi_{1_{x_1}}(\zeta) - i\phi_{1_{x_2}}(\zeta)\right] d\zeta$$

$$= \frac{1}{2\beta_\infty}\left[(z-2)\sqrt{z^2-2z} - z^2+3z\right] + \frac{1}{2\pi\beta_\infty}\int_0^z d\zeta \int_0^2 \frac{dT_2(\xi)}{d\xi}\,\frac{1}{\zeta-\xi} \tag{3.89}$$

where we have chosen the arbitrary constant such that $F(0) = 0$, consistent with Eq. (2.21b).

The analysis of the airfoil-gust interaction for the case of a general thickness distribution follows closely that for the Joukowski airfoil. In fact, it turns out that only minor modifications appear in the final expressions for the far-field sound. In this section, we outline the modifications which occur in the various asymptotic regions.

First consider the local leading-edge region. Recall that the appropriate length scale in this region is the disturbance wavelength. The analysis requires local expansions for the mean-flow perturbation and drift function, given by Eqs. (3.5) for the case of a Joukowski airfoil. To extend the theory to the case of a general symmetric airfoil, local expansions for the terms involving $T_2(x_1)$ are required. Introducing a local variable $Z = kz$,

$$\int_0^2 \frac{dT_2(\xi)}{d\xi}\,\frac{d\xi}{z-\xi} = \int_0^2 \frac{dT_2(\xi)}{d\xi}\,\frac{d\xi}{Z/k-\xi} \le O(\ln(k)) \,. \tag{3.90}$$

Hence the perturbation velocity in the local leading-edge region is

$$q - i\mu \sim \frac{\epsilon\sqrt{k}}{\sqrt{2}\sqrt{R}\,\beta_\infty}\left(-\sin\frac{\theta}{2} - i\cos\frac{\theta}{2}\right) + O(\epsilon\ln(k)) \tag{3.91}$$

where the terms which have been retained in Eq. (3.91) arise from the Joukowski thickness distribution, $T_1(x_1)$. Thus, Eq. (3.5a) remains valid for a general airfoil shape, except for a modification in the magnitude of the term that has been neglected. Similarly, introducing the variable $Z$ into Eq. (3.89) and utilizing (2.21b), the drift function has the local expansion

$$g \sim \frac{\epsilon}{\pi\beta_\infty}\int_0^2 \frac{T(\xi)}{\xi}\,d\xi - \frac{2\sqrt{2}\,\epsilon\sqrt{R}\sin\theta/2}{\beta_\infty\sqrt{k}} + O(\epsilon k^{-1}\ln(k)) \,. \tag{3.92}$$

For a Joukowski airfoil, the integral in Eq. (3.88) takes the value $3\pi/2$ consistent with Eq. (3.5b).

These results show that the airfoil thickness distribution influences the equations in the local leading-edge region in two ways. The local mean-flow gradients which enter in the source terms and the coefficients of the differential equation are determined by the nose radius of the airfoil, and hence are not influenced by $T_2(x_1)$. Similarly, the local variation of the drift function depends only on the airfoil nose radius. However, the drift function contains a constant term which depends on the global thickness distribution of the airfoil, and here the contributions due to $T_1$ and $T_2$ are of the same order. Recall that this constant term represents a phase shift for the unsteady perturbation, representing the fact that the mean-flow perturbation due to airfoil thickness slows down the approach of the convected disturbance to the leading edge. Other than this phase shift, the results of Section 3.1 apply without modification.

Next consider the outer region. The derivation of the leading-edge ray field in Section 3.2.1 applies without modification. After matching with the local leading-edge solution, the final solution is the same as Eqs. (3.49) except that the phase is given by

$$\sigma_l(r,\theta) = wr + V(\theta)\int_0^r q(r',\theta)\,dr' + \frac{\epsilon}{\pi\beta_\infty}\int_0^2 \frac{T(\xi)}{\xi}\,d\xi \tag{3.93a}$$

$$= wr + \epsilon\, V(\theta)\,\mathrm{Re}\left\{e^{-i\theta}\left[F(z) - F(0)\right]\right\} + \frac{\epsilon}{\pi\beta_\infty}\int_0^2 \frac{T(\xi)}{\xi}\,d\xi \tag{3.93b}$$

with $F(z)$ defined by Eq. (3.89). The far-field expansion of $\sigma_l$, $r >> 1$, is found to be

$$\sigma_l(r,\theta) = wr + \epsilon F(-\infty)\, V(\theta) \cos\theta + \frac{\epsilon}{\pi\beta_\infty} \int_0^2 \frac{T(\xi)}{\xi}\, d\xi + O(r^{-1}) . \qquad (3.93c)$$

The corresponding expressions for the trailing-edge phase function $\sigma_t$ are given below.

For the solution of the leading-edge transition region, the results in Section 3.3 are carried over with minor modifications. The phase shift term $3\epsilon/2\beta_\infty$ which appears in Eq. (3.54b) must be replaced by the constant term in Eq. (3.92), and the function $q(r',0)$ in (3.54b) must be calculated from (3.88). Furthermore, a portion of the function $b(\phi)$ which appears in the boundary condition (3.54d) arises from the derivative

$$\frac{\partial}{\partial\psi} \int_0^r q(r',\theta)\, dr'$$

which occurs in the right-hand side of Eq. (3.53). Utilizing Eqs. (3.88) and (3.89) to calculate this derivative for a general thickness distribution, the function

$$b_2(\phi) = \sqrt{2-\phi}\,(\phi+1) \qquad (3.94a)$$

which appears in (3.54e) is replaced by

$$b_2(x_1) = \frac{-2\beta_\infty}{\sqrt{x_1}} \left[ \operatorname{Im}\{F(z)\}\Big|_{x_2=0+} + x_1 \frac{dT}{dx_1} \right] . \qquad (3.94b)$$

Carrying through the analysis, the far-field solution for the leading edge, incorporating transition region effects, is then given by Eq. (3.63) with $\sigma_l(r,\theta)$ replaced by Eq. (3.93c) and $b_2(\tau)$ replaced by Eq. (3.94b).

Next consider the local trailing-edge region. For a general airfoil thickness distribution, the position of the trailing edge in the $(\phi,\psi)$ plane in given by

$$z_0 = 2 + \epsilon F(2) , \qquad (3.95)$$

where $F(2) = 1/\beta_\infty$ for the Joukowski airfoil. In the local trailing-edge region, an expansion similar to Eq. (3.90) shows that the function $q - i\mu$ is at most $O(\epsilon \ln(k))$, and hence can be neglected in the leading-order analysis. The mean flow in the local trailing-edge region is then uniform, and the trailing-edge problem reduces to the scattering of the leading-edge pressure field as analyzed in Section 3.4. The general airfoil thickness distribution modifies the leading-edge pressure field through Eqs. (3.93c) and (3.94b). Carrying through the analysis of Section 3.4, the far-field form of the trailing-edge acoustic field is given by Eq. (3.72), with the trailing-edge phase function

$$\sigma_t(r_t, \theta_t) = wr_t + V(\theta_t) \int_0^{r_t} q(r_t', \theta_t)\, dr_t' \tag{3.96a}$$

$$= wr_t + \epsilon\, V(\theta_t)\, \mathrm{Re}\left\{ e^{-i\theta_t} \left[ F(z - z_0) - F(z_0) \right] \right\} \tag{3.96b}$$

and with the modified forms of $\sigma_l$ and $b_2$ utilized in the calculation of $pj(0)$. In the far field, the trailing-edge phase function simplifies to

$$\sigma_t(r_t, \theta_t) = wr_t + \epsilon \left[ F(-\infty) - F(2) \right] V(\theta_t) \cos\theta_t + O(r_t^{-1}) \ . \tag{3.96c}$$

The trailing-edge transition solution also involves the scattering of the leading-edge pressure field. Carrying through the analysis of Section 3.5 with the modified form of the leading-edge pressure field, the far-field solution for the trailing edge, incorporating transition region effects, is Eq. (3.80) with appropriate modifications. Specifically, modifications as discussed above must be made to the expression $pj(0)$, the leading-edge phase $\sigma_l$ evaluated at the location of the trailing edge, the trailing-edge phase $\sigma_t$ and the function $b_2(\tau)$.

Finally, it is the difference in phase between the leading-edge and trailing-edge fields that enters in the normalized power levels and directivity patterns presented in Chapter 4. The far-field phase difference $k\sigma_d(\theta)$ for the case of a general thickness distribution is given in Eq. (3.82c).

The calculation of the far-field sound for an airfoil with a general thickness distribution involves a numerical integration to determine $b_2(\phi)$, followed by numerical integrations related to the transition region solutions. The situation is considerably simpler for the case of a Joukowski airfoil, since the function $b_2(\phi)$ is then known in closed form. Therefore, much of the parametric study presented in Chapter 4 considers the case of a Joukowski airfoil. However, in Section 4.6 we present results for other airfoil shapes. These results demonstrate that the primary correlating parameter for the influence of airfoil thickness on airfoil-gust interaction noise is the Strouhal number (3.84) based on the airfoil nose radius.

# CHAPTER 4

## NUMERICAL RESULTS AND DISCUSSION

In this chapter we present numerical results for the acoustic far field which is generated by the interaction of a Joukowski airfoil with a high-frequency disturbance. The influences of the airfoil thickness and of the gust and mean-flow parameters on the sound field are analyzed through parametric studies.

There are eight independent parameters in the expression (3.81) for the far-field sound. Five of the six gust-velocity and wavevector components ($A_t, A_n, A_3, k_t, k_n, k_3$) are independent. The requirement that the gust be solenoidal provides one constraint,

$$A_t + A_n k_n \beta_\infty + A_3 k_3 = 0 \ . \tag{4.1}$$

The entropy fluctuation $B$, Mach number $M_\infty$ and airfoil thickness parameter $\epsilon$ are additional independent parameters. With such a large number of parameters, it is difficult to systematically study all possible combinations. To make the number of parameters more manageable, we primarily concentrate on the case of two-dimensional gusts for which $k_3 = A_3 = 0$.

The most important quantity for the sound field is the total amount of acoustic power radiated. We shall examine the changes in the total power level as a function of the above parameters. An expression for acoustic intensity in the presence of a nonzero mean flow was given by Goldstein (1976) as

$$I = \left[p'/\rho_0 + \nabla G' \cdot U_0\right] (\rho_0 \nabla G' + \rho' U_0) \ . \tag{4.2a}$$

We define a normalized sound power as

$$\text{Normalized Power} = \frac{\text{Power/Span}}{\rho_\infty U_\infty^3\, b\, A^2 * 2} \tag{4.2b}$$

where

$$A = \sqrt{A_t^2 + A_n^2 + A_3^2} \tag{4.2c}$$

is the amplitude of the vortical gust. For cases involving entropy gusts, an appropriate replacement for $A$ is defined later. Since the governing equation and boundary conditions are linear functions of the disturbance amplitude, the acoustic intensity and total sound power are quadratic in this quantity. Thus, the normalized power defined by (4.2b) is independent of the amplitude of the convected disturbances. Transforming from the physical coordinates to the potential-streamfunction coordinates, and integrating the far-field expressions over a large cylindrical surface surrounding the airfoil, Myers (1987) showed that the normalized sound power produced by the airfoil-gust interaction is given by

$$\text{Normalized Power} = k^2\, \delta\, w\, \beta_\infty^2 \int_0^{2\pi} h \cdot h^* \, (\beta_\infty \cos^2\theta + \sin^2\theta) \sqrt{\beta_\infty^2 \sin^2\theta + \cos^2\theta}\; r\, d\theta \tag{4.2d}$$

where $h^*$ is the complex conjugate of $h$. The square of the gust amplitude $A^2$ has been absorbed in our definition of normalized power and therefore the amplitude $A$ is set equal to one in the right-hand side of Eq. (4.2d). Since the phase factor $e^{ik\sigma_l}$ cancels out in evaluating $h \cdot h^*$ from the far-field expression (3.81), the only radial dependence of $h \cdot h^*$ is the $1/r$ decay which cancels with the $r$ in the differential element of length. The integrand is then a function of $\theta$ only, the polar angle in $(\phi,\psi)$ space.

Changes in the sound field will also be studied through far-field pressure-directivity patterns. The directivity patterns which we plot are the magnitude of the pressure as a function of angle at a constant distance from the leading edge in the physical plane. Using the relationship, $(\phi,\psi) = (x_1,\ \beta_\infty x_2) + O(\epsilon)$, the angles in physical $(x_1,x_2)$ and Prandtl-Glauert $(\phi,\psi)$ space are related by

$$\cos\xi = \frac{\beta_\infty \cos\theta}{\sqrt{1 - M_\infty{}^2 \cos^2\theta}}, \tag{4.3a}$$

$$\sin\xi = \frac{\sin\theta}{\sqrt{1 - M_\infty{}^2 \cos^2\theta}} \tag{4.3b}$$

where $\theta = \tan^{-1}(\psi/\phi)$ is the angle in $(\phi,\psi)$ space and $\xi = \tan^{-1}(x_2/x_1)$ the angle in the physical space.

The directivity pattern represents the angular distribution of the far-field pressure. Sample directivity patterns are shown in figure 4.1. In the directivity pattern plots, the origin corresponds to the airfoil leading edge. The directivity patterns plotted in figure 4.1 are for the interaction of a zero-thickness airfoil with a vorticity gust. The dotted line shows the pressure distribution of the leading-edge acoustic field and is the $\cos\theta/2$ pattern of $L_0(\theta)$ (converted to pressure). The distortion of the cardiod is due to the transformation from $(\phi,\psi)$ to $(x_1, x_2)$ coordinates. The solid line illustrates the interference between the leading- and trailing-edge fields. For small angles, the trailing-edge field cancels the antisymmetric leading-edge field. For larger angles, regions of constructive and destructive interference between the leading-edge field and the weaker trailing-edge field can be observed.

Our parametric study is divided into six sections. The first four sections contain results for vortical gusts. In Section 4.1, we study the effect of varying the orientation of a two-dimensional gust. Then the effect of the spanwise component of a wavevector and the cut-off phenomenon are briefly discussed. In Section 4.2, we analyze the behavior of the sound field as the Mach number is changed. We investigate how the sound field changes as a function of airfoil thickness in Section 4.3. The directivity patterns are examined in Section 4.4. In Section 4.5, cases involving entropy gusts are discussed. Finally, in Section

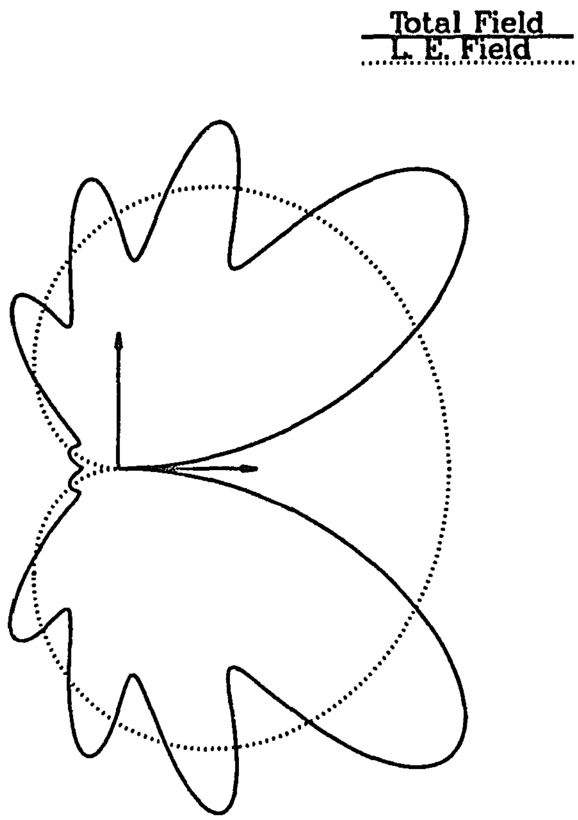


Figure 4.1 Far-field pressure directivity patterns for a flat plate, vertical gust, $M_\infty = 0.6$ and $k = 7$. (*a*) Total field (solid line). (*b*) Leading-edge field (dotted line).

4.6 the normalized power and directivity patterns for airfoils whose shape differs from a Joukowski airfoil are briefly examined.

### 4.1 Influence of Gust Orientation for Vortical Gusts

In this section we examine the influence of gust orientation on the total sound power level produced by interaction of a vortical gust with a symmetric Joukowski airfoil. Results are presented as a function of gust orientations for constant values of frequency, Mach number and airfoil thickness.

Throughout most of this section, we consider two-dimensional gusts ($k_3 = A_3 = 0$). For convenience in interpretation of the results, results are presented in terms of the gust orientation in physical space. The relationship between the normal wavenumber components (which are perpendicular to the mean flow streamlines at upstream infinity) in physical space and Prandtl-Glauert space is $k_{np} = \beta_\infty k_n$, where $k_{np}$ and $k_n$ correspond to physical space and Prandtl-Glauert space, respectively. Since the $(\phi,\psi)$ and $(x_1, x_2)$ unit vectors coincide far upstream, we can physically visualize the gusts by thinking in Cartesian coordinates. Recall from Eq. (3.1e) that the streamwise wavenumber has been normalized to a value of one. Thus, at upstream infinity, the angle of the gust wavevector in physical space relative to the mean flow streamlines is given by

$$\theta_g = \tan^{-1} k_{np} \quad . \tag{4.4}$$

In physical space, the solenoidal requirement (4.1) for the vortical gust takes the form

$$A_t + A_n k_{np} = 0 \quad . \tag{4.5}$$

Since the magnitude of the gust velocity has been absorbed in the definition of the normalized power, we can assume without loss of generality that $A_t^2 + A_n^2 = 1$. Thus, specification of the gust angle $\theta_g$ also determines $A_t$ and $A_n$. The solution then depends on four free parameters, $\theta_g$, $k$, $\epsilon$, and $M_\infty$. Incidentally, Eq. (4.1) also shows that the vorticity gust is a transverse wave, i.e., the direction of the velocity fluctuations is perpendicular to the gust wavevector.

Another requirement that must be satisfied as the input disturbance is varied is the high-frequency condition, $k >> 1$. Recall that $k = \omega b/U_\infty$, i.e., $k$ is a nondimensional frequency. Since the efficiency of the sound generation process is strongly dependent on frequency, we consider fixed values of $k$ in performing parametric variations. Thus our calculations are performed at constant horizontal wavenumber rather than constant wavevector magnitude. Actually, the high frequency condition $k >> 1$ can be relaxed considerably. Amiet (1975) has given some justification for using the value $kw = kM_\infty/\beta_\infty^2 = \pi/4$ as the dividing line between high and low frequencies. He showed for the case of zero-thickness that the leading-edge term alone predicts the unsteady lift on the airfoil with an error of less than 10% for $kw \geq \pi/4$. When a trailing-edge correction is included, as is the case for us, the lower limit can be decreased even further. Amiet's criterion does not apply directly to our problem, but we will use it as a rough lower limit. The upper limit of $k$ is determined by the criterion $\epsilon k = O(1)$ (or $\epsilon^2 k << 1$.) We take $2 < k < 12$ for most of our parametric study, and assume without loss of generality that $k > 0$.

The results of four sets of calculations, for $k = 2.5$, 5.0, 7.5 and 10.0 at $M_\infty = 0.60$, are shown in figures 4.2 through 4.5. Results are presented for five different values of the airfoil thickness ratio, ranging from zero to 10%. The thickness ratio is defined as the maximum thickness of the Joukowski airfoil divided by airfoil chord. For example, the 5%

thickness case corresponds to $3\sqrt{3}\epsilon/4 = 0.1$.

In figures 4.2 through 4.5, the sound power is seen to be a symmetric function of $\theta_g$, as expected due to the symmetry of the airfoil. A second important feature is that the maximum sound power level occurs at or near $\theta_g = 0$. The peak at $\theta_g = 0$ for the zero thickness case is easily understood. For a zero-thickness airfoil the mean flow is uniform, and the only sound generation mechanism is the blocking of the normal component of the gust by the airfoil surface. Thus, the pressure level is linearly proportional to $A_n$, leading to a normalized power which is proportional to $A_n{}^2 = \cos^2\theta_g$ for this case.

A surprising feature of the results for $M_\infty = 0.6$ presented in figures 4.2 through 4.5 is that moderate amounts of leading-edge thickness may actually decrease the sound radiation. For this Mach number airfoil thickness has the most significant effect on the sound power for gust angles $|\theta_g| < 45^o$. At larger gust angles the sound power is less sensitive to airfoil thickness, experiencing rather small increases in level. For the case $k = 2.5$ shown in figure 4.2, the sound power at small gust angles decreases monotonically with airfoil thickness over the range of 0% to 10% thickness ratio. For higher values of $k$, the sound power at small gust angles at first decreases with airfoil thickness, but passes a minimum and has started to rise by the time a 10% thickness ratio is reached. For $k = 10$, the minimum sound power level occurs in the vicinity of 5% thickness ratio. Essentially, small amounts of airfoil thickness distort the gust in such a way as to decrease the velocity component perpendicular to the surface, causing a decrease in the generated sound level. This effect is particularly noticeable for gust angles near $\theta_g = 0^o$. However, with further increases in thickness, the stronger gust distortion increases the amplitude of the quadrupole volume sources, leading to an increase in the radiated sound level. This pattern occurs for smaller values of $\epsilon$ at larger $k$, consistent with a dependence on the product $\epsilon\sqrt{k}$.

The pattern discussed above can be identified mathematically by considering the

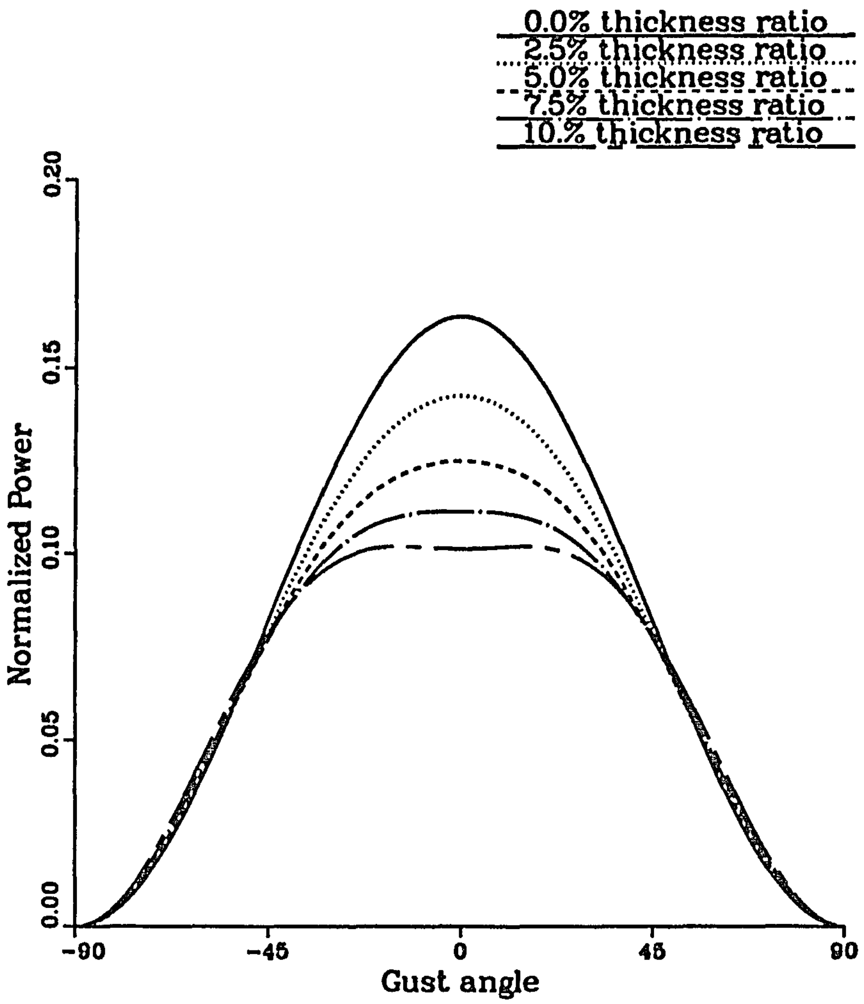


Figure 4.2 Normalized power *vs*. gust angle for $M_\infty = 0.60$ and $k = 2.5$.

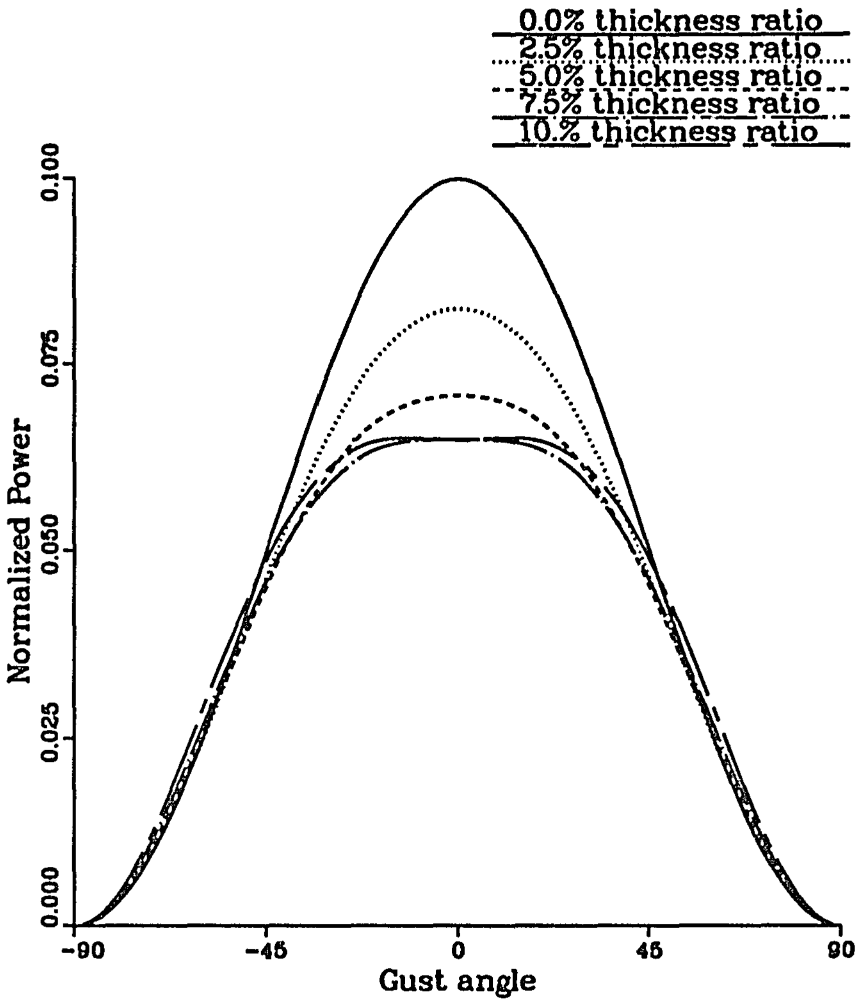


Figure 4.3 Normalized power *vs*. gust angle for $M_\infty = 0.60$ and $k = 5$.

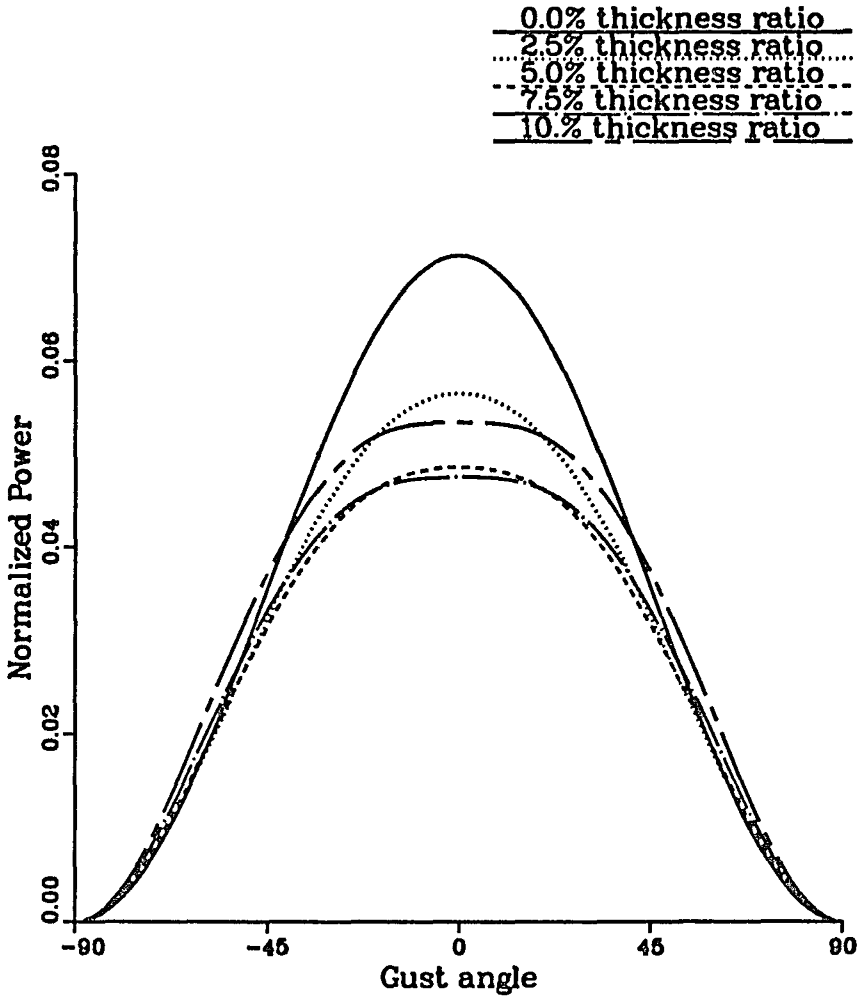


Figure 4.4 Normalized power *vs*. gust angle for $M_\infty = 0.60$ and $k = 7.5$.

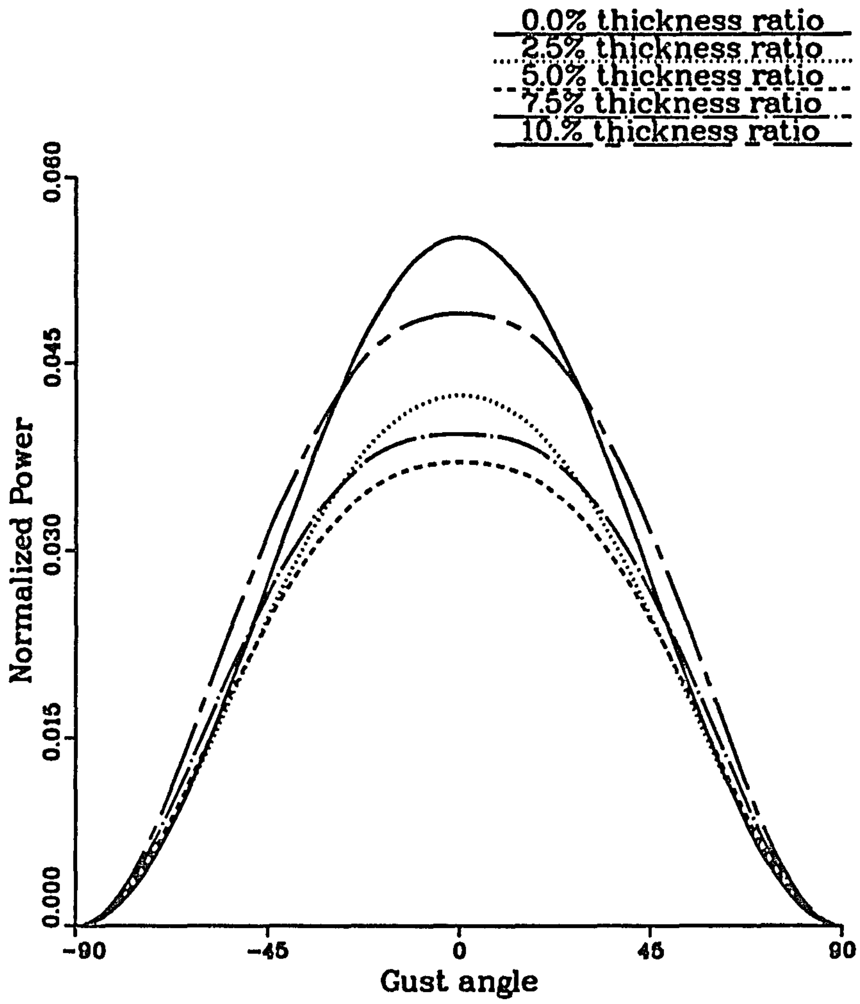


Figure 4.5 Normalized power *vs*. gust angle for $M_\infty = 0.60$ and $k = 10$.

interaction of the zero-thickness term $L_0(\theta)$ and the contribution $L_2(\theta)$ from the volume quadrupole source. (The propagation source is relatively unimportant at this Mach number.) For the two-dimensional case considered here the function $L_0$ takes the form

$$L_0(\theta) = \frac{A_n \cos\theta/2 \, \beta_\infty^2 \, (i-1)}{\sqrt{2}\,\sqrt{\pi}\,\sqrt{1+M_\infty}\,(1-M_\infty \cos\theta)} . \tag{4.6}$$

As the gust angle approaches zero, $A_t$ and $k_n$ approach zero. Therefore, the leading order contributions to $L_2$ is

$$L_2(\theta) = A_n \cos\theta/2 \left[ \frac{i M_\infty}{\sqrt{2}} + \frac{\beta_\infty^2 \, (2 - M_\infty^2)}{\sqrt{2}\,(1-2M_\infty \cos\theta + M_\infty^2)\,(1+M_\infty)} \right] + O(k_n, A_t) \ . \tag{4.7}$$

The expression (4.7) comes from the complementary solution $H_{2c}$, i.e. this sound field arises from the scattering of the volume quadrupole sources by the airfoil leading edge. The imaginary components of these functions have the same sign, while the real components have opposite signs. For small to moderate $\epsilon\sqrt{k}$, the cancellation between the real parts outweighs the increase due to the imaginary parts, resulting in a decrease in the total sound power level. However, at large $\epsilon\sqrt{k}$ the sum of the imaginary parts becomes important, leading to an increase in the total sound power level.

The influence of trailing-edge scattering on the total sound power level is illustrated in figure 4.6. The normalized power for the leading edge field alone and for the combined leading and trailing edge fields are plotted for $k = 7.5$, $M_\infty = 0.6$ and two values of airfoil thickness, 0% and 10%.

Consider first the zero-thickness case. For both the leading-edge field alone and the total sound field, the normalized power is proportional to $\cos^2\theta_g$. Including the scattered field from the trailing edge is seen to reduce to total sound power by 11.7%. The explanation for this decrease in sound power can be understood by looking at figure 4.1, which presents the leading edge and total directivity patterns for the zero-thickness airfoil.

The scattered field from the trailing edge is seen to cancel the sound radiation in the downstrem direction, leading to a decrease in the total sound power.

Next consider the results for 10% thickness presented in figure 4.6. For small gust angles, the inclusion of trailing edge scattering decreases the total sound power, with this effect being slightly stronger than for the case of zero thickness. However, for the 10% thickness airfoil and gust angles on the order of $45^0$ and larger, the inclusion of trailing-edge scattering produces only a slight decrease in normalized power. The trailing-edge scattering is less important in this case because the strongest radiation from the leading edge is no longer in the downstream direction, as will be illstrated by the directivity patterns presented in Section 4.4.

Normalized sound power levels as a function of gust angle for $M_\infty = 0.8$ and $k = 2.5$, 5.0, 7.5 and 10.0 are presented in figures 4.7 through 4.10. At this Mach number, there is a noticeable shift of the maximum power away from $\theta_g = 0^0$. The behavior at small gust angles is similar to that observed earlier for $M_\infty = 0.6$, i.e., small to moderate values of airfoil thickness lead to a decrease in sound power. As before, this behavior can be explained by the cancellation between $L_0$ and $L_2$. Since the gust velocity components are given by $(A_n, A_t) = (\cos\theta_g, \sin\theta_g)$, the contributions from terms involving $A_n$ become less important, while those from terms involving $A_t$ become more important, as the gust angle increases. The tangential component of gust velocity $A_t$ appears in $L_1$ and $L_2$, corresponding to modifications in the surface boundary condition and to contributions from the quadrupole sources, respectively. It is primarily the contribution from the volume quadrupole sources which produces the shift of maximum power away from $\theta_g = 0^0$.

A constant value of airfoil thickness produces a stronger effect on the sound power at larger values of $k$, as can be seen by comparing figures 4.7 and 4.10. This trend is

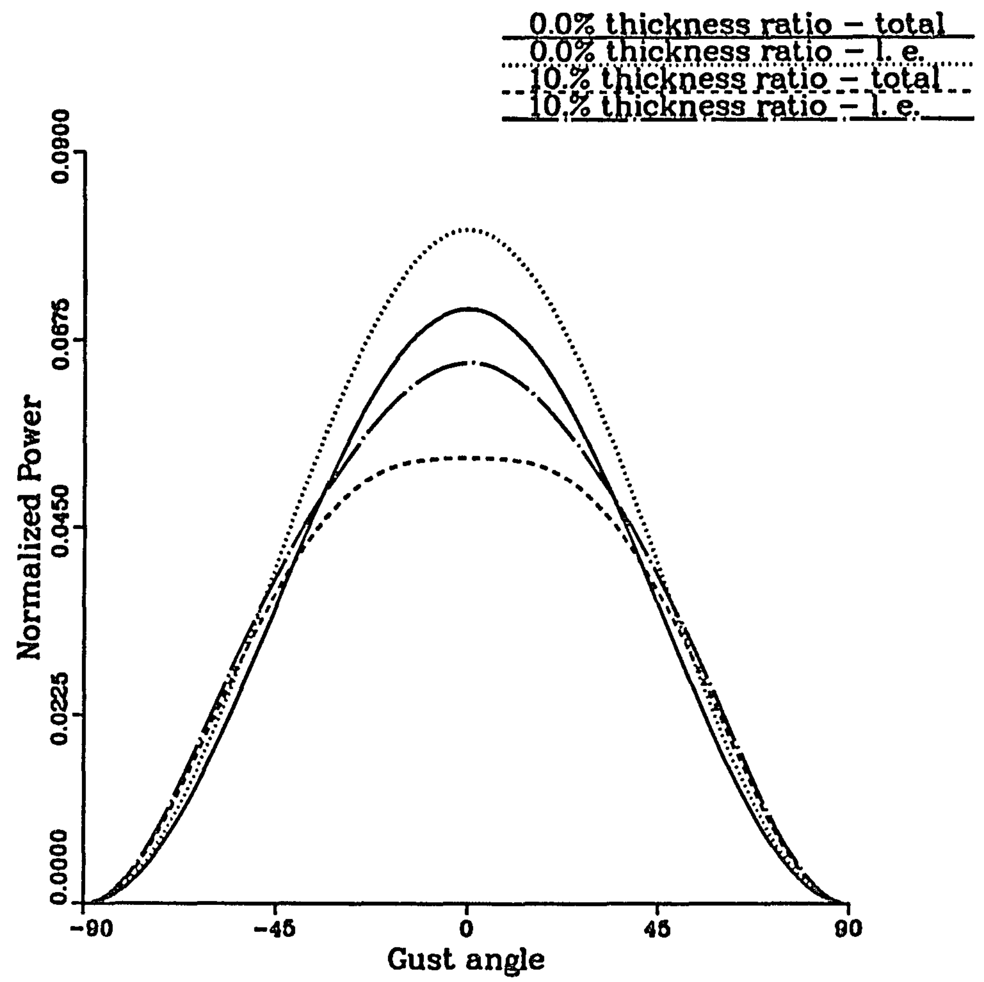


Figure 4.6 Comparison of the normalized power levels generated by the total and leading-edge acoustic fields for $M_\infty = 0.60$ and $k = 7.5$.

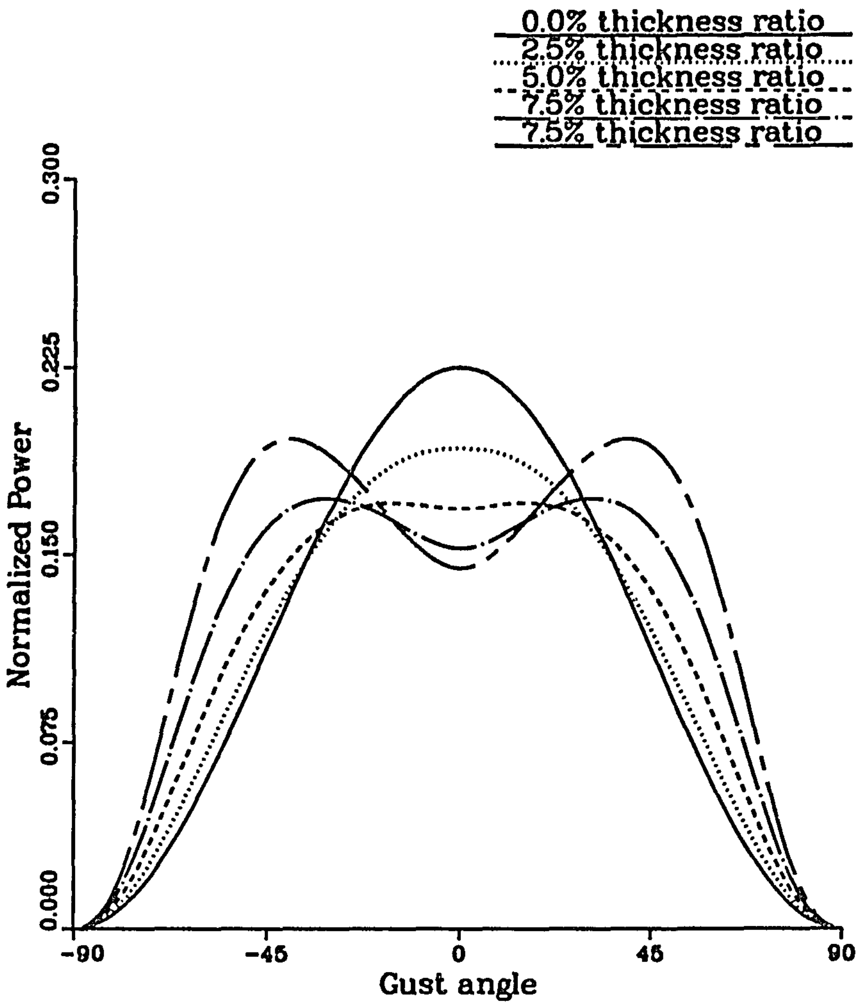


Figure 4.7 Normalized power *vs*. gust angle for $M_\infty = 0.80$ and $k = 2.5$.

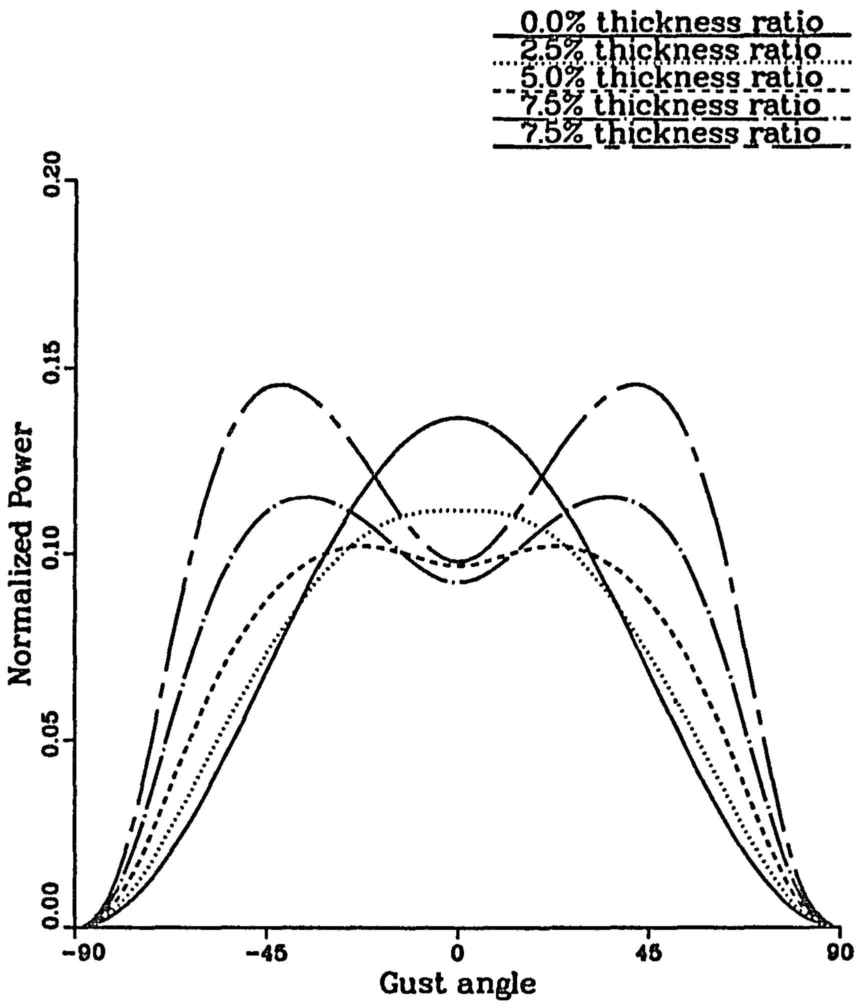


Figure 4.8 Normalized power *vs.* gust angle for $M_{\infty} = 0.80$ and $k = 5$.

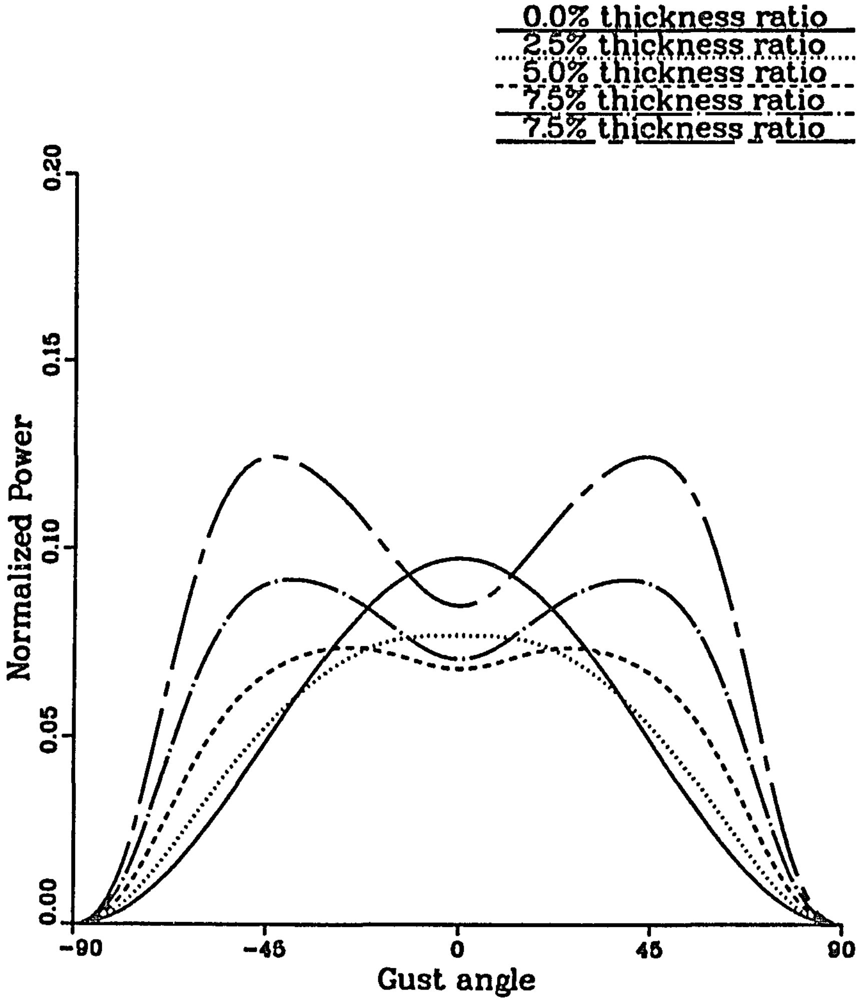


Figure 4.9 Normalized power *vs.* gust angle for $M_\infty = 0.80$ and $k = 7.5$.

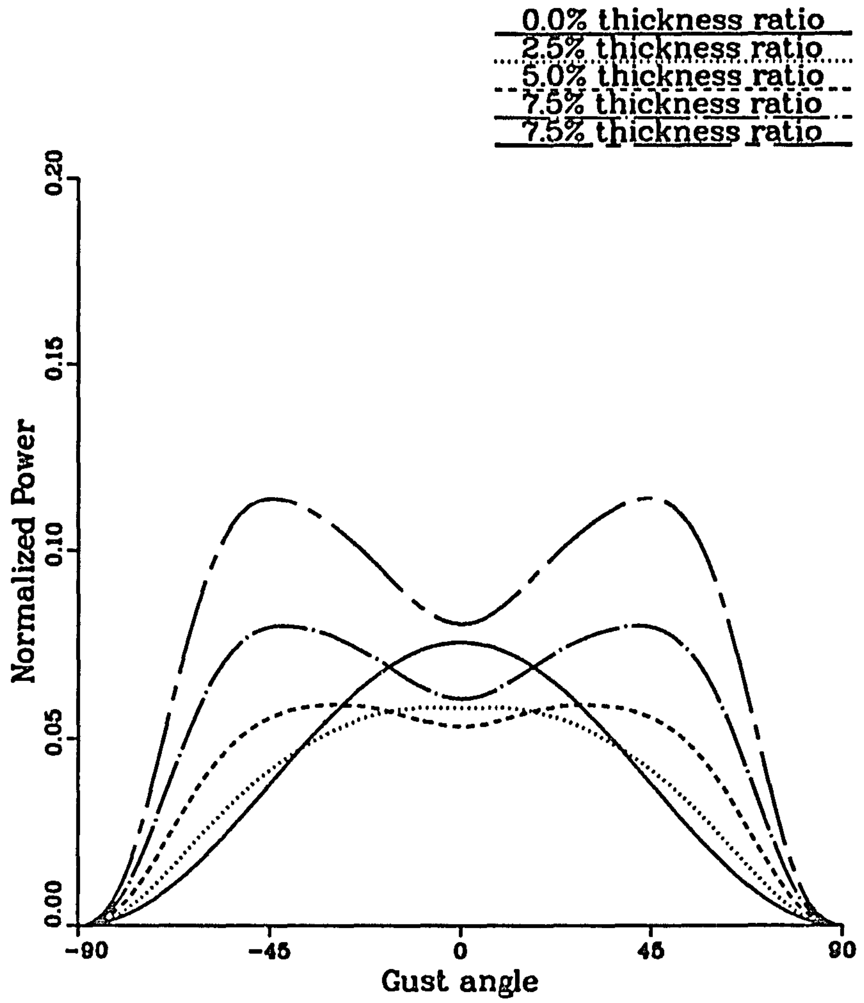


Figure 4.10 Normalized power *vs.* gust angle for $M_\infty = 0.80$ and $k = 10$.

consistent with the results presented earlier for $M_\infty = 0.6$. The influence of Mach number can be seen by comparing figures 4.5 and 4.10. A given value of airfoil thickness has a much larger effect on the sound power level at $M_\infty = 0.8$ than at $M_\infty = 0.6$. This is primarily due to an increase in the radiation from the quadrupole sources at the higher Mach number.

In figures 4.11 and 4.12, the maximum value of the normalized power (with respect to gust angle), and the gust angle at which this maximum occurs, is plotted as a function of airfoil thickness for the case $M_\infty = 0.8$ and $k = 10$. The maximum normalized power at first decreases as thickness is introduced. The minimum value of maximum normalized power occurs at 3.5% thickness, beyond which the maximum normalized power increases rapidly with airfoil thickness. From figure 4.12, it can be seen that the gust angle corresponding to the maximum normalized power remains at $\theta_g = 0^0$ until a thickness of approximately 2% is reached. For larger values of thickness, the gust angle corrresponding to the maximum normalized power gradually increases, leveling off near $\theta_g = 45^0$ for airfoil thicknesses greater than 11%.

A common feature of all the results presented in this section is that the normalized power vanishes as $\theta_g$ approaches $\pm 90^0$. This feature is not surprising when one recalls that the gust frequency, and hence streamwise wavenumber, is held constant as the gust angle is varied. Thus the magnitude of the gust wavevector approaches infinity as $\theta_g \rightarrow 90^0$, corresponding to a vanishing gust wavelength. In addition, the direction of the gust velocity approaches the streamwise direction, so that the only sound generation mechanism is the distortion of the gust by the mean-flow gradients. This is ineffective in generating sound, due to the vanishing wavelength of the gust vorticity field.

In mathematical terms, both $L_0$ and $L_3$ are proportional to $A_n$ and hence these

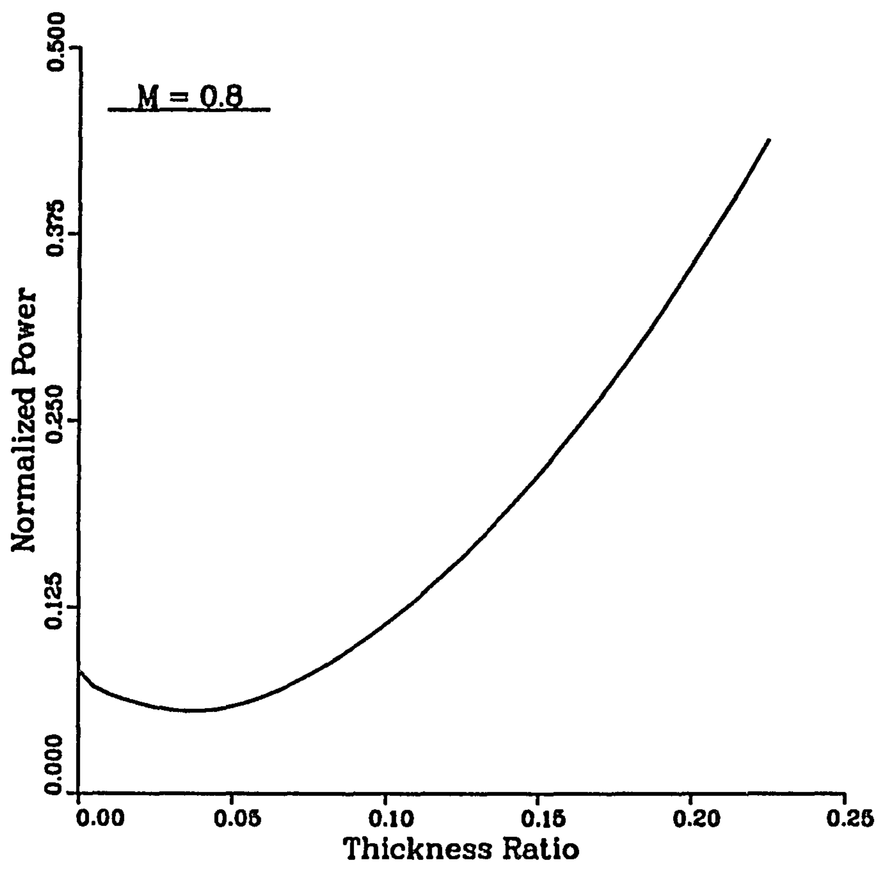


Figure 4.11 Maximum normalized power *vs.* thickness for $M_\infty = 0.80$ and $k = 10$.

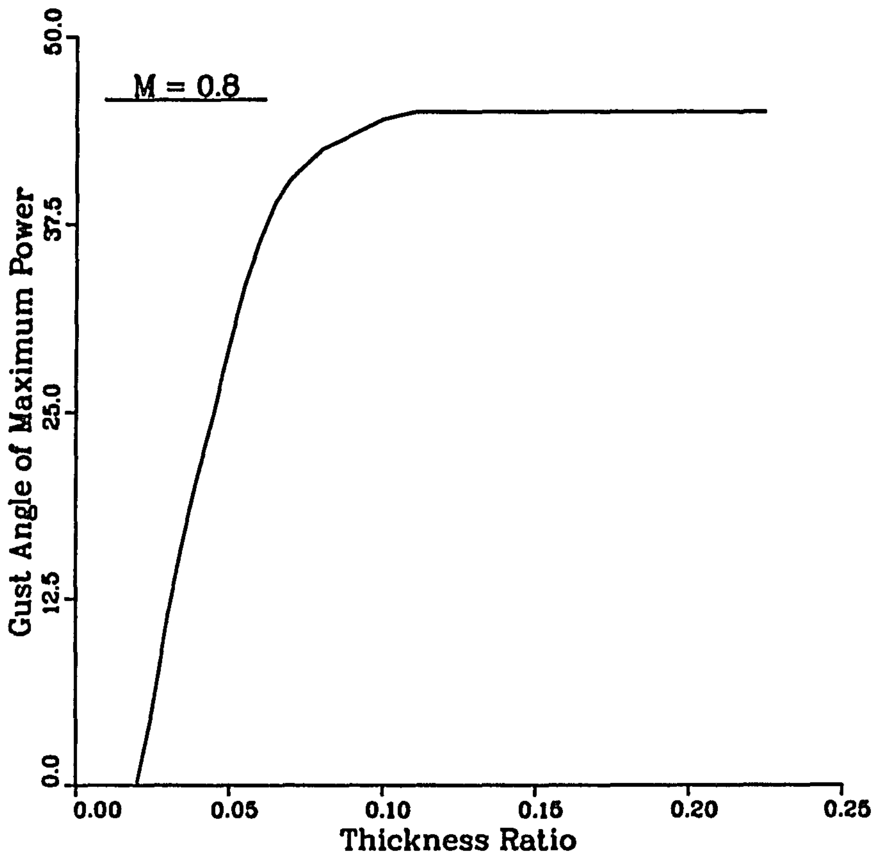


Figure 4.12 Gust angle of maximum normalized power *vs.* thickness for $M_\infty = 0.80$ and $k = 10$.

functions vanish as $\theta_g \rightarrow 90^o$. The contribution $L_1$ from the modification to the boundary conditions and the contribution $L_2$ from the quadrupole sources remain, but these cancel as $\theta_g \rightarrow 90^o$. Setting $\theta_g = \pi/2 - \alpha$, $A_n \sim \alpha$, $A_t \sim 1 - O(\alpha^2)$, and $k_n \sim 1/\beta_\infty \alpha$, $L_2(\theta)$ can be expanded as

$$L_2(\theta) = \frac{i\, \beta_\infty\, A_t^*}{\sqrt{M_\infty}\, \sqrt{1 - M_\infty \cos\theta}} + O(A_n, k_n^{-1}) \tag{4.8}$$

and the leading term of this expression cancels $L_1(\theta)$ exactly.

We next consider the dependence of normalized power on gust angle at high subsonic Mach numbers. Results for $M_\infty = 0.9$ and five different values of airfoil thickness are presented in figure 4.13. Increasing the Mach number from 0.8 to 0.9 has a dramatic influence on the sound power level, as can be seen by comparing figure 4.13 with figure 4.10. The maximum normalized power level for the 10% thickness airfoil has increased by a factor of five. There has also been a significant change in the shape of the normalized power curve as a function of gust angle. At $M_\infty = 0.8$, the maximum power level for the 10% thickness airfoil occurs near $\theta_g = 45^o$ and there is a significant dip in the curve at small gust angles. In contrast, at $M_\infty = 0.9$ the location of the maximum power level has shifted to $\theta_g = 0^o$ for all values of airfoil thickness.

The function $L_3(\theta)$ corresponding to the propagation source is responsible for the increase in sound power level for small gust angles and nonzero airfoil thickness at $M_\infty = 0.9$. As $M_\infty$ approaches one, the dominant contribution from the propagation source is given by $L_{3p}(\theta)$, which takes the form

$$L_{3p}(\theta) = \frac{i\, A_n\, (\gamma+1)\, M_\infty^{5/2}}{4\, \sqrt{1+M_\infty}\, \beta_\infty^{\,2}} \left[ \frac{M_\infty}{2} \sin 2\theta + \sin\theta \right] \tag{4.9}$$

for a two-dimensional gust. Thus, the sound power associated with the propagation source is proportioal to $\beta_\infty^{-4}$ for $M_\infty$ near one. However, if the propagation source were the only significant contribution to the result for the 10% thickness airfoil in figure 4.13, the dependence on gust angle would be proportional to $\cos^2\theta_g$, since Eq. (4.9) contains only $A_n$. The presence of a second contribution to the sound power level is clearly evident for gust angles in the vicinity of $\theta_g = 45°$ in figure 4.13. This contribution comes from the quadrupole source terms associated with $H_2$. Thus we conclude that the sound field at high subsonic Mach numbers is generated by a combination of the quadrupole source and the propagation source. Of course, since our mean flow description has neglected nonlinear transonic effects, there is some question regarding the quantitative accuracy of our predictions for Mach numbers very near one.

To conclude our investigation of gust-orientation effects, we briefly consider three-dimensional gusts. We examine the effect of increasing $k_3$, while keeping $A_3$ zero. In figure 4.14, the normalized power level is plotted as a function of $k_3$ for $M_\infty = 0.6$, $k = 7.5$ and $\theta_g = 0°$. The power level exhibits a monotonic decrease as a function of $k_3$, tending toward zero in the vicinity of $k_3 = 0.75$. From Eqs. (3.2$a,c$), nonzero values of $k_3$ are seen to reduce the effective frequency $kw$. As the acoustic wavenumber $w$ approaches zero, care must be taken in interpreting our high-frequency solution, due to problems in convergence of the iterative treatment of the leading- and trailing-edge regions. In fact, the character of the governing equation changes when the critical value $k_3 = M_\infty/\beta_\infty$ corresponding to $w = 0$ is reached. This critical value is 0.75 for the results presented in figure 4.14. For larger values of $k_3$, the pressure field decays exponentially with distance from the airfoil and no sound is radiated to the far field. This critical value of $k_3$ corresponding to cut off of the sound field can be interpreted as the condition for which the trace speed of the intersection point between the airfoil leading edge and a gust constant phase line becomes subsonic, see Kerschen and Envia (1983) for additional details.

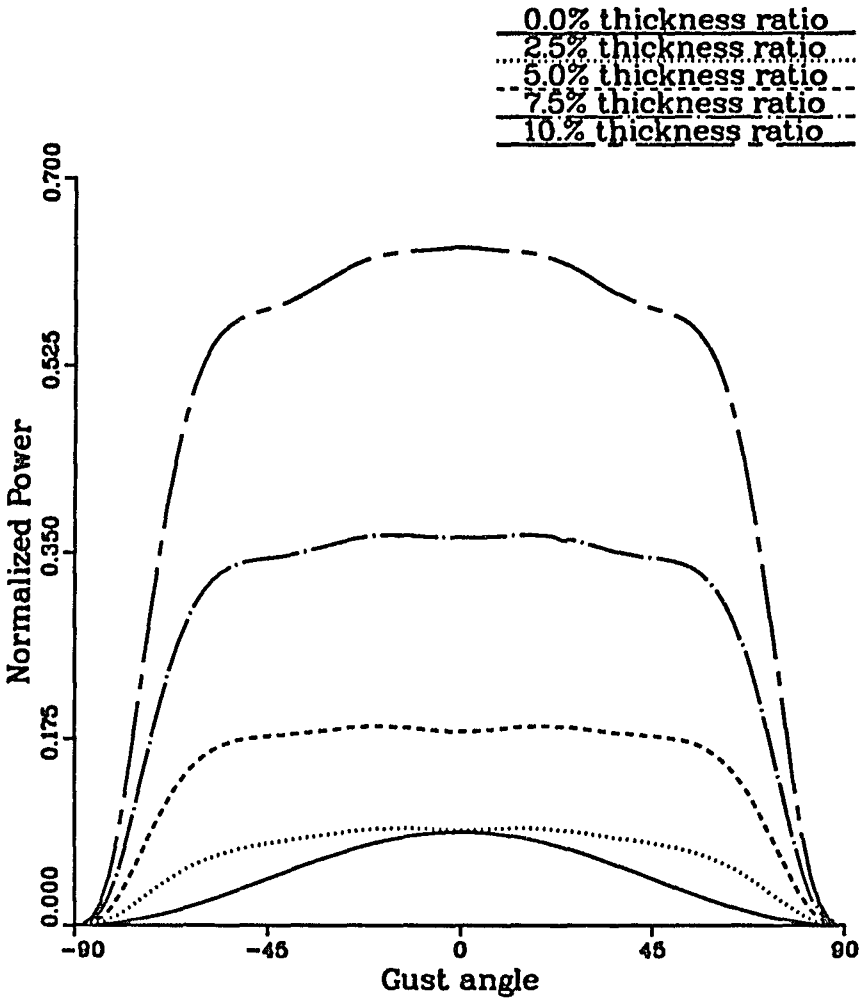


Figure 4.13 Normalized power *vs*. gust angle for $M_\infty$ = 0.90 and $k$ = 10.

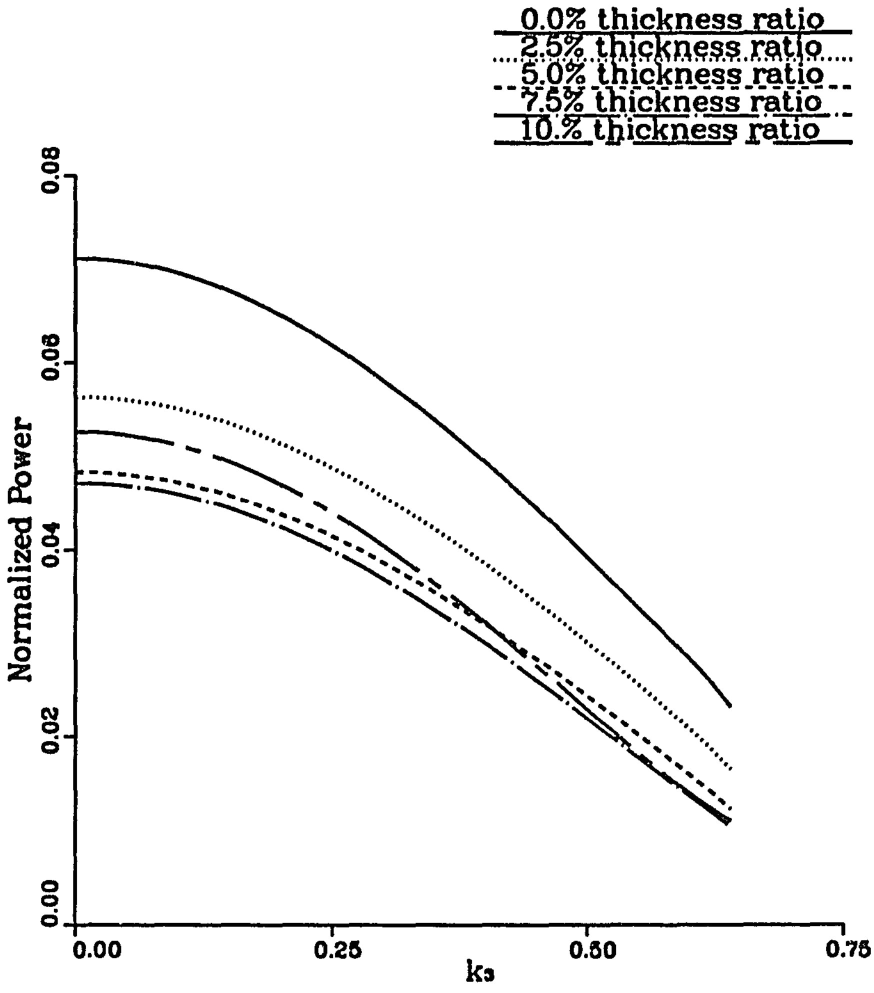


Figure 4.14 Normalized power *vs.* spanwise wavenumber for $\theta_g = 0$, $k = 7.5$ and $M_\infty = 0.6$.

## 4.2 Influence of Mach number

The influence of Mach number on sound generated by high-frequency gust-airfoil interactions is examined in this section. The primary concentration is placed on vorticity gusts, but some discussion is presented for entropy gusts in the low Mach number limit, $M_\infty << 1$.

We wish to examine the sound generation process for the full range of subsonic Mach numbers, including the limits $M_\infty << 1$ and $M_\infty \to 1$. In the low Mach number limit, the acoustic wavelength becomes long compared to the gust wavelength. Thus, even for high-frequency gusts, the acoustic wavelength may not be short compared to the airfoil chord. In this situation the iterative procedure that we have used to account for the presence of the trailing edge does not converge very rapidly, and the two term expansion we have employed may not accurately represent the influence of the trailing edge. However, our main interest is in how the Mach number affects the noise generation mechanisms, and our theory has shown that these mechanisms are concentrated in the local leading-edge region, with the trailing edge acting only as a scatterer of this leading-edge field. Therefore, in this section we consider only the leading-edge acoustic field.

In figures 4.15 and 4.16, the amount of power radiated by the leading edge alone is plotted as a function of Mach number for $k$ = 7.5 and several values of airfoil thickness. Figures 4.15 and 4.16 present results for $\theta_g = 0^0$ and $45^0$, respectively. At low Mach numbers, the normalized power for each case varies linearly with $M_\infty$, corresponding to a dimensional sound power which scales as $M_\infty{}^4$. This scaling law corresponds to a pole of 3/2 order, intermediate between a monopole and a dipole, for the two-dimensional case. The origin of this pole of 3/2 order will be discussed below. For the zero-thickness case, the normalized sound power level remains almost a linear function of $M_\infty$, out to high subsonic Mach numbers. In contrast, airfoil thickness causes a rapid rise in the normalized power at high subsonic Mach numbers.

Our previous result that moderate amounts of thickness reduce the normalized power can easily be seen in figures 4.15 and 4.16. For $\theta_g = 0^o$, the power levels for cases with nonzero thickness remain below that for the zero-thickness case out to Mach numbers in the vicinity of $M_\infty = 0.75$. For $\theta_g = 45^o$ (figure 4.16), the presence of airfoil thickness does not produce as much reduction in the power level at moderate Mach numbers, and the rise in sound power level begins at a lower Mach number. The increase in sound power relative to the zero-thickness case which occurs at high Mach numbers is also more dramatic for $\theta_g = 45^o$ than for $\theta_g = 0^o$.

Our theory has shown that sound is generated in the local leading-edge region by four physical mechanisms. For a zero-thickness airfoil the only nonzero term is $H_0$, which arises from the blocking of the undistorted gust velocity by the airfoil surface. When airfoil thickness is introduced, three additional source mechanisms arise. The mean-flow gradients modify the unsteady vorticity field, and the influence of this on the airfoil surface boundary condition is contained in $H_1$. The interaction of the gust with the mean-flow gradients also produces a volume source $\nabla\cdot(\rho_0 v')/\rho_0$ which generates the field $H_2$. Finally, the variations in the local flow speed and speed of sound in the vicinity of the airfoil leading edge generate additional sound by interacting with the leading-order field $H_0$. This effect is captured in the term $H_3$.

In order to assess the relative importance of the various source mechanisms as a function of Mach number, we plot the magnitude of the four directivity functions, $L_0(\theta)$, $L_1(\theta)$, $L_2(\theta)$ and $L_3(\theta)$, in Prandtl-Glauert space for three different Mach numbers. The

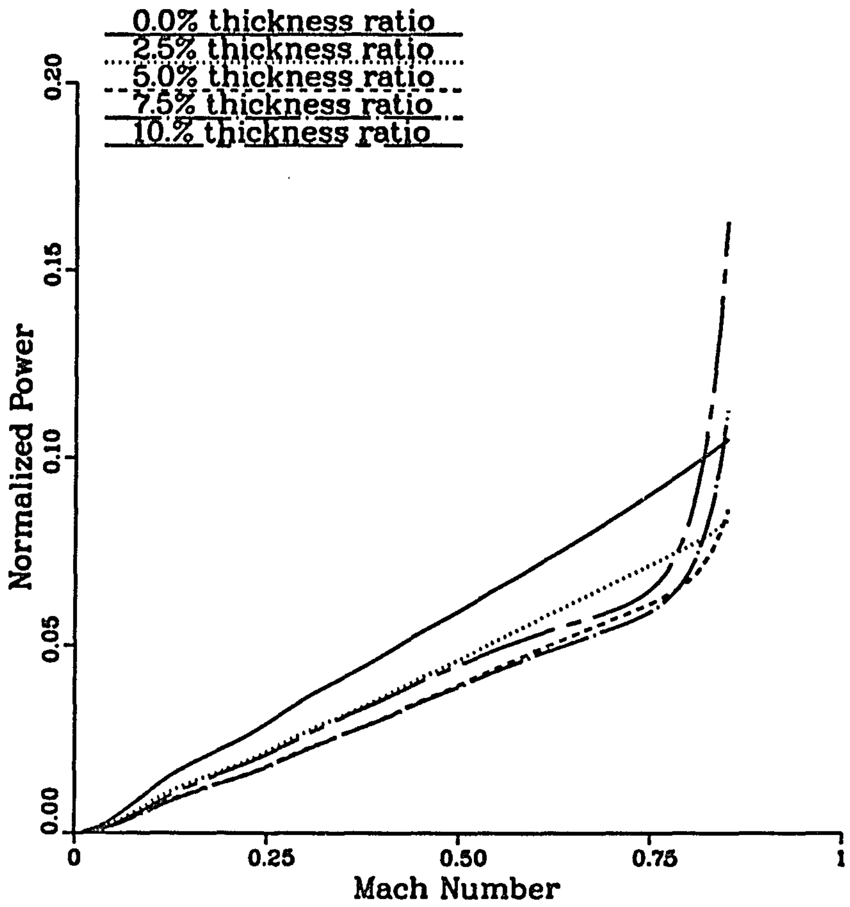


Figure 4.15 Normalized power for the leading-edge acoustic field *vs.* Mach number for $\theta_g = 0^0$ and $k = 7.5$.

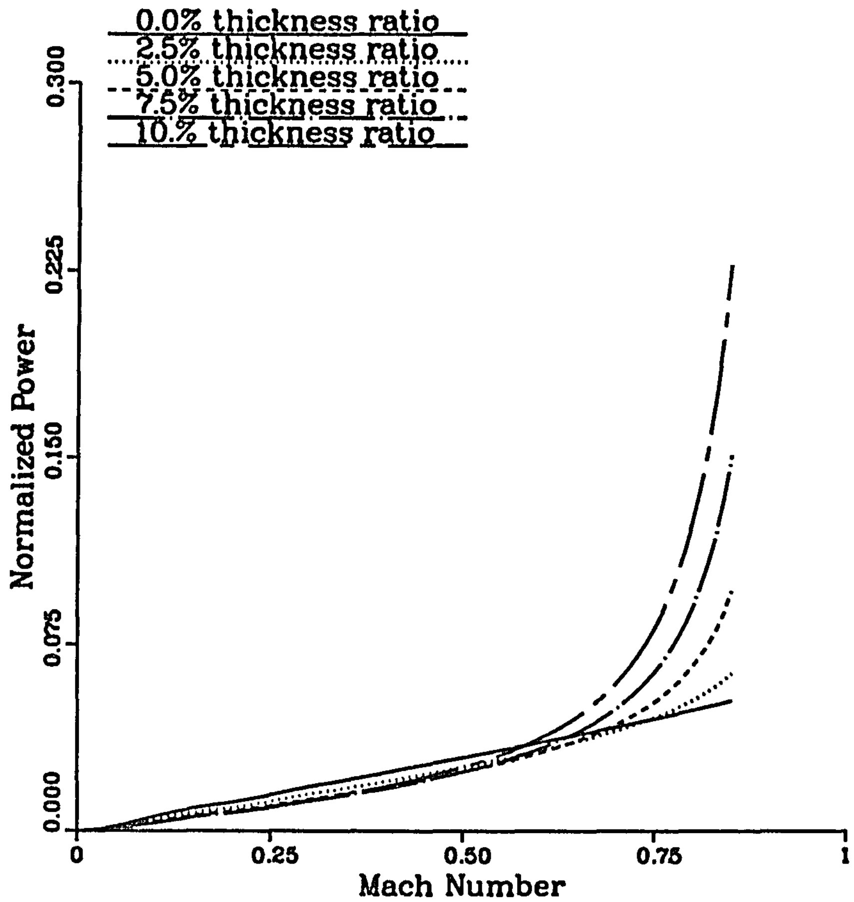


Figure 4.16 Normalized power for the leading-edge acoustic field *vs.* Mach number for $\theta_g = 45^0$ and $k = 7.5$.

function $L_3$ is the sum of $L_{3p}$, $L_{3c_1}$, $L_{3c_2}$, $L_{3c_3}$ and the integral terms in Eq. (3.63). Because $L_3$ is weakly dependent on $k$, we set $k = 10$. Figures 4.17, 4.18 and 4.19 present results for $\theta_g = 45^o$, $k = 10$, and $M_\infty = 0.01$, 0.5 and 0.9, respectively. For the intermediate Mach number case illustrated in figure 4.18, the three additional contributions to the sound field which arise due to airfoil thickness are seen to have similar orders of magnitude. The functions $L_1$, $L_2$ and $L_3$ are large compared to $L_0$, but in calculating the sound field the former three functions are multipled by the small paramter $\epsilon\sqrt{k}$. However, the results in figures 4.17 and 4.19 show that there are significant differences in the importance of the three additional source terms at low and high Mach numbers.

For the low Mach number case $M_\infty = 0.01$ (figure 4.17), the functions $|L_1(\theta)|$ and $|L_2(\theta)|$ dominate over the other contributions. The values of these two functions are essentially identical, and the uniform directivity pattern shows that $H_1$ and $H_2$ correspond to monopole sources in the low Mach number limit. However, a monopole source corresponds to a fluctuation in volume flux, which should not be present in a low Mach number, incompressible flow. In fact, we shall show shortly that in the low Mach number limit the functions $L_1(\theta)$ and $L_2(\theta)$ have opposite sign and cancel, leaving the much smaller contributions from $H_0$ and $H_2$ as the actual sound field. The contribution $H_3$ from the propagation source is of $O(M^2)$ relative to $H_0$, and hence negligible for $M << 1$.

In order to clarify the physics of the low Mach number limit, some general comments are in order. For low Mach numbers, the acoustic wavelength becomes large compared to the gust wavelength, and the appropriate length scale in the local leading-edge region is the gust wavelength. This is the "source region," which is called "acoustically compact" because its dimensions are small compared to the acoustic wavelength. On the scale of the gust wavelength, the flow appears incompressible. This local, incompressible flow can then be matched to an acoustic field which exists at distances from the leading edge on the order of

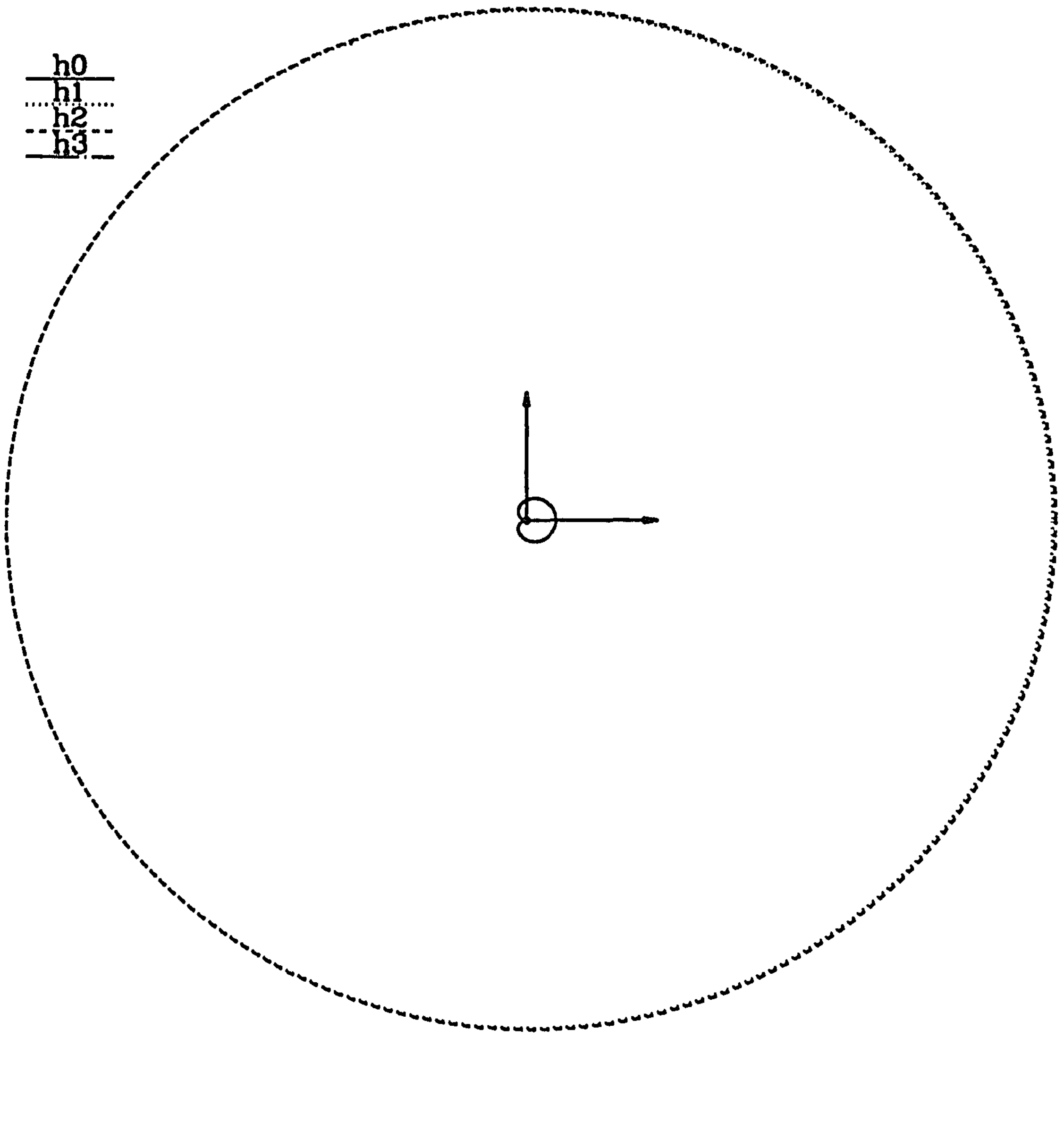


Figure 4.17 Polar plots of the magnitudes of $L_0$, $L_1$, $L_2$ and $L_3$ for $M_\infty = 0.01$, $\theta_g = 45^0$ and $k = 10$ in Prandtl-Glauert space.

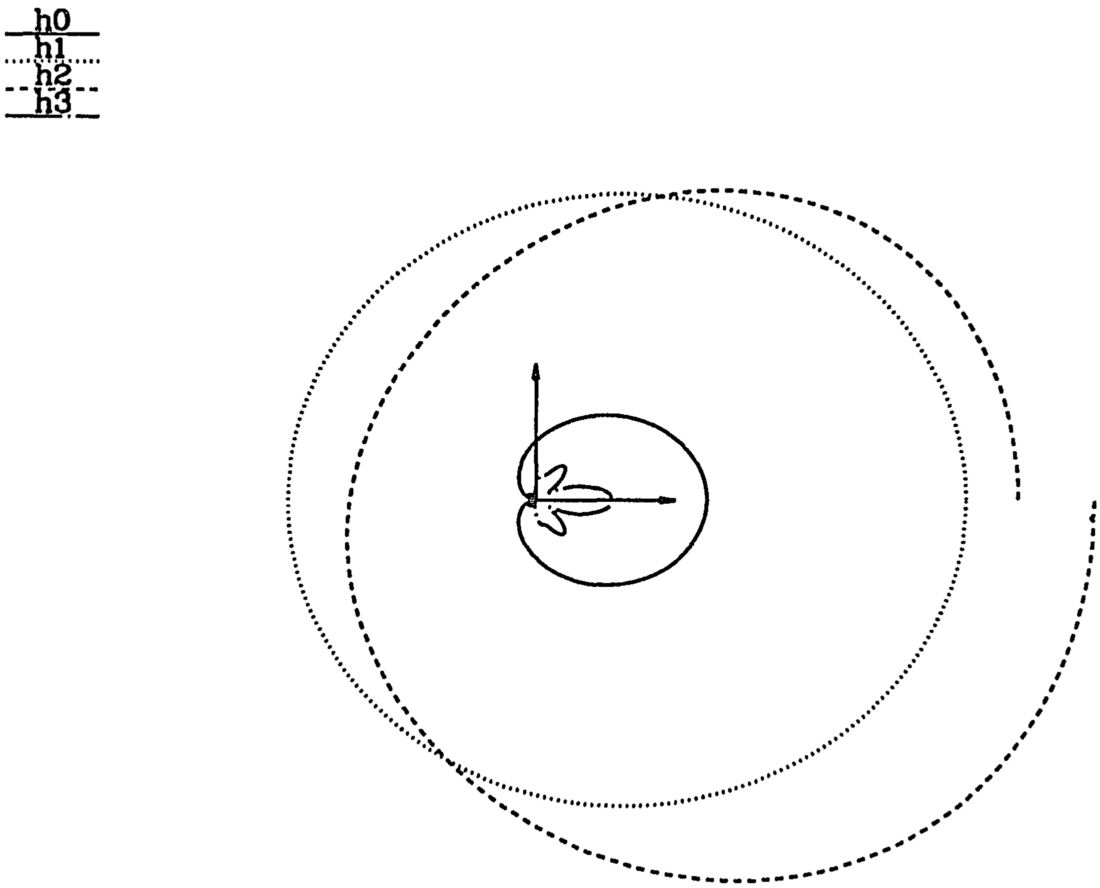


Figure 4.18 Polar plots of the magnitudes of $L_0$, $L_1$, $L_2$ and $L_3$ for $M_\infty$ = 0.50, $\theta_g$ = 45° and $k$ = 10 in Prandtl-Glauert space.

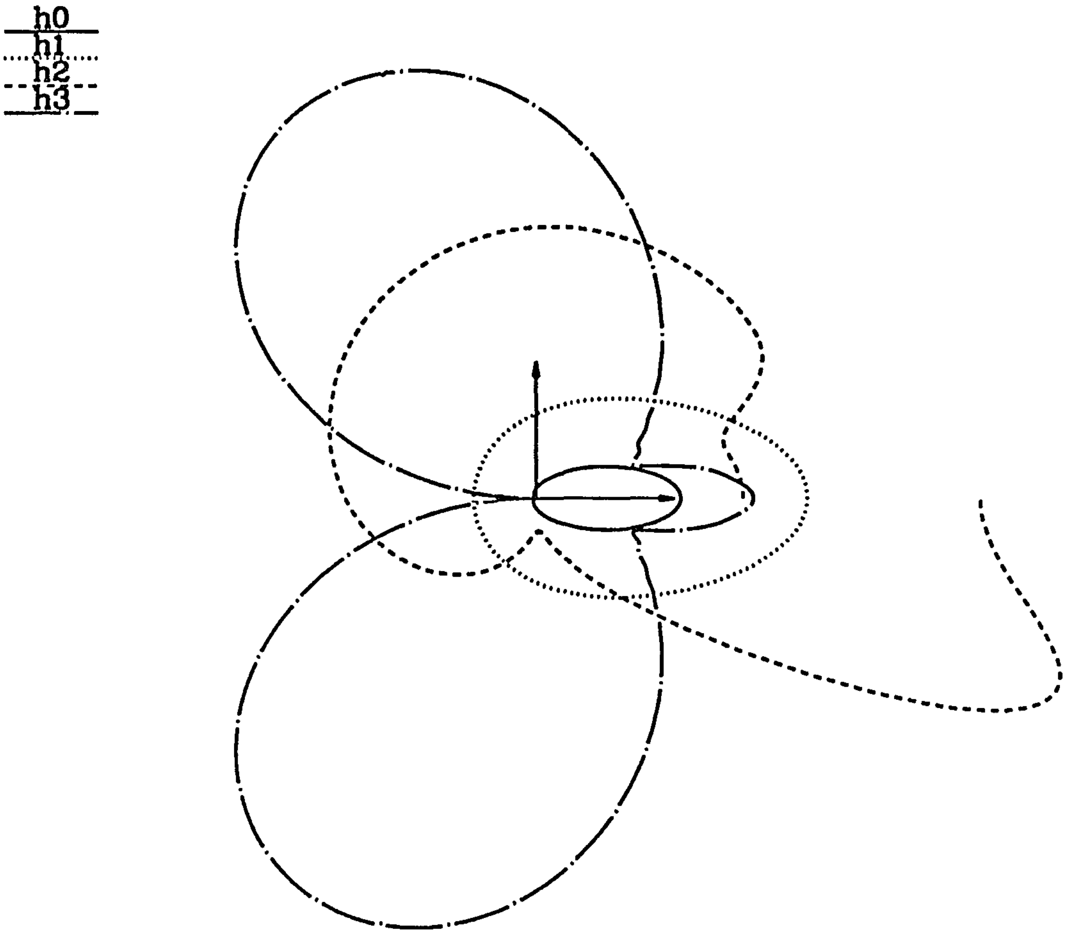


Figure 4.19 Polar plots of the magnitudes of $L_0$, $L_1$, $L_2$ and $L_3$ for $M_\infty = 0.90$, $\theta_g = 45^o$ and $k = 10$ in Prandtl-Glauert space.

the acoustic wavelength. Finally, at distances from the leading edge large compared to the acoustic wavelength ($wR >> 1$), the acoustic field takes the simple form of a cylindrical wave with directivity pattern $L(\theta)$.

An important result of the general theory for compact sources is that the sound field is determined by the lowest order nonvanishing pole of the large $R$ expansion of the incompressible solution. For an unbounded region, the large $R$ expansion is in terms of integral pole orders (monopole, dipole, etc.). Neglecting the trailing edge, in the present case the body appears as a half plane, which introduces half integer poles in the above expansion. The presence of specific pole orders in the expansion of the incompressible solution can generally be determined by evaluating certain integrals of the source function. For example, there are no external sources of volume flux in the local incompressible leading edge problem, and hence the monopole term in the large $R$ expansion must vanish. This implies that, in the $M << 1$ limit, the dominant source characteristic should be that of a pole of 3/2 order. For this pole order, the pressure directivity pattern is proportional to $\cos\theta/2$, and the dimensional sound power can be shown to be proportional to $U_\infty{}^4$.

It is easily seen from Eq. (3.10) that the solution $H_0$ for zero thickness is a pole of 3/2 order, since the directivity pattern $L_0$ is proportional to $\cos\theta/2$ for $w << 1$. In contrast, expanding the expressions (3.13b) and (3.18b) for $L_1(\theta)$ and $L_2(\theta)$ in the low Mach number limit, $w = \delta M_\infty << 1$, $\delta = O(1)$, we obtain

$$L_1(\theta) = \frac{-i\,A_t^*}{\sqrt{M_\infty}} - \frac{i}{2}\,A_t^*\,\sqrt{M_\infty}\cos\theta + O(M_\infty^{3/2}) \qquad (4.10a)$$

and

$$L_2(\theta) \;=\; \frac{i\,A_t^*}{\sqrt{M_\infty}} \;-\; \frac{\sqrt{2}\,A_n\,\cos\theta/2}{\sqrt{1+k_n{}^2}} \;+\; O(\sqrt{M_\infty})\;. \qquad (4.10b)$$

It can be seen that these functions contain monopoles of equal amplitude and opposite sign. The monopole terms are of $O(M_\infty^{-1/2})$ relative to $L_0$. The origin of the monopole terms can be seen by examining the forcing terms in Eqs. (3.11b) and (3.14a). The boundary condition (3.11b) governing $H_1$ corresponds to a source distribution along the surface of the half plane. The outflow is an oscillatory function of $\Phi$, but does not integrate to zero. The monopole contribution for $H_2$ arises because the vortical velocity $v'$ is not solenoidal. However, since the total velocity field in the local leading-edge region must be solenoidal at low Mach number, the monopole contributions from $H_1$ and $H_2$ must cancel identically. The next term in the $M_\infty << 1$ expansion of $L_1$ is a dipole, whose pressure field is $O(M_\infty^{1/2})$ relative to that for $L_0$ and hence negligible for $M_\infty << 1$. In contrast, the next term in the expansion of $L_2$ is a pole of 3/2 order, which comes from the complmentary solution $L_{2c}$ representing the "scattered quadrupole source" of Ffowcs Williams and Hall (1970). These results also show that the leading-edge directivity pattern for $M_\infty << 1$ is the simple cardiod $\cos\theta/2$, even for non-zero thickness airfoils.

It is also interesting to compare the efficiency of sound generation by vortical and entropic gusts in the low Mach number limit. In contrast to the case of vortical gusts, an entropy gust interacting with a zero-thickness airfoil in uniform flow produces no sound. The entropy gust generates sound only through interaction with a nonuniform mean flow. For the case of a zero-thickness, cambered airfoil at moderate values of leading-edge loading $\alpha_{eff}$ in the low Mach number limit, Kerschen and Myers (1987b) found that vortical and entropic gusts generated similar sound power levels. However, we shall show that for the present case of a symmetric airfoil with thickness, the entropy gust generates very little sound for $M << 1$.

Note that the amplitude $B$ of the entropy gust enters only in $A_t^* = A_t - B$, which appears only in $L_1(\theta)$ and $L_2(\theta)$. A pure entropy gust corresponds to $A_n = A_t = 0$. It can be seen from Eqs. (4.10) that for $M_\infty << 1$, the pole of 3/2 order vanishes identically for a pure entropy gust. This leaves only a much less efficient dipole contribution to the sound field. The dimensional sound power associated with the dipole for the pure entropy gust scales as ${U_\infty}^5$, compared to the scaling as ${U_\infty}^4$ for a gust containing a vortical component.

Finally, we note that with the neglect of the trailing edge, a scaling of the results can be introduced which absorbs the dependence on both the Mach number and frequency in the low Mach number limit. This is achieved by defining a Leading-Edge Power,

$$\text{Leading-Edge Power} = (\text{Normalized Power}) \, \frac{k}{M} \, . \tag{4.11}$$

The leading-edge power is then independent of Mach number for $M_\infty << 1$, corresponding to a dimensional sound power which scales as ${M_\infty}^4$. Furthermore, with the exception of a weak dependence on $\ln(k)$, the leading-edge thickness and the frequency enter only through the combination of parameters, $\epsilon\sqrt{k}$.

Next consider the behavior for subsonic Mach numbers approaching $M_\infty = 1$. Of course, our theory is not valid for Mach numbers very close to one, since we have not included the nonlinear effects which arise in the transonic small-disturbance theory for the mean flow. However, it is instructive to compare the trends predicted by our theory, for these provide insight into the dominant phsysical mechanisms for high subsonic Mach numbers. In figure 4.19, the magnitudes of $L_0(\theta)$, $L_1(\theta)$, $L_2(\theta)$ and $L_3(\theta)$ are plotted for the case $\theta_g = 45^o$, $k = 10$ and $M_\infty = 0.9$. The largest contribution at most angles comes from the $L_3$, corresponding to the "propagation source." The second largest contribution comes from $L_2(\theta)$ corresponding to the quadrupole sources. In comparison, the contribution $L_1(\theta)$ from the modified boundary conditions is seen to be relatively unimportant. These results illustrate the importance of the propagation source for high subsonic Mach numbers. This source mechanism is often neglected in heuristic models based on the acoustic analogy.

### 4.3 Behavior with Changing Thickness for Vortical Gusts

In this section, results which illustrate the variation in normalized power as a function of airfoil thickness ratio are presented for fixed values of the Mach number, frequency and gust orientation. Figures 4.20 through 4.23 present results for four different gust angles, $\theta_g = 0^o$, $15^o$, $30^o$ and $45^o$. The frequency is set to $k = 5$, and results for five different Mach numbers are shown on each figure. In general, the normalized power first decreases with airfoil thickness before reaching a minimum value beyond which the sound power increases with airfoil thickness. The magnitude of the initial decrease in normalized power, and the thickness ratio at which this minimum occurs, are functions of both the gust angle and the Mach number. Relative to the sound power at zero thickness, the minimum level of sound power is lower for small gust angles. At larger gust angles there is only a minor, if any decrease in sound power before the levels start rising with increasing thickness. At Mach number $M_\infty = 0.6$ and below, the increases in sound power due to thickness are relatively modest; at this Mach number and the gust angles considered in figures 4.20 through 4.23, thickness ratios of up to 25% do not cause more than a factor of two increase in sound power over the zero-thickness level.

However, at larger Mach numbers the sound power level rises rapidly with increasing airfoil thickness, especially for non-zero values of gust angle. This increase in sound power is caused by the quadrupole sources and the propagation source. For $M_\infty = 0.8$ and $\theta_g = 45^o$, the sound power level has doubled compared to its zero-thickness value at an airfoil thickness of 8.5%, tripled at an airfoil thickess of 13.5%, and quadrupled at a thickness of 16.5%. The strong influence of Mach number in the high subsonic range is also evident from figures 4.20 through 4.23. The differences in sound power between $M_\infty = 0.7$ and 0.8 are much larger than those for comparable changes in $M_\infty$ in the lower Mach number range. It can be seen from this trend that even small increases in Mach number beyond $M_\infty = 0.8$ would significantly increase the noise level for airfoils with nonzero thickness. It should also be pointed out that these results are for Joukowski airfoils, in which the nose radius is $O(\epsilon^2 b)$ compared to a maximum thickness of aprroximately $1.3\epsilon b$. Results presented in Section 4.6 show that it is the airfoil nose radius rather than the maximum thickness of the airfoil which is primarily responsible for the increase in sound power level. Some turbine and compressor blade designs feature relatively large nose radii, which would further accentuate the effects discussed above.

### 4.4 Directivity Patterns for Vortical Gusts

In addition to the total level of the radiated sound power, the directivity pattern of the sound field is also of interest in aeronautical applications. Furthermore, features of the underlying physics can be identified from directivity patterns. Therefore, directivity patterns for some typical cases are presented in this section.

To illustrate the effect of trailing-edge scattering, figure 4.1 is a polar plot of the far-field sound pressure in "airfoil coordinates" for $M = 0.8$, $k = 5$, $\theta_g = 0^0$ and a zero-thickness airfoil. For a zero-thickness airfoil, there is no distortion of the gust vorticity by the mean flow and sound is generated only by the airfoil surface blocking the gust velocity. The dotted line corresponds to the directivity pattern for the leading edge alone, while the solid line corresponds to the pattern for the total field. The directivity patterns above and below the airfoil are symmetric, but the pressure fields are out of phase. The pattern for the

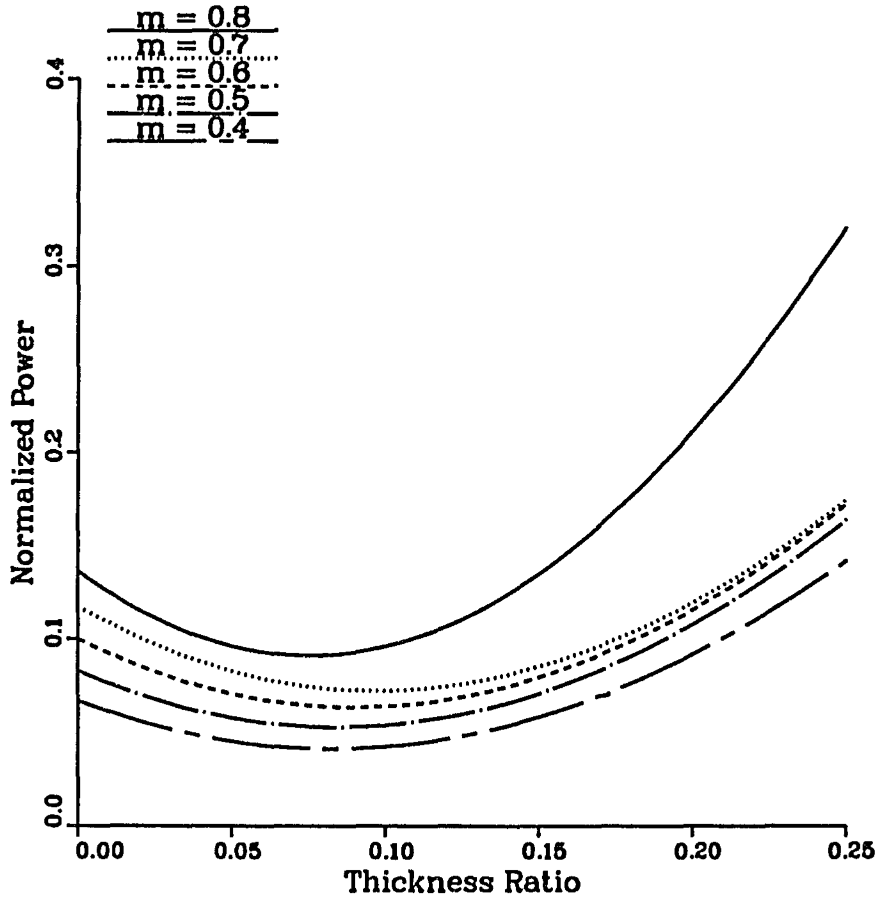


Figure 4.20 Normalized power *vs*. thickness ratio for $\theta_g = 0^0$ and $k = 5$.

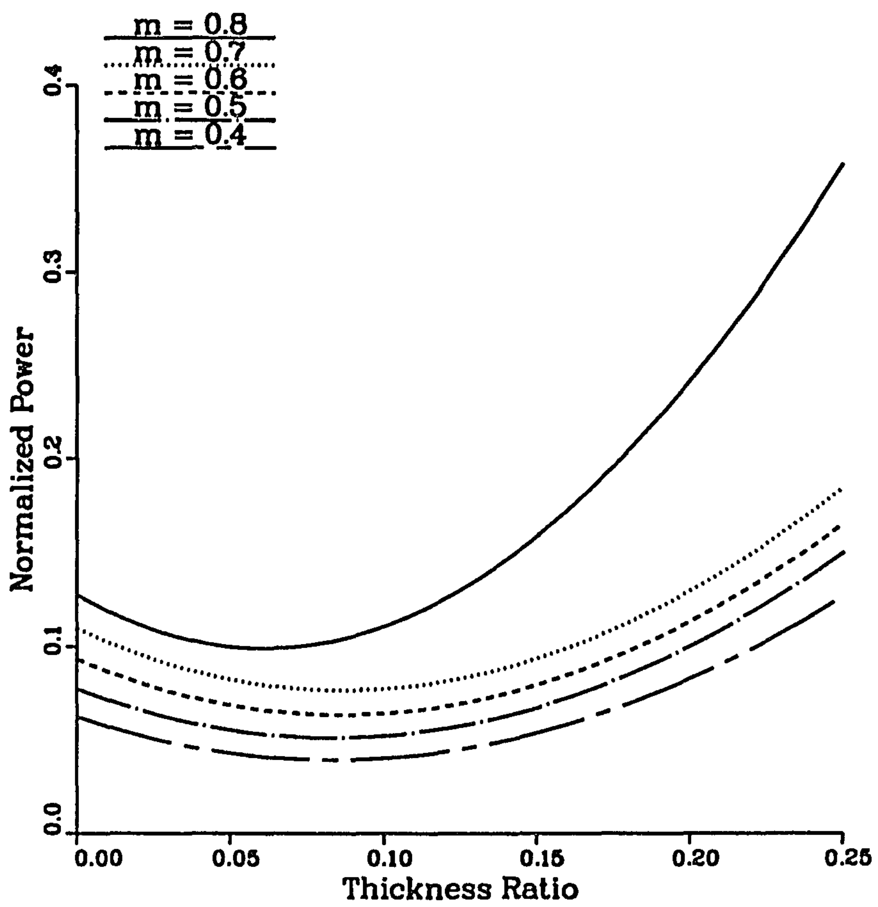


Figure 4.21 Normalized power *vs.* thickness ratio for $\theta_g = 15^0$ and $k = 5$.

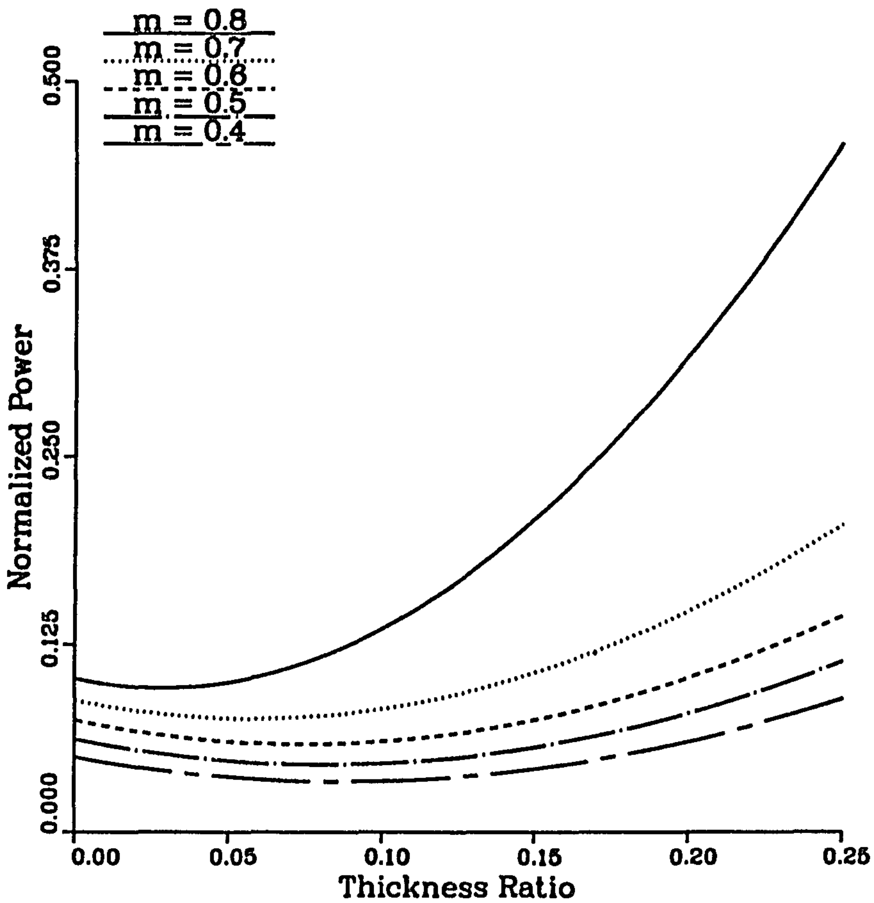


Figure 4.22 Normalized power *vs.* thickness ratio for $\theta_g = 30^0$ and $k = 5$.

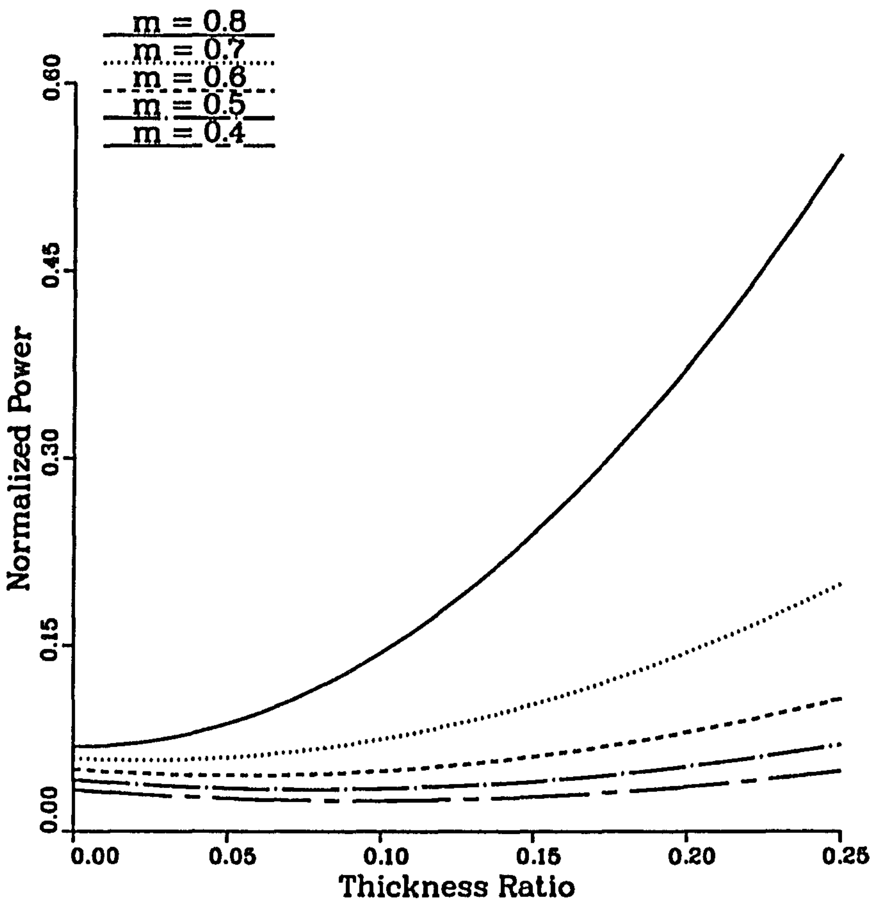


Figure 4.23 Normalized power *vs.* thickness ratio for $\theta_g = 45^o$ and $k = 5$.

leading edge alone is smoothly varying and exhibits a nonzero value in the downstream direction, leading to scattering by the trailing edge. The pattern for the total field contains peaks and valleys, corresponding to constructive and destructive interference between the primary field from the leading edge and the secondary field from the trailing edge. Although the scattering by the trailing edge has a significant effect on the directivity pattern, it has only a modest influence on the normalized power, as was illustrated in figure 4.6 and discussed in Section 4.1. Some comments on conventions for and interpretation of the directivity plots were also made in Section 4.1.

In figure 4.24, the directivity pattern for a Joukowski airfoil with 5% thickness is presented for the case $M_\infty = 0.8$, $k = 5$ and $\theta_g = 45^o$. Directivity patterns for the leading edge alone and for the total field are plotted. The directivity pattern for the leading edge alone is now asymmetric with respect to the airfoil chord, with a strong peak in the direction of the gust wavevector. In relative terms, the radiation of the leading-edge field in the downstream direction is weaker than for the case presented in figure 4.1. Therefore, the scattered field from the trailing edge has a smaller influence on the total directivity pattern, and the constructive and destructive interference is noticeable only for the aft part of the directivity pattern. From a comparison of the dotted and solid lines in figure 4.24, it is evident that in this case the trailing edge scattering has even less influence on the sound power level than for the case presented in figure 4.1.

In figure 4.25, the sound radiated by 5% and 10% thickness Joukowski airfoils is compared to that for a zero-thickness airfoil for $M = 0.8$, $k = 5$ and $\theta_g = 0^o$. The introduction of airfoil thickness is seen to cause significant changes in the directivity pattern. In particular, the airfoil thickness has signficantly increased the pressure level in the upstream quadrants. This might suggest that the introduction of airfoil thickness has increased the total sound power, but in fact this is not the case. The total power levels for

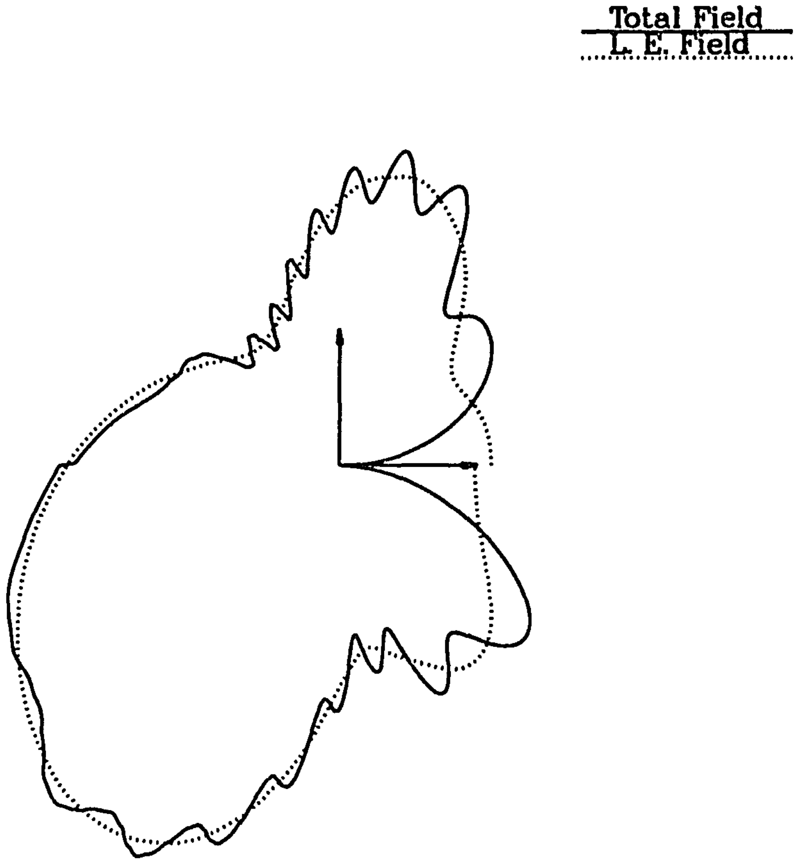


Figure 4.24 Polar plots of the far-field sound pressure for $M_\infty = 0.8$, $k = 5$, $\theta_g = 45^o$ and 5% thickness ratio.

the 5% and 10% thickness cases are approximately 30% below the zero-thickness case, as can be seen from figure 4.8. This apparent discrepancy is explained by accounting for the effect of the mean flow on the the pressure level and the acoustic intensity. It can be seen from Eq. (3.68) that in the upstream direction the mean flow amplifies the pressure level relative to that for the potential, due to the factor $(\delta - w\cos\theta)$. A similar factor is not present in Eq. (4.2d) for the normalized sound power, since the increase in the pressure is compensated for by the fact that the mean flow also decreases the speed at which the acoustic energy propagates in the upstream direction.

The corresponding results for $\theta_g = 45^0$ are presented in figure 4.26. For this case, the introduction of 5% airfoil thickness has caused a dramatic rise in the amplitude of the pressure field, with a particularly strong peak below the airfoil in the forward quadrant. The 5% airfoil thickness has led to a 25% increase in the total sound power level. An increase of the airfoil thickness ratio to 10% further amplifies the pressure peak in the third quadrant. For the 10% thick airfoil, the total sound power has increased by a factor of two compared to the zero-thickness case. A comparison of figures 4.25 and 4.26 demonstrates that the effect of airfoil thickness is a strong function of the gust orientation.

The influence of Mach number on pressure directivity patterns is illustrated in figures 4.27 and 4.28. In figure 4.27, directivity patterns for $M_\infty$ = 0.4, 0.6 and 0.8 are plotted for the case $k = 5$, $\theta_g = 0^0$ and 10% thickness ratio. The changes in the directivity pattern when the Mach number increases from 0.4 to 0.6 are relatively modest. The pattern for $M_\infty = 0.6$ has more of a lobed structure, due to the increase in the the product $kw$. However, when the Mach number is raised from 0.6 to 0.8, a dramatic increase occurs in the amplitude of the pressure field in the upstream direction. There are also many more lobes in the pattern for $M_\infty = 0.8$.

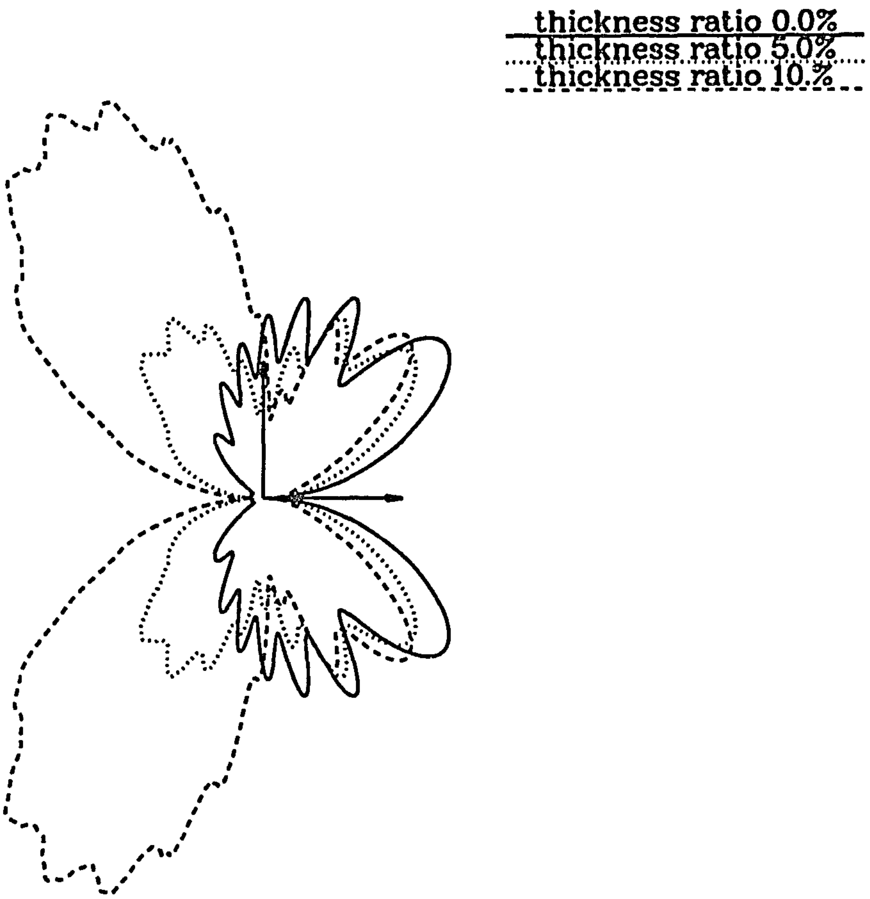


Figure 4.25 Polar plots of the far-field sound pressure for $M_\infty = 0.8$, $k = 5$ and $\theta_g = 0^o$.

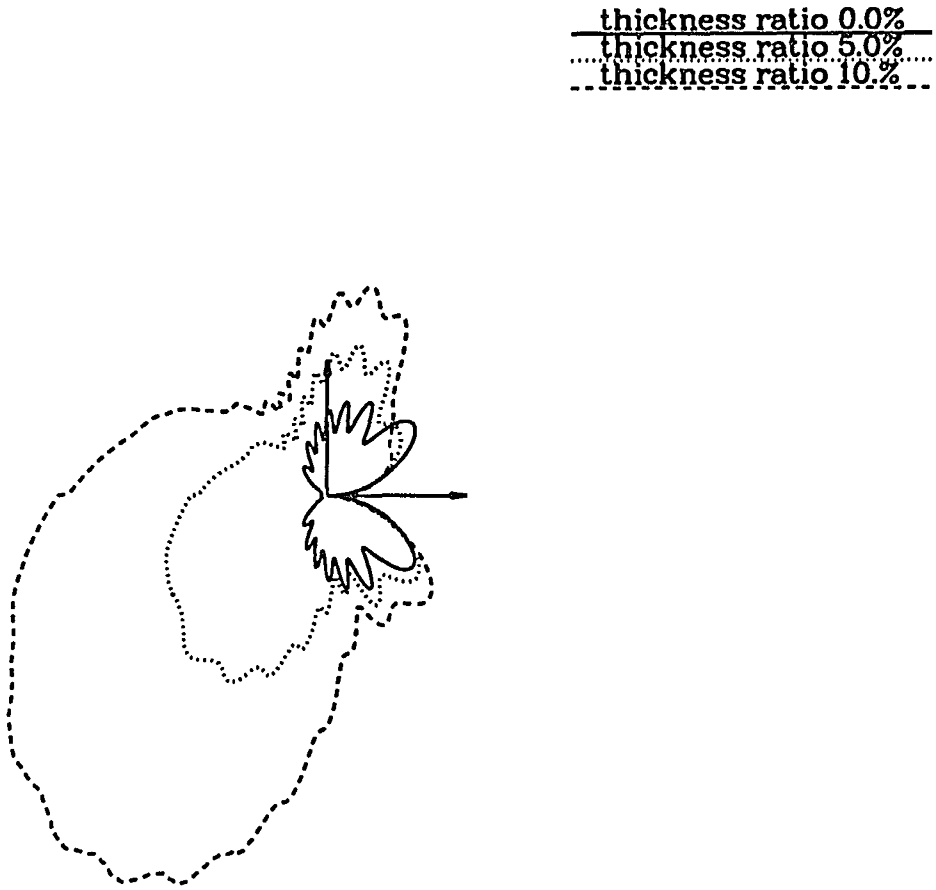


Figure 4.26 Polar plots of the far-field sound pressure for $M_\infty = 0.8$, $k = 5$ and $\theta_g = 45^0$.

The corresponding results for $\theta_g$ = 45° are shown in figure 4.28. For this gust angle, the airfoil thickness has a stronger effect on the pressure field, and the effects of Mach number variations are also greater. The directivity pattern for $M_\infty$ = 0.4 exhibits a definite asymmetry above and below the airfoil, indicating a significant influence of airfoil thickness. The pressure level generally rises, and substantial changes in the shape of the directivity pattern occur when the Mach number is raised from 0.4 to 0.6. It can be seen from figure 4.23 that this change also doubles the normalized sound power level. With a further increase in the Mach number from 0.6 to 0.8, the amplitude of the pressure field rises dramatically, accompanied by a large changes in the shape of the directivity pattern. The pressure field now exhibits a strong lobe in the forward direction below the airfoil. The normalized sound power level for $M_\infty$ = 0.8 is approximately six times that for $M_\infty$ = 0.4.

The results presented in this section illustrate that airfoil thickness produces dramatic changes in the directivity pattern of the sound field, and also influences the total sound power level. In practical applications, changes in the directivity pattern could be even more important than changes in the total power level. For example, in fan, compressor or turbine noise, the overall sound power level radiated by the system is often strongly influenced by constructive and destructive interference between the sound fields from different blades. The interaction of the dramatic changes in directivity patterns produced by airfoil thickness with the constructive and destructive interference which occurs in propulsion system geometries could significantly modify the overall sound level produced by aeronautical propulsion systems.

### 4.5 Combinations of Vortical Gusts and Entropic Gusts

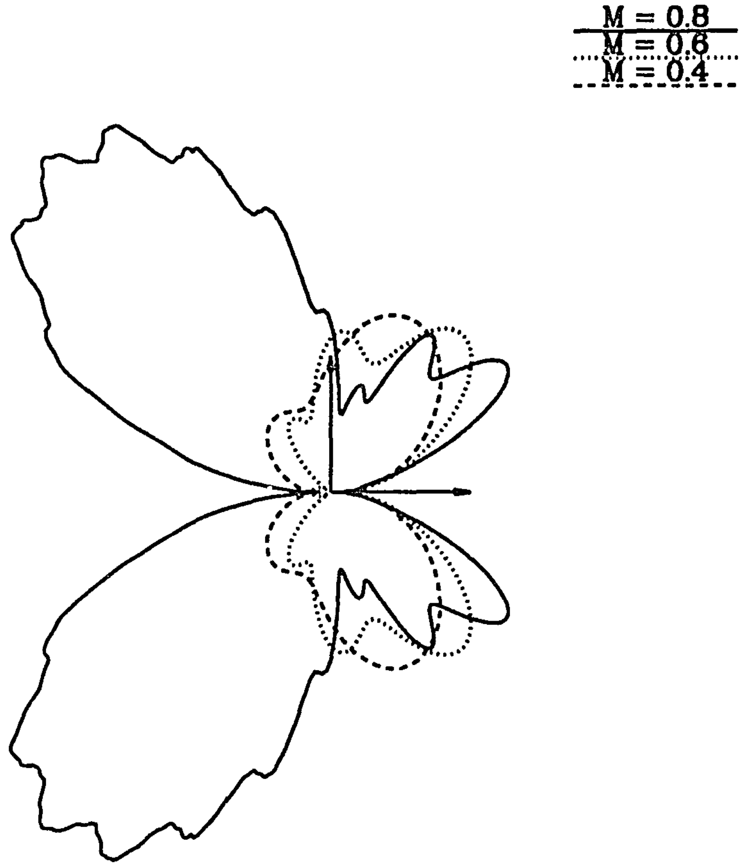


Figure 4.27 Polar plots of the far-field sound pressure for $k = 5$, $\theta_g = 0^0$ and 10% thickness ratio.

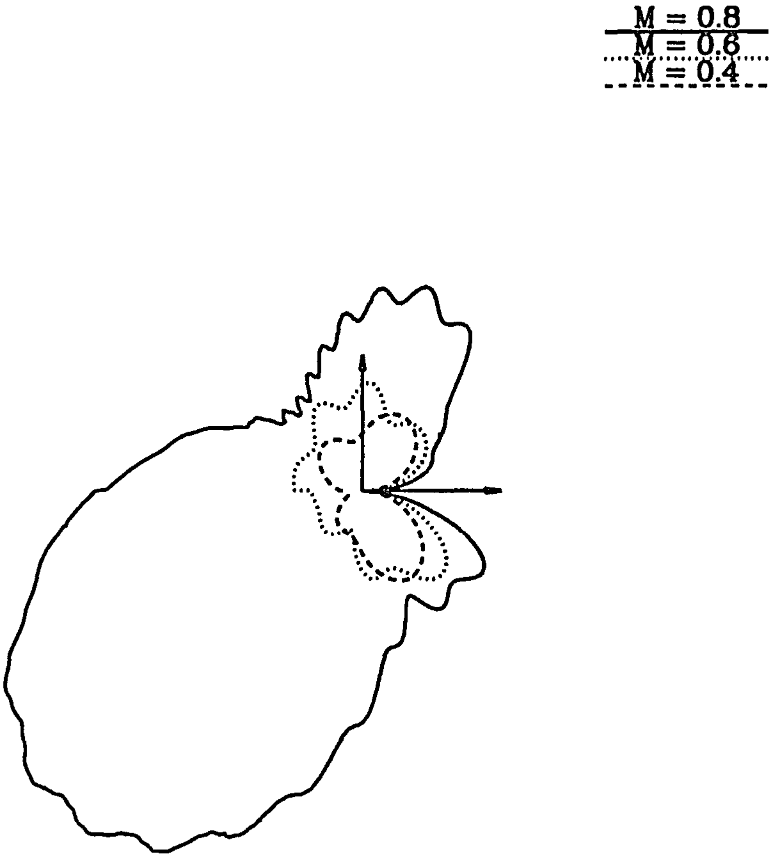


Figure 4.28 Polar plots of the far-field sound pressure for $k = 5$, $\theta_g = 45^0$ and 10% thickness ratio.

Most previous work on sound generation by airfoil-gust interactions has considered only vortical gusts. Vortical gusts may represent the wakes of upstream airfoils or struts, or inflow turbulence. However, there are a number of important applications in which the inflow has unsteady temperature (or entropy) disturbances, often combined with unsteady vorticity disturbances. Examples of such applications are the unsteady disturbances generated in combustors of aircraft engines. These disturbances then pass through the turbine, generating airfoil-gust interaction noise in the process. Another application involving a combination of vortical and entropic gusts is a pusher propfan geometry designed by Pratt and Whitney, in which the turbine exit flow exhausts over the root section of the pusher propfan.

In this section, we consider the case of combined, two-dimensional vortical and entropic gusts. Generalizing the definition (4.2c) of the gust amplitude to include entropic disturbances, we set

$$\mathrm{A} = \sqrt{A_t^{\,2} + A_n^{\,2} + B^2} \tag{4.12a}$$

where $B$ is the nondimensional amplitude of the entropy disturbance as defined by Eq. (2.7a). A parameter denoting the fraction of the gust which is vortical can then be defined as

$$frac = \sqrt{A_t^{\,2} + A_n^{\,2}} \,/\, A \ . \tag{4.12b}$$

Since there may in general be a difference in phase between the vorticity and entropy disturbances, we set

$$B = \sqrt{1 - frac^2}\, e^{i\, phased} \tag{4.13}$$

where *phased* is the phase difference between the vortical and entropic gusts. Thus, *frac* lies between zero and one, with *frac* = 0 corresponding to a pure entropy gust and *frac* = 1 corresponding to a pure vorticity gust.

In our formulation, the effect of the entropy gust enters only in $L_1(\theta)$ and $L_2(\theta)$ through $A_t^* = A_t - B$. Thus, the interaction of a pure entropy gust with a zero-thickness flat plate produces no sound. In order to generate sound, it is necessary for the entropy gust to interact with mean-flow gradients. Furthermore, for a pure entropy gust the total sound power is proportional to the square of the airfoil thickness. In contrast, the interaction of a vortical gust with a zero-thickness plate generates sound by blocking the normal component of the gust velocity. Thus, for small levels of airfoil thickness, the sound due to a pure vorticity gust has a linear dependence on the thickness parameter.

The dependence of the normalized power on *frac* is illustrated as a function of gust angle in figures 4.29 through 4.35. Results for five values of *frac* are plotted in each figure. The frequency is set to $k$ = 10, and the phase difference *phased* = 0° in figures 4.29 through 4.34, while it set to 45° in figure 4.35. Figures 4.29 through 4.34 consist of three pairs, corresponding to results for airfoil thicknesses of 5% and 10% for three different Mach numbers, $M_\infty$ = 0.4, 0.6 and 0.8.

Results for a 5% thickness airfoil and $M_\infty$ = 0.4 are plotted in figure 4.29. The normalized power is a symmetric function of $\theta_g$ for the pure entropy and pure vorticity gusts, *frac* = 0 and 1. This is to be expected due to the symmetry of the airfoil. However, this symmetry is broken by the presence of both vorticity and entropy gusts, and the peak value shifts to negative gust angles for the case of combined gusts. For this Mach number and airfoil thickness, the pure vorticity gust generates about three and one-half times as much sound power as the pure vorticity gust. For combined gusts, the total power level lies between the results for *frac* = 0 and *frac* = 1.

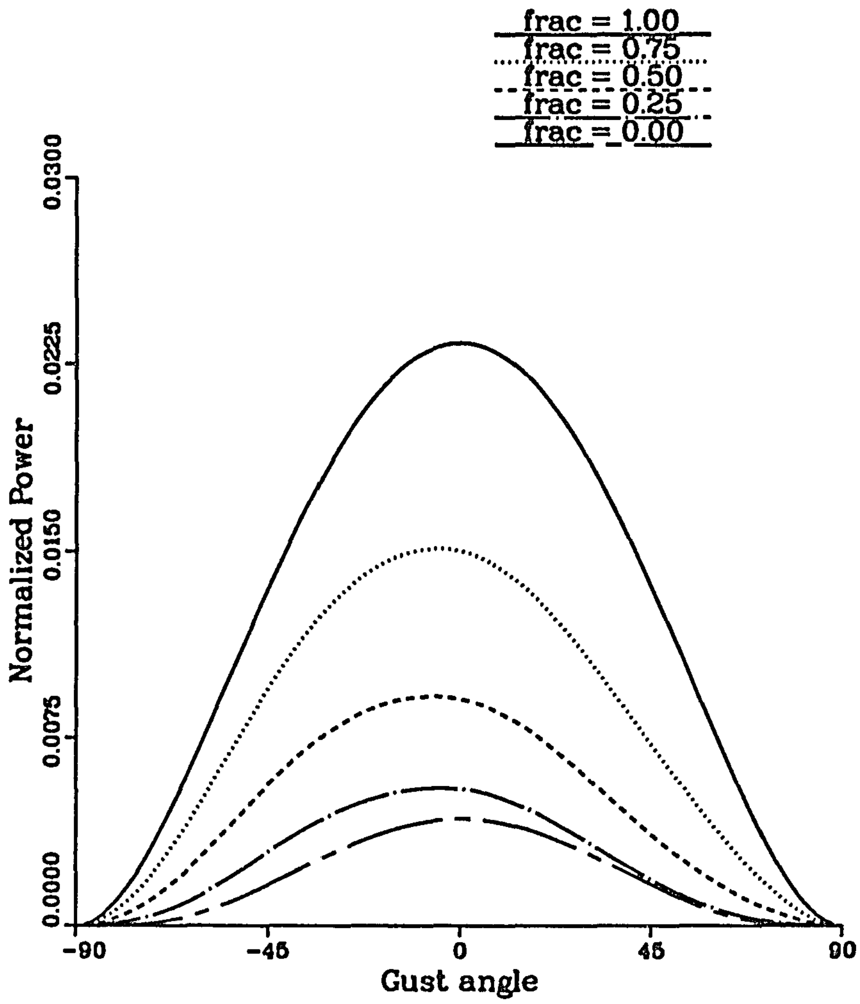


Figure 4.29 Normalized power *vs.* gust angle for $M_{\infty} = 0.40$, $k = 10$, *phased* = $0^0$ and 5% thickness ratio.

The corresponding results at $M_\infty$ = 0.4 for a 10% thickness ratio are shown in figure 4.30. The general features found for the 5% thickness airfoil remain valid here, but there are changes in the normalized power magnitudes for the two types of gusts. The maximum power level for the pure entropy gust has increased by a factor of four, consistent with the above discussion, while the maximum power level for the pure vorticity gust has increased only by a factor of 1.43. There is now less than a factor of two difference in the maximum levels of the normalized power for the pure vorticity and entropy gusts. As before, the results for combined gusts lie between the results for the two pure gusts.

Figure 4.31 presents results for $M_\infty$ = 0.6 and 5% thickness ratio. At this higher Mach number, the maximum power level generated by the vorticity gust is 2.42 times that for the entropy gust. At $M_\infty$ = 0.4, this ratio was approximately 3.5. The maximum power level for intermediate values of *frac* has been shifted more dramatically to negative values of $\theta_g$. In addition, for *frac* = 0.25 and 0.5, the power level at some positive values of $\theta_g$ lies below the result for the pure entropy gust. Thus, for these cases there has been some cancellation between the sound fields generated by the vortical and entropic components of the gust field.

Results for $M_\infty$ = 0.6 and a thickness ratio of 10% are plotted in figure 4.32. For these conditions, the entropy gust generates more sound power than the vorticity gust in the range $|\theta_g| \leq 45^o$. The maximums in the normalized power for *frac* = 0.25, 0.50 and 0.75 are at nearly the same level as for the pure entropy gust, though the maximums gradually shift to larger negative gust angles as *frac* increases. For the intermediate values of *frac*, the total sound power generaly lies above the result for the pure vorticity gust for negative values of $\theta_g$. In contrast, for positive values of $\theta_g$ the sound power is generally lower than that for the pure vorticity gust, indicating that destructive interference between the sound fields generated by the vortical and entropic gust components has occured.

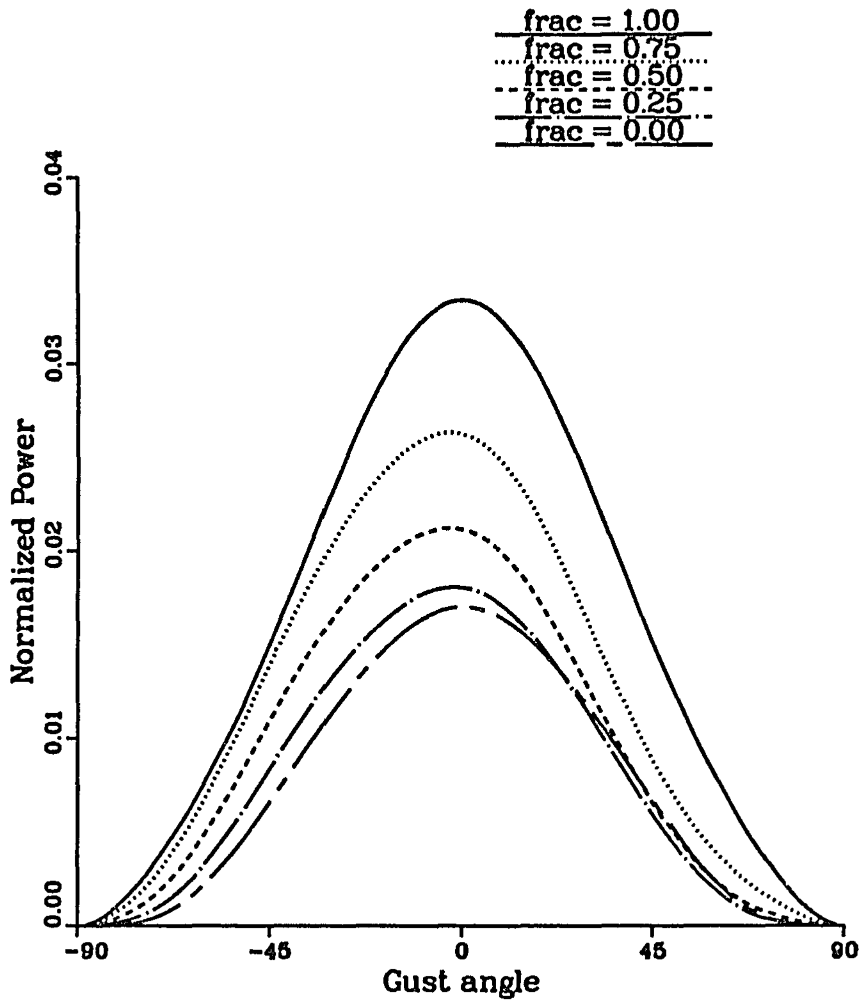


Figure 4.30 Normalized power *vs.* gust angle for $M_\infty$ = 0.40, $k$ = 10, *phased* = $0^0$ and 10% thickness ratio.

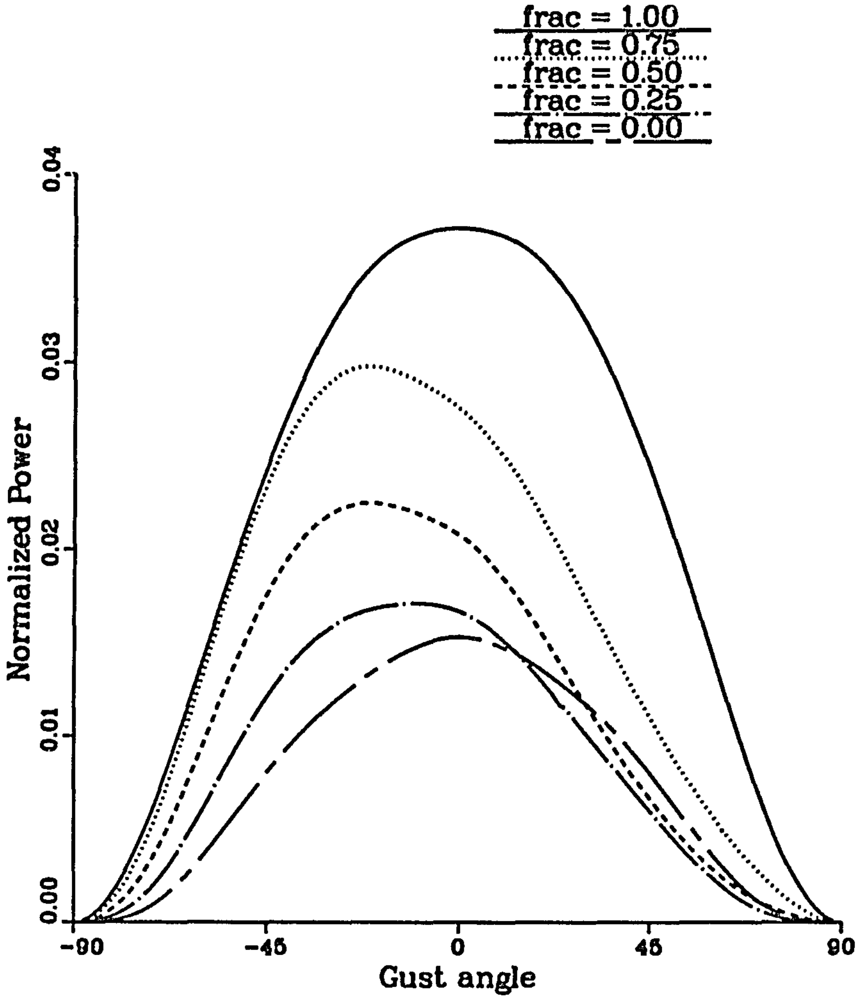


Figure 4.31 Normalized power *vs.* gust angle for $M_{\infty}$ = 0.60, $k$ = 10, *phased* = $0^{0}$ and 5% thickness ratio.

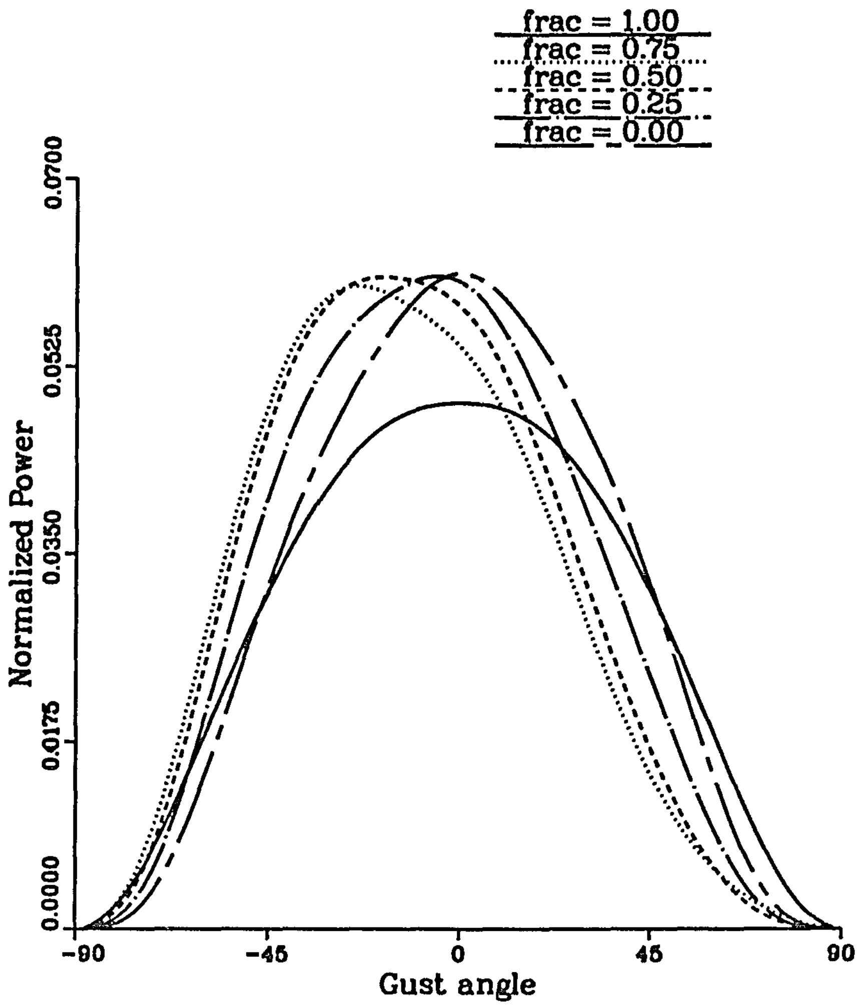


Figure 4.32 Normalized power *vs.* gust angle for $M_{\infty} = 0.60$, $k = 10$, *phased* $= 0^{o}$ and 10% thickness ratio.

In figures 4.33 and 4.34, results are presented for $M_\infty = 0.8$ and 5% and 10% thickness ratios. With the increase in Mach number to 0.8, there has been a dramatic increase in the sound power level for the entropy gust. At a thickness ratio of 5% (figure 4.33), the maximum power level for the entropy gust is slightly above that for the vorticity gust, while at 10% thickness (figure 4.34) the maximum value for the entropy gust is over twice that for the vorticity gust. The peak level for the entropy gust occurs at $\theta_g = 0^o$, while the peak level for the vorticity gust occurs in the vicinity of $\theta_g = 45^o$. The interaction between the vorticity and entropy gust components for intermediate values of *frac* has also grown stronger. Constructive interference generally occurs for negative gust angles, leading to power levels that exceed those of the entropy or vorticity gust alone, by approximately 50% for the 5% thickness airfoil. In contrast, destructive interference generally occurs for positive gust angles, leading to a decrease in power level relative to the cases of a pure entropy or vorticity gust. This decrease at positive gust angles is particularly significant for *frac* = 0.5 and 0.75.

Certain results regarding the influence of the phase difference between the vortical and entropic gusts, *phased*, can be derived from symmetry arguments. The ampliltude $B$ of the entropy gust enters the solution only through $A_t^* = A_t - B$. Note that a 180° shift in the value of *phased* corresponds to a change in the sign of B. Similarly, by combining the solenoidal condition (4.5) and the definition (4.4) of $\theta_g$, it can be seen that the sign of $A_t$ is changed by changing the sign of $\theta_g$. Now, since the airfoil shape is symmetric, it does not introduce a preferred direction with respect to the normal coordinate. Therefore two cases related by $(A^*_{t\,2}, A_{n\,2}) = (-A^*_{t\,1}, A_{n\,1})$ must have the same total power level. It can then be concluded that the introduction of an 180° shift in the value of *phased* simply transforms the total power level into its mirror image through a change in the sign of $\theta_g$. Thus, for conditions corresponding to those in figures 4.29 through 4.34 except with *phased* = 180°,

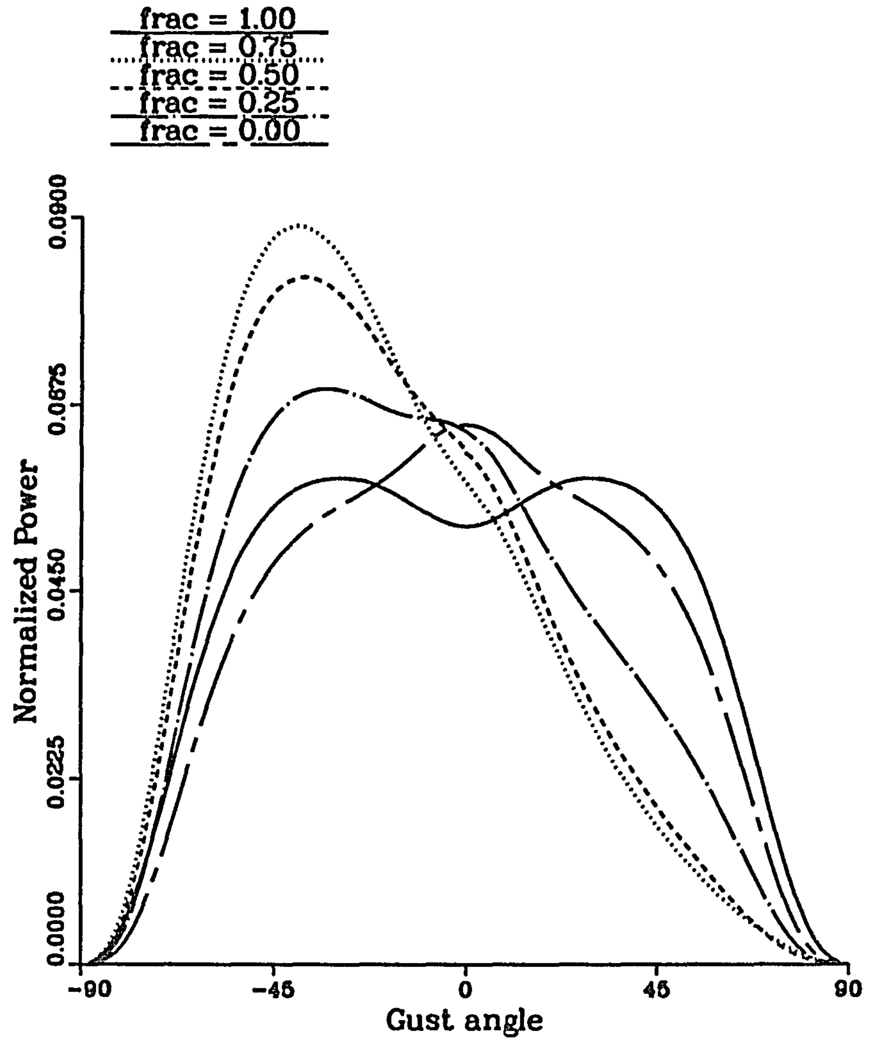


Figure 4.33 Normalized power *vs.* gust angle for $M_\infty = 0.80$, $k = 10$, *phased* = $0^o$ and 5% thickness ratio.

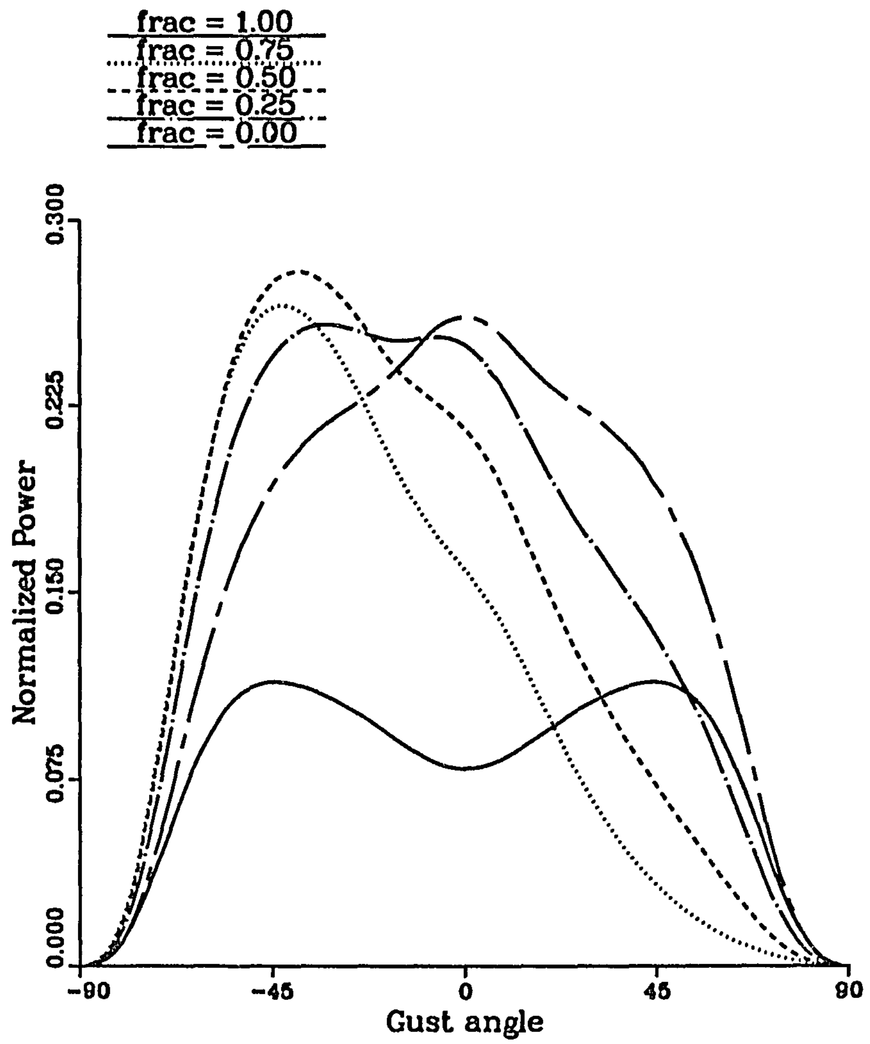


Figure 4.34 Normalized power *vs.* gust angle for $M_\infty$ = 0.80, $k$ = 10, *phased* = $0^0$ and 10% thickness ratio.

the locations of the maximum power levels for intermediate values of *frac* would shift to positive values of $\theta_g$.

A typical case for which the influence of the phase difference cannot be related to previous results is presented in figure 4.35. For this figure *phased* = 45°, and the other parameters are the same as in figure 4.33, i.e. $M_\infty = 0.8$, $k = 10$, and 5% thickness ratio. Comparing figures 4.33 and 4.35, it can be seen that the change in the phase difference between the vortical and entropic gusts has produced only modest changes in the normalized power. These results suggest that the overall characteristics of the total sound power are not terribly sensitive to the exact value of the phase difference between the vortical and entropic gusts. However, details such as the pressure directivity pattern or the angle at which the maximum normalized power occurs, clearly depend on *phased*.

Finally, figures 4.36 and 4.37 present examples of the pressure directivity patterns, for the case $M_\infty = 0.6$, $k = 5$, $\theta_g = 0°$, *phased* = 0° and 10% thickness ratio. Figures 4.36 and 4.37 contain results for $\theta_g = 0°$ and 45°, respectively, and in each figure results for three different values of *frac* are presented. The directivity patterns for pure vorticity (*frac* = 1) and pure entropy (*frac* = 0) gusts for $\theta_g = 0°$ in figure 4.36 are symmetric above and below the airfoil, as could have been predicted on symmetry grounds. The directivity patterns for these two cases are quite different. For the entropy gust there is a strong radiation field in the forward direction. Since the pressure field for the entropy gust with $\theta_g = 0°$ is in phase above and below the airfoil, there is no trailing edge scattering and a secondary pressure lobe is present directly behind the airfoil.

In contrast, for the vorticity gust with $\theta_g = 0°$ the pressure field is out of phase above and below the airfoil. Therefore, even though the field for the leading-edge alone has a significant level directly behind the airfoil, there is a pressure jump associated with this antisymmetric field which cannot persist beyond the trailing edge. The trailing-edge

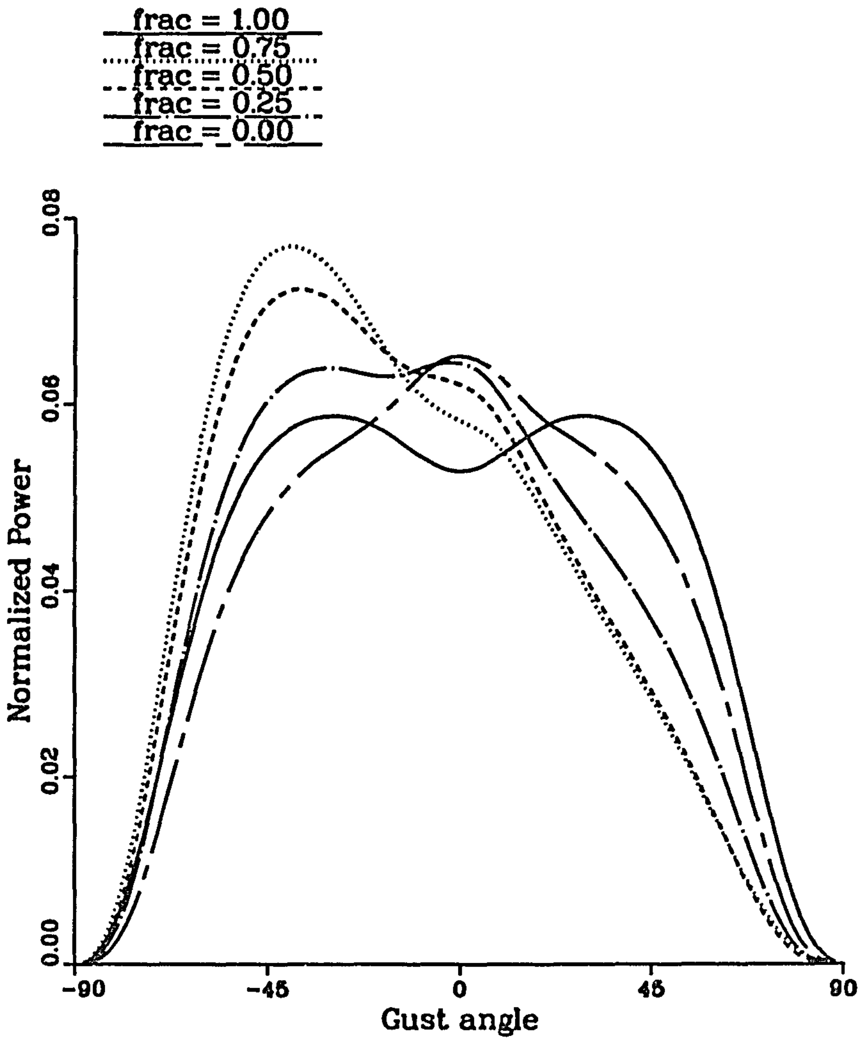


Figure 4.35 Normalized power *vs.* gust angle for $M_\infty$ = 0.80, $k$ = 10, *phased* = 45° and 5% thickness ratio.

scattering which cancels this pressure jump completely removes the radiation in the downstream direction, and the complete directivity pattern for the vorticity gust has its peaks in the cross-stream directions. The directivity pattern for *frac* = 0.5 is fairly close to that for the pure entropy gust, consistent with the fact that the normalized power levels for *frac* = 0 and 0.5 at $\theta_g = 0^0$ in figure 4.32 are nearly equal.

The corresponding directivity patterns for $\theta_g = 45^0$ are shown in figure 4.37. The non-zero gust angle has destroyed the symmetry above and below the airfoil. The pure entropy gust again exbibits a strong pressure field in the forward direction. A secondary lobe is also present, but it is very small and oriented slightly away from the downstream direction. The vorticity gust again has its primary radiation in the cross stream directions, but the radiation in the upstream direction is not insignificant. Trailing-edge scattering has almost completely eliminated radiation in the downstream direction for the vorticity gust. The radiation field for the combined gust case *frac* = 0.5 is weaker than that for either the entropy or vorticity gust, consistent with the normalized power results for $\theta_g = 45^0$ contained in figure 4.32.

To summarize the results of this section, we have found that vortical gusts generate more sound at small values of airfoil thickness and low Mach numbers, while entropic gusts generate higher sound levels for larger values of airfoil thickness, particularly at higher Mach numbers. Combinations of vortical and entropic gusts may generate more or less sound than the sum of the results for the component gusts, depending on the gust angle and on the phase difference between the vortical and entropic components of the gust field.

## 4.6 Thin Airfoil with Parabolic Nose

In Section 3.7, our solution for the airfoil-gust interaction problem was extended to

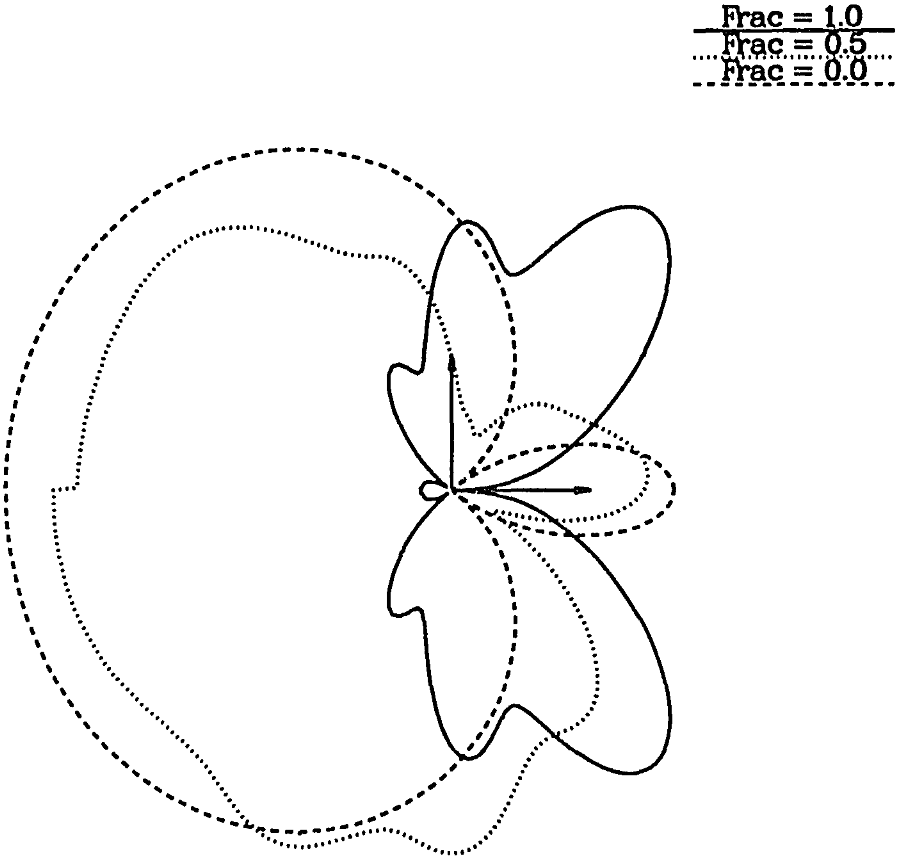


Figure 4.36 Polar plots of the far-field sound pressure for $M_{\infty} = 0.6$, $k = 5$, $\theta_g = 0^o$, *phased* = $0^o$ and 10% thickness ratio.

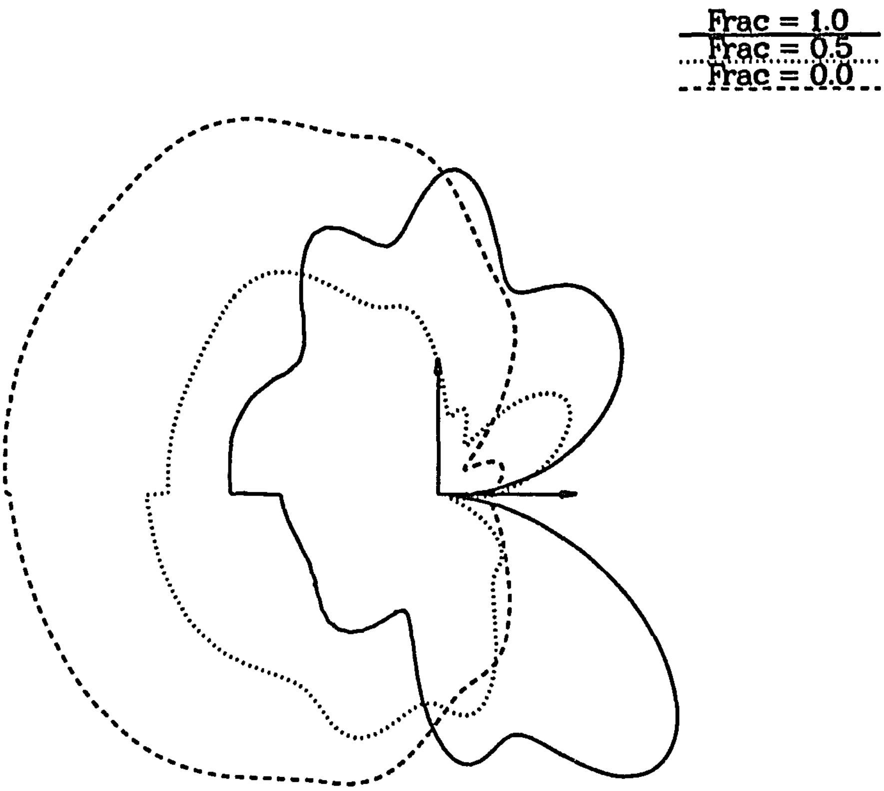


Figure 4.37 Polar plots of the far-field sound pressure for $M_{\infty} = 0.6$, $k = 5$, $\theta_g = 45^{0}$, *phased* = $0^{0}$ and 10% thickness ratio.

the case of a symmetric airfoil with a general thickness distribution. The airfoil is assumed to have a parabolic nose shape, consistent with conventional airfoil designs. This analysis shows that the airfoil thickness enters in the gust interaction problem in two different ways. In the local leading-edge region, the solution is modified through terms that depend on the airfoil nose radius $r_n$. Specifically, the first-order corrections due to airfoil thickness are proportional to $\sqrt{St} = \sqrt{\omega r_n / U_\infty}$. In contrast, for the scattered field from the trailing edge, the phase depends on the global thickness distribution of the airfoil. The solutions in the transition regions also depend on the global thickness distribution. In this section, we present results which illustrate the separate influences of the airfoil nose radius and the overall thickness of the airfoil on the far-field sound.

To examine the relative importance of the airfoil nose radius and the overall thickness of the airfoil, we present results for airfoil shapes which correspond to a superposition of the thickness distributions for a Joukowski airfoil and a double-circular-arc airfoil. The airfoil surface is given by the equation

$$x_2 = \pm \epsilon (1 - x_1/2) \sqrt{2x_1 - x_1^2} \pm \tau x_1 (2 - x_1) \ . \tag{4.14}$$

where $\epsilon$ is the thickness parameter for the Joukowski thickness distribution and $\tau$ the parameter for the double-circular-arc thickness distribution. The airfoil nose radius is independent of $\tau$ and is given by $r_n = \epsilon^2 b$, while the maximum thickness of the airfoil depends on both $\epsilon$ and $\tau$. The velocity potential for this airfoil is

$$F(z) = \frac{\epsilon}{2\beta_\infty}\left[(z-2)\sqrt{z^2-2z} - z^2 + 3z\right] + \frac{\tau}{\pi\beta_\infty}\left[z(2-z)\ln(1-2/z) - 2z\right] \ . \tag{4.15}$$

The far-field sound can be obtained by using Eqs. (3.63) and (3.80), suitably modified according to the discussion in Section 3.7 (see also Section 3.6).

Since the primary sound source is concentrated in the local leading-edge region, it is natural to anticipate that the airfoil nose radius may be a more important parameter than the overall airfoil thickness. To examine this possibility, in figures 4.38 through 4.40 we have presented results for a fixed value of the airfoil nose radius (corresponding to $\epsilon = 0.1$) and three values of the overall thickness (corresponding to $\tau = 0$, 0.05 and 0.1). The three values of $\tau$ correspond to the case of a Joukowski airfoil of 5% thickness ratio and to increases in the maximum thickness of approximately 5% and 10%, respectively. The parameters $M_\infty = 0.8$, $k = 5$ and $frac = 1$ are held fixed in figures 4.38 through 4.40.

In figures 4.38 and 4.39, we have plotted the pressure directivity patterns for $\theta_g = 0^0$ and $45^0$, respectively. First consider the pressure directivity patterns for $\theta_g = 0^0$ (figure 4.38). The additional thickness has slightly weakened the sound radiation in the downstream direction, and has produced slight shifts in the angular locations of the lobes of the directivity pattern. There is very little change in the overall amplitude of the pressure field. The differences between the three cases are remarkably small, particularly when one considers that the variation in the maximum thickness of the airfoil is almost a factor of three. The corresponding results for $\theta_g = 45^0$ are plotted in figure 4.39. Again there are only very minor differences in the pressure directivity patterns for the three values of airfoil thickness.

The corresponding results for the normalized power are plotted as a function of gust angle in figure 4.40. For gust angles less than $45^0$, the additional airfoil thickness has resulted in a decrease in the total power level. However, the decreases are quite small. The case of 10% thickness added corresponds to a tripling of the airfoil thickness, but the change in sound power level is less than 8%. For gust angles larger than $45^0$, the increases in airfoil thickness are seen to have a negligible influence on the normalized power levels.

The results presented in this section provide a convincing demonstration that the airfoil nose radius is the primary parameter which affects the characteristics of the far-field sound. In contrast, the overall thickness of the airfoil has only a very minor effect. Thus, in order to generalize the results of the parametric study presented in previous sections of this chapter, it is only necessary to replace the combination of parameters $\epsilon\sqrt{k}$ by $\sqrt{St} = \sqrt{\omega r_n / U_\infty}$, the square root of the Strouhal number based on the airfoil nose radius as defined by Eq. (3.84). With this generalization, the results presented previously for the case of a Joukowski airfoil then provide a good approximation to the results for a symmetric airfoil of general shape.

This completes our parametric study of the characteristics of the far-field sound. The most important conclusions will be summarized in the next chapter, and some suggestions for future extensions of this work will also be made.

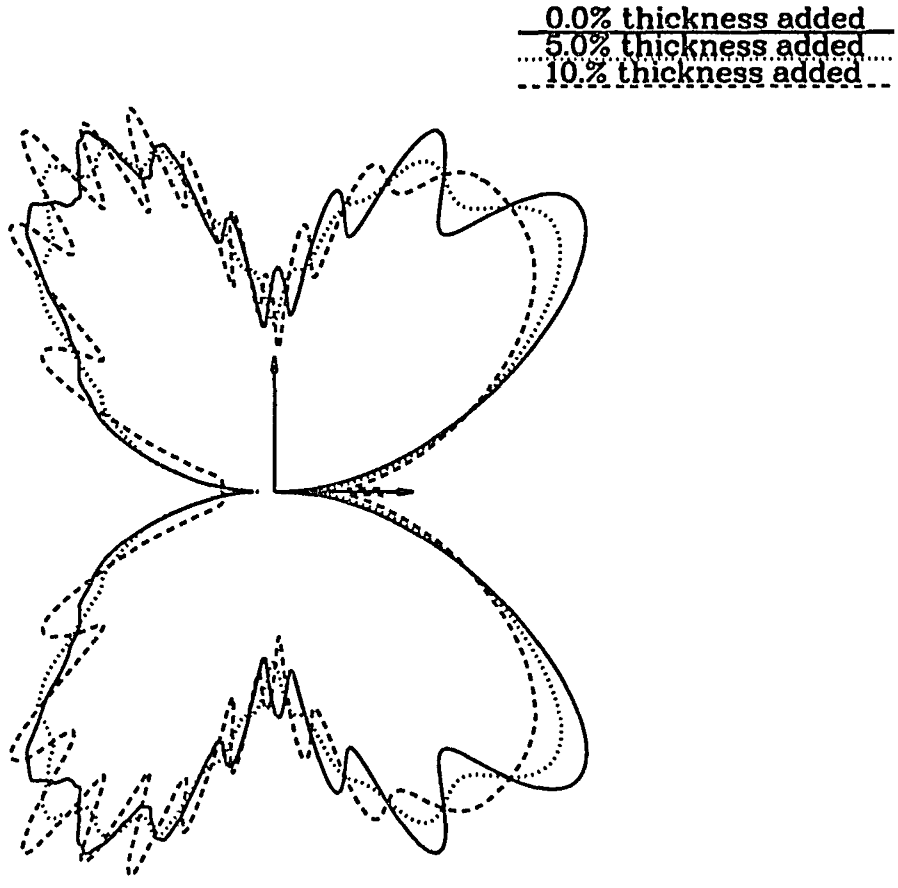


Figure 4.38 Polar plots of the far-field sound pressure for $M_{\infty} = 0.8$, $k = 5$, $\theta_g = 0^o$, $\epsilon = 0.1$ and $frac = 1$.

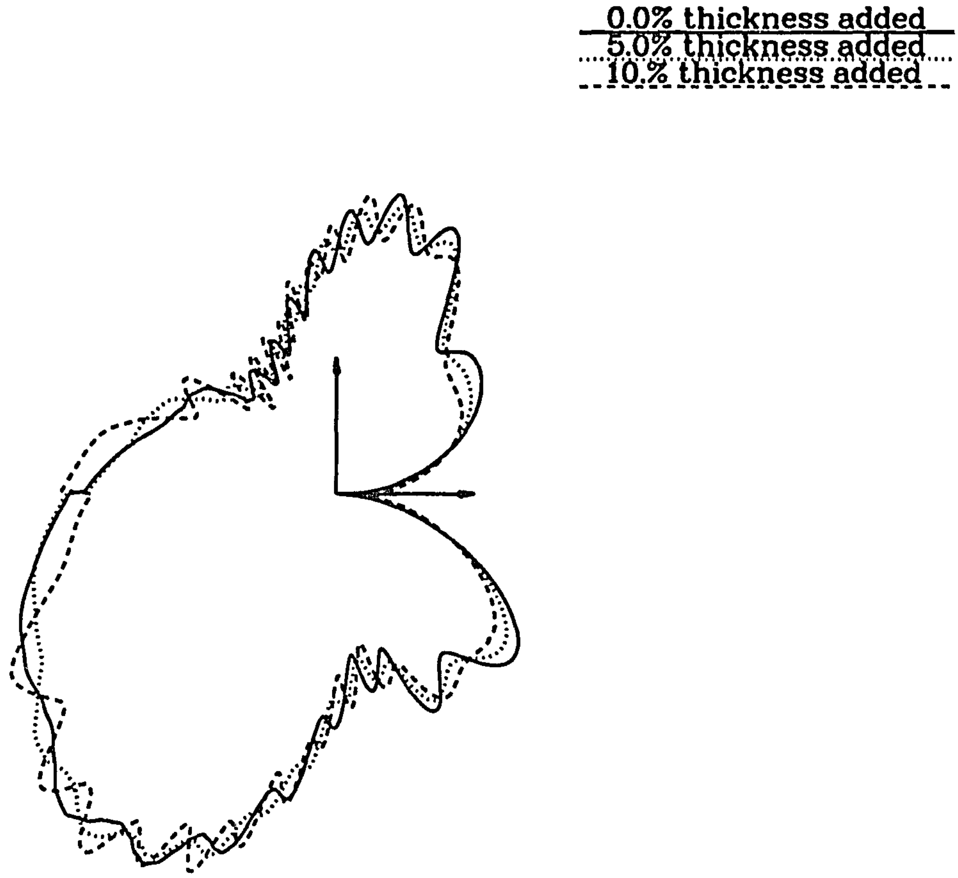


Figure 4.39 Polar plots of the far-field sound pressure for $M_\infty = 0.8$, $k = 5$, $\theta_g = 45^o$, $\epsilon = 0.1$ and $frac = 1$.

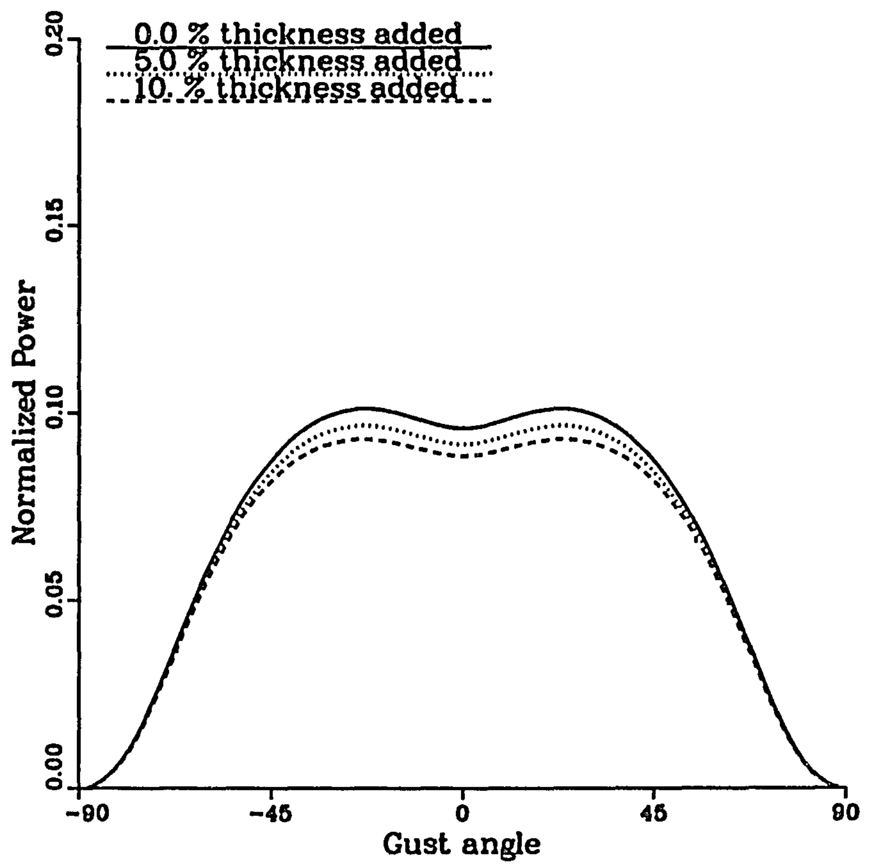


Figure 4.40 Normalized power *vs.* gust angle for $M_\infty = 0.8$, $k = 5$, $\epsilon = 0.1$, *phased* $= 0^0$ and *frac* $= 1$.

# CHAPTER 5

## CONCLUSIONS

In this dissertation, a theory has been developed for the influence of airfoil thickness on sound generated by the interaction of high-frequency convected disturbances with a symmetric airfoil at zero angle of attack. This analysis was based on Goldstein's rapid distortion theory, which is a linearization of the inviscid equations of motion about a non-uniform mean flow. The mean flow was assumed to be two-dimensional and subsonic. A singular perturbation approach based on two asymptotic parameters was utilized. The airfoil thickness to chord ratio was assumed small ($\epsilon << 1$), and the aerodynamic reduced frequency was assumed large ($k = \omega b/U_\infty >> 1$). Here $\omega$ is the frequency of the unsteady disturbance, $b$ is the airfoil semi-chord and $U_\infty$ is the speed of the mean flow far from the airfoil. The product $\epsilon k$ was assumed to be $O(1)$.

Several asymptotic regions were identified in the singular perturbation structure. These are the local leading-edge, leading-edge transition, local trailing-edge, trailing-edge transition and outer regions. Asymptotic solutions which retained $O(\epsilon\sqrt{k},\ 1/\sqrt{k})$ terms relative to the zero-thickness high-frequency solution, but ignored $O(\epsilon,\ \epsilon^2 k,\ 1/k)$ terms, were developed in each asymptotic region. In the geometric far field (many chord lengths away from the airfoil), the forms of the transition solutions are greatly simplified. The method of matched asymptotic expansions was used to join the solutions in the individual regions.

Our solution revealed that essentially all of the sound generation is concentrated in the local regions, with the leading edge being the primary source and the trailing edge a scatterer of the field generated in the local leading-edge region. The interaction of the convected disturbance with the leading edge produces sound through a variety of mechanisms. In addition to the blocking of the undisturbed gust by the airfoil surface (the only sound source for a zero-thickness airfoil), these mechanisms include the blocking of vorticity distortions by the boundary, the interaction of the gust with the non-uniform mean flow and the local scattering of acoustic waves in the leading-edge region.

The interaction of the convected disturbance with the trailing edge, on the other hand, produces negligible sound. This result is a consequence of the Kutta condition at the trailing edge. Due to the steady Kutta condition, the volume source is very small at the trailing edge, and due to the unsteady Kutta condition, the shed vorticity in the wake is essentially a continuation of the bound vorticity in the airfoil and no change in boundary condition is felt by the convected disturbance. Both the bound and shed vorticity in the local trailing-edge region convect at the free-stream speed, and hence generate no pressure fluctuations. Thus, the trailing edge influences the far-field sound only by scattering the acoustic waves generated in the local leading-edge region.

The propagation of the sound generated at the leading edge into the outer region is described by geometric acoustics. This is essentially a cylindrical wave field, with slight ray distortion due to the gradients of the mean flow. The phase of the geometric-acoustic field contains an $O(\epsilon k)$ (i.e., $O(1)$) distortion $\sigma_{l\,1}$ due to the propagation in a nonuniform medium. The asymptotic matching showed that the directivity of the leading-edge ray field is given by

$$L(\theta) = L_0(\theta) + \epsilon\sqrt{k}\left[L_1(\theta) + L_2(\theta) + L_{3p}(\theta) + L_{3c_1}(\theta) + L_{3c_2}(\theta) + L_{3c_3}(\theta)\right] .$$

However, the leading-edge ray field fails to satisfy the boundary condition on the curved surface of the airfoil. An additional asymptotic region, which we called the leading-edge transition region, is needed. The leading-edge transition region lies above and below the airfoil, in a region of angular extent $\theta = O(1/\sqrt{k})$. The solution in this region has much in common with the grazing ray fields that arise in diffraction of a high-frequency wave by a curved surface. This local diffraction field has a complex dependence on radius and azimuthal angle. However, in the geometric far field the expression can be greatly simplified. A uniformly valid expression which contains both the leading-edge ray field and the transition field was obtained. We call this uniformly valid solution the leading-edge acoustic field.

The zero-thickness amplitude $L_0(\theta)$ is antisymmetric with respect to the airfoil surface, and hence in the case of zero thickness the waves above and below the airfoil are $180^0$ out of phase at the trailing edge. This creates a pressure jump along the wake region. A scattered field arises in the local trailing-edge region to cancel the pressure jump due to the leading-edge ray field. This scattering by the trailing edge is the source of additional rays in the outer region. The trailing-edge ray field is similar in form to the leading-edge ray field. It contains an $O(\epsilon k)$ phase distortion $\sigma_{t\,1}$ and its directivity pattern $T_t(\theta)$ is obtained by matching with the local trailing-edge region. The ray description of the trailing-edge outer field fails at shallow angles. For trailing-edge angles of size $\theta_t = O(1/\sqrt{k})$, a transition region exists. The mathematical form of this trailing-edge transition solution is similar to the leading-edge transition solution. Using procedures similar to those for the leading-edge solution, a uniformly valid solution which represents the far-field form of both the trailing-edge ray field and the transition field was found. We call this uniformly valid field the trailing-edge acoustic field.

Characteristics of the acoustic far field were investigated through a series of parametric studies in Chapter 4. Calculations of normalized power showed that the sound field depends strongly on the orientation of the gust wavevector. The velocity fluctuations for a vortical gust are perpendicular to the gust wavevector. A zero gust angle corresponds to a wavevector aligned with the airfoil chord. For a two-dimensional vortical gust, the sound power is a symmetric function of the gust angle due to the symmetry of the airfoil. Moderate amounts of leading-edge thickness actually decrease the sound generation for small gust angles. However, with further increases in the airfoil thickness the sound level rises rapidly. At moderate Mach numbers (e.g., $M_\infty = 0.6$) the maximum sound power level occurs for $\theta_g = 0^0$. However, at higher subsonic Mach numbers (e.g., $M_\infty = 0.8$) the maximum sound power generation shifts toward $\theta_g = 45^0$ as the thickness increases. This shift is caused by the volume quadrupole source. At even higher subsonic Mach numbers (e.g., $M_\infty = 0.90$), the propagation source dominates the solution for small gust angles, while the propagation source and volume quadrupole source are both important for larger gust angles. A brief discussion of the effects of gust three-dimensionality was also presented in Chapter 4.

The behavior of our solution at low Mach numbers was also investigated. Since our theory shows that, for high frequencies ($k >> 1$), the sound generation is concentrated in the local leading-edge region, we considered only the leading-edge acoustic field in the low Mach number limit. Thus, we effectively assumed that the airfoil chord remains long compared to the acoustic wavelength. For $M_\infty << 1$, the term $H_0$ corresponding to the zero-thickness airfoil is a pole of 3/2 order, intermediate between a monopole and dipole. The sound power associated with $H_0$ scales as $M_\infty{}^4$. The functions $H_1$ and $H_2$ are found to have monopole contributions, but these cancel exactly. The residual field due to $H_1$ is a dipole, while that due to $H_2$ is a pole of 3/2 order. Thus, in terms of Mach number scaling, $H_0$ and $H_2$ are of equal importance in the low Mach number limit. The dipole field due to $H_1$ is weaker by one power of $M_\infty$, while the field $H_3$ due to the propagation source is weaker by a factor of $M_\infty{}^2$.

In order to place the above conclusions in perspective, we briefly discuss their relation to the quadrupole source theories of Ffowcs Williams. Recall that Ffowcs Williams and Hawkings (1969a,b) identified "free" quadrupole sources whose sound power scales as $M_\infty^8$. Subsequently, Ffowcs Williams and Hall showed that, at low Mach numbers, the scattering of a quadrupole field by a sharp edge produces a scattered field whose sound power scales as $M_\infty^5$. The conventional scaling for the dipole field associated with the body surface is a sound power proportional to $M_\infty^6$. Thus, Ffowcs Williams and Hall concluded that, at low Mach numbers, the scattered quadrupole field dominates over the dipole field associated with the body surface.

Ffowcs Williams considered three-dimensional sources, while we considered two-dimensional airfoil-gust interactions in the $M_\infty << 1$ limit. For the two-dimensional case, the sound power levels for monopoles, dipoles and quadrupoles scale as $M_\infty^3$, $M_\infty^5$ and $M_\infty^7$, respectively, while for the three-dimensional case each source has its scaling increased by one power of $M_\infty$. The pole of 3/2 order has a sound power that scales as $M_\infty^4$ in the two-dimensional case and $M_\infty^5$ in the three-dimensional case. Thus, Ffowcs Williams' scattered quadrupole is essentially a pole of 3/2 order.

Our theory confirms that scattering of the volume quadrupole field ($H_2$) leads to a pole of 3/2 order in the $M_\infty << 1$ limit, and also provides explicit results for the amplitude of this scattered quadrupole field. However, our theory shows that the sources on the airfoil surface ($H_0$) also sum together to produce a pole of 3/2 order! Thus, in contradiction to the conclusion of Ffowcs Williams and Hall, we have shown that the sources on the airfoil surface and the scattered quadrupole field have the same scaling with respect to Mach number in the limit $M_\infty << 1$. Finally, we point out that our conclusions, and those of Ffowcs Williams and Hall, rest on the assumption that the airfoil chord is long compared to the acoustic wavelength. In cases where the airfoil chord is short compared to the acoustic wavelength the conventional dipole scaling is recovered.

We also compared the generation of sound by entropy gusts to that by vorticity gusts. Our results show that entropic gusts generate higher sound levels than vorticity gusts for thicker airfoils and higher subsonic Mach numbers. For a very thin airfoil or a low Mach number, vortical gusts generate more sound than entropic gusts. In fact, in the $M_\infty << 1$ limit, a pure entropy gust is a dipole source whose sound power scales as $M_\infty{}^5$, while a pure vorticity gust is a source of 3/2 order whose sound power scales as $M_\infty{}^4$. For an isolated vortical or entropic gust, the normalized power is symmetric with respect to gust angle. However, for gusts which contain a combination of vortical and entropic components, the normalized power is highly asymmetric with respect to the gust angle.

Pressure directivity patterns were also presented in Chapter 4. The pressure patterns are strongly influenced by airfoil thickness, in many cases bearing little resemblance to the corresponding results for a zero-thickness airfoil.

The separate influences of the airfoil nose radius and the airfoil total thickness were examined by comparing results for a Joukowski airfoil to results for an airfoil with the same nose radius as the Joukowski airfoil but with different thickness distributions. These comparisons demonstrated that the size of the airfoil nose radius is a much more important parameter than the overall thickness of the airfoil. Thus, the total power level for different shape airfoils can be correlated quite closely by utilizing the nose radius as a correlating parameter. Furthermore, the influence of the aerodynamic reduced frequency can also be absorbed in such a correlation. The parameter which correlates these effects is the Strouhal number based on the airfoil nose radius, $St = \omega r_n / U_\infty$. This may be the most important conclusion of our study.

Regarding future continuations of the work in this dissertation, two important extensions are necessary to properly model turbomachinery noise. The first step is to combine the present theory for the influence of airfoil thickness with Myer's (1987) theory for the influence of airfoil mean loading. Since the mean flow is assumed to be a small perturbation of a uniform flow in the leading-edge region, the effects of incidence angle, camber, and thickness are locally additive. The situation is slightly more complicated in the outer region. The mean-flow disturbance is given by a simple superposition of the three effects, but the complete mean-flow disturbance must be used in calculating the distortion of the geometric-acoustic field. Similar remarks apply for the transition regions along the airfoil surface and behind the airfoil.

The second proposed extension to the work in this dissertation is to consider a cascade of airfoils rather than a single airfoil. The mean flow through the cascade can be obtained by a periodic conformal mapping, hence the variable coefficients appearing in Goldstein's wave equation can be obtained in a straightforward way. The local analysis of the cascade leading-edge regions would be very similar to that developed in this dissertation. The total upstream sound field could then be calculated following the procedure of Envia and Kerschen (1986). They developed an approximate solution for the sound generated by a convected gust interacting with a cascade of swept airfoils. This was done by summing the fields from the infinite row of leading edges using the Dirac delta function to represent the infinite summation inside an integral. The approach of Envia and Kerschen is a high-frequency approximation and should be applicable to the cascade problem.

The calculation of rearward-radiated noise for the cascade is more difficult, since it is necessary to account for the reflection of sound off adjacent airfoils. If surface-curvature effects can be neglected, at least to lowest order, the problem appears tractable. It is encouraging to note that surface-curvature effects arose only in higher-order terms in the present analysis. However, the level of complication produced by surface curvature can only be ascertained by an actual analysis of the problem.

When the described extensions to the model have been made, comparison of our results with experiment will be possible. For example, using empirically-determined rotor-wake velocities as an upstream convected disturbance, we could calculate the far-field sound generated by the rotor-stator interaction in a turbomachine. Considerable experimental data exists for this interaction.

This dissertation, together with Myers' (1987) work, has considerably extended previous analytical work in the area of turbomachinery and propeller noise due to gust interactions. The closed-form solution, together with the parametric study of Chapter 4, provides much new information regarding the specific mechanisms through which airfoil thickness influences the total sound field. The present asymptotic work complements the related numerical solutions developed by Scott and Atassi (1989).

# APPENDIX A

## INTEGRAL-FORM SOLUTION BY THE WIENER-HOPF TECHNIQUE

Some of the mixed boundary-value problems which arise in the analysis of the local leading-edge region contain boundary conditions which are so complicated that the calculation of explicit, closed-form solutions does not seem possible. An alternative approach is to develop the solution in terms of an integral of the complicated function which appears in the boundary condition. In this appendix, the Wiener-Hopf technique is utilized to find an integral-form solution of a mixed boundary-value problem.

Consider the reduced wave equation for the case of harmonic time dependence of form $e^{-i\omega t}$,

$$\frac{\partial^2 E}{\partial \Phi^2} + \frac{\partial^2 E}{\partial \Psi^2} + w^2 E = 0 \quad , \tag{A.1a}$$

with a boundary condition specified on the half plane,

$$\left.\frac{\partial E}{\partial \Psi}\right|_{\substack{\Phi > 0 \\ \Psi = 0}} = d(\Phi) \quad , \tag{A.1b}$$

where $d(\Phi)$ is continuous for all $\Phi > 0$. The function $E(\Phi,\Psi)$ satisfies the radiation condition as $R = \sqrt{\Phi^2 + \Psi^2} \rightarrow \infty$. The radiation condition is enforced by introducing a small positive imaginary part into the constant $w$ and requiring the solution to approach zero as $R \rightarrow \infty$. The small imaginary part is then allowed to approach zero at the end of the analysis.

From the above equations, it can readily be seen that $E(\Phi,\Psi)$ is an anti-symmetric function of $\Psi$. Due to the presence of the Laplacian operator in Eq. (A.1a), the function $E(\Phi,\Psi)$ and its derivatives must be continuous at all points off the half-plane $\Psi = 0$, $\Phi > 0$. Utilizing this continuity property and the anti-symmetry with respect to $\Psi$, we have

$$E(\Phi,0)\Big|_{\Phi < 0} = 0 \ . \tag{A.1c}$$

If either $\partial E/\partial\Psi(\Phi,0)$ or $E(\Phi,0)$ were known for all values of $\Phi$, the solution could be calculated directly by the application of a Fourier transform. However, the present problem is a mixed boundary-value problem, since $\partial E/\partial\Psi(\Phi,0)$ is known for $\Phi > 0$ while $E(\Phi,0)$ is known for $\Phi < 0$. The solution to such problems can be found by utilizing the Wiener-Hopf technique.

To develop the solution, first apply a Fourier transform with respect to $\Phi$,

$$\overline{E}(\lambda,\Psi) = \int_{-\infty}^{\infty} E(\Phi,\Psi)\, e^{i\lambda\Phi}\, d\Phi \ . \tag{A.2}$$

The differential equation is transformed into

$$\frac{\partial^2\overline{E}}{\partial\Psi^2} - (\lambda^2 - w^2)\,\overline{E} = 0 \ . \tag{A.3}$$

Noting the anti-symmetry with respect to $\Psi$ and utilizing the radiation condition to eliminate an exponentially growing contribution, this ordinary differential equation has the solution

$$\overline{E} = -\operatorname{sgn}(\Psi)\, A(\lambda)\, e^{-\sqrt{\lambda^2 - w^2}\,|\Psi|} \ . \tag{A.4}$$

The branch cuts in the $\lambda$ plane are shown in figure 3.3. Taking the inversion of the Fourier transform, the solution has the form

$$E(\Phi,\Psi) = \frac{-\operatorname{sgn}(\Psi)}{2\pi} \int_{-\infty}^{\infty} A(\lambda)\, e^{-i\lambda\Phi - |\Psi|\sqrt{\lambda^2 - w^2}}\, d\lambda \ . \tag{A.5}$$

The solution for $A(\lambda)$ is found utilizing an analytic continuation argument in the complex $\lambda$ plane. The Fourier transform of $E(\Phi,0\pm)$ is

$$\bar{E}(\lambda, 0\pm) = \int_0^\infty E(\Phi, 0\pm)\, e^{i\lambda\Phi}\, d\Phi = -\operatorname{sgn}(\Psi)\, A(\lambda) \quad . \tag{A.6}$$

For values of $\lambda$ in the upper-half $\lambda$ plane, the integral $\int_0^\infty E(\Phi, 0\pm)\, e^{i\lambda\Phi}\, d\Phi$ which defines $A(\lambda)$ converges absolutely, showing that $A(\lambda)$ is analytic in this region. For convenience in the analysis below, a + or - subscript will be introduced to denote the region of analyticity of the various functions which arise in the analysis. These functions are called "plus" and "minus" functions. Accounting for the presence of a small imaginary part in $w$, the plus and minus regions correspond to $\mathrm{Im}(\lambda) > -\mathrm{Im}(w)$ and $\mathrm{Im}(\lambda) < \mathrm{Im}(w)$, respectively. Note that the plus and minus functions have a common region of analyticity, $-\mathrm{Im}(w) < \mathrm{Im}(\lambda) < \mathrm{Im}(w)$.

The Fourier transform $D(\lambda)$ of $\partial E/\partial\Psi(\Phi, 0)$ can be separated into plus and minus functions,

$$D(\lambda) = D_-(\lambda) + D_+(\lambda) \quad , \tag{A.7a}$$

where

$$D_-(\lambda) = \int_{-\infty}^0 \left.\frac{\partial E}{\partial \Psi}\right|_{\Psi = 0} e^{i\lambda\Phi}\, d\Phi \quad , \tag{A.7b}$$

$$D_+(\lambda) = \int_0^\infty d(\Phi)\, e^{i\lambda\Phi}\, d\Phi \quad . \tag{A.7c}$$

Note that $d(\Phi)$ is a specified function and hence $D_+(\lambda)$ is known, but $D_-(\lambda)$ remains unknown at this stage of the analysis. Alternatively, the Fourier transform of $\partial E/\partial\Psi(\Phi, 0)$ can be calculated from Eq. (A.5). Equating these results leads to

$$\sqrt{\lambda^2 - w^2}\, A_+(\lambda) = D_-(\lambda) + D_+(\lambda) \quad . \tag{A.8a}$$

In order to apply the analytic continuation argument, Eq. (A.8a) must be separated into plus and minus functions. The function $\sqrt{\lambda^2 - w^2}$ is easily factored into plus and minus functions. Dividing Eq. (A.8a) by the minus function, we have

$$\left[\sqrt{\lambda + w}\right]_+ A_+(\lambda) = \frac{D_-(\lambda)}{\left[\sqrt{\lambda - w}\right]_-} + \frac{D_+(\lambda)}{\left[\sqrt{\lambda - w}\right]_-} \ . \tag{A.8b}$$

It remains to decompose the last term on the right-hand side of Eq. (A.8b). Assuming that $D_+(\lambda)$ vanishes as $\lambda \rightarrow \pm\infty$, this mixed function can be decomposed into plus and minus functions through an application of the Cauchy integral formula,

$$\frac{D_+(\lambda)}{\left[\sqrt{\lambda - w}\right]_-} = F_-(\lambda) + F_+(\lambda) \tag{A.9a}$$

where

$$F_-(\lambda) = \frac{-1}{2\pi i} \int_{C_2} \frac{D_+(\kappa)}{\sqrt{\kappa - w}} \frac{d\kappa}{\kappa - \lambda} \ , \tag{A.9b}$$

$$F_+(\lambda) = \frac{1}{2\pi i} \int_{C_1} \frac{D_+(\kappa)}{\sqrt{\kappa - w}} \frac{d\kappa}{\kappa - \lambda} \ . \tag{A.9c}$$

and the contours $C_1$, $C_2$ and branch cuts in the $\kappa$-plane are shown in figure A.1. The contours $C_1$ and $C_2$ both lie in the common region of analyticity, $-\mathrm{Im}(w) < \mathrm{Im}(\lambda) < \mathrm{Im}(w)$.

Utilizing Eq. (A.9a) in (A.8b) and rearranging, we have

$$\left[\sqrt{\lambda + w}\right]_+ A_+(\lambda) - F_+(\lambda) = \frac{D_-(\lambda)}{\left[\sqrt{\lambda - w}\right]_-} + F_-(\lambda) \ . \tag{A.10}$$

The left side of Eq. (A.10) is analytic in the upper-half $\lambda$ plane and the right side is analytic in the lower-half $\lambda$ plane. The two sides of the equation are equal in the region $-\mathrm{Im}(w) < \mathrm{Im}(\lambda) < \mathrm{Im}(w)$, and hence by analytic continuation Eq. (A.10) defines a function which is analytic in the entire $\lambda$ plane. Liouville's theorem (Noble 1958) states that the most general entire function is a polynomial, say $J(\lambda)$. To determine this polynomial, the edge

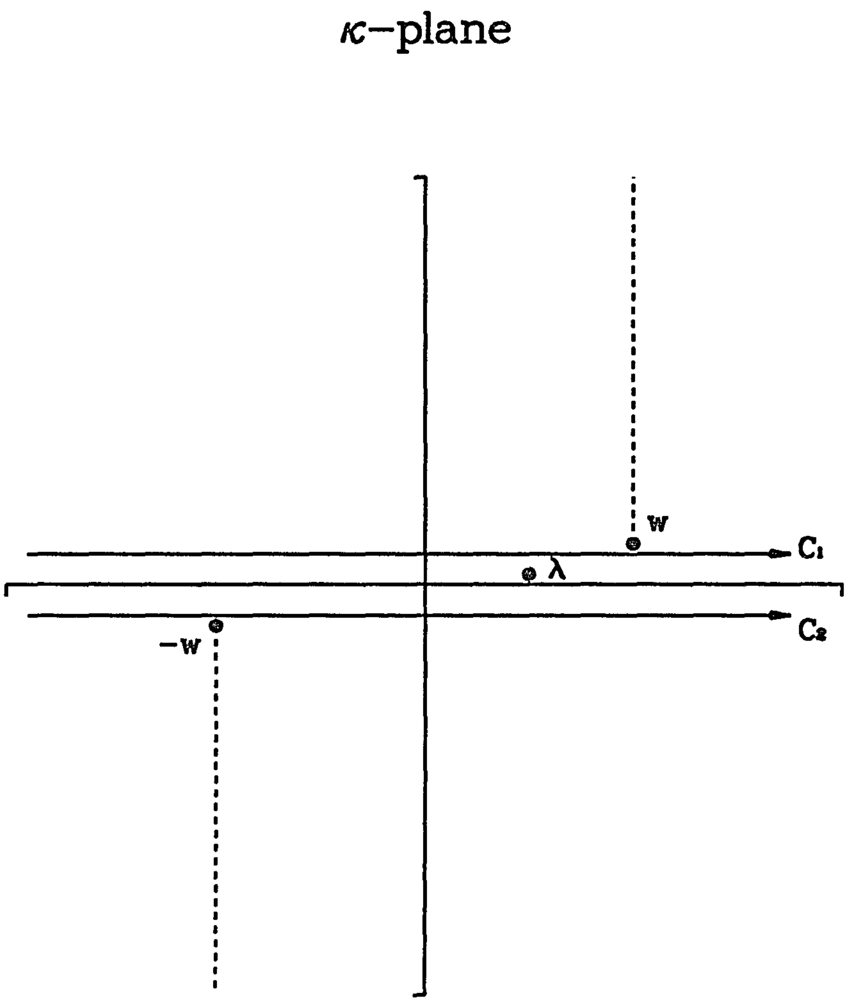


Figure A.1 Branch cuts and contours of integration for Wiener-Hopf split.

conditions must be examined.

The edge conditions define the physically acceptable behavior for the solution in the vicinity of the plate edge, $x = y = 0$. For the present purposes it is sufficient to note that, very near the sharp edge of the plate, Eq. (A1.a) reduces to the Laplace equation. Simple conformal mapping arguments then show that the most singular physically realizable solution has a square root singularity, $E(\Phi,\Psi) \propto \mathrm{Re}\{\sqrt{\Phi+i\Psi}\}$, corresponding to a potential flow around the sharp edge. Thus, we have

$$E(\Phi,0\pm) \quad \propto \quad \pm\,\Phi^{1/2} \qquad \text{as} \qquad \Phi \rightarrow 0+ \ , \tag{A.11a}$$

$$\partial E/\partial\Psi(\Phi,0) \quad \propto \quad \Phi^{-1/2} \qquad \text{as} \qquad \Phi \rightarrow 0- \ . \tag{A.11b}$$

(Note that the behavior of $E$ as $\Phi \rightarrow 0-$ and of $\partial E/\partial\Psi$ as $\Phi \rightarrow 0+$ is specified by Eqs. (A.1c) and (A.1b), respectively.)

Now, a general property of Fourier transforms is that the behavior in physical space for small values of $\Phi$ is related to the behavior in transform space for large values of $\lambda$. Specifically, substituting (A.11a) into (A.6) and assuming that $\lambda$ lies in the upper half-plane, the integral can be evaluated to show that

$$A_+(\lambda) \;\propto\; \lambda^{-3/2} \qquad \text{as} \qquad \lambda \rightarrow \infty\ ,\ \ (\mathrm{Im}(\lambda) > 0)\ . \tag{A.12a}$$

Similarly, substituting (A.11b) into (A.7b) and integrating, one finds that

$$D_-(\lambda) \;\propto\; \lambda^{-1/2} \qquad \text{as} \qquad \lambda \rightarrow \infty\ ,\ \ (\mathrm{Im}(\lambda) < 0)\ . \tag{A.12b}$$

These estimates are sufficient to show that the terms in (A.10) involving $A_+(\lambda)$ and $D_-(\lambda)$ approach zero as $\lambda \rightarrow \infty$ in the respective half-planes.

Finally, consider the behavior of $F_-(\lambda)$ and $F_+(\lambda)$ as $\lambda \rightarrow \infty$. If $D_+(\kappa)$ in (A.9b,c) is integrable at the origin and decays more rapidly than $\kappa^{-1/2}$ as $\kappa \to \infty$, it is easy to show that $F_-(\lambda)$ and $F_+(\lambda)$ are proportional to $\lambda^{-1}$ as $\lambda \to \infty$. Then all terms in (A.10) approach zero as $\lambda \to \infty$. The only polynomial having this behavior is the trivial function, $J(\lambda) = 0$. Thus, both sides of (A.10) are identically equal to zero, and we can solve for $A_+(\lambda)$ and $D_-(\lambda)$,

$$A_+(\lambda) = \frac{F_+(\lambda)}{\sqrt{\lambda + w}}, \qquad D_-(\lambda) = -\sqrt{\lambda - w}\, F_-(\lambda) . \tag{A.13a,b}$$

Thus the solution is

$$E(\Phi,\Psi) = \frac{-\operatorname{sgn}(\Psi)}{2\pi} \int_{-\infty}^{\infty} F_+(\lambda) \frac{e^{-i\lambda\Phi - |\Psi|\sqrt{\lambda^2 - w^2}}}{\sqrt{\lambda + w}}\, d\lambda \tag{A.14a}$$

where

$$F_+(\lambda) = \frac{1}{2\pi i} \int_{C_1} \frac{d\kappa}{\sqrt{\kappa - w}\,(\kappa - \lambda)} \int_0^{\infty} dx\, d(x)\, e^{i\kappa x} . \tag{A.14b}$$

The sequence of integrations over $x$ and $\kappa$ can be formally interchanged. Noting that only positive values of $x$ are of interest, the integral over $\kappa$ can be evaluated in closed form by closing the contour in the upper half-plane. The result is

$$F_+(\lambda) = \int_0^{\infty} \frac{d(x)\, e^{i\lambda x}}{\sqrt{\lambda - w}} \operatorname{erf}(e^{i\pi/4}\sqrt{(\lambda - w)x})\, dx . \tag{A.14c}$$

Finally, Eq. (A.14c) is substituted into (A.14a). For determination of the far-field sound, only the asymptotic behavior of the local leading-edge solution for $R = \sqrt{\Phi^2 + \Psi^2} >> 1$ is required. Again we interchange the order of the integrations over $x$ and $\lambda$. Assuming suitable behavior of the functions involved, the integral over $\lambda$ can then be evaluated by the method of steepest descent (see Appendix B). The leading-order term of the asymptotic expansion for $R >> 1$ is found as

$$E(\Phi,\Psi) \sim \frac{-\operatorname{sgn}(\Psi)\, e^{i\pi/4}}{\sqrt{2\pi w}} \frac{e^{iwR}}{\sqrt{R}} \int_0^{\infty} d(x)\, e^{-iw\cos\theta x} \operatorname{erf}(e^{-i\pi/4}\sqrt{w(1+\cos\theta)x})\, dx \qquad \text{(A.15)}$$

where $\theta = \tan^{-1}\Psi/\Phi$ .

In deriving Eqs. (A.14) and (A.15), it was assumed following Eqs. (A.12) that $D_+(\lambda)$ approached zero faster than $\lambda^{-1/2}$ as $\lambda \to \infty$. From Eq. (A.7c), one can see that this corresponds to $d(\Phi)$ being less singular than $x^{-1/2}$ as $x \to 0+$. However, the criterion for convergence of the integral (A.14c) is less stringent, requiring only that $d(x)$ be less singular than $x^{-3/2}$. In Section 3.1.4, Equation (A.14c) is utilized to calculate the solution for $H_{3c_2}$ for which $d(\Phi) \propto e^{iw\Phi}/\Phi$. It can be verified by direct substitution that the solution (3.30a,c) satisfies the boundary condition corresponding to Eq. (3.28c).

# APPENDIX B

## UNIFORM ASYMPTOTIC EXPANSIONS BY VAN DER WAERDEN'S METHOD

For matching with the outer and transition regions, asymptotic expansions of the solutions in the local leading-edge and trailing-edge regions for $R >> 1$ and $R_t >> 1$, respectively, are required. In most cases, these expansions can be calculated by the method of steepest descent (Bender and Orszag 1978). Consider an integral of form

$$F(R,\theta) = \int_{-\infty}^{\infty} A(\lambda)\, e^{-Rg(\lambda;\theta)}\, d\lambda \tag{B.1a}$$

where

$$g(\lambda;\theta) = i\,\lambda\cos\theta + |\sin\theta|\,\sqrt{\lambda^2 - w^2}\ . \tag{B.1b}$$

In the method of steepest descent, the original path of integration along the real $\lambda$ axis is deformed onto the steepest descent path, which passes through the saddle point of the exponent function $g(\lambda)$ at $\lambda_0 = -w\cos\theta$ and along which $\mathrm{Im}(g(\lambda))$ is constant. Closed-form expressions for the steepest descent path can be found in Appendix B of Myers (1987). The steepest descent path for a typical case, $\theta = 45^o$, is plotted in figure B.1. As $R$ becomes large, the integral is dominated by the region surrounding the saddle point and local approximations to $A(\lambda)$ and $g(\lambda)$ can be made. Evaluating the resulting integral, the leading term of the $R >> 1$ asymptotic expansion is

$$F(R,\theta) \sim \sqrt{2\pi w}\, A(\lambda_0)\, |\sin\theta|\, \frac{e^{iwR - i\pi/4}}{\sqrt{R}}\,. \tag{B.2}$$

In deriving Eq. (B.2), $A(\lambda)$ is assumed to be analytic in the neighborhood of the saddle point $\lambda = \lambda_0$. In fact, higher order terms in the asymptotic expansion would be found by considering additional terms in the Taylor series. Thus, it can be seen that the method of steepest descent fails for observation angles where the saddle point at $\lambda_0 = -w\cos\theta$ is coincident with or in close proximity to a singular point of $A(\lambda)$. This situation occurs for two integrals which arise in the present analysis, Eqs. (3.30a,c) and (3.71a).

In this appendix, a generalization of the steepest descent method due to Van Der Waerden (1950) is utilized to derive asymptotic expansions for these integrals which are uniformly valid for all values of $\theta$. The basic approach is to separate the original integral into two integrals. One of these contains the singularity of $A(\lambda)$ in a simplified form so that the resulting integral can be evaluated exactly. The other integral contains a modified form of $A(\lambda)$ which is analytic for all values of $\lambda = \lambda_0$, so that the method of steepest descent can be applied directly.

First consider the integral which arises in Eq. (3.30a,c),

$$F_1(\Phi,\Psi) = \int_{-\infty}^{\infty} \frac{e^{-Rg(\lambda;\theta)}}{\sqrt{\lambda^2 - w^2}} \ln\left[\frac{\sqrt{2w} + i\sqrt{\lambda - w}}{\sqrt{2w} - i\sqrt{\lambda - w}}\right] d\lambda \ . \tag{B.3}$$

The function $A(\lambda)$ in Eq. (B.3) has a logarithmic singularity at $\lambda = -w$. Thus for this integral the standard method of steepest descent fails for angles near $\theta = 0$ and $2\pi$. To apply Van Der Waerden's method, we begin by introducing a change of variable,

$$s^2 = g(\lambda;\theta) - g(\lambda_0;\theta) \tag{B.4a}$$

where $g(\lambda_0;\theta) = -iw$. The inverse transformation is

$$\lambda = -i\cos\theta\,(s^2 - i\,w) \pm s\,|\sin\theta|\,\sqrt{s^2 - 2\,i\,w} \ . \tag{B.4b}$$

The plus sign for the transformation is selected, which maps the steepest descent path onto the real axis in the $s$ plane. Utilizing Eqs. (B.4) to express the integral (B.3) in terms of $s$, we obtain

$$F_1 = e^{iwR} \int_{-\infty}^{\infty} \mathcal{A}(s)\, e^{-Rs^2}\, ds \tag{B.5a}$$

where

$$\mathcal{A}(s) = \frac{2}{\sqrt{s^2-2iw}} \ln\left[\frac{\sqrt{2w} + i\sqrt{-i\cos\theta(s^2-iw)+s\left|\sin\theta\right|\sqrt{s^2-2iw}-w}}{\sqrt{2w} - i\sqrt{-i\cos\theta(s^2-iw)+s\left|\sin\theta\right|\sqrt{s^2-2iw}-w}}\right] . \tag{B.5b}$$

The transformation has simplified the exponential function in the integral, the saddle point in the $\lambda$ plane at $\lambda_0 = -w\cos\theta$ having been mapped to the origin of the $s$ plane. The branch points of $\sqrt{\lambda^2 - w^2}$ in the $\lambda$ plane disappear in the $s$ plane, essentially having been unfolded by the transformation. Although it is not immediately apparent, the denominator of the logarithmic term in Eq. (B.5b) contains a branch point at $s_1 = -e^{i\pi/4}\sqrt{w(1-\cos\theta)}$. This is the image of the logarithmic branch point at $\lambda = -w$ in the $\lambda$ plane. The location of this logarithmic branch point, which is a function of observation angle, approaches the saddle point as $\theta$ approaches 0 (or $2\pi$). Since the numerator of the logarithmic term in (B.5b) is never zero in the first Riemann sheet of the $s$ plane, there is no logarithmic branch point associated with this expression. Finally, the transformation has introduced two new branch points into the $s$ plane at $s = \pm e^{i\pi/4}\sqrt{2w}$. The singularity structure in the $s$ plane is illustrated in figure B.1.

The failure of the method of steepest descent arises due to the coalescence of the logarithmic branch point at $s = s_1$ with the saddle point at $s = 0$. To isolate the contribution due to the logarithmic singularity, we expand $\mathcal{A}(s)$ in the vicinity of $s = s_1$,

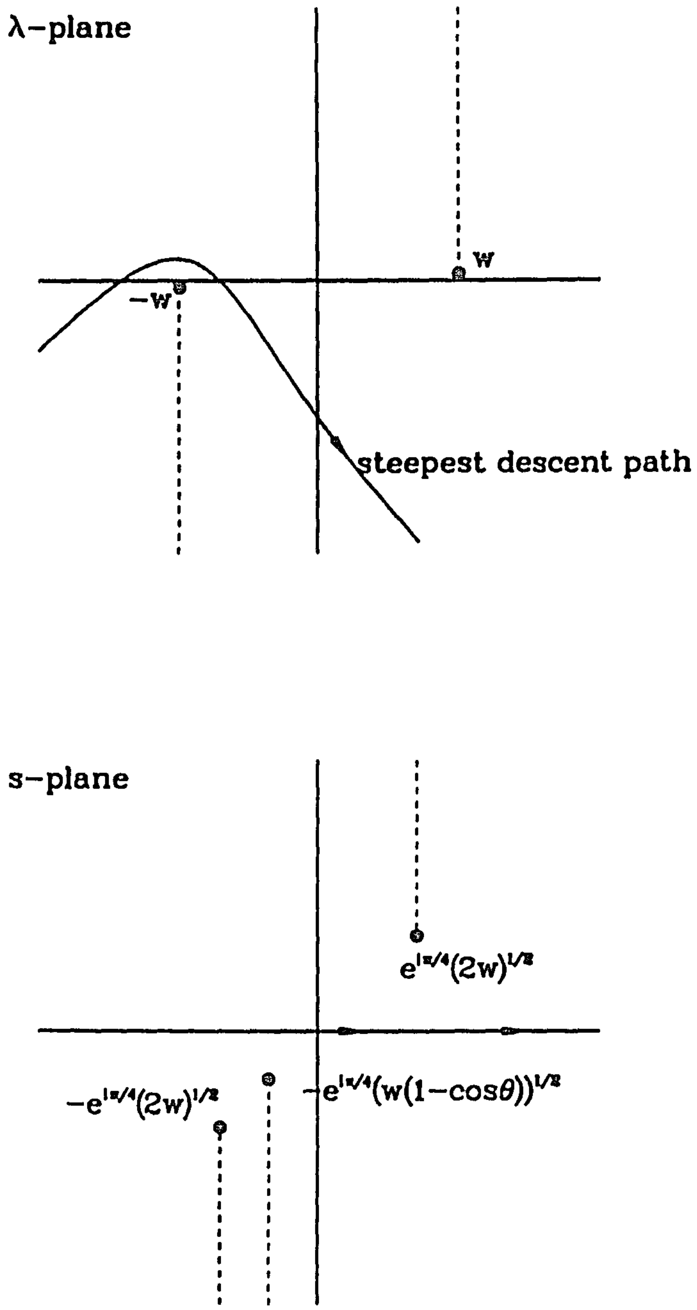


Figure B.1 Singularities and steepest descent paths for the $\lambda$ plane and the $s$ plane.

$$\mathcal{A}(s) = \frac{4 \ln(s - s_1)}{\sqrt{s_1^2 - 2iw}} + \text{constant} + \mathcal{O}(s - s_1) \ . \tag{B.6}$$

Thus, the function

$$\mathcal{A}_1(s) = \mathcal{A}(s) - \frac{4 \ln(s - s_1)}{\sqrt{s_1^2 - 2iw}} \tag{B.7}$$

is analytic at $s = 0$ for all values of $\theta$. Substituting into Eq. (B.5), we have

$$F_1 = e^{iwR} \left[ \int_{-\infty}^{\infty} \mathcal{A}_1(s)\, e^{-Rs^2}\, ds + \frac{4}{\sqrt{s_1^2 - 2iw}} \int_{-\infty}^{\infty} \ln(s - s_1)\, e^{-Rs^2}\, ds \right] . \tag{B.8}$$

The first integral can then be evaluated by the method of steepest descent, while the second integral can be simplified slightly by absorbing a factor of $\sqrt{R}$ in the definition of $s$. The final result for the $R >> 1$ asymptotic expansion of $F_1$ which is uniformly valid in $\theta$ is

$$F_1(R,\theta) \sim \frac{\sqrt{2\pi}\, e^{i\pi/4}}{\sqrt{w}} \left\{ \ln\left[\frac{\sqrt{2}+\sqrt{1+\cos\theta}}{\sqrt{2}-\sqrt{1+\cos\theta}}\right] + \frac{\sqrt{2}\ln(1-\cos\theta)}{\sqrt{1+\cos\theta}} + \frac{i\pi + 2\ln(w)}{\sqrt{2}\sqrt{1+\cos\theta}} \right\} \frac{e^{iwR}}{\sqrt{R}}$$
$$- \frac{4e^{i\pi/4}}{\sqrt{w}\sqrt{1+\cos\theta}} \left\{ \int_{-\infty}^{\infty} \ln(s + e^{i\pi/4}\sqrt{w(1-\cos\theta)R})\, e^{-s^2}\, ds - \frac{\sqrt{\pi}}{2}\ln(R) \right\} \frac{e^{iwR}}{\sqrt{R}} \tag{B.9}$$

where the $\ln(R)$ term in the second line has arisen from the change of variable in the integral. The remaining integral in Eq. (B.9) must be evaluated numerically when the product $R(1-\cos\theta)$ is $\mathcal{O}(1)$ or small. For large values of $R(1-\cos\theta)$, the integral can be evaluated asymptotically and the result for $F_1(R,\theta)$ reverts to that found by a standard application of the method of steepest descent.

The second integral arising in the present study which requires the use of Van Der Waerden's method to find a uniform asymptotic expansion is

$$F_2(\Phi,\Psi) = \int_{-\infty}^{\infty} \frac{e^{-Rg(\lambda;\theta)}}{(\lambda+w)\sqrt{\lambda-w}}\, d\lambda \ . \tag{B.10}$$

The integrand for $F_2$ has a pole at $\lambda = -w$, whereas the integrand for $F_1$ had a logarithmic branch point at this location. The method of steepest descent again fails for values of $\theta$ near 0 or $2\pi$ due to the coalescence of the saddle point and the pole. Following the same procedure as above, the variable of integration is transformed to the s plane and the pole singularity is extracted from the coefficient function $\mathscr{A}(s)$ and treated separately. Thus we obtain

$$F_2 = e^{iwR}\int_{-\infty}^{\infty}\left\{\frac{2\left[-i\,s\cos\theta + (s^2 - i\,w)\,|\sin\theta|\,/\sqrt{s^2-2iw}\right]}{\left[-is^2\cos\theta+w(1-\cos\theta)+s\,|\sin\theta|\sqrt{s^2-2iw}\right]\sqrt{s|\sin\theta|\sqrt{s^2-2iw}-i(s^2-iw)\cos\theta-w}}\right.$$
$$\left. - \frac{\sqrt{2}\,i}{\sqrt{w}\,(s - s_1)}\right\} e^{-Rs^2}\, ds \ + \ e^{iwR}\int_{-\infty}^{\infty} \frac{\sqrt{2}\,i}{\sqrt{w}\,(s - s_1)}\, e^{-Rs^2}\, ds \ . \tag{B.11}$$

The first integral can be evaluated asymptotically by the method of steepest descent and the second integral can be evaluated exactly. It turns out that for the first integral the leading-order term of the coefficient function vanishes at $s = 0$, showing that the integral is of $O(R^{-3/2})$ for large $R$ and hence negligible compared to the contribution from the second integral. The leading-order term of the uniform asymptotic expansion is then given by the second integral,

$$F_2 \sim \frac{\sqrt{2}\,\pi\, e^{iwR\cos\theta}}{\sqrt{w}}\left[1 - \mathrm{erf}\left(e^{-i\pi/4}\sqrt{w(1-\cos\theta)R}\right)\right] \ . \tag{B.12}$$

# APPENDIX C

## EXPANSIONS OF INTEGRALS FOR SMALL ARGUMENT

To examine the behavior of the solution in the local leading-edge region for $R << 1$, integrals arising from Fourier-transform inversions must be expanded in this limit. These expansions are developed in this appendix.

The basic approach we utilize is to apply contour integration in the complex $\lambda$ plane, which results in pole contributions and in line integrals arising from branch cuts. Denoting distance along the branch cut by the variable $\rho$, the line integrals extend over the semi-infinite domain $0 \leq \rho \leq \infty$. The integrands for these line integrals are then expanded for small values of R. These expansions have a singular structure, involving a local region in which $\rho = O(1)$ and a global region in which $\rho = O(1/R)$. The expansions of the integrand in the local and global regions are then combined into a composite expansion which is uniformly valid for all values of $\rho$. The composite expansion is then integrated to determine the $R << 1$ expansion for the integral. The procedure is first illustrated in detail for the expansion of $H_0$. Following that, the results needed to determine the $R << 1$ expansion of $H_{3p}$ are presented.

Introducing polar coordinates into Eqs. (3.9), we have

$$H_0(R,\theta) = \frac{-A_n \operatorname{sgn}(\Psi)}{\beta_\infty 2\pi\sqrt{\delta+w}} \int_{-\infty}^{\infty} \frac{e^{R(-i\lambda\cos\theta - |\sin\theta|\sqrt{\lambda^2-w^2})}}{(\lambda+\delta)\sqrt{\lambda+w}}\, d\lambda \tag{C.1}$$

where the path of integration is along the real axis and the branch cuts in the $\lambda$ plane are shown in figure 3.3. The expansion of the integral for $R << 1$ is desired. For convenience, only the case $\cos\theta > 0$ is discussed. The procedure to obtain the expansion for $\cos\theta < 0$ is very similar. For $\cos\theta > 0$, the integration contour can be closed in the lower half of the $\lambda$

plane, resulting in a residue from the pole at $\lambda = -\delta$ and an integral along the branch cut extending from $\lambda = -w$. Upon combining the contributions from the left and right sides of the branch cut, we obtain

$$H_0(R,\theta) = \frac{A_n\ \mathrm{sgn}(\Psi)}{\beta_\infty \pi\sqrt{\delta+w}}\left\{ \frac{\pi\, e^{R(i\delta\cos\theta - |\sin\theta|\sqrt{\delta^2-w^2})}}{\sqrt{\delta-w}} - e^{iwR\cos\theta + i\pi/4}\, I_1(R,\theta)\right\} \tag{C.2}$$

where

$$I_1(R,\theta) = \int_0^\infty \frac{e^{-\rho R\cos\theta}\cos(R|\sin\theta|\rho\sqrt{1-i2w/\rho})}{(\rho + i(\delta-w))\sqrt{\rho}}\,d\rho\ . \tag{C.3}$$

We next develop a composite expansion for the integrand of $I_1$ in the limit $R << 1$. It proves convenient in the final integration to leave the function $e^{-\rho R\cos\theta}$ unexpanded, and to develop a composite expansion for

$$\frac{\cos(R|\sin\theta|\rho\sqrt{1-i2w/\rho})}{(\rho + i(\delta-w))\sqrt{\rho}}\ . \tag{C.4}$$

In the local region where $\rho = O(1)$, this function can be expanded as

$$\frac{1}{(\rho + i(\delta-w))\sqrt{\rho}} + O(R)\ . \tag{C.5a}$$

However, this expansion becomes invalid for values of $\rho$ of $O(1/R)$. Introducing the global variable, $\rho^* = \rho R$, the expansion of this function for small $R$ takes the form

$$\frac{\cos(\rho^*|\sin\theta|)}{\rho^{*3/2}}R^{3/2} + O(R^{5/2})\ . \tag{C.5b}$$

An additive composite expansion (Van Dyke 1975) is formed by summing (C.5a) and (C.5b) and subtracting the common term. The common term is found either by expanding (C.5a) in the global variable $\rho^*$ or by expanding (C.5b) in the local variable $\rho$. The common term is

$$\frac{1}{\rho^{*\,3/2}} R^{3/2} \ . \tag{C.5c}$$

Combining (C.5a,b,c), the composite expansion for the integrand is given by

$$\frac{1}{(\rho + i(\delta - w))\sqrt{\rho}} + \frac{\cos(\rho^* |\sin\theta|)}{\rho^{*\,3/2}} R^{3/2} - \frac{1}{\rho^{*\,3/2}} R^{3/2} \ . \tag{C.6}$$

Note that both the global and common term contributions to the composite expansion for the integrand have non-integrable singularities at the origin. However, these singularities cancel and hence the composite expansion is integrable. Substituting the composite expansion into Eq. (C.3) and replacing $\rho$ by $\rho^*/R$ for convenience, $I_1(R,\theta)$ can then be approximated as

$$I_1 \sim \int_0^\infty \frac{e^{-\rho R \cos\theta}\, d\rho}{(\rho + i(\delta - w))\sqrt{\rho}} + \int_0^\infty \frac{e^{-\rho^* \cos\theta}\left[\cos(\rho^* |\sin\theta|) - 1\right]}{\rho^{*\,3/2}} R^{1/2}\, d\rho^* \ . \tag{C.7}$$

Evaluating the integrals and neglecting higher-order terms, we obtain

$$I_1(R,\theta) \sim \frac{\pi\, e^{-i\pi/4}}{\sqrt{\delta - w}} - 2\sqrt{\pi}\, \mathrm{sgn}(\Psi) \cos\theta/2 \sqrt{R} + \text{H.O.T.} \ . \tag{C.8}$$

Combining Eq. (C.8) with the residue contribution in Eq. (C.2) and keeping only the leading-order term for small $R$, we find

$$H_0(R,\theta) \sim \frac{2 A_n\, e^{i\pi/4}}{\beta_\infty \sqrt{\pi} \sqrt{\delta + w}} \sqrt{R} \cos\theta/2 + \text{H.O.T.} \qquad \text{for} \qquad R \ll 1 \ . \tag{C.9}$$

A similar procedure is utilized to calculate the $R \ll 1$ behavior of the particular solution $H_{3p}$. The integrals that appear in Eq. (3.22c) for $H_{3p}$ are

$$I_2(R,\theta) = \int_{-\infty}^{\infty} \sqrt{\lambda - w}\,(\lambda+\delta)\left[\frac{1}{(\lambda+\delta)^2} - \frac{(\gamma+1)M_\infty^{\;4}}{2\beta_\infty^{\;4}\,w^2}\right] e^{a(\lambda,R,\theta)}\,d\lambda\ , \tag{C.10a}$$

$$I_3(R,\theta) = \int_{-\infty}^{\infty} \frac{\lambda(\lambda+\delta)}{\sqrt{\lambda+w}}\left[\frac{1}{(\lambda+\delta)^2} - \frac{(\gamma+1)M_\infty^{\;4}}{2\beta_\infty^{\;4}\,w^2}\right] e^{a(\lambda,R,\theta)}\,d\lambda\ , \tag{C.10b}$$

$$I_4(R,\theta) = \int_{-\infty}^{\infty} \sqrt{\lambda - w}\; e^{a(\lambda,R,\theta)}\,d\lambda\ , \tag{C.10c}$$

$$I_5(R,\theta) = \int_{-\infty}^{\infty} \frac{\lambda}{\sqrt{\lambda+w}}\, e^{a(\lambda,R,\theta)}\,d\lambda \tag{C.10d}$$

where $a(\lambda,R,\theta) = -R(i\lambda\cos\theta + |\sin\theta|\sqrt{\lambda^2 - w^2})$. Assuming that $\cos\theta > 0$ and closing the integral in the lower half of the $\lambda$ plane, residue contributions arise from poles at $\lambda = -\delta$ and integrals arise from the deformation around the branch cut extending from $\lambda = -w$. The integrals can then be expressed as

$$I_2(R,\theta) = -2\,\pi\,\sqrt{\lambda+w}\; e^{R\,(i\,\delta\cos\theta\,-\,|\sin\theta|\sqrt{\delta^2-w^2})}$$

$$+\,2\,e^{i\,w\,R\cos\theta\,+\,i\,\pi/4}\left[I_{21}(R,\theta) + \frac{(\gamma+1)M_\infty^{\;4}}{2\,\beta_\infty^{\;4}\,w^2}\,I_{22}(R,\theta)\right]\ , \tag{C.11a}$$

$$I_3(R,\theta) = \frac{2\pi\delta}{\sqrt{\delta - w}}\, e^{R\,(i\,\delta\cos\theta\,-\,|\sin\theta|\sqrt{\delta^2-w^2})}$$

$$+\,2\,e^{i\,w\,R\cos\theta\,-\,i\,\pi/4}\left[I_{31}(R,\theta) + \frac{(\gamma+1)M_\infty^{\;4}}{2\,\beta_\infty^{\;4}\,w^2}\,I_{32}(R,\theta)\right]\ , \tag{C.11b}$$

$$I_4(R,\theta) = 2\,e^{i\,w\,R\cos\theta\,-\,i\,\pi/4}\,I_{41}(R,\theta)\ , \tag{C.11c}$$

$$I_5(R,\theta) = -\,2\,e^{i\,w\,R\cos\theta\,+\,i\,\pi/4}\,I_{51}(R,\theta) \tag{C.11d}$$

where

$$I_{21}(R,\theta) = \int_0^{\infty} \frac{\sqrt{\rho - i2\,w}}{\rho + i(\delta - w)}\, e^{-\rho R \cos\theta} \sin(R\,|\sin\theta|\,\rho\sqrt{1 - i2w/\rho})\, d\rho\ , \tag{C.12a}$$

$$I_{22}(R,\theta) = \int_0^{\infty} (\rho + i(\delta - w))\, \sqrt{\rho - i2w}\, e^{-\rho R \cos\theta} \sin(R\,|\sin\theta|\,\rho\sqrt{1 - i2w/\rho})\, d\rho\ , \tag{C.12b}$$

$$I_{31}(R,\theta) = \int_0^{\infty} \frac{\rho - i\,w}{\sqrt{\rho}\,(\rho + i(\delta - w))}\, e^{-\rho R \cos\theta} \cos(R\,|\sin\theta|\,\rho\sqrt{1 - i2w/\rho})\, d\rho\ , \tag{C.12c}$$

$$I_{32}(R,\theta) = \int_0^{\infty} \frac{(\rho - iw)(\rho + i(\delta - w))}{\sqrt{\rho}}\, e^{-\rho R \cos\theta} \cos(R\,|\sin\theta|\,\rho\sqrt{1 - i2w/\rho})\, d\rho\ , \tag{C.12d}$$

$$I_{41}(R,\theta) = \int_0^{\infty} \sqrt{\rho - i2w}\, e^{-\rho R \cos\theta} \sin(R\,|\sin\theta|\,\rho\sqrt{1 - i2w/\rho})\, d\rho\ , \tag{C.12e}$$

$$I_{51}(R,\theta) = \int_0^{\infty} \frac{\rho - iw}{\sqrt{\rho}}\, e^{-\rho R \cos\theta} \cos(R\,|\sin\theta|\,\rho\sqrt{1 - i2w/\rho})\, d\rho\ . \tag{C.12f}$$

Asymptotic expansions for the integrals defined by Eqs. (C.12) in the limit $R << 1$ are calculated by combining local and global expansions to form composite expansions for the integrands, and then integrating the resulting expressions. As for $H_0$, care must be taken to group terms appropriately to avoid non-integrable singularities as $\rho^* \to 0$ or $\infty$. Substituting the results into Eqs. (C.11) and expanding for $R << 1$, we obtain the asymptotic expansions

$$\begin{aligned} I_2(R,\theta) \sim\ & -2\pi\sqrt{\lambda + w}\, e^{R\,(i\delta\cos\theta - |\sin\theta|\sqrt{\delta^2 - w^2})} + 2\, e^{iwR\cos\theta + i\pi/4}\sqrt{\pi}\Bigg\{ \frac{\sin\theta/2}{\sqrt{R}} \\ & + \frac{(\gamma+1)M_\infty{}^4}{2\beta_\infty{}^4\, w^2}\Bigg[ \frac{3}{4}\,\frac{\sin 5\theta/2}{R^{5/2}} + \frac{i(\delta - 2w)}{2}\,\frac{\sin 3\theta/2}{R^{3/2}} - \frac{3iw}{4}\,\frac{\sin\theta\cos 5\theta/2}{R^{3/2}} \\ & + \frac{3w^2}{8}\,\frac{\sin^2\theta\,\sin 5\theta/2}{\sqrt{R}} + \frac{(2\delta - 3w)w}{4}\,\frac{\sin\theta\cos 3\theta/2}{\sqrt{R}} + \frac{w(2\delta - w)}{2}\,\frac{\sin\theta/2}{\sqrt{R}}\Bigg]\Bigg\}, \end{aligned} \tag{C.13a}$$

$$I_3(R,\theta) \sim \frac{2\pi\delta}{\sqrt{\delta-w}} e^{R\left(i\delta\cos\theta - |\sin\theta|\sqrt{\delta^2-w^2}\right)} + 2\, e^{iwR\cos\theta - i\pi/4}\,\mathrm{sgn}(\Psi)\,\sqrt{\pi}\left\{\frac{\cos\theta/2}{\sqrt{R}}\right.$$

$$+\frac{(\gamma+1)M_\infty{}^4}{2\beta_\infty{}^4\, w^2}\left[\frac{3}{4}\,\frac{\cos 5\theta/2}{R^{5/2}} + \frac{3iw}{4}\,\frac{\sin\theta\,\sin 5\theta/2}{R^{3/2}} + \frac{i(\delta-2w)}{2}\,\frac{\cos 3\theta/2}{R^{3/2}}\right.$$

$$\left.\left. + \frac{3w^2}{8}\,\frac{\sin^2\theta\,\cos 5\theta/2}{\sqrt{R}} - \frac{w(2\delta-3w)}{4}\,\frac{\sin\theta\,\sin 3\theta/2}{\sqrt{R}} + w(\delta-w)\,\frac{\cos\theta/2}{\sqrt{R}}\right]\right\}, \quad \text{(C.13b)}$$

$$I_4(R,\theta) \sim 2\, e^{iwR\cos\theta - i\pi/4}\sqrt{\pi}\left\{\frac{\sin 3\theta/2}{2R^{3/2}} - \frac{iw}{2}\,\frac{\sin\theta\,\cos 3\theta/2}{\sqrt{R}} - iw\,\frac{\sin\theta/2}{\sqrt{R}}\right.$$

$$\left. + \frac{w^2\sin^2\theta}{4}\sin 3\theta/2\,\sqrt{R} - \frac{w^2}{2}\sin\theta\,\cos\theta/2\,\sqrt{R} + w^2\sin\theta/2\,\sqrt{R}\right\}, \quad \text{(C.13c)}$$

$$I_5(R,\theta) \sim -2\, e^{iwR\cos\theta + i\pi/4}\,\mathrm{sgn}(\Psi)\,\sqrt{\pi}\left\{\frac{\cos 3\theta/2}{2R^{3/2}} + \frac{iw}{2}\,\frac{\sin\theta\,\sin 3\theta/2}{\sqrt{R}}\right.$$

$$\left. - iw\,\frac{\cos\theta/2}{\sqrt{R}} + \frac{w^2\sin^2\theta}{4}\cos 3\theta/2\,\sqrt{R} + \frac{w^2\sin\theta}{2}\sin\theta/2\,\sqrt{R}\right\}. \quad \text{(C.13d)}$$

# APPENDIX D

## LOCAL ANALYSIS OF LEADING-EDGE REGION

In this appendix, we use the elegance of a complex variable to perform a local integration of the inhomogeneous partial differential equation (3.11a) governing the function $H_3$. The objective of this local analysis is to determine the appropriate behavior for $H_3$ in the vicinity of the airfoil leading edge ($\Phi = \Psi = 0$).

The function $H_3$ satisfies the differential equation

$$D(H_3) = \frac{-\sqrt{2}\, w^2 \beta_\infty \sin\theta/2}{\sqrt{R}} H_0 + \frac{(\gamma+1) M_\infty{}^4 \sin\theta/2}{\sqrt{2}\,\beta_\infty{}^3 \sqrt{R}} \left[ \frac{\partial^2 H_0}{\partial \Psi^2} + 2i\delta \frac{\partial H_0}{\partial \Phi} + (w^2+\delta^2) H_0 \right]$$
$$+ \frac{(\gamma+1) M_\infty{}^4 \sin 3\theta/2}{2\sqrt{2}\,\beta_\infty{}^3 R^{3/2}} \left[ \frac{\partial H_0}{\partial \Phi} - i\delta H_0 \right] , \qquad \text{(D.1a)}$$

where

$$D = \frac{\partial^2}{\partial \Phi^2} + \frac{\partial^2}{\partial \Psi^2} + w^2 , \qquad \text{(D.1b)}$$

$$H_0 = \frac{-A_n \operatorname{sgn}(\Psi)}{\beta_\infty 2\pi \sqrt{\delta + w}} \int_{-\infty}^{\infty} \frac{e^{-i\lambda\Phi - |\Psi|\sqrt{\lambda^2 - w^2}}}{(\lambda+\delta)\sqrt{\lambda + w}}\, d\lambda . \qquad \text{(D.1c)}$$

Equations (D.1) were derived utilizing the disturbance wavelength as the appropriate length scale. However, for distances from the leading edge which are small compared to the disturbance wavelength, these equations can be further simplified. In order to deduce the proper simplifications, a new, local length scale which is short compared to the disturbance wavelength could be introduced into the differential equations. It is easily seen that the derivatives then dominate over the constant term in the operator $D$, so that

$$D(H_3) \sim \frac{\partial^2 H_3}{\partial \Phi^2} + \frac{\partial^2 H_3}{\partial \Psi^2} \tag{D.2}$$

for $R = \sqrt{\Phi^2+\Psi^2} << 1$. Next consider the source term. The asymptotic expansion of $H_3$ for $R << 1$ was derived in Appendix C. From Eq. (C.9), we have

$$H_0(R,\theta) \sim \frac{2\, A_n\, e^{i\pi/4}}{\beta_\infty \sqrt{\pi}\, \sqrt{\delta+w}} \sqrt{R}\, \cos\theta/2 \;+\; \text{H.O.T.}\;. \tag{D.3}$$

Utilizing this expansion to evaluate the source term of Eq. (D.1a), we find that this differential equation can be approximated as

$$\frac{\partial^2 H_3}{\partial \Phi^2} + \frac{\partial^2 H_3}{\partial \Psi^2} = \frac{e^{i\pi/4}\, A_n\, (\gamma+1) M_\infty{}^4}{2\sqrt{2\pi}\, \sqrt{\delta+w}\, \beta_\infty{}^3} \frac{\sin 2\theta}{R^2} \tag{D.4}$$

for $R << 1$.

To integrate this differential equation, it is convenient to introduce the complex variable $Z = \Phi + i\Psi$ and its complex conjugate $\overline{Z} = \Phi - i\Psi$. Expressing Eq. (D.4) in terms of $Z$ and $\overline{Z}$, we have

$$4\, \frac{\partial^2 H_3}{\partial Z\, \partial \overline{Z}} = \frac{e^{-i\pi/4}\, A_n\, (\gamma+1) M_\infty{}^4}{4\sqrt{2\pi}\, \sqrt{\delta+w}\, \beta_\infty{}^3} \left[ \frac{1}{\overline{Z}^2} - \frac{1}{Z^2} \right]. \tag{D.5}$$

This equation is easily integrated with respect to $Z$ and $\overline{Z}$, leading to

$$\begin{aligned} H_3 &\sim \frac{e^{-i\pi/4}\, A_n\, (\gamma+1) M_\infty{}^4}{16\sqrt{2}\, \sqrt{\pi}\, \sqrt{\delta+w}\, \beta_\infty{}^3} \left[ \frac{\overline{Z}}{Z} - \frac{Z}{\overline{Z}} \right] + f(Z) + g(\overline{Z}) \\ &= \frac{-\, e^{i\pi/4}\, A_n\, (\gamma+1) M_\infty{}^4}{8\sqrt{2}\, \sqrt{\pi}\, \sqrt{\delta+w}\, \beta_\infty{}^3} \sin 2\theta + f(Z) + g(\overline{Z}) \end{aligned} \tag{D.6}$$

where $f(Z)$ and $g(\overline{Z})$ are functions of integration which represent solutions of the homogeneous equation. Setting $f$ and $g$ equal to zero generates a particular solution which is consistent with the function $H_{3p}^*$ defined by Eq. (3.25). Enforcement of the boundary condition (3.19b) in the local analysis would determine the functions $f$ and $g$, consistent with the local behavior of $H_{3c}$ defined by Eqs. (3.29) and (3.30).

# REFERENCES


Ashley, H. and M. Landahl, *Aerodynamics of Wings and Bodies*, Dover, New York (1965).

Adamczyk, J.J., "Passage of a Swept Airfoil through an Oblique Gust," *J. Aircraft*, 11,281-287 (1974).

Amiet, R.K., "Effects of Compressibility in Unsteady Arifoil Lift Theories," Proc. of a Symposium on Unsteady Aerodynamics, Univ. of Arizona (1975).

Amiet, R.K., "High-Frequency Thin-Airfoil Theory for Subsonic Flow," *AIAA Journal*, 14, 1076-1082 (1976).

Atassi, H.M., "Effect of Loading and Rotor Wake Characteristics on the Acoustic Field of Stator Blades," AIAA paper No. 76-566 (1976).

Babich, V.M. and N.Y. Kirpichnikova, *The Boundary-Layer Method in Diffraction Problems*, Springer-Verlag, New York (1979).

Bender, C.M. and S.A. Orszag, *Advanced Mathematical Methods for Scientists and Engineers*, McGraw-Hill, New York (1978).

Crighton, D.G., "The Kutta Condition in Unsteady Flow," *Ann. Rev. Fluid Mech.*, 17, 411-445 (1985).

Envia, E. and E.J. Kerschen, "Noise Generated by Convected Gusts Interacting with Swept Airfoil Cascades," AIAA Paper No. 86-1872 (1986).

Ffowcs-Williams, J.E. and L.H. Hall, "Aerodynamic Sound Generation by Turbulent Flow in the Vicinity of a Scattering Half-Plane," *J. Fluid Mechanics*, 40, 657-670 (1970).

Ffowcs-Williams, J.E. and D.L. Hawkings, "Sound Generation by Turbulence and Surfaces in Arbitrary Motion," *Phil. Trans. of Royal Soc. A*, 264, 321-342 (1969a).

Ffowcs-Williams, J.E. and D.L. Hawkings, "Theory Relating to the Noise of Rotating Machinery," *J. Sound Vib.* 10, 10-21 (1969b).

Fock, V.A., *Electromagnetic Diffraction and Propagation Problems*, Pergamon Press, New York (1965).

Ginder, R.B. and D.R. Newby, "An Improved Correlation for the Broadband Noise of High Speed Fans," *J. Aircraft*, 14, 844-849 (1977).

Goldstein, M.E., "Unsteady Vortical and Entropic Disturbances of Potential Flows Round Arbitrary Obstacles," *J. Fluid Mechanics*, 93, 209-224 (1978).

Goldstein, M.E., *Aeroacoustics*, McGraw-Hill, New York (1976).

Goldstein, M.E., and H. Atassi, "A Complete Second Order Theory for the Unsteady Flow about an Airfoil due to a Periodic Gust," *J. Fluid Mechanics*, 74, 741-765 (1976).

Goldstein, M.E., B.M. Rosenbaum, and L.U. Albers, "Sound Radiation from a High-Speed Axial-Flow Fan due to the Inlet Turbulence Quadrupole Interaction," NASA TN *D*-7667 (1974).

Howe, M.S., "A Review of the Theory of Trailing Edge Noise," *J. Sound Vib.*, 61, 437-465 (1978).

James, G.E., *Geometric Theory of Diffraction for Electromagnetic Waves*, The Institution of Electrical Engineers, London (1980).

Jones, R.T. and D. Cohen, *High Speed Wing Theory*, Princeton University Press, Princeton, NJ (1960).

Kerschen, E.J. and T.F. Balsa, "Transformation of the Equation Governing Disturbances of a Two-Dimensional Compressible Flow," *AIAA Journal*, 19, 1367-1370 (1981).

Kerschen, E.J. and M.R. Myers, "Perfect Gas Effects in Compressible Rapid Distortion Theory," *AIAA Journal*, 25, 504-507 (1987a).

Kerschen, E.J. and M.R. Myers, "*A* Parametric Study of Mean Loading Effects on Airfoil Gust Interaction Noise," AIAA paper No. 87-2677 (1987b).

Kovasnay, L.S.G., "Turbulence in Supersonic Flow," *J. Aero. Sci.*, 20, 657-674 (1953).

Landahl, M.T., "Theoretical Studies of Unsteady Transonic Flow - IV. The Oscillating Rectangular Wing with Control Surface," Aeronautical Research Institute of Sweden (FFA), Rept. 80 (1985).

Lighthill, M.J., "Drift," *J. Fluid Mechanics*, 1, 31-53 (1956).

Mani, R., "Isolated Rotor Noise due to Inlet Distortion or Turbulence," NASA CR 2479 (1974).

Martinez, R. and S.E. Widnall, "Unified Aerodynamic-Acoustic Theory for a Thin Rectangular Wing Encountering a Gust," AIAA Journal **18**, 636-645 (1980).

Myers, M.R., "Effect of Airfoil Mean Loading on High-Frequency Gust Interaction Noise," Diss. U. of Arizona, (1987).

Myers, M.R. and E.J. Kerschen, "Effect of Airfoil Mean Loading on Convected Gust Interaction Noise," AIAA paper No.84-2324 (1984).

Myers, M.R. and E.J. Kerschen, "Effect of Airfoil Camber on Convected Gust Interaction Noise," AIAA paper No.86-1873 (1986).

Myers, M.R. and E.J. Kerschen, "The Acoustic Field of a Near-Surface Source at Intermediate Distances: *A* Simple Result Using Matched Asymptotic Expansions," *J. of the Acoustical Society of America*, accepted for publication.

Noble, B., *Methods Based on the Wiener-Hopf Technique*, Pergamon Press, New York (1958).

Scott, J.R. and H.M. Atassi, "Numerical Solution of Periodic Vortical Flows About a Thin Airfoil," NASA TM-101998, (1989).

Van Der Waerden, B.L., "On the Method of Saddle Points," *App. Sci. Res.*, B2 (1950).

Van Dyke, M., *Perturbation Methods in Fluid Mechanics*, Parabolic Press, Stanford, Ca. (1975).

Woods, L.C., *The Theory of Subsonic Plane Flow*, Cambridge University Press, London (1961).